ROLLING HILLS RESEARCH
C O R P O R A T I O N

Turboelectric Distributed Propulsion Test Bed Aircraft

LEARN Phase II

Final Report

Contract Number NNX14AF44A

Principal Investigator: Michael Kerho
Rolling Hills Research Corporation
Sept. 15, 2015

420 North Nash Street, El Segundo, CA 90245
www.RollingHillsResearch.com aero@RollingHillsResearch.com
(310) 640-8781 (310) 640-0031 fax

1. Project Summary

A successful TeDP implementation poses significant challenges. The development of a flying sub-scale demonstrator for TeDP concepts and technologies would allow early investigation of complex aerodynamics, propulsion, and systems vital to the success of a TeDP configuration. A flying demonstrator reduces development risk of a larger, dedicated TeDP configuration by testing concepts, performance, and technologies at a smaller and relatively inexpensive scale. Although significant differences in vehicle size, thrust level, Reynolds number and cruise speed exist, several technologies and concepts scale well from the subscale test bed to the full scale aircraft.

Previous research identified a proposed test bed aircraft and then designed and tested a multi-fan boundary layer ingesting model based on the conceptual test bed aircraft TeDP installation.[1] Both a CFD and wind tunnel investigation were performed. The wind tunnel test measured installed fan thrust, inlet distortion, surface pressures, boundary layer profiles, and required fan power for a three fan model based on the full-scale test bed aircraft design. The test also examined the effects of adjacent fan thrust level on neighboring fan performance and distortion.

The Phase II TeDP program focused on the detailed design and examination of a TeDP system for the proposed flying test bed aircraft. The overall objective of the Phase II program was to test a pseudo 3D wind tunnel model with a set of 5 boundary-layer ingesting (BLI) electric ducted fans mounted on a 2D straight wing. The test examined multi-fan effects on aerodynamic/propulsive coupling, BLI, and thrust based circulation effects. Specifically, the effect of thrust levels and mass flow on both the overall wing and sectional aerodynamic characteristics including lift, drag, and pitching moment were investigated. The test also focused on the effect of different thrust levels on the aerodynamics of higher angle-of-attack conditions. The effects of spanwise differential thrust, specifically the effects of changing fan mass flow and spillage on adjacent fan flowfield were studied. Prior to the wind tunnel test, a detailed 2D and 3D computational fluid dynamics (CFD) study was performed to study thrust angle effects and to optimize the inlet and duct geometry, and to choose a thrust angle.

Overall, the experimental results compared well with the computational predictions. All major flowfield features and trends present in the computational predictions were observed in the experimental results. Variations in thrust level between low and high thrust levels showed that while differences in force and moment results exist with thrust level, they are generally smaller than were anticipated based on previous 2D estimations. Changes in lift of 3%-4% between the low and high thrust levels were observed in the CFD, with 5%-6% observed in the experimental data. Differential thrust results showed that the blockage produced by a reduced thrust level fan only affects the adjacent fan, and does not extend beyond the adjacent fan. While minor reductions in lift were recorded, the most significant differential thrust effect was an increase in drag. The Phase II program has produced an extremely unique, first of its kind data set for multi-fan distributed propulsion BLI configurations.

2. Table of Contents

3. Introduction

In order to meet future goals for aircraft efficiency for proposed large reductions in fuel burn, emissions, and noise, next generation aircraft will have to employ new technologies for both aerodynamics and propulsion. One configuration which shows significant promise is the Hybrid Blended Wing Body (HBWB) coupled with a turboelectric distributed propulsion (TeDP) system. The revolutionary TeDP propulsion concept uses electric motor driven fans to provide propulsive thrust, with gas turbine generators providing electric power for the system. The TeDP concept can also be used to with other aircraft configurations.

The TeDP concept has several distinct advantages, including boundary layer ingestion (BLI), re-energizing the wake of the airframe with the fan thrust stream, decoupling the propulsion from the power source, a very high effective bypass ratio, redundancy for increased safety, and differential thrust control for directional stability and trim. There are also significant challenges associated with TeDP, including increased inlet distortion due to BLI. The TeDP concept also leads to very close coupling between the aerodynamics and propulsion of the airframe. Significant interactions exist between the sectional aero performance and thrust level. Changes in thrust and mass flow through the fan affect circulation, spillage, blockage, and stagnation point movement, producing changes in sectional lift and moment. Changes in individual fan thrust can affect adjacent fan inlet conditions, distortion, and performance.

RHRC proposes the development of a distributed propulsion system for a small test bed aircraft. The development of a flying demonstrator for TeDP concepts, systems, and technologies allows early investigation of complex aerodynamics, propulsion, and systems vital to the success of a TeDP configuration. The flying demonstrator reduces development risk of a larger, dedicated TeDP configuration by testing concepts, performance, and technologies at a smaller and relatively cheaper scale. The subscale test bed can be used to study the effects of BLI, aerodynamic/thrust coupling, angle-of-attack, differential thrust on adjacent fan performance and distortion, inlet area design, and power generation topology.

The Phase I program first identified a proposed test bed aircraft and then designed and tested a multi-fan boundary layer ingesting model based on that conceptual test bed aircraft TeDP installation. The test bed aircraft chosen was the TG-14A motor glider. Both a computational CFD and wind tunnel investigation were performed. CFD was used to design and investigate various TeDP challenges for the proposed test bed aircraft. The final wind tunnel test measured installed fan thrust, inlet distortion, surface pressures, boundary layer profiles, and required fan power for a three fan model based on the full-scale test bed aircraft design. The test examined the effects of adjacent fan thrust level on neighboring fan performance and distortion.

Phase II focused on a more detailed design and examination of a TeDP system for the proposed test bed. The overall objective of the Phase II program was to test a pseudo 3D wind tunnel model with a set of 5 BLI electric ducted fans mounted on a 2D straight wing. The test examined multi-fan effects on aerodynamic/propulsive coupling, BLI, circulation effects, and reenergizing the wake with the thrust stream. Specifically, the effect of thrust levels and mass flow on both the overall wing and sectional aerodynamic characteristics including lift, drag, and pitching moment were investigated. The test also focused on the effect of different thrust levels on the aerodynamics of higher angle-of-attack conditions. The effects of spanwise differential thrust, specifically the effects of changing mass flow and spillage on adjacent fan flowfield was also studied. Prior to the wind tunnel investigation, a detailed 2D and 3D computational fluid dynamics (CFD) study was performed to study thrust angle effects and to optimize the inlet and duct geometry. The Phase II program has produced an extremely unique, first of its kind data set for multi-fan TeDP BLI configurations.

The final report will present work completed during the Phase II program. This includes scaling of the proposed test bed aircraft airfoil and fan section to a wind tunnel model scale. generation, development, study, and optimization of a 3D CFD model to continue thrust angle effect studies, inlet geometry optimization, thrust level/mass flow effects, angle-of-attack effects, and differential thrust effects. After detailed development and study of the 3D CFD model, the final wind tunnel test discussed above was performed.

4. Wind Tunnel Scaling

The sub-scale wind tunnel model developed during the Phase II program was tested in the University of Illinois at Urbana-Champaign's (UIUC) Aerodynamics Research Laboratory (ARL) low-speed wind tunnel. The low-speed wind tunnel at ARL is a 3 ft x 4 ft open return type tunnel with a maximum free-stream speed of approximately 140 mph (200 ft/s). Results and lessons learned from the Phase I investigation were used to scale the model, fan and inlet sizes for the new model. Model Reynolds number, boundary layer height to fan diameter, thrust level and mass flow effects were chosen to maximize the applicability/scalability of the results to both the test bed aircraft and a full-scale transport configuration.

4.1. Test Bed Aircraft TeDP Configuration

The proposed test bed aircraft is the TG-14A motor glider. The TG-14A motor glider was selected as an excellent candidate for conversion to an electric aircraft test bed under a previous STTR Phase I study (Contract # NNX11CI08P). The TG-14A was chosen for a combination of factors including aerodynamic performance, available space for batteries and instrumentation, maximum take-off gross weight, and ease of modification. A table showing basic information for the TG-14A is shown in Table 1 with a three-view CAD model rendering of the TG-14A shown in Figure 1.

Aircraft	Manufacturer	Type	# of Seats	Motor
TG-14A	Grupo Aeromot	Motor Glider	2	Rotax 912, 100 Hp
				Propeller
Wingspan	57.3 ft	Max Speed (V_{NE})	132 kts	Hoffman HO-V62R-1/170FA
Length	26.5 ft	Maneuver (V_A)	97 kts	
Height	6.3 ft	Stall	39 kts	Endurance 5 hrs
Width	42.5"			
		Glide Ratio	31-1	
Empty Wt	1334 lbs	Airfoil	NACA 64_3-618	
Takeoff Wt	1874 lbs			

Table 1: TG-14A general information.

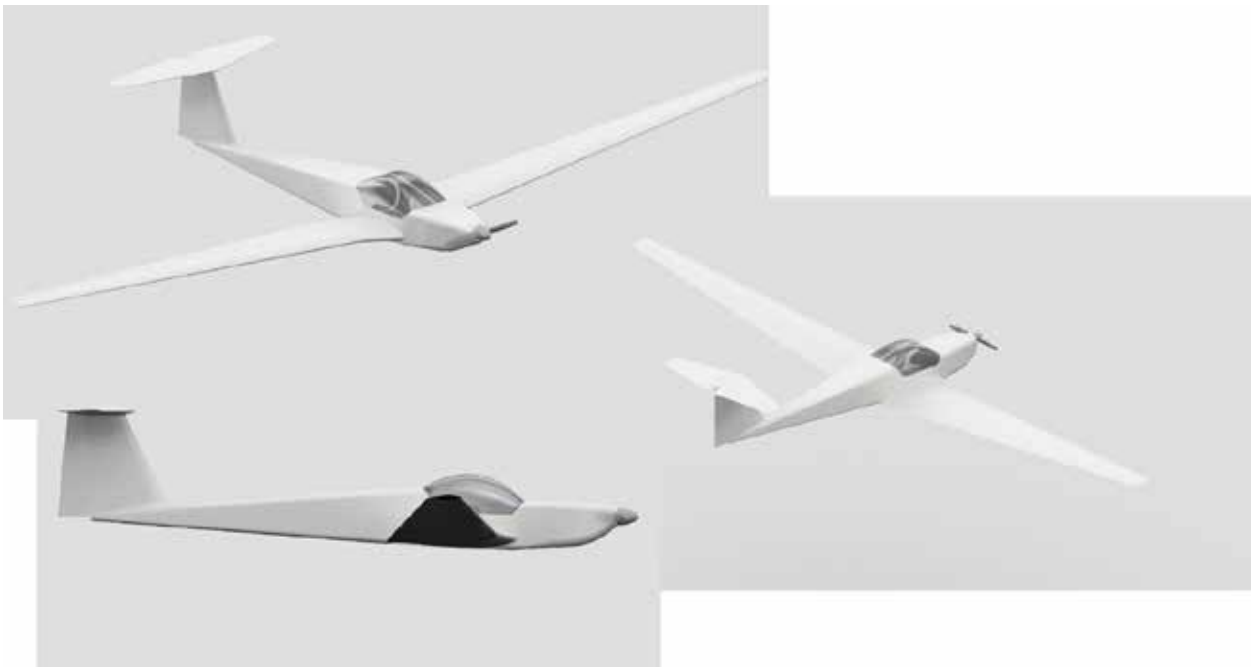

Figure 1: Three-View CAD model rendering of the TG-14A.

Under the Phase I STTR electric aircraft conversion study, a detailed performance model of the TG-14A was developed. This performance model of the TG-14A was used to develop an understanding of the thrust performance required for the converted TG-14A platform. A plot showing the thrust available and required for the TG-14A for a take-off weight of 1,830 lbs and a cruise altitude of 1,000 ft is shown in Figure 2. The baseline engine for the TG-14A is a 100 Hp Rotax 912 with a 67 inch diameter Hoffman HO-V62R-1/170FA propeller, which provides approximately 550 lbs static thrust. From the TG-14A flight manual, maximum cruise speed at 75% power is approximately 97 kts. From Figure 2, to replicate the TG-14A power available at 97 kts, a TeDP propulsion system would have to produce 270 lbs of thrust. For the purposes of this study, the TeDP system designed to replace the baseline TG-14A power plant was sized for a static thrust of approximately 550 lbs with a cruise thrust available at 97 kts of 270 lbs.

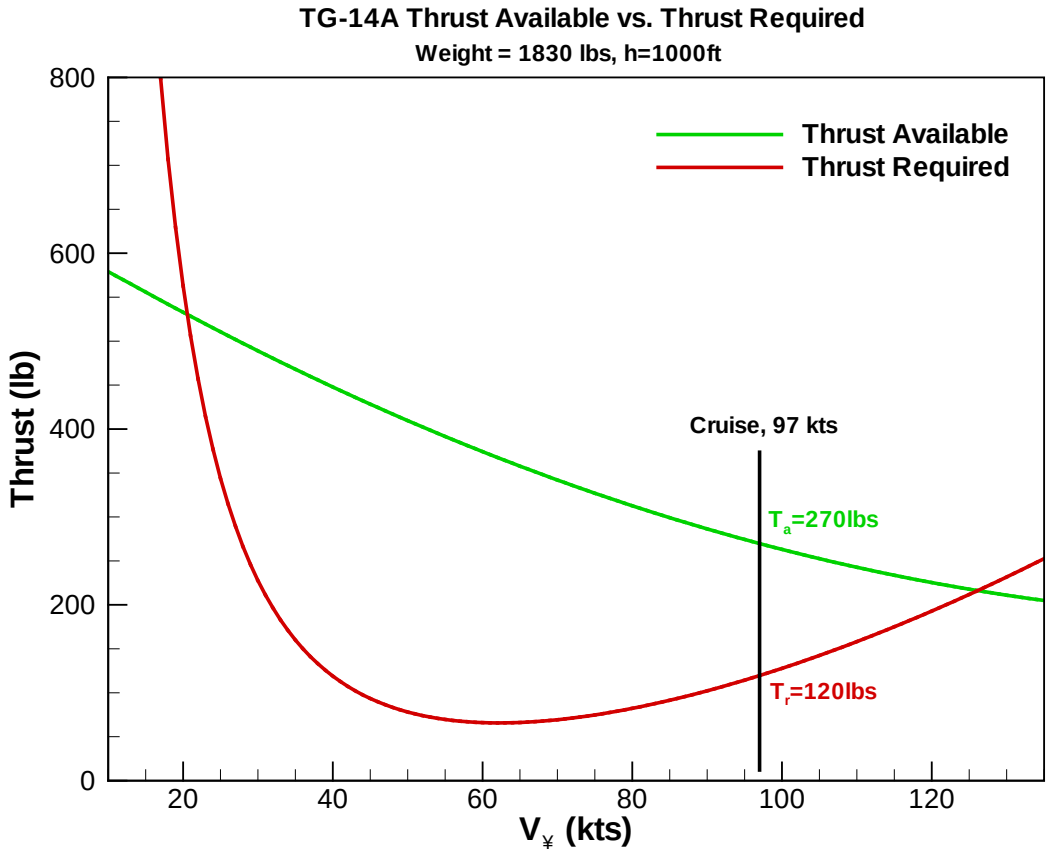

Figure 2: Calculated thrust available and thrust required for the TG-14A aircraft with a take-off weight of 1830 lbs for an altitude of 1000ft.

4.1.1. TG-14A Test Bed Fan Choice

Based on the above analysis, a Schuebeler DS-94-DIA HST DSM6745-700 electric ducted fan (EDF) was chosen for the TG-14A TeDP system. The Schuebeler DS-94-DIA HST DSM6745-700 was chosen as it provided the best combination of thrust level, efficiency, power required, and the number of required units to match the baseline TG-14A power plant performance. The DS-94-DIA HST DSM6745-700 has a fan inner duct diameter of 5.04 inches, for a fan swept area (FSA) of 14.57 in^2. The manufacturer quoted static thrust for the fan is 29 lbs with an input power of 9.8 kW. 18 individual fans are required to replace the TG14A 100 Hp baseline Rotax powerplant. The 18 fans would be split between the two wings, 9 on each side. A ProE mock-up of the notional test bed aircraft with the 9 fans per wing is shown in Figure 3.

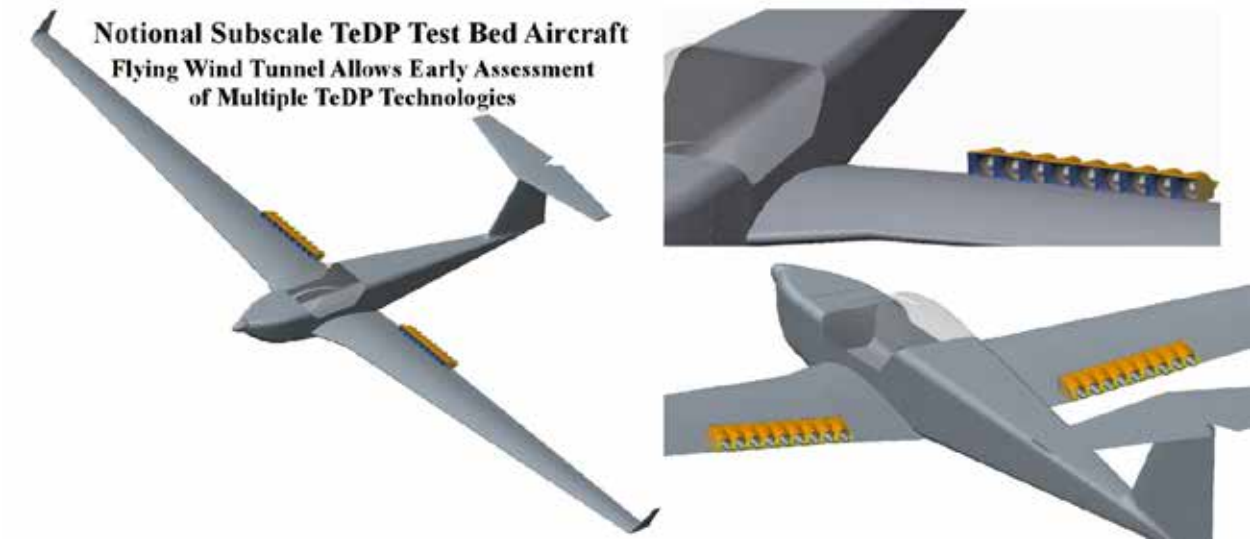

Figure 3: CAD mock-up of notional TG-14A based subscale TeDP test bed aircraft.

4.1.2. TG-14A Airfoil Section and Cruise Conditions

The airfoil section used on the TG-14A is the NACA 64_3-618. The NACA 64_3-618 is an 18% thick section with max thickness at x/c=0.35 and max camber at x/c=0.55. As shown in Figure 3, the initial spanwise location on the wing of the fans is just outside the first break in the wing chord after the side-of-body at y=4.0 ft. The fans are spaced 6 inches on center. The y location of the last fan is at y=8.5 ft. The spanwise locations, local chord lengths, and Reynolds numbers for these locations are shown in Table 2.

EDF Locations	y (ft)	Chord (in)	Reynolds #*
Spanwise Start	4	58.80	5.10×10^6
Spanwise End	8.5	51.06	4.43×10^6
Average	6.25	54.93	4.76×10^6

*Based on 97 kts Cruise Speed

Table 2: Spanwise EDF locations on the proposed TG-14A test bed aircraft.

The average spanwise location of the fans is at y=6.25 ft with a corresponding chord length of 54.93 inches and Reynolds number of 4.76×10^6. This average location was used as the basic cruise condition for the wind tunnel model scaling. In addition to determining the average chord length and Reynolds number, the average cruise C_l at this location was also determined in order to estimate the boundary layer thickness at these conditions. The cruise C_l was estimated using a trimmed vortex lattice model (VLM) developed for the TG-14. The VLM program that was used was AVL (Athena Vortex Lattice), which was written and released from MIT by Mark Drela.[2] AVL is capable of using a VLM to estimate aerodynamic loading, and can perform dynamic analysis on a prescribed aircraft surface configuration. This includes the ability to calculate the

trim conditions of an aircraft and the resulting required control surface deflections based on weight and center-of-gravity location.

Prior to using the AVL code, the geometry of the wing and tail surfaces had to be defined in more detail than were used to develop the ProE model shown in Figure 1 and Figure 3. The geometry of the TG-14A wing and tail were estimated from the scale drawing in the aircraft flight manual,[3] and was implemented in AVL. The scale drawing for the TG-14A is shown in Figure 4.

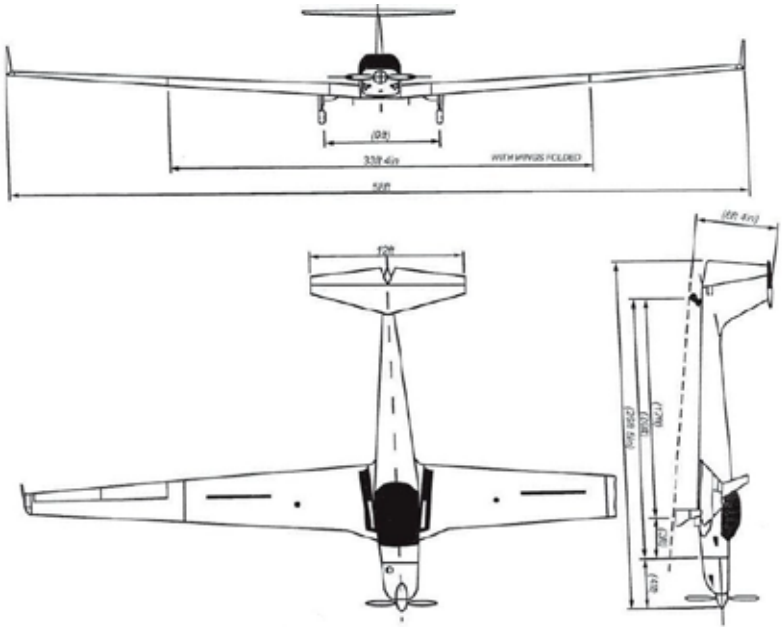

Figure 4: TG-14A scale drawings obtained from the flight manual.[3]

The AVL model generated for the TG-14A is shown in Figure 5. The coordinate system used in defining the aircraft geometry in Figure 5 was defined as having its origin at the firewall. Included in the geometry definition is the elevator on the horizontal stabilizer. The horizontal stabilizer airfoil section is a NACA 65_1-010. The elevator on the horizontal stabilizer varies from approximately 40% chord at the stabilizer root to 50% chord at the tip.

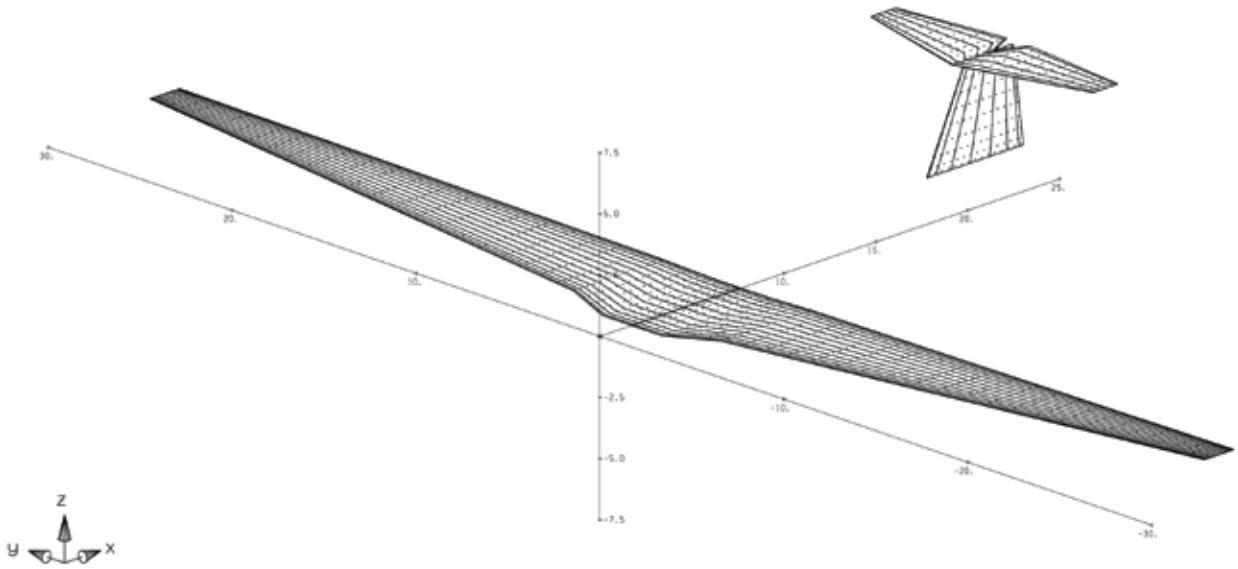

Figure 5: TG-14A wing, horizontal and vertical stabilizer model in AVL.

From AVL, for an aircraft weight of 1,830 lbs, a center-of-gravity location of x_{cg}=4.4 ft, and velocity of 97 kts, the trimmed overall C_L for the aircraft is C_L=0.286. The AVL predicted spanwise wing lift distribution for the TG-14A at cruise conditions is shown in Figure 6. Also shown in Figure 6 is the spanwise area covered by the EDF units and the average C_l over this area, C_{lavg}=0.328.

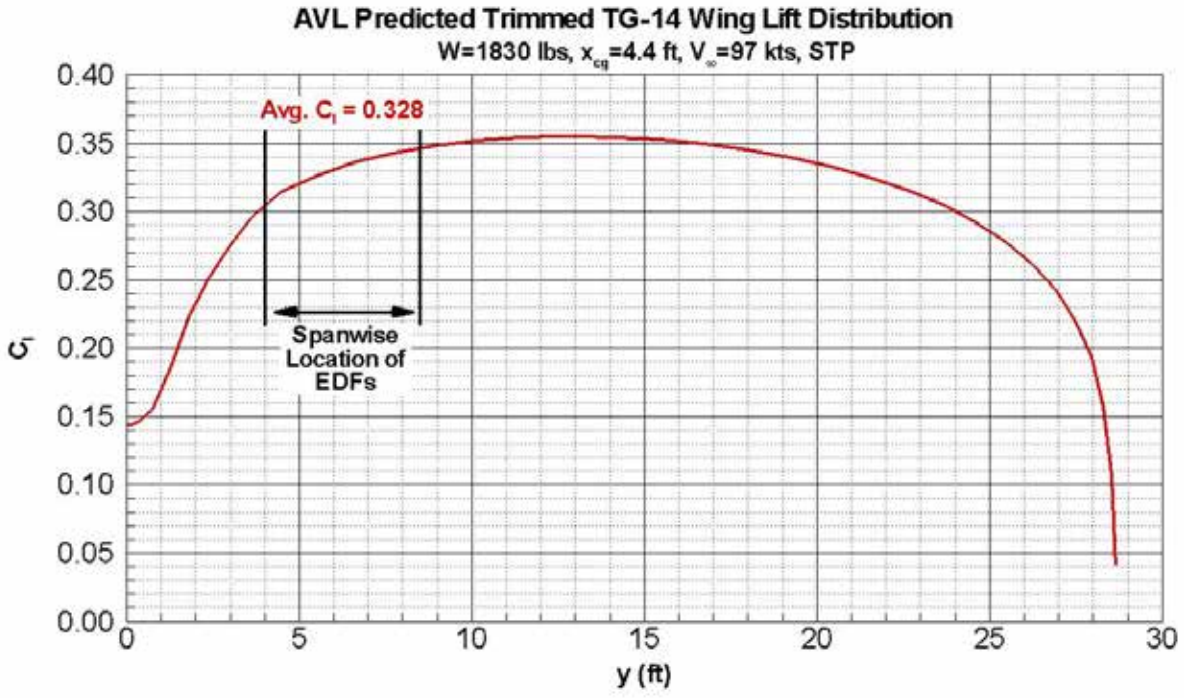

Figure 6: AVL predicted TG-14A cruise spanwise wing lift distribution showing average C_l across EDF location.

The XFOIL analysis and design code was next used to obtain estimates of the airfoil pressure distribution and boundary-layer for the average chord, Reynolds number, and C_l. Transition for the estimates were fixed at x/c=0.05 for both the upper and lower surface. At C_l=0.328, Re=4.76x10^6, the XFOIL predicted pressure distribution is shown in Figure 7.

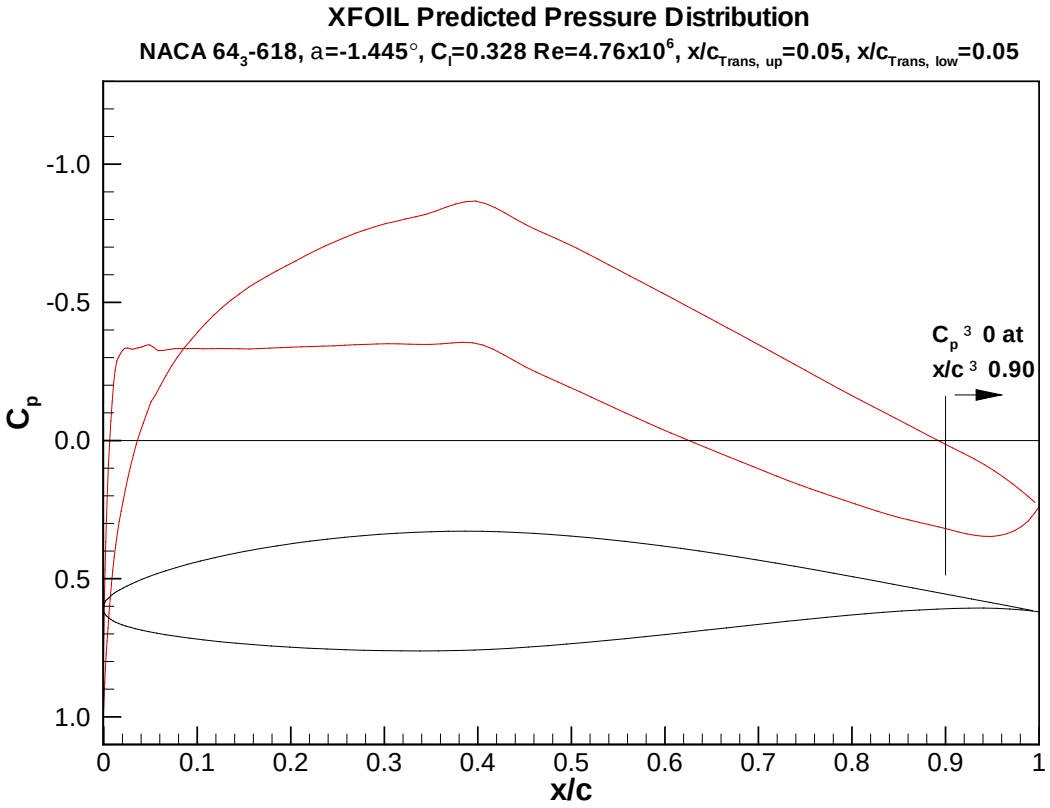

Figure 7: XFOIL predicted pressure distribution for the NACA 64$_3$-618 section at C_l=0.328, Re=4.76x10^6.

From Figure 7, the chordwise location on the upper surface of the embedded EDF should be far enough aft so that the local velocity is as near to free-stream velocity as possible to maximize the fan thrust. At C_ps less than zero on the upper surface, the boundary-layer edge velocity is greater than the free-stream velocity. Since the basic fan thrust is equal to the mass flow through the fan times the difference between the fan exit velocity and the effective inlet velocity, increased inlet velocities reduce the fan net thrust. As a result, the fan should be placed at, or downstream of the x/c location where $C_p \geq 0$. The boundary-layer edge velocity does not approach free-stream until x/c=0.90 on the upper surface. In order to maximize the BLI benefit, the inlet should therefore be placed at x/c=0.90. The XFOIL estimated boundary-layer thickness at this location is approximately d=1.21 inches.

4.2. **Wind Tunnel Model Sizing**

The low-speed wind tunnel at UIUC's ARL is a 3 ft x 4 ft open return type tunnel with a maximum free-stream speed of approximately 140 mph (200 ft/s). The tunnel test section has a width of 4 ft, with a height of 2.8 ft and length of 8 ft. The test section floor and ceiling are parallel, with the test section walls slightly diverging to account for boundary-layer growth on the walls. For 2D airfoil testing, models are mounted vertically in the tunnel, spanning the tunnel floor to ceiling. Performance data can be obtained from a floor mounted balance or surface static pressures and wake rake measurements. 2D airfoil model chords have traditionally ranged from 18 inches to 21 inches. In order to reduce blockage effects and keep tunnel corrections to a moderate level, model chords should be minimized. From Barlow, Rae, and Pope[4], solid blockage levels, defined as the ratio between the model frontal area to the test section area are typically between 1% and 10%, with 5%-7% being relatively common. A plot showing the model solid blockage percentage versus chord length for chords from 18 inches to 22 inches is given in Figure 8. Also included in Figure 8 is a plot showing the corresponding Reynolds number versus tunnel speed for the model chord lengths considered.

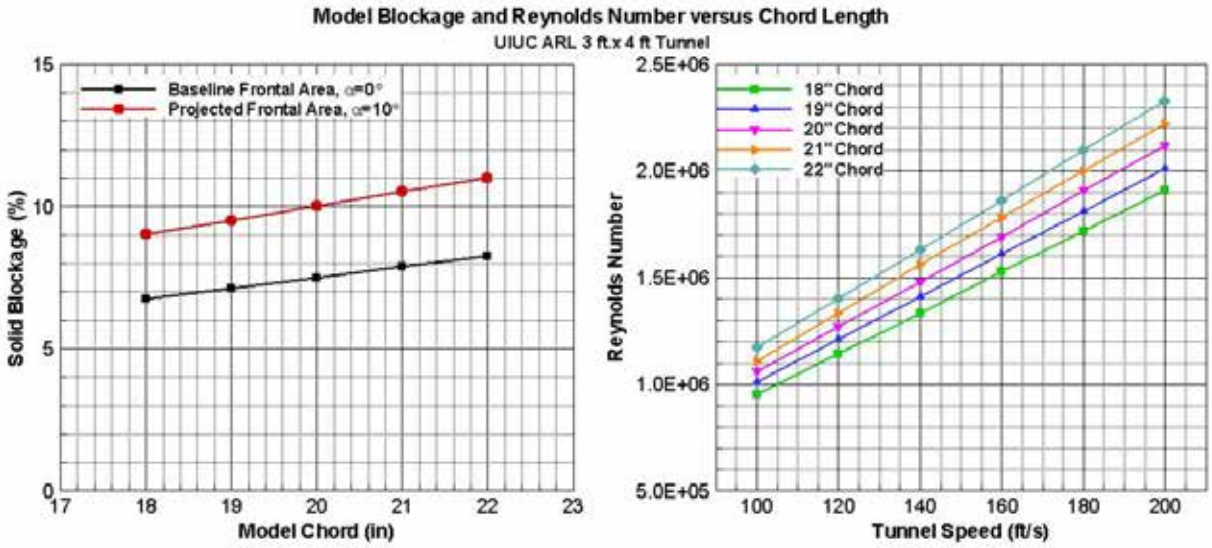

Figure 8: Model solid blockage and Reynolds number versus chord length.

For the solid blockage percentages shown in Figure 8, a baseline blockage using the model frontal area at α=0° is shown along with a solid blockage using a projected frontal area with the model at α=10°. From Figure 8, at α=0° the solid blockage is below 8% for all of the model chord lengths considered. Increasing the model angle-of-attack up to 10°, however increases the blockage percentage by approximately 2.5%. As a result, model chords above 20 inches produce blockages above 10%. The maximum Reynolds number achievable is $Re=2.33 \times 10^6$ for the 22 inch chord model at a tunnel free-stream velocity of 200 ft/s. This Reynolds number is approximately half of the 4.76×10^6 full-scale cruise value, which is unfortunately an unavoidable consequence of sub-scale testing. The use of grit strips to trip the flow at the model leading-edge will help to minimize any Reynolds number differences between the sub-scale wind tunnel model and the full-scale flight vehicle. A 19 inch or 20 inch chord model would appear to

provide a reasonable Reynolds number of Re $\geq 1.5x10^6$ at moderate tunnel speeds with a blockage below 10%.

4.3. **COTS EDF Fans**

Prior to investigating the thrust scaling of the EDF fans for the sub-scale model, a list of currently commercially available off-the-shelf fans was performed. EDF fans come in a range of typical sizes, usually classified by the fan duct inner diameter. These sizes include 40 mm, 50 mm, 55 mm, 65 mm, 70 mm, 80 mm, and 90 mm, and 120 mm. For the proposed sub-scale model, the largest fan sizes investigated were the 70 mm fans. A table showing individual fans across the diameter classes from 40 mm through 70 mm is given in Table 3. Although several manufacturers exist for each diameter class, only the highest thrust performing fans are shown in Table 3. In addition to the static thrust, the required voltage and amperage required to obtain that thrust is given. During the Phase I effort, the large DS-94-DIA HST DSM6745-700 required 52 volts at 130 amps. Due to the high power requirements a reasonable power supply could not be found to power the fans, requiring use of lithium polymer batteries which significantly limited run times and test productivity.

Fan	Manufacturer	Motor	Diam (mm)	T_S (lbs)	Volts	Amps
GWEDF404B	Grand Wing Servo-Tech	BL2013-3	40	0.915	14.8	26.5
Changesun	EDF Hobbies	5200kV Inrunner	50	1.76	11.1	73
Hyperflow	Great Planes	GPMG5185	54.5	1.9	14.8	32.6
VASAFAN 55	VASA	Viper 1030/16	55	1.74	22.8	18.7
DS-26-DIA HDT	Scheubeler	Outrunner	65	4	??	??
DS-30-AXI HDS	Scheubeler	Tenshock	69	4.8	21.5	62
VASAFAN 70	VASA	Mega 16/25/2	70	4.83	22	67

Table 3: Commercially available electric ducted fan units.

From Table 3, in addition to the basic 55 mm and 70 mm fans, a 54.5 mm and 69 mm fan was included. It is interesting to note that the fan diameters generally increase in 5 mm increments, except between 55 mm and 65 mm. This jump in size seems to be the result of switching between inrunner and outrunner motors. Only one or two 60 mm fans were found to exist, both using inrunner motors. These fans were unfortunately found to have poor performance and are not shown in Table 3. Also of significant note is the fact that the static thrust T_s takes a large jump between the 55 mm class and the 65 mm class. This jump in thrust is a result of two primary factors, the first being the switch between inrunner and outrunner motors, and the increase in fan swept area (FSA) between the smaller and larger fans. Due to their smaller FSA, the smaller diameter fans must move significantly more mass flow than the larger fans at a higher speed through a smaller area, making higher thrust levels difficult to achieve as the fan RPM in some of the units shown in Table 3 are operating upwards of 55,000 RPM.

4.4. Thrust Scaling Coefficients

Of primary importance for the project is the thrust scaling between the full-scale TG-14A test bed and the sub-scale wind tunnel investigation. Thrust coefficients can be found for generic propulsors and propeller specific applications. For a generic propulsor, the thrust coefficient is usually defined as[5]:

$$C_T = \frac{T}{q_\infty A_p}$$

Equation 4-1

where q_∞ = free-stream dynamic pressure, T = total thrust, and A_p = propulsor area. For propeller or ducted fan specific applications, the thrust coefficient is slightly different and usually written as[4]:

$$C_{T(prop)} = \frac{T}{\rho V_\infty{}^2 d^2}$$

Equation 4-2

where V_∞ = free-stream velocity and d = propeller diameter. Equation 4-2 is related to Equation 4-1 by a constant, but the value of d is less clear if you use FSA for the propulsor area. Finally, the thrust coefficient for a propeller or ducted fan can also be written as[4]:

$$C_{T(prop)} = \frac{T}{\rho n^2 d^4}$$

Equation 4-3

where n = propeller rotation rate in rev/sec. Equation 4-3 uses the propeller rotation rate, n, where nd can be thought of as the reference velocity and d^2 as the area. Since Equation 4-1 and Equation 4-2 are related by a constant, the only significantly different thrust coefficient is that proposed by Equation 4-3, which incorporates the propeller rotation rate. If the free-stream velocity is chosen based on the advance ratio as defined by $J=V_\infty/(nd)$, then all three equations are essentially equivalent. Since we are replacing the thrust of the TG-14A Rotax with multiple smaller propulsors who's RPM varies significantly from the propeller baseline, the generic thrust coefficient in Equation 4-1 based on dynamic pressure and propulsor area was chosen as the primary thrust scaling coefficient.

The next question to be answered in the scaling process deals with which thrust to scale from, the propeller based thrust of the TG-14A Rotax or the thrust produced by the individual Schuebeler DS-94-DIA HST DSM6745-700 EDF units chosen to replace the Rotax and single propeller. For the DS-94-DIA HST DSM6745-700 EDF, 18 individual units are required to replace the Rotax/propeller. If the Rotax/propeller based system is scaled, to scale from the flight vehicle to the wind tunnel model, the full-scale flight vehicle thrust coefficient is first calculated. The propeller diameter is then scaled to the wind tunnel model size. Finally the new model scale A_p

is calculated and the model scale thrust determined based on the wind tunnel q_∞ (Equation 4-1). This model scale thrust would then be divided by 18 (# of individual fans required to replace the Rotax on the flight vehicle) to arrive at the individual fan scale thrust. The fan is then chosen that is able to physically provide the required thrust that also best matches the full-scale ratio of the boundary-layer height to fan diameter at the fan location (δ/d), and also the ratio of the fan diameter to the wing chord (d/c).

The other option is to scale the thrust produced by an individual DS-94-DIA HST DSM6745-700 EDF unit directly. If the individual DS-94-DIA HST DSM6745-700 thrust is scaled, the sub-scale EDF unit thrust required is determined by calculating the thrust coefficient based on the FSA and thrust of the DS-94-DIA HST DSM6745-700. Since the wind tunnel EDF units used will be one of the commercially available units shown in Table 3 and come in given sizes, the sub-scale fan FSA is set and the thrust required to match the full-scale DS-94-DIA HST DSM6745-700 thrust coefficient at the wind tunnel dynamic pressure is calculated. Then, like the scaling based on the Rotax/propeller, the fan is chosen that is able to physically provide the required thrust that also best matches the full-scale ratio of the boundary-layer height to fan diameter at the fan location (δ/d), and also the ratio of the fan diameter to the wing chord (d/c).

In both cases, the EDF unit is chosen that can physically provide the required scaled thrust and that best matches the δ/d and d/c of the full-scale vehicle. The best combination of these three parameters will provide the most accurate scaled wind tunnel representation and behavior of the full-scale flight system and performance. A significant difference between scaling from the Rotax/propeller based thrust and the individual DS-94-DIA HST DSM6745-700 thrust is that since the propeller diameter scales from the full-scale to the sub-scale model, the sub-scale thrust required to match the full-scale thrust coefficient has some dependence upon the model scale. The scaled thrust varies with the model chord. If the thrust is scaled from the DS-94-DIA HST DSM6745-700, there is no direct dependence on model scale other than trying to match δ/d and d/c. Having the scaled thrust dependent upon the model chord would seem to provide a more physically relevant and preferred approach.

4.5. **Scaling Results**

The scaling of the wind tunnel model was done based on matching the thrust available at cruise for the TG-14A. From Section 4.1, the full-scale thrust available at cruise is 270 lbs, or 15 lbs/fan. Model chords of 18 inches to 22 inches were investigated at tunnel speeds ranging from 100 ft/s to 200 ft/s. For boundary-layer thickness based comparisons, the fan units are assumed to be placed at x/c=0.90 on the model upper surface. Although the preferred approach chosen was to scale using the Rotax/propeller based methodology, scaling from the individual DS-94-DIA HST DSM6745-700 fan thrust was also done for comparison. The scaling was performed for each fan shown in Table 3. All of the fans below the 54.5 mm diameter Hyperflow were found to not physically produce enough thrust to scale by either method for any model chord between the tunnel speeds of 100 ft/s to 200 ft/s. The 54.5 mm and larger fans were found to produce sufficient thrust to properly scale. Scaling results for the 54.5 mm Hyperflow fan are shown in Figure 9. Included in Figure 9 are the thrust required by the fan from both of the

scaling methods, the Rotax/prop based and the DS-94-DIA EDF unit based as a function of tunnel speed. The thrust available produced by the sub-scale fan is also shown. Also included in Figure 9 are plots of d/d and d/c as compared to the full-scale EDF installation, and a plot showing the model Reynolds number. From Figure 9, the scaled thrust required using the fan based thrust coefficient method is independent of the model chord, increases with increasing tunnel speed, and is higher than the prop based thrust coefficient method for all chord lengths investigated. The prop based thrust coefficient also increases with increasing tunnel speed, and increases with increasing model chord. The thrust available from the 54.5 mm Hyperflow fan decreases with increasing tunnel speed as expected. The thrust available from the Hyperflow fan is always less than the thrust required based on the fan related thrust coefficient across the speeds investigated. At the lowest tunnel speeds, around 100 ft/s, the Hyperflow fan thrust available is greater than the prop based thrust required for all of the model chords. At 100 ft/s, model Reynolds numbers range from 0.95×10^6 to 1.17×10^6, with all of the model chord lengths producing d/d values within the 4% of the full-scale vehicle. The ratio of the fan diameter to model chord is larger than the full-scale value for all of the model chords. From Figure 9, a 19" to 20" chord model at a tunnel speed of 100 ft/s would appear to provide a good combination of scaling both the thrust and d/d and d/c ratios at a Reynolds number of at least 1×10^6. Based on the blockage results shown in Figure 8, the 19" to 20" chord would also provide acceptable blockage. The maximum thrust available of the Hyperflow 54.5 mm fan at 100 ft/s is approximately T_a=0.97 lbs, with the thrust required to match the scaled thrust available being T_r=0.67 lbs for the 19 inch chord model and T_r=0.74 lbs for the 20 inch chord model. At the full thrust available of T_a=0.97 lbs, the Hyperflow fan draws 14.8 volts at 32.6 amps, well within the range of a cost effective power supply allowing extended run times.

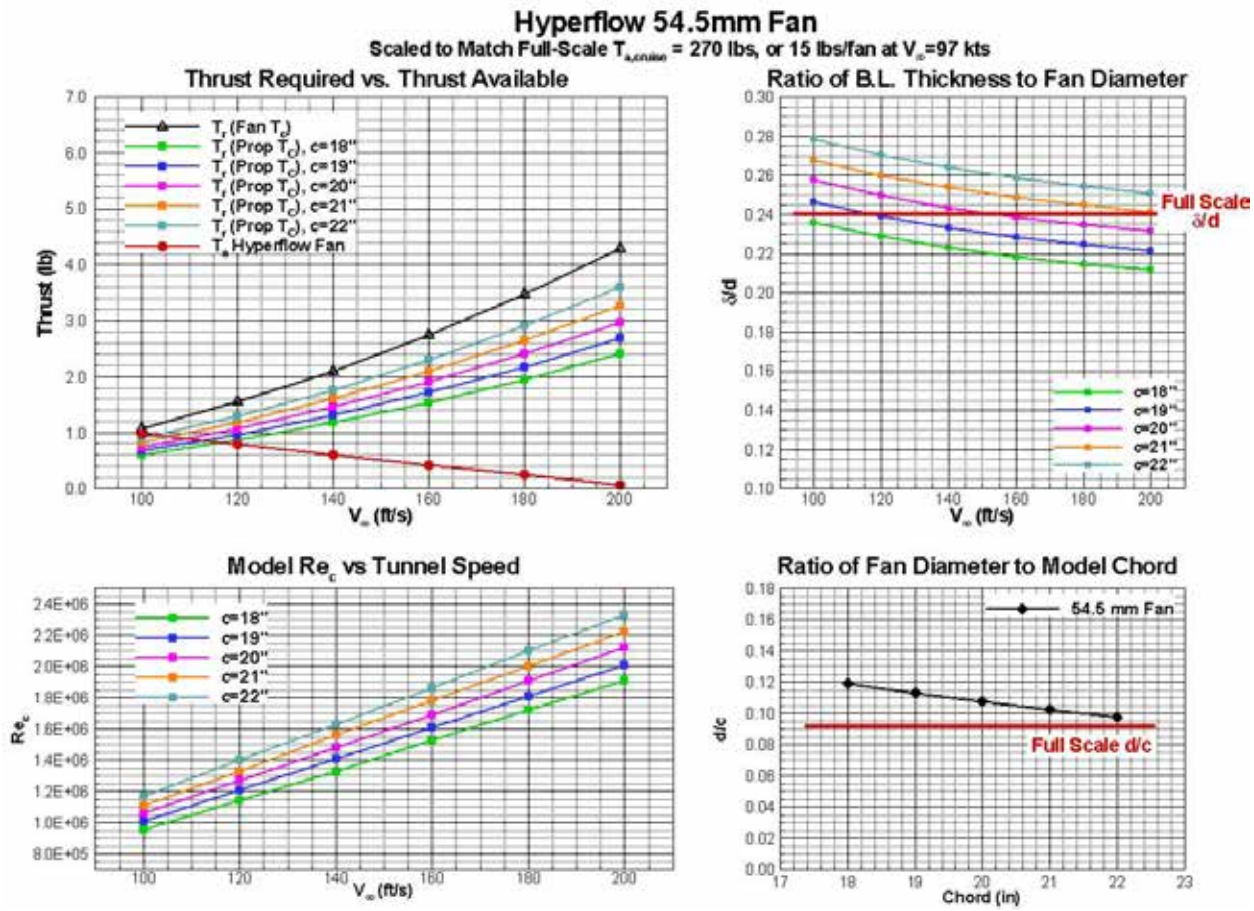

Figure 9: Scaling results for the Hyperflow 54.5 mm EDF unit.

Scaling results for the 65 mm diameter Schuebeler DS-26-DIA HDT fan is shown in Figure 10. From Figure 10, the thrust available from the DS-26-DIA fan is more than double that produced by the 54.5 mm Hyperflow. Whereas the thrust required using the Rotax/prop method does not change with the increased fan diameter, the fan based thrust required is larger than that for the Hyperflow fan. Based on the Rotax/prop method, the DS-26-DIA fan thrust available is greater than the thrust required for all model chord lengths up to a tunnel speed of 140 ft/s, producing a maximum Reynolds number of 1.63×10^6 for the 22 inch chord model. All chords produce δ/d ratios between 2% and 5% below the full-scale vehicle. The d/c values are also larger and further off from the full-scale vehicle than those produced by the Hyperflow fan. A 19 inch or 20 inch chord model at a tunnel speed of 120 ft/s producing a Reynolds number of $Re \approx 1.22 \times 10^6$ would provide a better balance of scaling parameters. At 120 ft/s, the maximum thrust required is well below the thrust available from the DS-26-DIA fan.

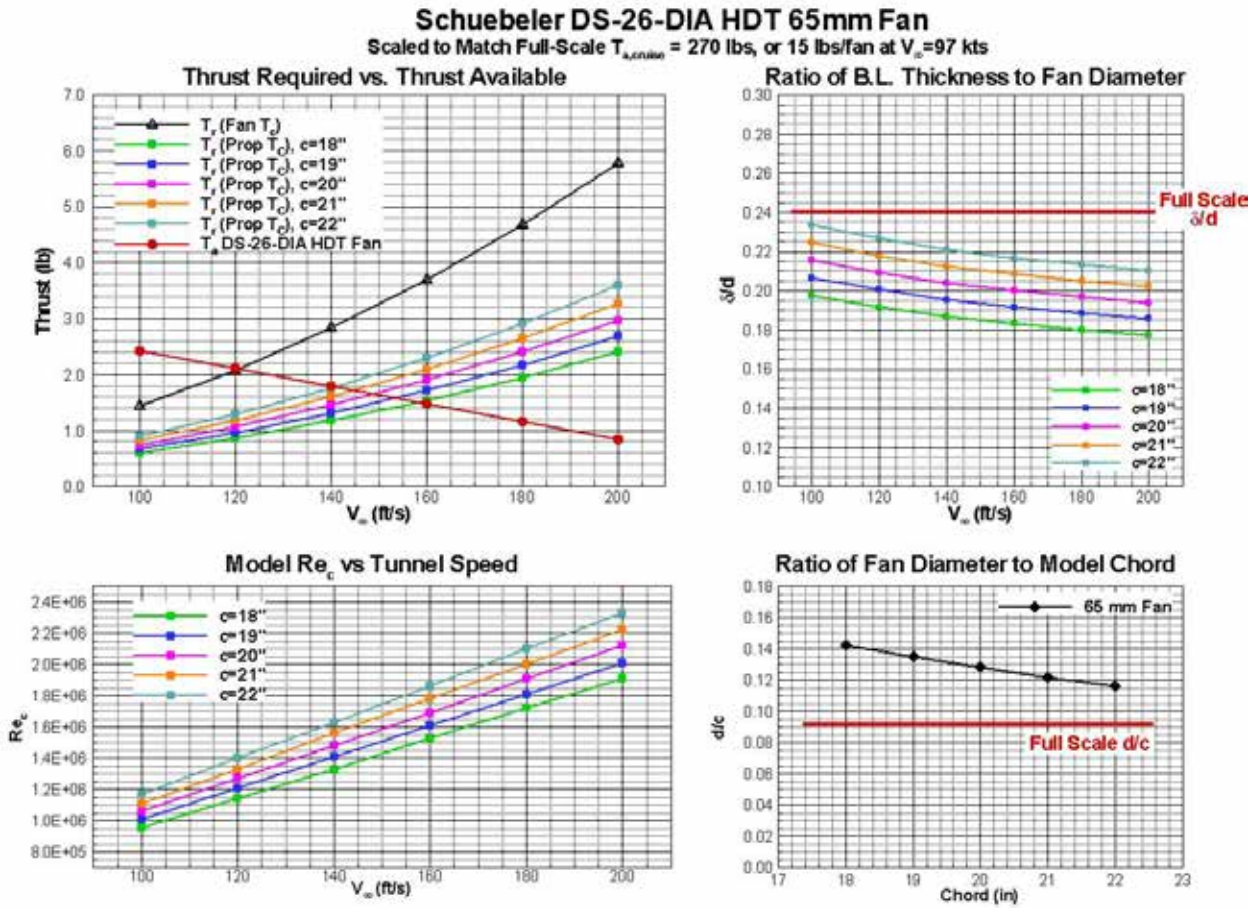

Figure 10: Scaling results for the Schuebeler DS-26-DIA HDT 65 mm EDF unit.

Results for the DS-30-AXI 69 mm and VASAFAN 70 mm fans are shown in Figure 11 and Figure 12. The DS-30-AXI 69 mm and VASAFAN 70 mm produce similar results, with both fans producing a 25% increase in thrust over the 65 mm DS-26-DIA fan shown in Figure 10. Based on the Rotax/prop thrust coefficient, both fans produce adequate thrust for testing at tunnel speeds up to 150 ft/s, increasing the maximum Reynolds number up to Re≈1.75x10^6. Again, however, increasing the fan diameter to 69-70 mm further reduces the d/d ratio below the flight vehicle value, and further increases the d/c ratio above the flight value. A 19 inch or 20 inch chord model at a tunnel speed of 140 ft/s producing a Reynolds number of Re≈1.45x10^6 would provide the best balance of scaling parameters for these fans.

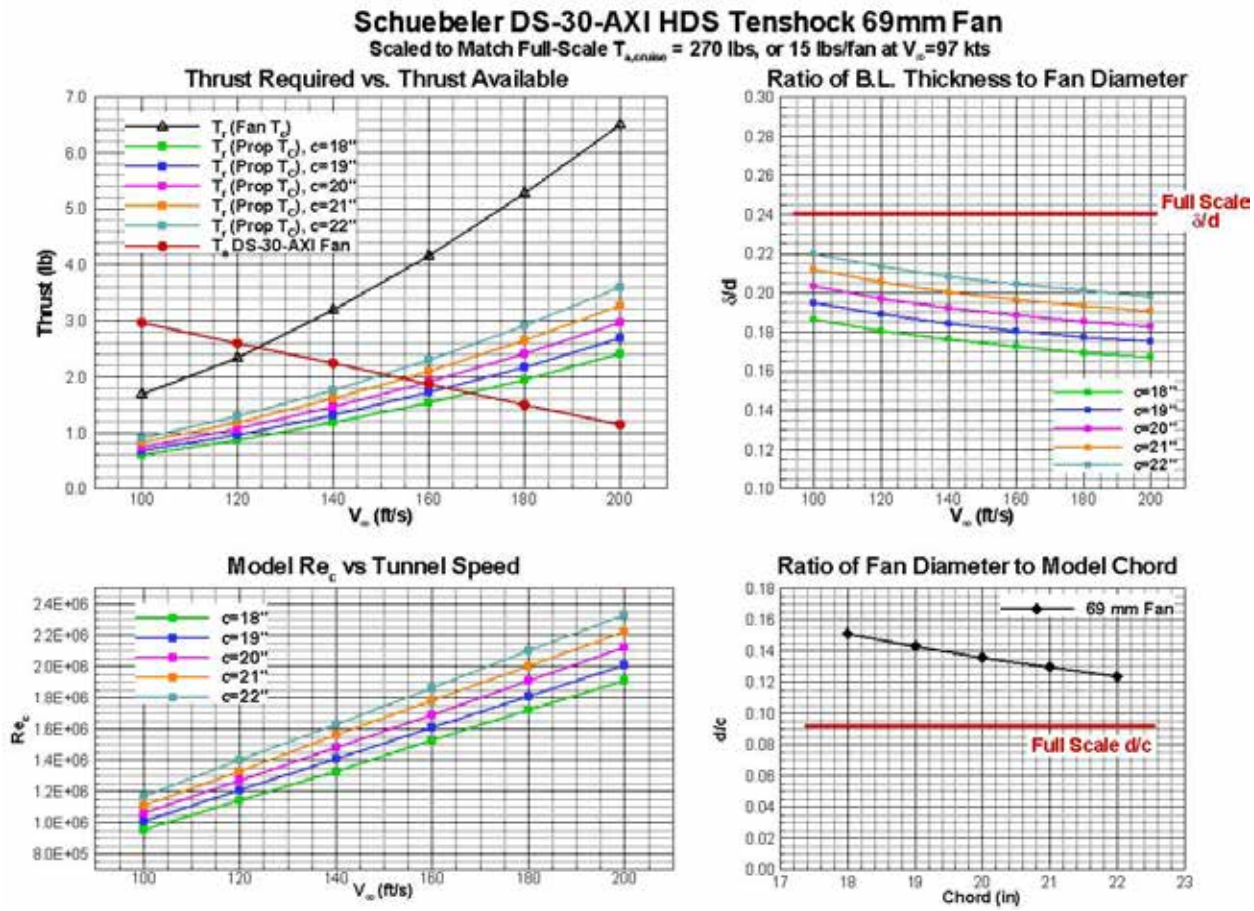

Figure 11: Scaling results for the Schuebeler DS-30-AXI HDS Tenshock 69 mm EDF unit.

Results from the thrust scaling study would indicate that either the Hyperflow 54.5 mm or Schuebeler DS-26-DIA fan would produce adequate thrust while balancing the d/d and d/c ratios. The DS-26-DIA would allow an increase in tunnel speed to 120 ft/s, increasing the model Reynolds number for a 19 -20 inch chord model to Re≈1.22x10^6 from Re≈1.03x10^6 at 100 ft/s. While increasing the tunnel speed from 100 ft/s to 120 ft/s produces a 19% increase in Reynolds number, aerodynamically the increase from 1.03x10^6 to 1.22x10^6 is not that significant. For both Reynolds numbers, however, the boundary-layer will need to be tripped at the leading-edge. The artificial trip will create a slightly thicker boundary-layer than a naturally transitioned flowfield. The thickness of the boundary-layer can also be artificially increased by increasing the size of the trip, making the d/d ratio closer to the full-scale flight vehicle for the larger 65 mm DS-26-DIA fan.

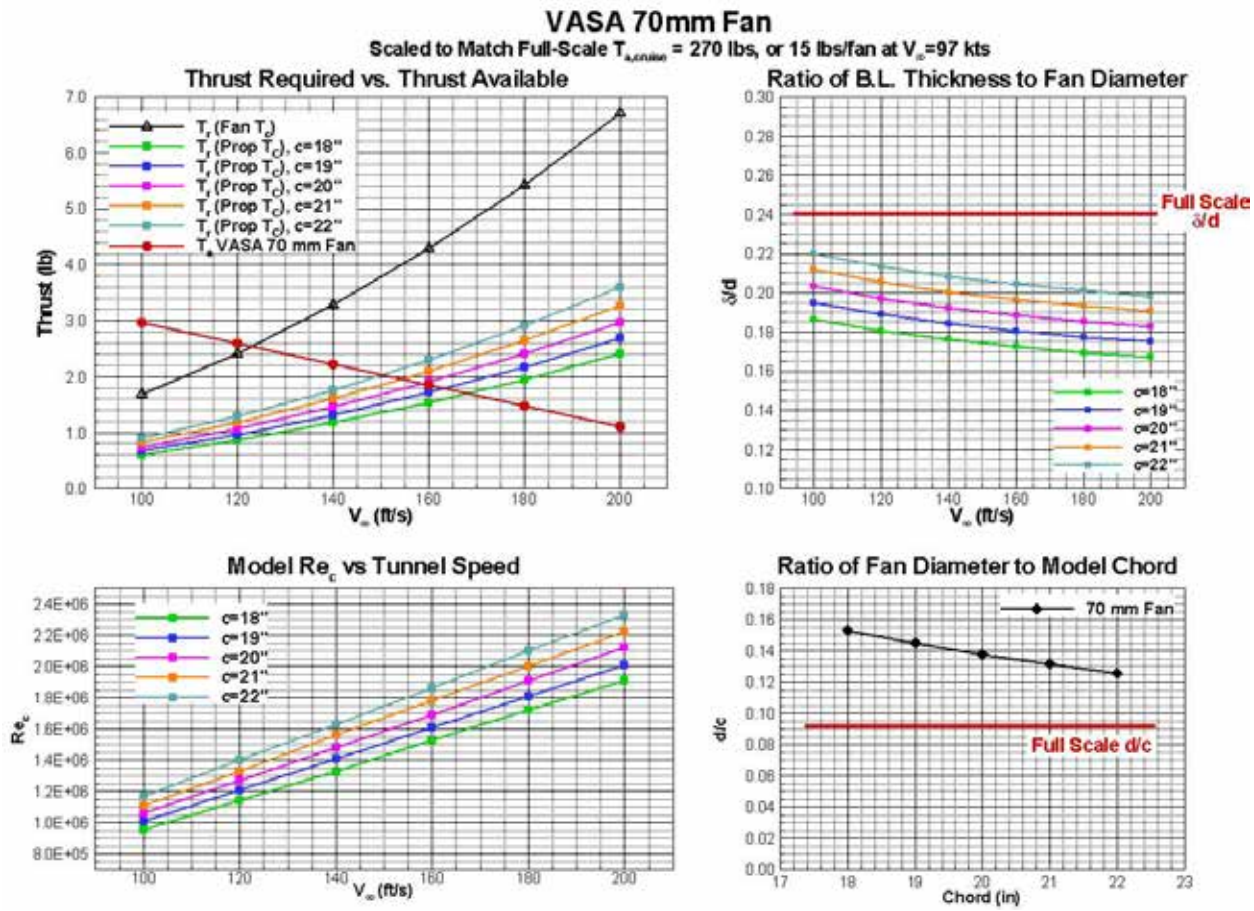

Figure 12: Scaling results for the VASA 70 mm EDF unit.

For static thrust scaling, a modification of Equation 4-1 is used since $q_\infty=0$. As a result, the static thrust is simply scaled by the propulsor area A_p. A plot showing the scaled static thrust as a function of model chord using the Rotax/prop based methodology is shown in Figure 13. Also shown in Figure 13 are the maximum available static thrust values produced by the Hyperflow and DS-26-DIA fans. From Figure 13, the Hyperflow fan static thrust is well below the thrust required to scale correctly for the static case. The DS-26-DIA fan thrust, however, scales well for a 19 or 20 inch chord model. In regards to the static thrust, however, the primary question is whether the static thrust matching is of value for the current program? The current program focuses on aerodynamic/propulsive coupling effects, BLI, circulation effects, and reenergizing the wake with the thrust stream, none of which are affected by the static performance of the fan. While the inlet duct and lip design should account for the mass flow and performance required at static conditions, is it enough of a concern for the current program to eliminate the Hyperflow fan?

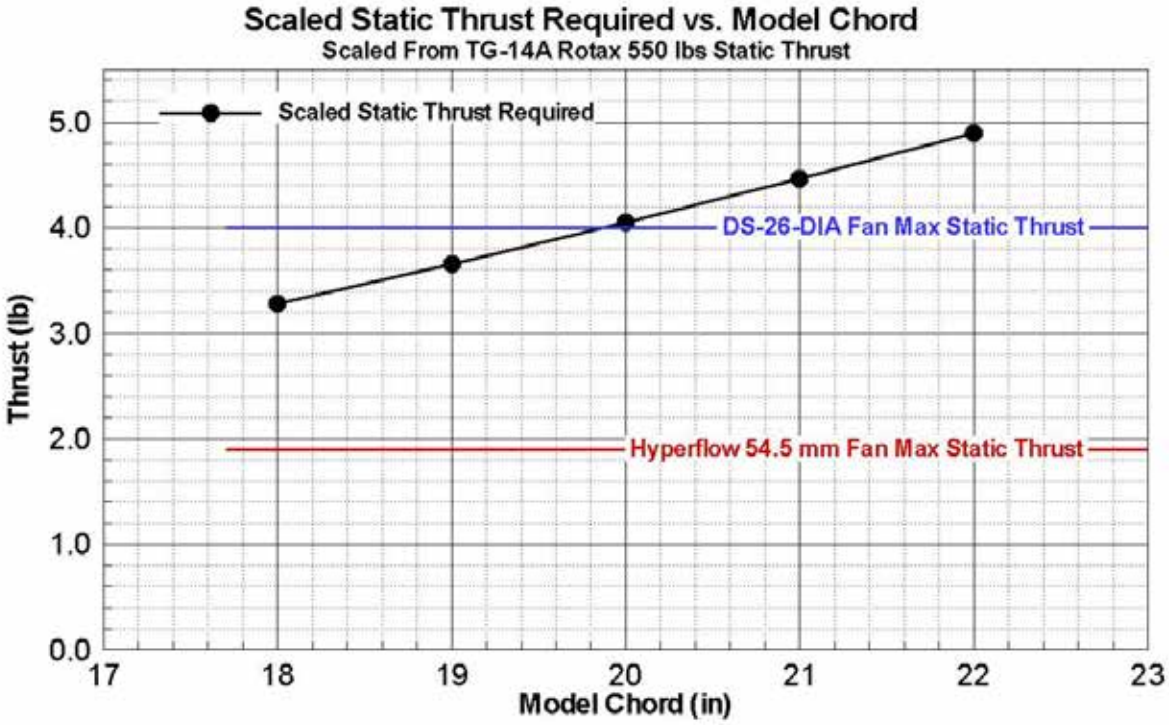

Figure 13: Scaled static thrust required versus model chord.

4.6. **Scaling Summary**

Results from the scaling summary show that multiple commercially available EDF units are capable of providing the thrust required to properly develop a sub-scale wind tunnel model capable of adequately representing the performance and characteristics of the full-scale vehicle. Either the 54.5 mm Hyperflow or 65 mm Schuebeler DS-26-DIA fans coupled with a 19 – 20 inch chord model provide a good combination of thrust, ɗ/d, and d/c ratios at reasonable Reynolds numbers between $Re \approx 1.03 \times 10^6$ to 1.22×10^6. The blockage produced by a 19 – 20 inch chord model is at or below 10% across the expected angle-of-attack range. Finally, the low power required by these fans is well within the capabilities of a moderately priced DC power supply. The above arguments for the Hyperflow fan assume that the static performance of the fan is of a secondary importance to its wind-on scaled performance. Based on the above arguments, the 54.5 mm Hyperflow fan was chosen with a 20 inch chord model for the sub-scale test.

5. 2D Thrust Angle Study

The second task of the Phase II effort was a 2D CFD study using the OVERFLOW CFD code to investigate thrust angle effects on aerodynamic/propulsive coupling in order to minimize coupling effects with changes in thrust/mass flow. Based on the results of the scaling study, a 20 inch cord NACA 64_3-618 model a lift coefficient of C_l=0.328 using the Hyperflow 54.5 mm fan

at free stream velocity of 100 ft/s ($Re=1.06x10^6$) were used as the baseline geometry/flow conditions. As discussed in Section 4.1.2, the fan face was placed at x/c=0.90. For the Hyperflow fan, the external fan diameter is 2.23 in. With an allowance for mounting hardware, an initial inlet width was set at 2.6 in.

5.1. **Baseline Airfoil**

Prior to generating the 2D CFD with the EDF fan system, the basic NACA 64_3-618 airfoil was run in OVERFLOW. The basic airfoil was run to generate a baseline for the aero/propulsive coupling effects and also to benchmark the CFD against available experimental data for the section. The 2D grid for the basic NACA 64_3-618 airfoil is shown in Figure 14.

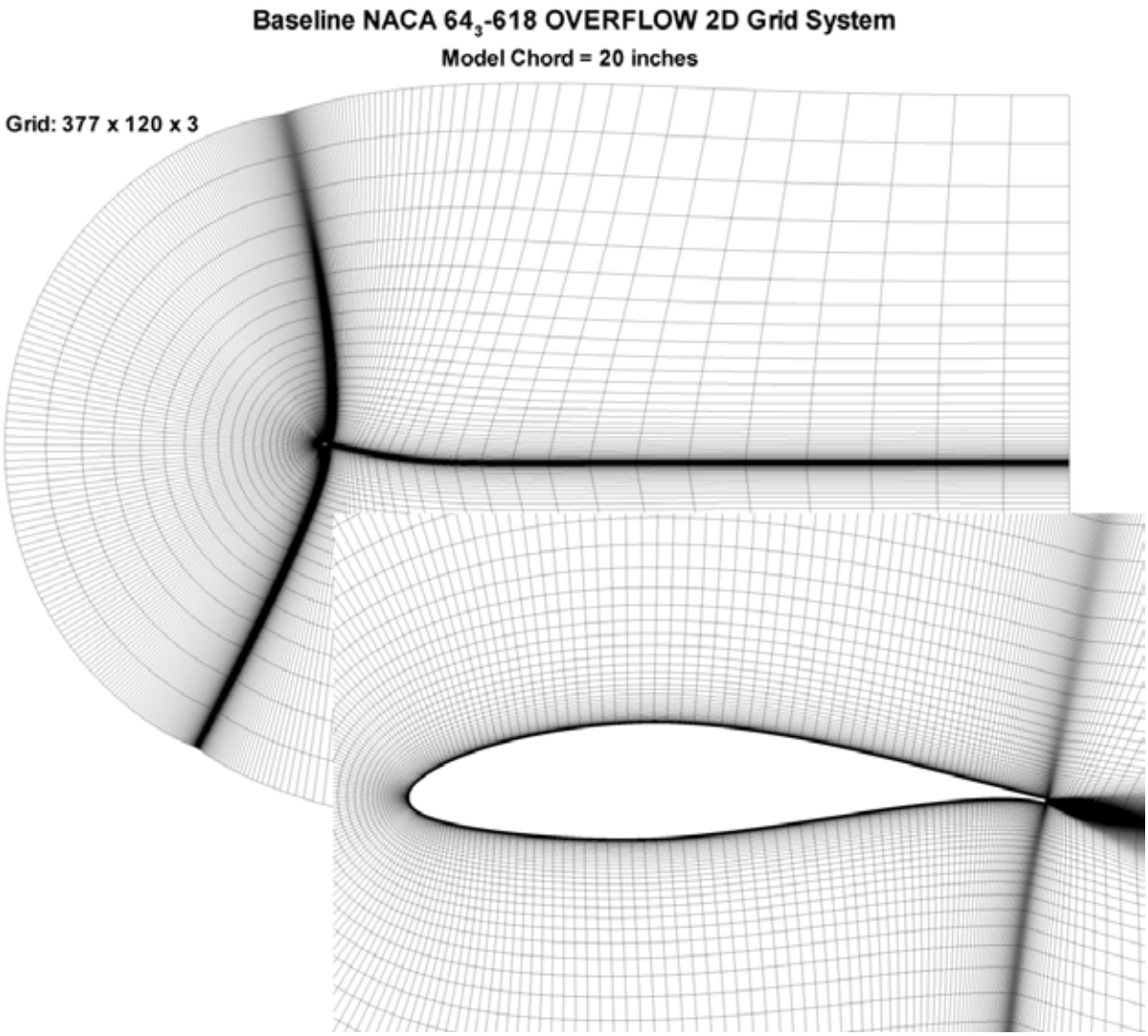

Figure 14: Baseline NACA 64_3-618 2D grid system.

The baseline NACA 64_3-618 airfoil was run using OVERFLOW 2.2e at Re=1.06x10^6 at angles-of-attack from a=-6° to 10°. Due to the low Reynolds number and Mach number (M=0.09), low-Mach preconditioning was used. The model was run fully turbulent using the Spalart-Allmaras turbulence model. Results were compared to experimental data found in Abbott and VonDoenhoff.[6] The data from Abbott and VonDoenhoff were obtained for a free transition case at Re=3.0x10^6. A comparison of the OVERFLOW predicted results and the experimental data from Abbott and VonDoenhoff is shown in Figure 15.

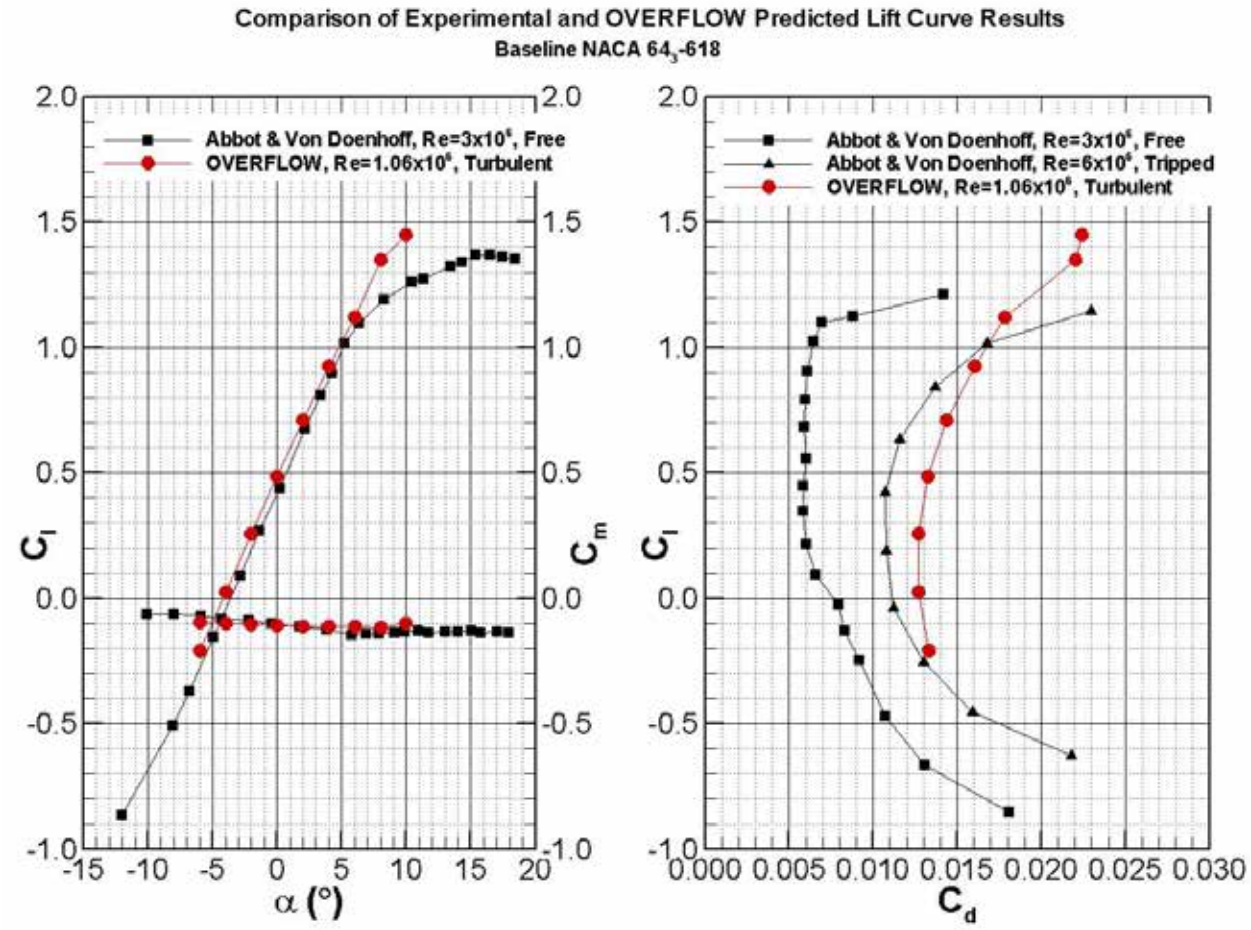

Figure 15: Comparison of OVERFLOW predicted and experimental results for the baseline NACA 64_3-618 section.

From Figure 15, for the linear portion of the lift curve, the OVERFLOW and experimental C_l and C_m data compare well, with a slight offset in lift curve denoting an absolute angle-of-attack offset. The stall behavior for the OVERFLOW and experimental data are clearly different, with OVERFLOW over predicting C_{lmax}. The higher Reynolds number of the experimental data (Re=3x10^6) should produce a higher C_{lmax} than the OVERFLOW data (Re=1x10^6). The free transition of the boundary-layer of the experimental results will also have a positive effect on C_{lmax}, producing a higher C_{lmax} than a fully turbulent boundary-layer, assuming laminar flow exists for the experimental set-up. The difference in C_{lmax} might also be due to the ability of the

low-Mach preconditioning to properly account for the very low Mach number. At low Mach numbers, the eigenvalues of the Navier-Stokes equations become widely separated and the equation set becomes stiff,[7] affecting the accuracy of the solution. Preconditioning is used to scale the eigenvalues in an attempt to remove this stiffness and improve the accuracy of the solution. The majority of the discrepancy between the OVERFLOW predicted and experimentally measured C_{lmax} can most likely be attributed to the usual CFD scapegoat of weaknesses in the turbulence model poorly predicting separated flows.

For the drag results, in addition to the free transition $Re=3.0x10^6$ experimental results, an additional experimental set at $Re=6.0x10^6$ is shown, which is tripped. As Reynolds number increases, the C_d value will decrease. Based on the Reynolds number differences between the OVERFLOW and experimental results, the OVERFLOW predicted C_d values appear reasonable.

Overall, other than the over predicted C_{lmax}, the OVERFLOW and experimental results for the baseline NACA 64_3-618 compare relatively well. The baseline NACA 64_3-618 airfoil results provide a benchmark for the aero/propulsive coupling effects to be studied with the EDFs modeled.

5.2. Initial Inlet Cowl Lip Sizing

Prior to the 2D CFD study, a basic inlet sizing was performed. The 2D inlet for the EDF was sized based on a rough estimation of the mass flow through the fan. After sizing the inlet height, an initial sizing for the upper cowl inlet lip was performed. As opposed to the inlet area sizing which is based on the mass flow of the fan and the ingested boundary-layer, the inlet lip sizing is based more on empirical rules-of-thumb. From Raymer[8], the cowl lip radius has a major influence up both engine performance and aircraft drag. For subsonic inlets, a large lip radius tends to minimize distortion, especially at high angles-of-attack and side-slip angles. The large lip radius also better accommodates changes in mass flow with variations in thrust level. For subsonic inlets, the lip radius ranges from 6-10% of the inlet radius. Also, for subsonic inlets, the lip radius is generally larger on the inside of the lip, than on the outside of the lip.[8] These values were checked against a boundary-layer ingesting inlet concept designed for the BWB and tested by Owens et al[9] and found to be of the same magnitude.

For the current design, the inlet lip is based on an ellipse with a different inner and outer lip radius. These radii, and the thickness of the lip are based on a percentage of the inlet radius, where the inlet radius is defined as half of the inlet height. A schematic of the inlet lip geometry is shown in Figure 16. For the baseline geometry, the outer lip radius was set at 4% of the inlet radius, with the inner lip radius set at 8% of the inlet radius. The lip thickness was set at 12% of the inlet radius. For the 2D study, an inlet height of 2.69 inches was used.

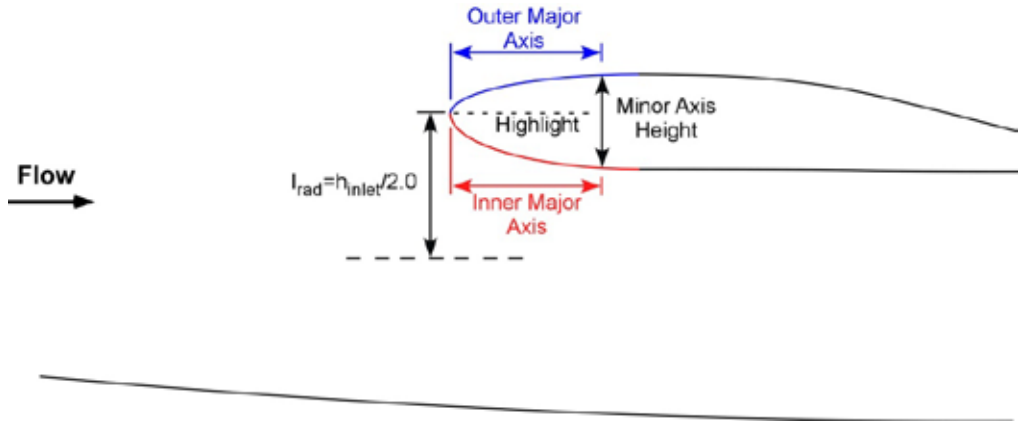

Figure 16: Inlet cowl lip schematic.

5.3. **Baseline 2D Model With EDF**

For the baseline 2D grid with the EDF installed, a thrust angle of 5° was used. This initial thrust angle was arrived at by interrogating the baseline airfoil results discussed in Section 5.1 to estimate the flow angle at the model trailing-edge. An inlet height of 2.69 in was used for the 2D study. An outer inlet lip radius of 4% of the inlet radius and an inner lip radius of 8% of the inlet radius was used to define the cowl lip along with a lip thickness of 12% of the inlet radius. The Hyperflow fan was modeled. Since no detailed drawings of the Hyperflow fan were available, dimensions were scaled off drawings for the fan length and fan plug.

5.3.1. Baseline EDF Grid System

For 2D grids in OVERFLOW, the grid is oriented so that the flow is in the X-Z plane. Three identical planes are used in the Y direction. The spanwise spacing of the planes is generally set at ±1 grid unit, which for the current model was ±1 inch. A boundary condition is used to produce a 2D flowfield for the 3D grid. A scripting system was used to generate the grid system based on an input file allowing various parameters to be changed. The script system uses Chimera Grid Tools and in-house written Fortran routines to generate the surface geometry and volume grid system. The scripting system allows very quick changes in geometry parameters to be studied. For the 2D grid system, these input parameters included the inlet height, EDF thrust angle, fan x/c location, and the inlet cowl lip geometry inner and outer radius and lip thickness. A schematic of the baseline 2D EDF grid system with a 5° thrust angle is shown in Figure 17.

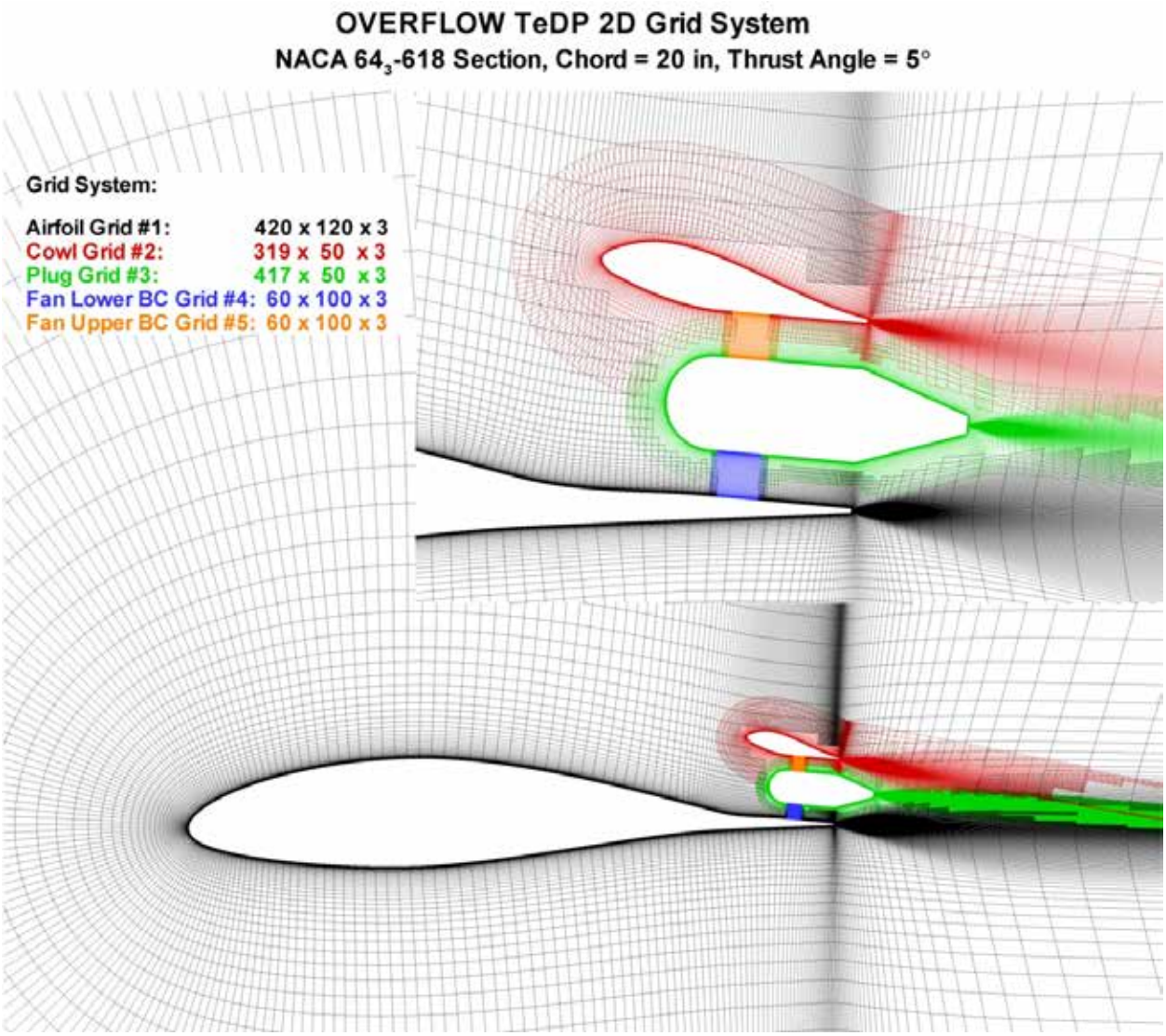

Figure 17: 2D NACA 64_3-618 EDF grid system with a 5° thrust angle.

From Figure 17, the 2D EDF OVERFLOW grid system consists of 5 grids. The main airfoil, fan cowl, fan plug, and an upper and lower fan boundary condition (BC) grid. The fan thrust is modeled using an actuator disk boundary condition that produces a prescribed DP at the BC location. This condition was most easily implemented using two separate grids on either side of the fan plug. Since the fan face is located at x/c=0.90 (x=18 in), the actual fan body and plug extend slightly beyond the 20 inches of the baseline model chord. For the 5° thrust angle shown in Figure 17, the plug end sits at 22.87 in.

5.3.2. Baseline EDF Results

The fan thrust is set using the actuator disk BC. As previously discussed, the actuator BC produces a DP at the prescribed BC location. The DP mimics the pressure rise across the fan. An initial guess at the correct DP for a given thrust level/mass flow can be obtained from

T= $\Delta P A_{exit}$. After an initial run, the ΔP is adjusted until the desired thrust/mass flow is obtained. When setting the thrust for the 2D cases, however, the differences between the 3D and 2D geometry need to be accounted for. For the 3D case, the fan and exit are circular, with the fan swept area (FSA) being the circular area between the motor plug and the fan radius. For the 2D case, however, the area is now a rectangular box comprised of the areas above and below the plug. Recall, that for the 2D boundary condition in OVERFLOW, the grid is made up of 3 spanwise planes, where the planes are set at ±1 grid unit, which for the current model is ±1 inch. As a result, the width of the fan area is 2 inches, combined with a height of 0.536 inches above and below the plug, producing an equivalent area of 2.14 in^2, as opposed to the circular 3D FSA=2.71 in^2. As a result of these differences, for the 2D simulations the thrust per unit width was matched between the 3D and 2D cases. For the 3D case the fans are separated by the inlet width. Assuming an inlet width of 2.6 inches, the thrust per unit width for the thrust available 3D case is then $T_{a(3D)}$=0.742 lbs/2.6 in = 0.285 lbs/in. For the 2D model, with a 2 in width, the equivalent thrust per unit width becomes $T_{a(2D)}$=0.285 lbs/in x 2 in = 0.571 lbs. For the baseline 2D EDF case, the ΔP was adjusted so that thrust available was $T_{a(2D)}$= 0.571 lbs. The equivalent 2D thrust required is $T_{r(2D)}$= 0.254 lbs. For thrust bookkeeping, the cowl and plug are included in the force integration.

$$T = \dot{m}_{fan}(v_{exit} - v_{Inlet}) + (P_{exit} - P_{\infty})A_{exit} - Drag_{Cowl} - Drag_{Plug}$$

Equation 5-1

Mach contours and streamlines for the model at the thrust available case for α=0°, Re=1.06x10^6, V_∞=100 ft/s is shown in Figure 18. From Figure 18, the Mach contours and streamlines show a well behaved flowfield with no apparent separation upstream of the fan, on the cowl, or in the inlet. The only separated flow appears to be just downstream of the plug end as would be expected due to its truncated shape. The presence of the boundary-layer upstream of the inlet is clearly visible in the Mach contours. From the flowfield streamlines, the incoming stream tube appears to be slightly smaller than the inlet height. At the lower mass flow thrust required case, the incoming stream tube will increase in height, most likely moving outside of the cowl highlight. The large cowl leading-edge, however, should be able to accommodate the larger capture area. The calculated thrust for the case shown in Figure 18 is T = 0.564 lbs, which compares well to the $T_{a(2D)}$= 0.571 lbs desired. Table 4 shows the results of the thrust bookkeeping for the thrust available case:

Case: Thrust Available	
α=0°, V_∞=100 ft/s, Re=1.06x10^6	
$T_{\dot{m}}$ (lbs)	0.736
$T_{\Delta P}$ (lbs)	-0.147
Cowl Drag (lbs)	0.0105
Plug Drag (lbs)	0.0145
T_{total} (lbs)	0.564

Table 4: Thrust breakdown, thrust available case, α=0°, Re=1.06x10^6, V_∞=100 ft/s.

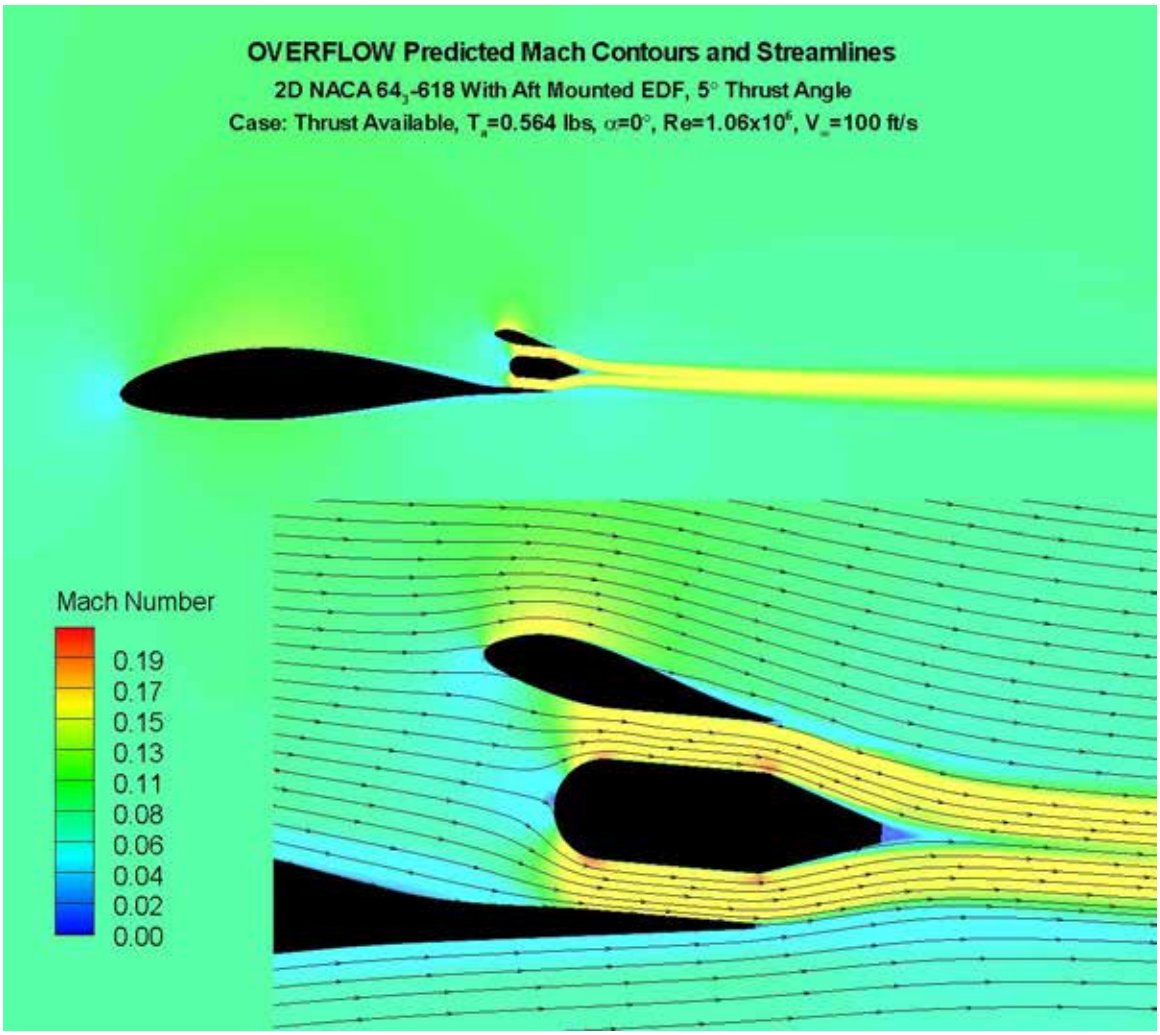

Figure 18: OVERFLOW predicted Mach contours and streamlines for the 2D NACA 64_3-618 EDF section with a 5° thrust angle, α=0°, Re=1.06x10^6, V_∞=100 ft/s.

Figure 19 shows the lift and pitching polars for an angle-of-attack sweep from α= -6.0° to 10.0° at the fan DP and mass flow conditions for the thrust available condition as set by the α= 0.0° case. The lift and pitching moments shown in Figure 19 are based on surface integrations of the pressure and shear forces and do not include the momentum based thrust effects. The lift and moments shown are for the complete airfoil+cowl+plug. The lift and moment results for the EDF geometry have been reduced with two different reference lengths/areas for comparison, one using the baseline airfoil reference length and area, and one using the actual EDF extended chord reference length and area. Usually, when planform modifications are made to a geometry, the baseline reference length/areas are used when comparing the results. Both reductions for the EDF geometry have been shown in Figure 19 to better understand the EDF thrust effects. From Figure 19, the lift curve for the EDF equipped section reduced using the baseline reference areas is rotated counter-clockwise from the baseline section. The pitching moment results for the baseline reference length/area show a more negative pitching moment for all of the angles-of-attack run. The general trend of the pitching moment is that the EDF based C_m is observed to

become more negative as compared to the baseline section with increasing angle-of-attack. One might be tempted to assign various flow related phenomena to the rotation of the lift curve and more negative pitching moment until noting the data re-reduced using the section's actual reference length and area. Using the EDF section's actual length and reference area, the large rotation of the lift curve is greatly reduced. The lift curve is still rotated, but to a much lesser degree. The moment results, however, still show a pronounced more negative increase which increases with increasing angle-of-attack. The differences between the lift and moment results for the EDF and baseline cases are better understood by examining the surface pressures for each case.

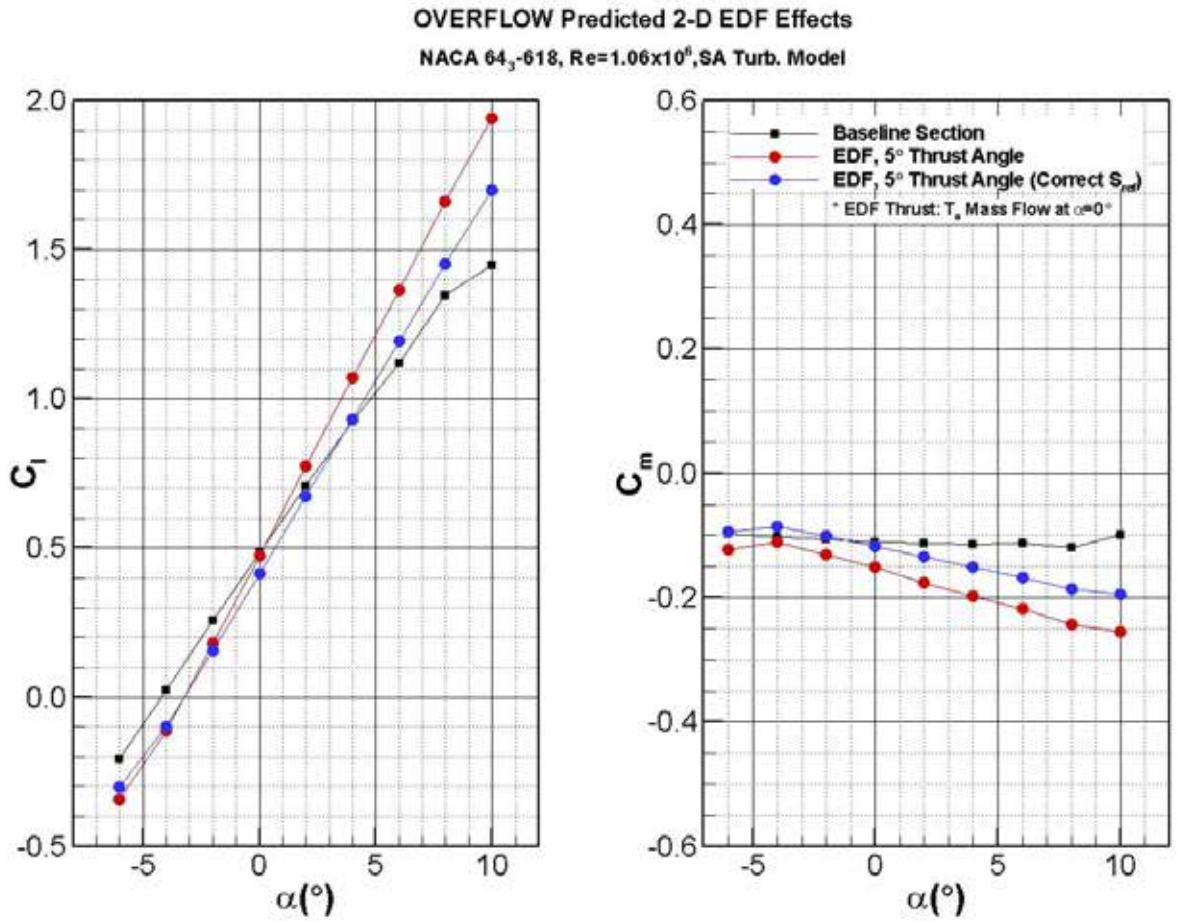

Figure 19: OVERFLOW predicted lift and pitching moment polars for the baseline and 5° thrust angle EDF 2D NACA 64₃-618, a=0°, Re=1.06x10⁶, V∞=100 ft/s.

A comparison of surface pressures for the main airfoil for the baseline and EDF geometry for the polar shown in Figure 19 are given in Figure 20. From Figure 20, the large increase in negative pitching moment is a result of the accelerated flow over the trailing-edge of the airfoil created by the EDF. At the low (negative) and higher angles-of-attack, increased circulation effects due to the fan are also visible. The increased circulation effects help to account for the rotation of the lift curve. The C_{lmax} of the section also appears to be significantly increased by the presence of the fan as would be expected. Clearly, as compared to the baseline airfoil, the EDF modified

geometry has a significant impact upon the lift and moment of the section, which varies with angle-of-attack.

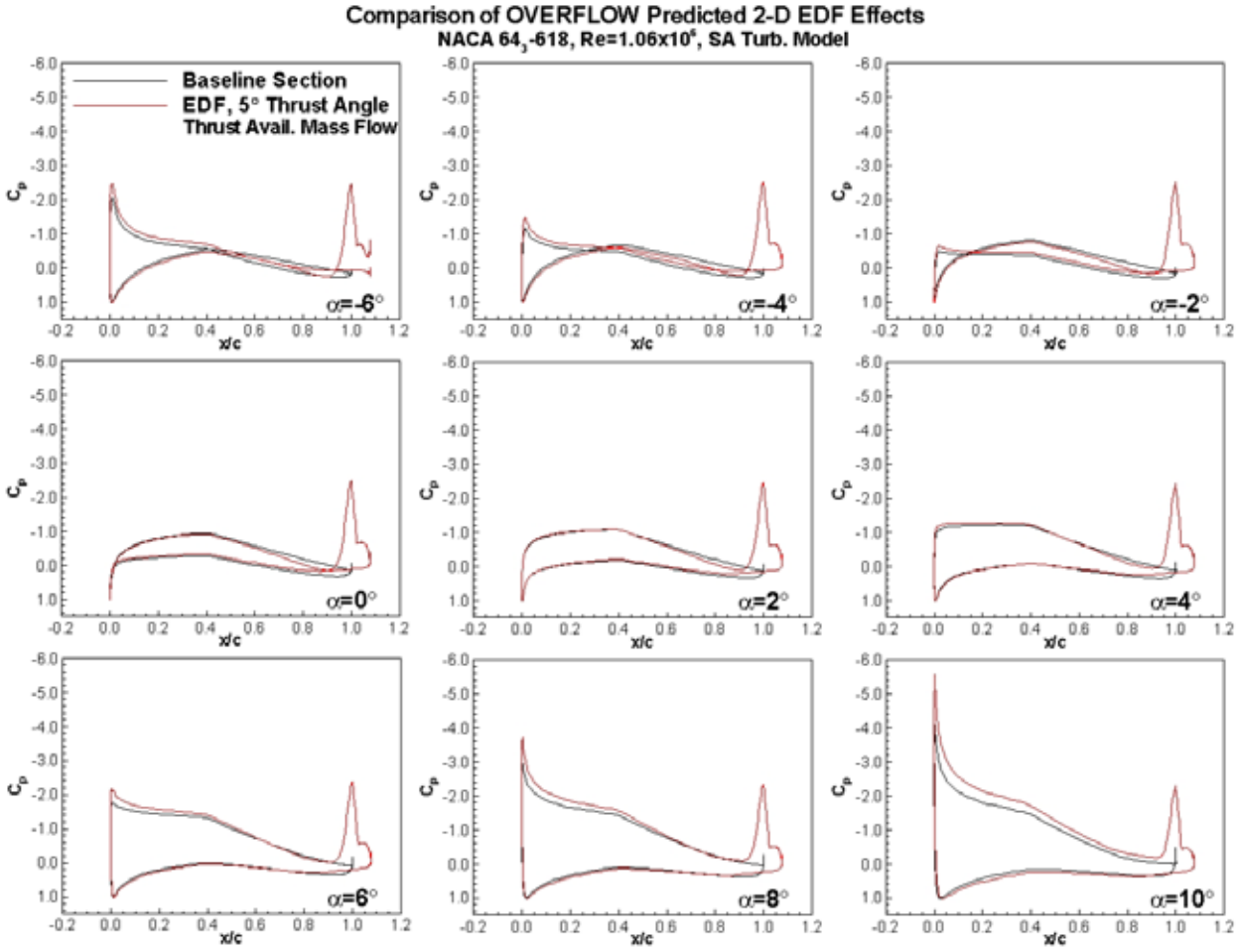

Figure 20: Comparison of OVERFLOW predicted surface pressures for the baseline and 5° thrust angle EDF 2D NACA 64_3-618, Re=1.06x10^6, V_∞=100 ft/s.

5.4. **Observed Thrust Angle Effects at T_a**

After examining the baseline 5° thrust angle at a thrust available setting, the effects of changing the thrust angle were investigated. Thrust angles of 0°, 2.5°, and 7.5° were also run. As discussed in Section 5.3.1, the grids were set-up using in a script system. As a result, changing the thrust angle only required re-running the scripts, allowing new grids to be generated in minutes. A plot showing the grids and geometry differences for the 4 thrust angles examined is shown in Figure 21. In order to keep the inlet location fixed at x/c=0.90, the cowl highlight point was used as the center of rotation for the various thrust angles. As a result, the actual chord length is slightly reduced with increased thrust angle. Lift and moment polars for the various thrust angles are shown in Figure 22. The lift and moment data shown in Figure 22 are reduced using the baseline reference length and area for comparison.

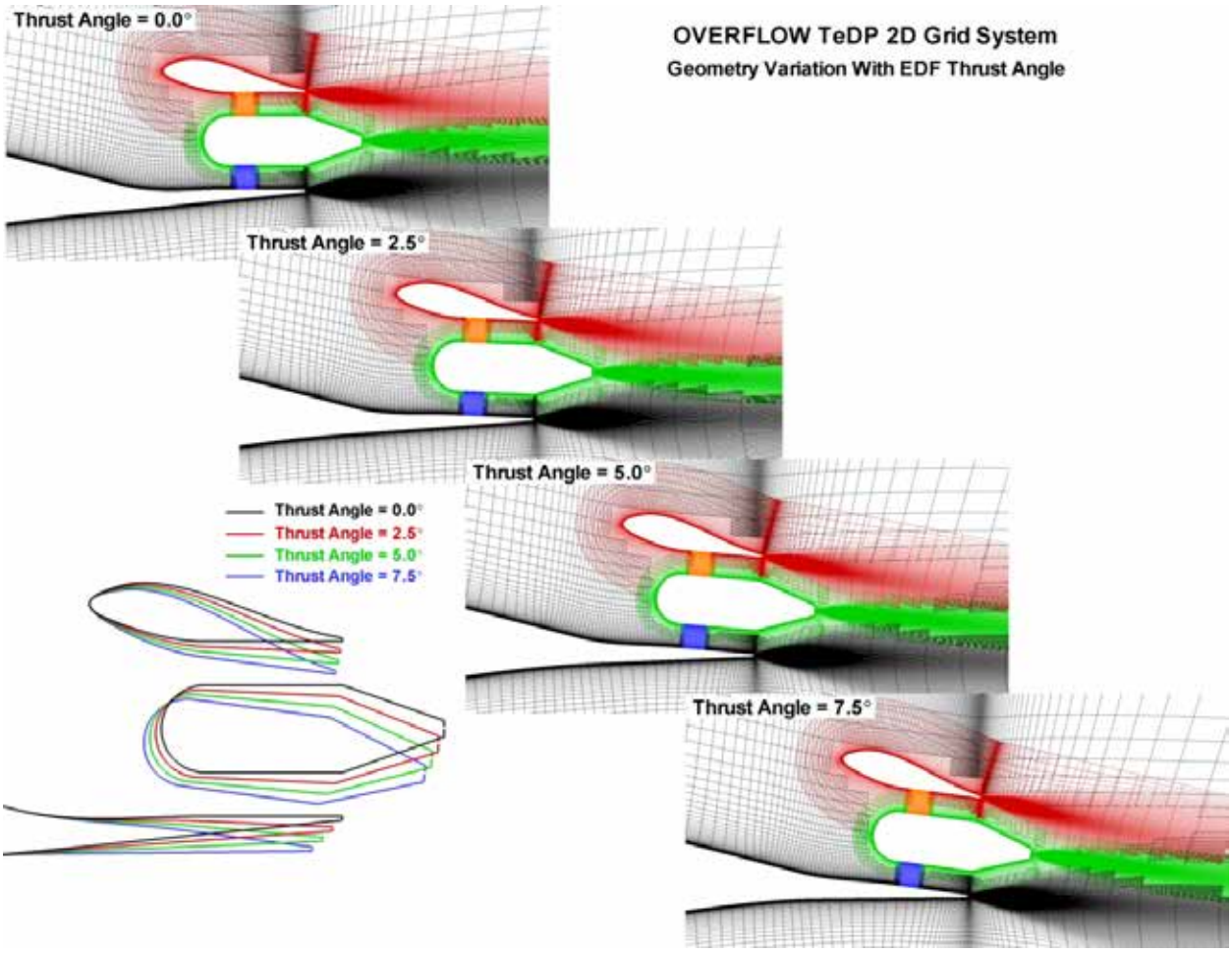

Figure 21: Comparison of grids and geometry variation with EDF thrust angle.

From Figure 22, as was observed for the 5° thrust angle case shown in Figure 19, the lift polars for the other thrust angles are also rotated as compared to the baseline airfoil. Recall that the majority of this rotation is due to the fact that the EDF data were reduced using the baseline reference length and area. The primary effect of changing the thrust angle is the shifting of the lift curves. Changing the thrust angle of the EDF effectively changes the camber of the section, shifting the lift curve to the left with increasing thrust angle. Increasing the thrust angle also shifts the moment curve more negative as also would be expected. Another interesting aspect of the thrust angle results is observed for the 7.5° thrust angle polar. Up to an angle-of-attack of α=2°, the polar follows a linear progression. At α=4°, however, a nonlinearity is observed with a reduction in lift. Above α=4°, the lift curve slope appears to be roughly equivalent to that up to α=2°, with the polar shifted. A similar nonlinearity is observed in the moment curve. The reason for this nonlinearity in the 7.5° thrust angle polar is best observed in the Mach contours and streamlines for the α=2° and α=4° cases as shown in Figure 23.

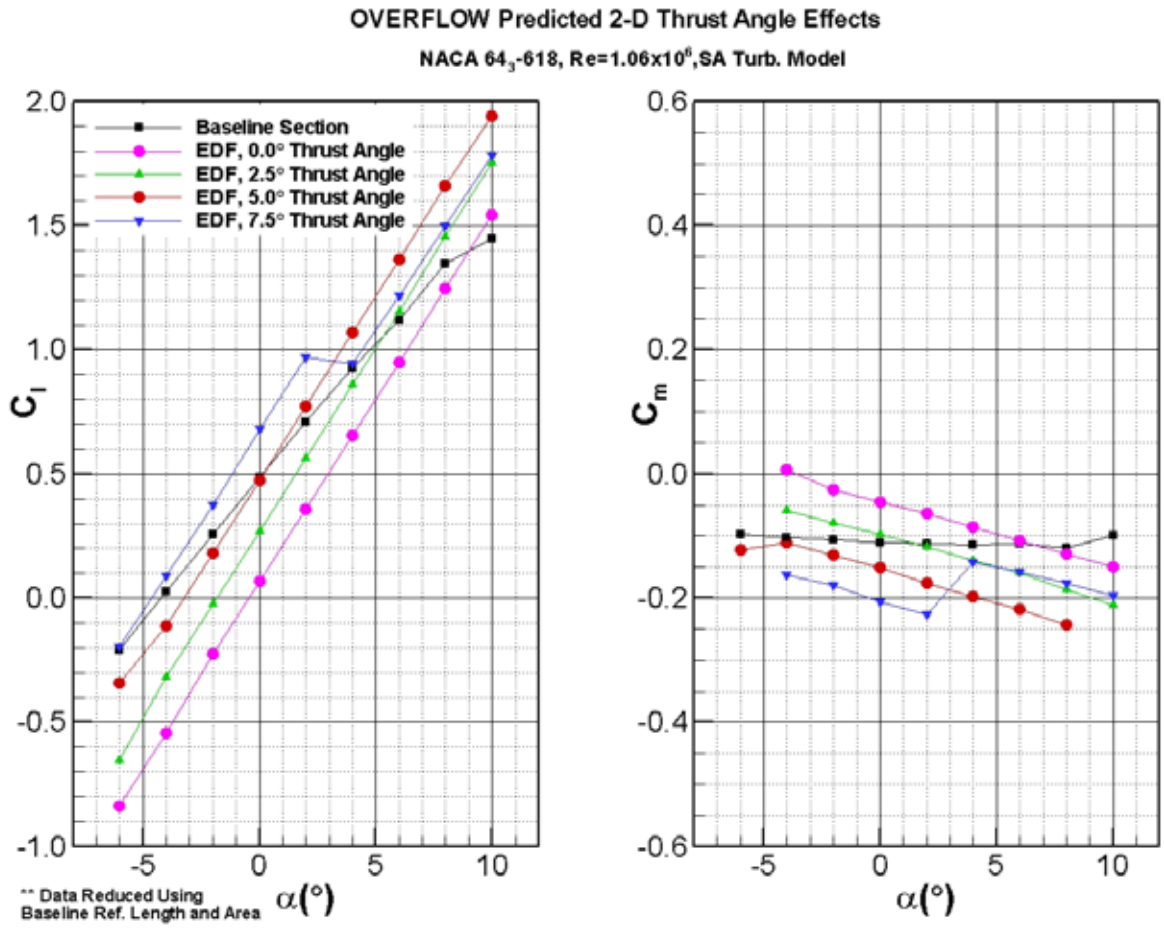

Figure 22: Comparison of OVERFLOW predicted thrust angle effects on lift and pitching moment for the baseline and EDF equipped 2D NACA 64$_3$-618, Re=1.06x10^6, V_∞=100 ft/s.

From Figure 23, the nonlinearity between a=2° and a=4° is due to the flow separating off the upper surface of the aft end of the plug. The cowl does not appear to separate, only the upper surface of the rear of the plug. In a 2D flowfield, the plug represents a spanwise infinite surface, extending to infinity in and out of the page. In the actual 3D flowfield, the plug is circular, with a significant 3D relieving effect as the flow moves up and around the plug at angle-of-attack. As a result, it is questionable as to whether or not the separation would exist in a 3D flowfield.

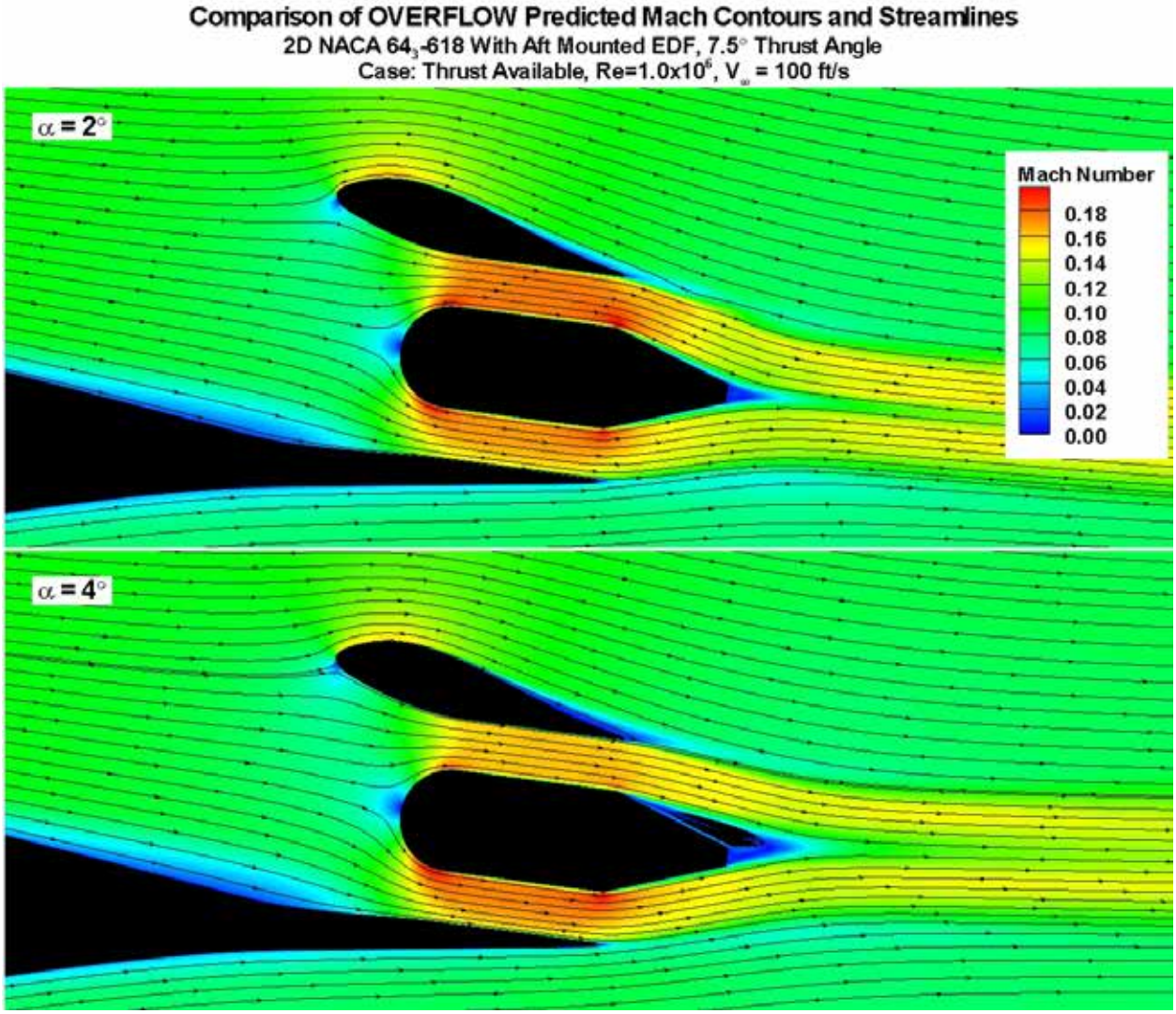

Figure 23: Comparison of OVERFLOW predicted Mach contours and streamlines for the EDF equipped 2D NACA 64_3-618 with a 7.5° thrust angle, α=2° and α=4°, Re=1.06x10^6, V_∞=100 ft/s.

Surface pressure for the thrust angle cases are shown in Figure 24. From the surface pressures shown in Figure 24, below α=2°, the leading-edge, plateau, and fan region pressures follow a consistent trend with thrust angle. At negative angles of attack, the leading-edge, plateau, and fan pressures decrease with increasing thrust angle. At positive angles-of-attack the leading-edge and plateau pressures increase with increasing thrust angle. The pressures in the fan region, however, still decrease with increasing thrust angle. Above α=2°, where the plug separates for the 7.5° thrust angle case, the plug separation is observed to have a global effect on the flowfield, altering the overall circulation of the section and reducing the leading edge and plateau pressures. Again, it is uncertain whether or not this separation would exist in a 3D flowfield.

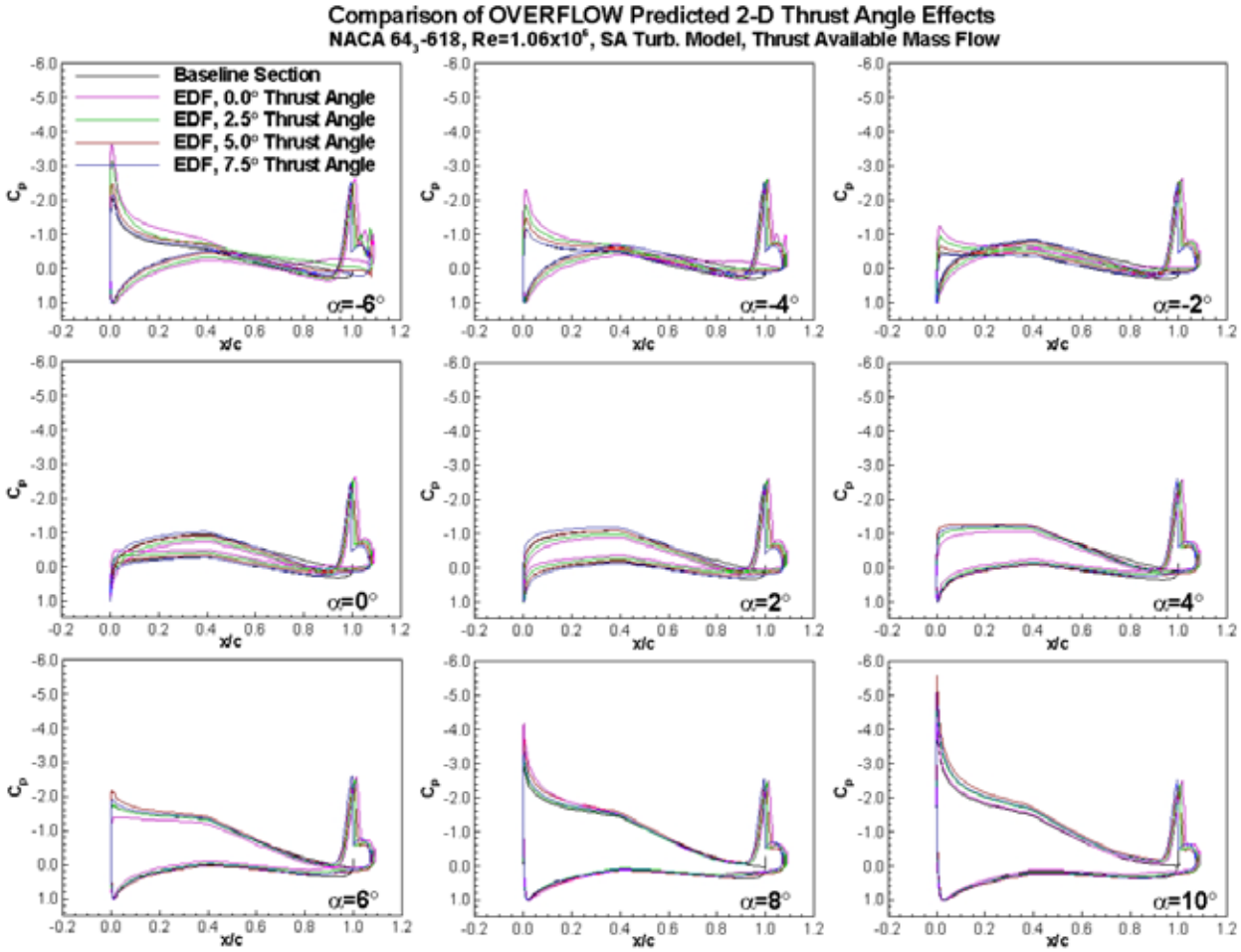

Figure 24: Comparison of OVERFLOW predicted surface pressures for increasing EDF thrust angle for the baseline and EDF equipped 2D NACA 64_3-618, Re=1.06x10^6, V_∞=100 ft/s.

5.5. **Observed Thrust Level Effects**

After investigating the thrust angle effects, the effect of thrust level was examined for the 5° thrust angle case. The thrust level was reduced from the thrust available level, $T_{a(2D)}$= 0.571 lbs to the thrust required level, $T_{r(2D)}$= 0.254 lbs. A plot showing the Mach contours and streamlines for the two thrust levels at a=0° is shown in Figure 25. From Figure 25, the increased back pressure resulting from the reduced mass flow ($\dot{m}_{Ta}$=0.0065 slugs/s and $\dot{m}_{Tr}$=0.0044 slugs/s) is readily apparent in the significantly larger low speed region near the wall for the thrust required case. This low speed flow near the wall just upstream of the inlet location also has a small separated region. Areas of separation also exist on the top rear of the cowl, and as with the 7.5° thrust angle case above a=2°, separation exists on the top rear of the plug. While the separation on the airfoil upstream of the inlet and the separation on the top rear of the cowl are most likely accurate with respect to the 2D/3D flowfield, the plug separation is again questionable. The influence that the plug separation has upon either the cowl separation or the airfoil separation is unknown. From the results shown in Figure 22 through Figure 24 for the 7.5° thrust angle case,

the plug separation can affect the overall circulation. As a result, a thrust level comparison between the thrust available and thrust required cases cannot be made.

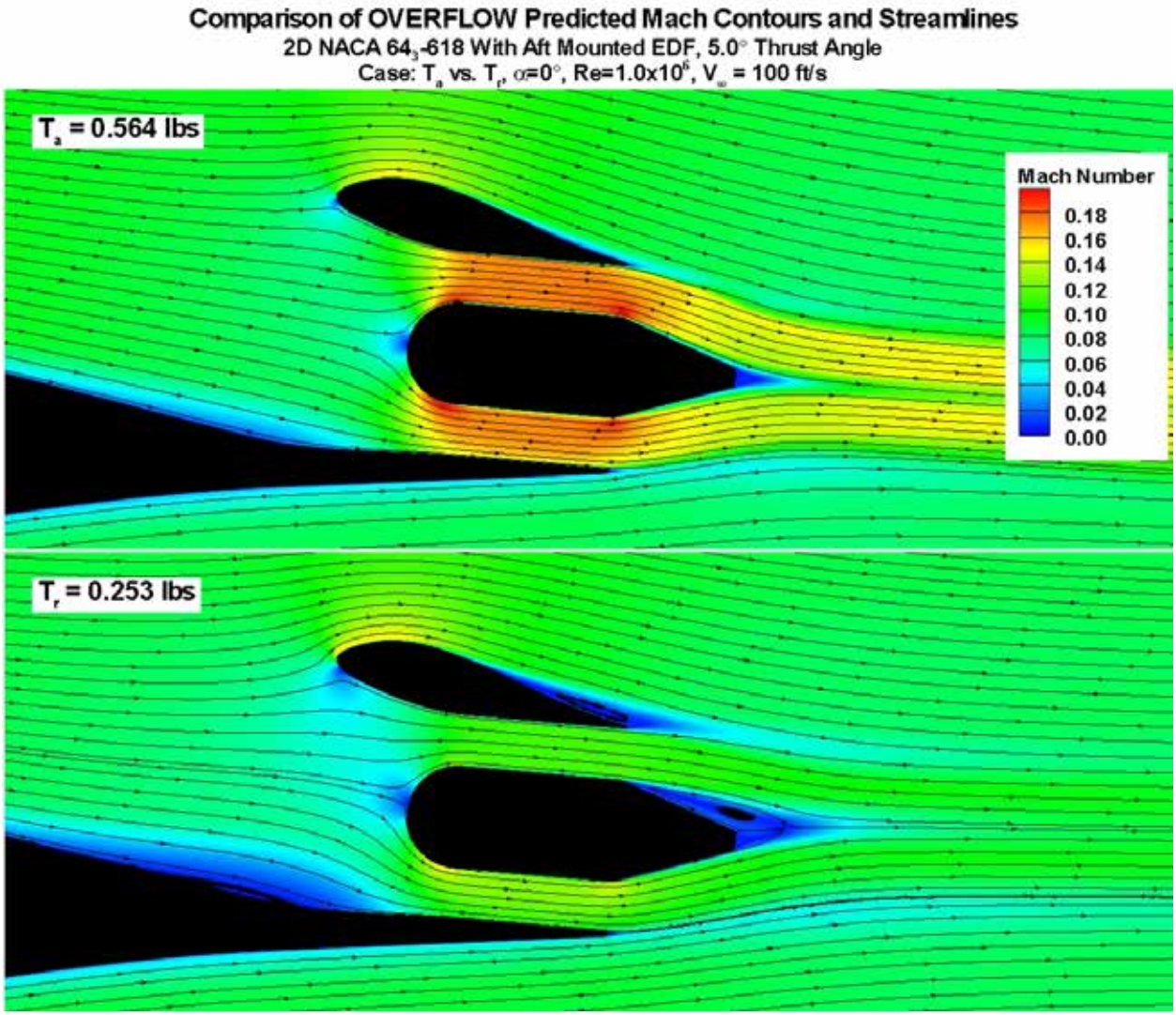

Figure 25: Comparison of OVERFLOW predicted Mach contours and streamlines for the 5° thrust angle EDF equipped 2D NACA 64_3-618 at two different thrust levels, a=0°, Re=1.06x10^6, V_∞=100 ft/s.

In an attempt to eliminate the plug separation at the thrust required case in order to produce a useful thrust level comparison, the inlet height was reduced from 2.69 in to 2.35 in. It was thought that reducing the inlet size would reduce the back pressure at the lower mass flow and eliminate the separation on the plug. After re-running the script system for the new inlet height for the 5° thrust angle geometry, the reduced inlet height was first run at the thrust available condition. Unfortunately the top rear of the plug again separated, negating a thrust level comparison between the two mass flows. Since it is believed that the 3D plug geometry will behave differently than the 2D, and trends in the aero/propulsive coupling cannot readily be discerned between separated and attached flowfields, the 2D study was halted in favor of the 3D study. The 2D study was advantageous from a low grid/geometry complexity and shorter

runtime standpoint, but questions about the fidelity of the simulation from the 2D to the actual 3D geometry indicate that time is better spent on the full 3D geometry.

5.6. **2D Investigation Summary**

For the 2D investigation, the baseline NACA 64_3-618 was first modeled in OVERFLOW and the results compared to experimental data. In the linear portion of the lift curve, the CFD and experimental results compared well. The CFD was observed to over predict C_{lmax} and the angle-of-attack at which it occurs. After completing the baseline airfoil benchmark, a 2D EDF geometry was developed using the Hyperflow fan. Thrust angles of 0.0°, 2.5°, 5.0°, and 7.5° were investigated at thrust levels ranging from a scaled thrust available to a thrust required level.

Overall, the initial inlet sizing and cowl shape produced a well ordered attached flowfield for the thrust available mass flow. Results from the 2D investigation have shown that for an attached flowfield, variations in the EDF thrust angle change the effective camber of the section, shifting the lift curve. For a given thrust angle, the EDF was also shown to rotate the lift curve counter-clockwise as compared to the baseline airfoil. This rotation of the lift curve results from increased negative pressures in the fan region as the flow is accelerated locally, and from an overall increase in circulation for the section due to the presence of the fan. The pitching moment was also observed to become more negative with increasing thrust angle. The majority of the increased negative pitching moment can be attributed to the significant increase in negative pressures in the fan region at the trailing-edge due to the locally accelerated flow. The EDF was also shown to significantly increase C_{lmax} of the section. The 5° thrust angle geometry appears to provide the best comparison to the baseline airfoil polar.

No significant optimization of the 2D geometry was performed. For the 7.5° thrust angle case at thrust available, the upper surface of the plug end was observed to separate above an angle-of-attack of α=2°. A similar separation was observed for the 5.0° thrust angle case at the lower thrust required mass flow. For the 2D geometry, the fan inlet, exit, and plug flowfield is rectangular. For the 3D geometry, the fan exit and plug flowfield are circular. It is believed that the circular aspect of the 3D plug flowfield will have a significant relieving effect, making the presence of the 2D separation questionable.

6. 3D Design and CFD Study

After separation issues were observed on the 2D plug geometry that were not believed to translate to the 3D flowfield, any optimization or geometry development on the 2D model was halted in favor of performing the remaining optimization, development, and simulation on the 3D geometry. As a result, the grid scripting system developed for the 2D geometry was significantly expanded for the 3D geometry. For the Phase I effort, the model/inlet/EDF geometry was developed in a 3D CAD environment (ProE) and the surfaces then transferred to the CFD environment. While adequate, changes in the surface geometry would not allow a

universal script system to be used to generate the computational geometry, hindering the optimization process. As a result, the Phase II approach was to perform all native surface generation in the computational environment and then only transfer the final geometry to the CAD environment. This CFD to CAD approach allowed the script system to fully define every aspect of the geometry, allowing an input table to be developed of important design parameters for the fan/inlet/airfoil system. Changes to the geometry can be entered into the input table and the script system re-run, completely generating new computational surfaces in minutes. The scripting system allows fast, parametric optimization of the geometry. A list of the design input parameters for the 3D EDF geometry is given in Table 5.

TeDP 3D Model Input Parameters	
Parameter	**Function**
Basic Model	
Chord	Model Chord Length
Coords	Model Coordinates: Allows Different Section to be Used
Span	Computational Model Span Distance
Fan Parameters	
# of Fans	Any Odd # of Fans Can Be Modeled (3, 5, 7, 9 ... etc)
Fan Location	EDF Fan Face x/c Based on Model Chord
Radius	Fan Inner Radius
Thrust Angle	EDF Exit Thrust Angle
Length	Fan Body Length
Plug	Plug Geometry
Inlet Parmeters	
Inlet Location	Inlet Face x/c Based on Model Chord
Height	Inlet Height
Width	Inlet Width
Outer Lip Radius	Cowl Outer Lip Radius (% of Inlet Height)
Inner Lip Radius	Cowl Inner Lip Radius (% of Inlet Height)
Lip Thickness	Cowl Lip Thickness (% of Inlet Height)
Cowl Parameters	
TE Thickness	Cowl Trailing-edge Thickness
Blend Height	Cowl Blend Height Between Fan Centerline and Area Between Fans (% of Fan Radius)
Side Blend Distance	Distance to Blend EDF Main Section and Baseline Wing
Rear Fairing Distance	Streamwise Distance to Extend Rear Fan-to-Fan Fairing
Fairing End Height	Rear Fairing End Height Relative to End Center Point (Allows Vertically Asymmetric Fairing)

Table 5: 3D TeDP model input parameters.

From the list of parameters shown in Table 5, the full 3D TeDP geometry can be defined and created. The scripting system uses a combination of Chimera Grid Tools (CGT) routines and geometry generation routines written in FORTRAN specifically for the current project. The script system generates fully trimmed surfaces. The scripting system also generates all required collar and volume grids. A 3-view layout and isometric views of the surfaces for a 5 fan system with a 5° thrust angle is shown in Figure 26.

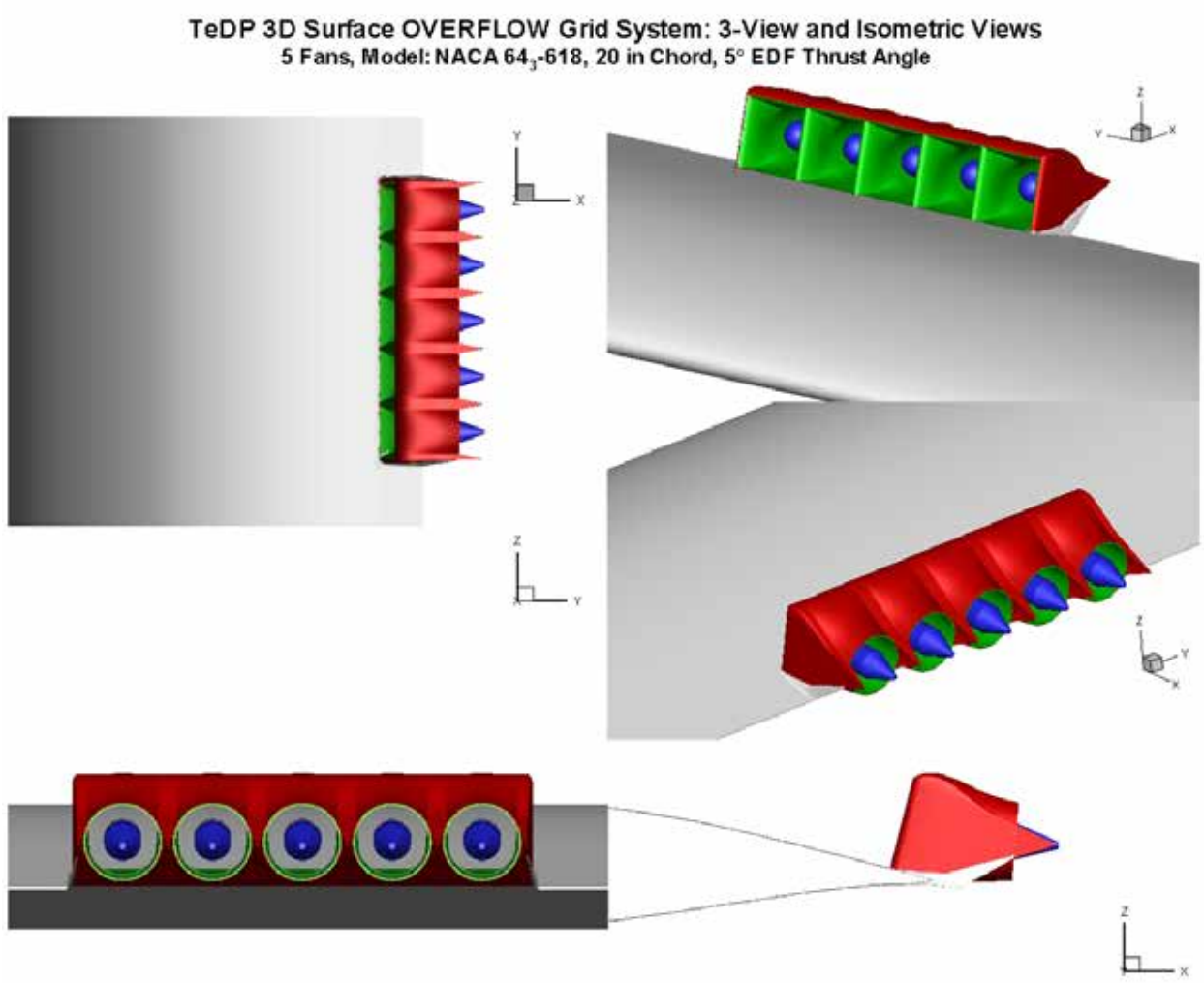

Figure 26: 3-View and isometric views of the 3D TeDP configuration with 5 fan layout and a 5° thrust angle.

For the basic 5 fan system there are 45 primary surface grids and 88 collar grids, for a total of 133 individual surface grids. With off body grids, the total # of grids in the system is 151. Volume grids were generated for a y+ of 1 or less. Also, for better drag and convergence, the first 4 cells off the surface have a constant spacing. The total # of grid points in the system is 63,648,464. The computational domain for the 3D TeDP system is a semi-infinite straight wing. The baseline NACA 64_3-618 section extends on either side of the main 5 fan span segment to 25 chord lengths. This semi-infinite wing with a span of +/- 25 chord lengths was run for the baseline clean NACA 64_3-618 section with no TeDP fans and the results compared to the traditional 2D simulation results presented in Section 5.1. Results and force and moment coefficients for the semi-infinite wing and the traditional 2D configuration compared extremely well. Since the fan face is located at x/c=0.90 (x=18 inches on the 20 inch chord model), the actual fan body and plug extend slightly beyond the 20 inches of the baseline model chord. The fan also extended slightly beyond the baseline 20 inch chord for the previous 2D study. Based on the lower surface trailing-edge of the TeDP fan cowl, the chord is approximately 21.5 inches.

This chord length is used as the reference length for force and moment computations for the TeDP configurations. It should be noted that the 21.5 inch chord length is for a fan thrust angle of 5°. Increasing the thrust angle rotates the trailing-edge of the fan and model downward, producing a slightly shorter chord length. A thrust angle of 10°, for example, produces a chord length of 21.25 inches. For cases where the thrust angle is changed, the force and moment results are based on the as run chord. A plot showing the 3D TeDP grid system for a 5° thrust angle is shown in Figure 27 with a close up of the surface grids shown in Figure 28

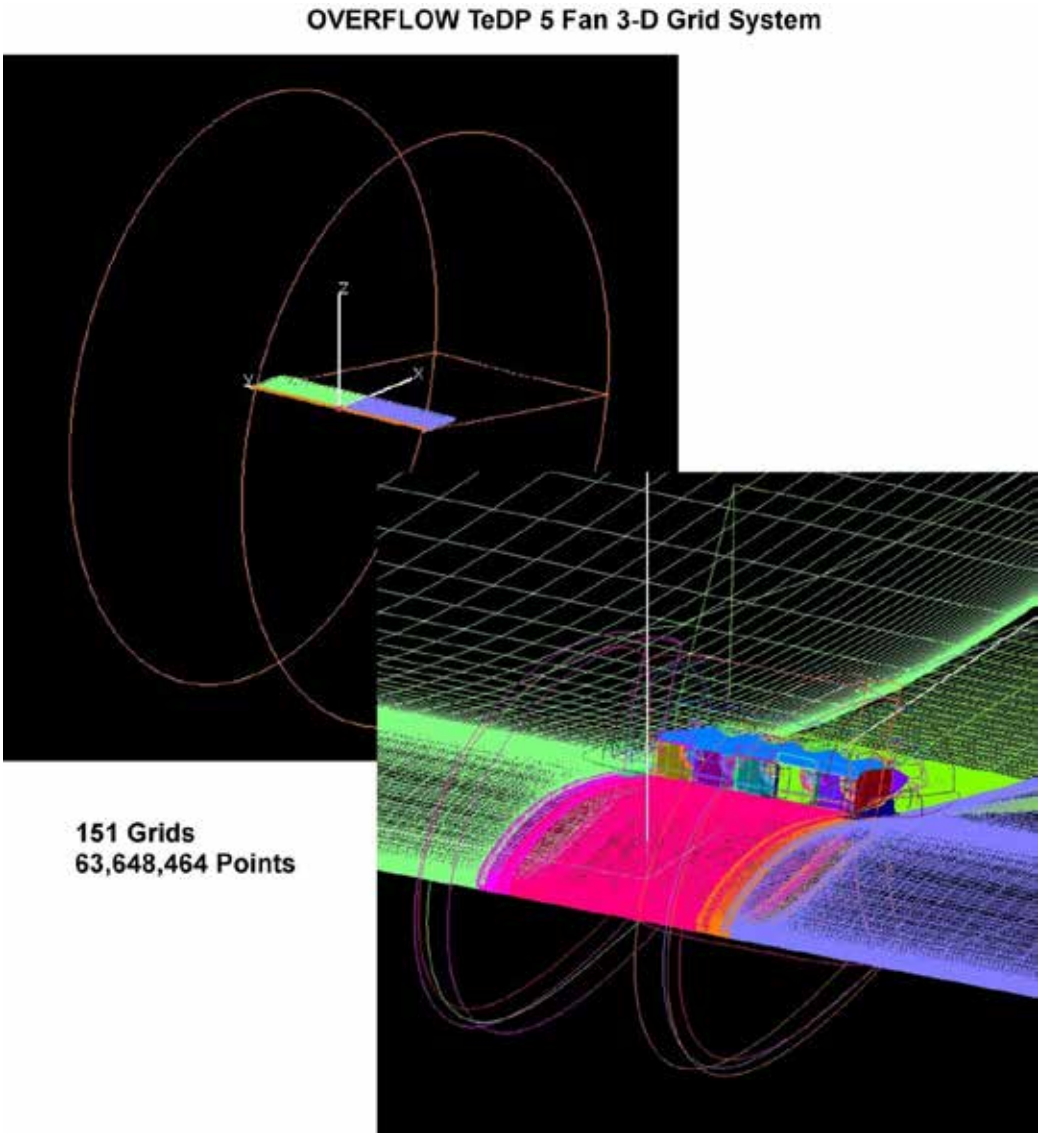

Figure 27: OVERFLOW TeDP 5 fan 3-D grid system.

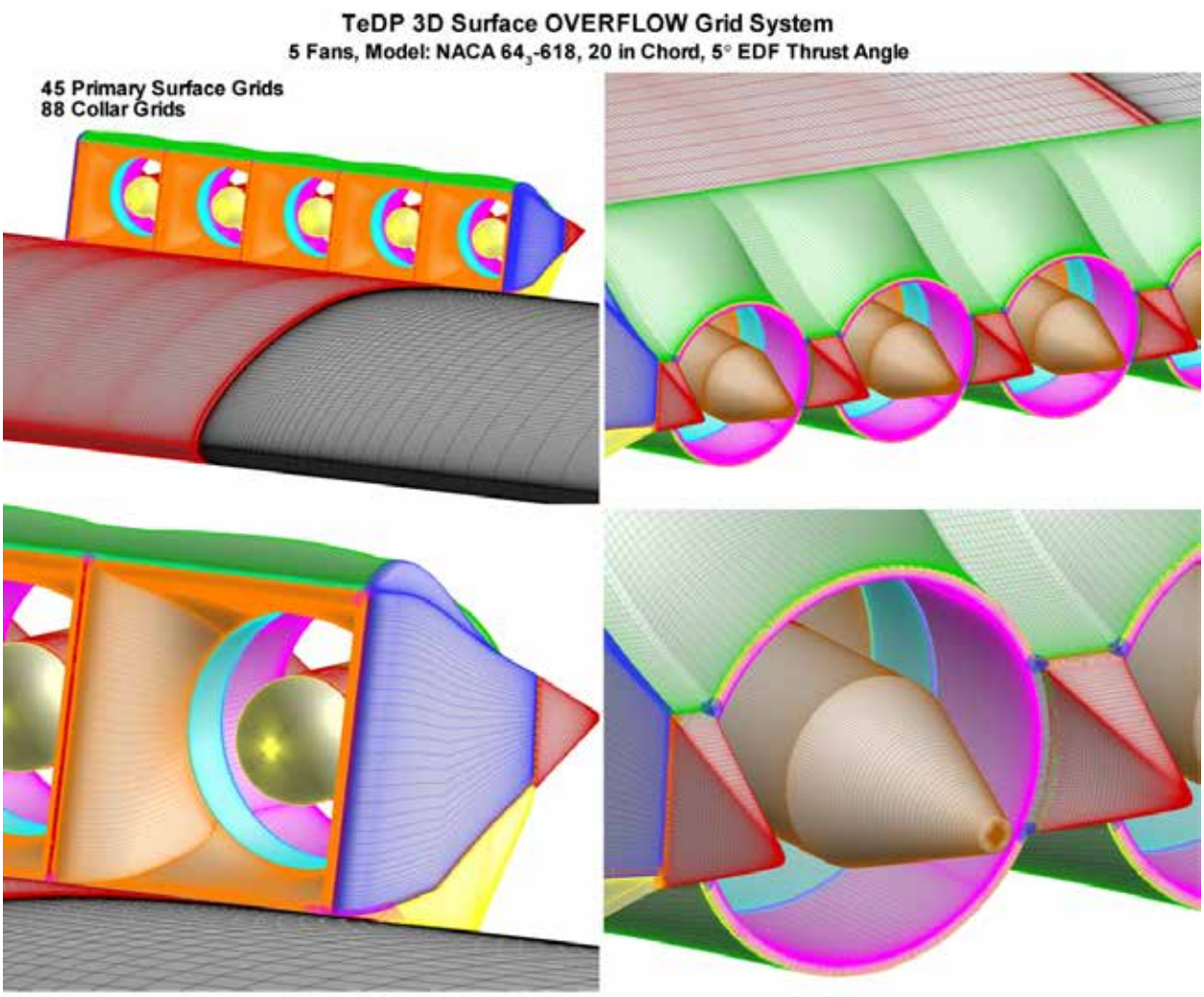

Figure 28: Surface grids for a 5 fan EDF system showing primary and collar grid surfaces for a 5° thrust angle.

In order to show the versatility of the surface generation scripting system, several different EDF configurations were run. These included different numbers of fans, different inlet widths, and different cowl blend heights. A plot showing the TeDP surfaces with 3, 5, 7 and 9 fan configurations is given in Figure 29.

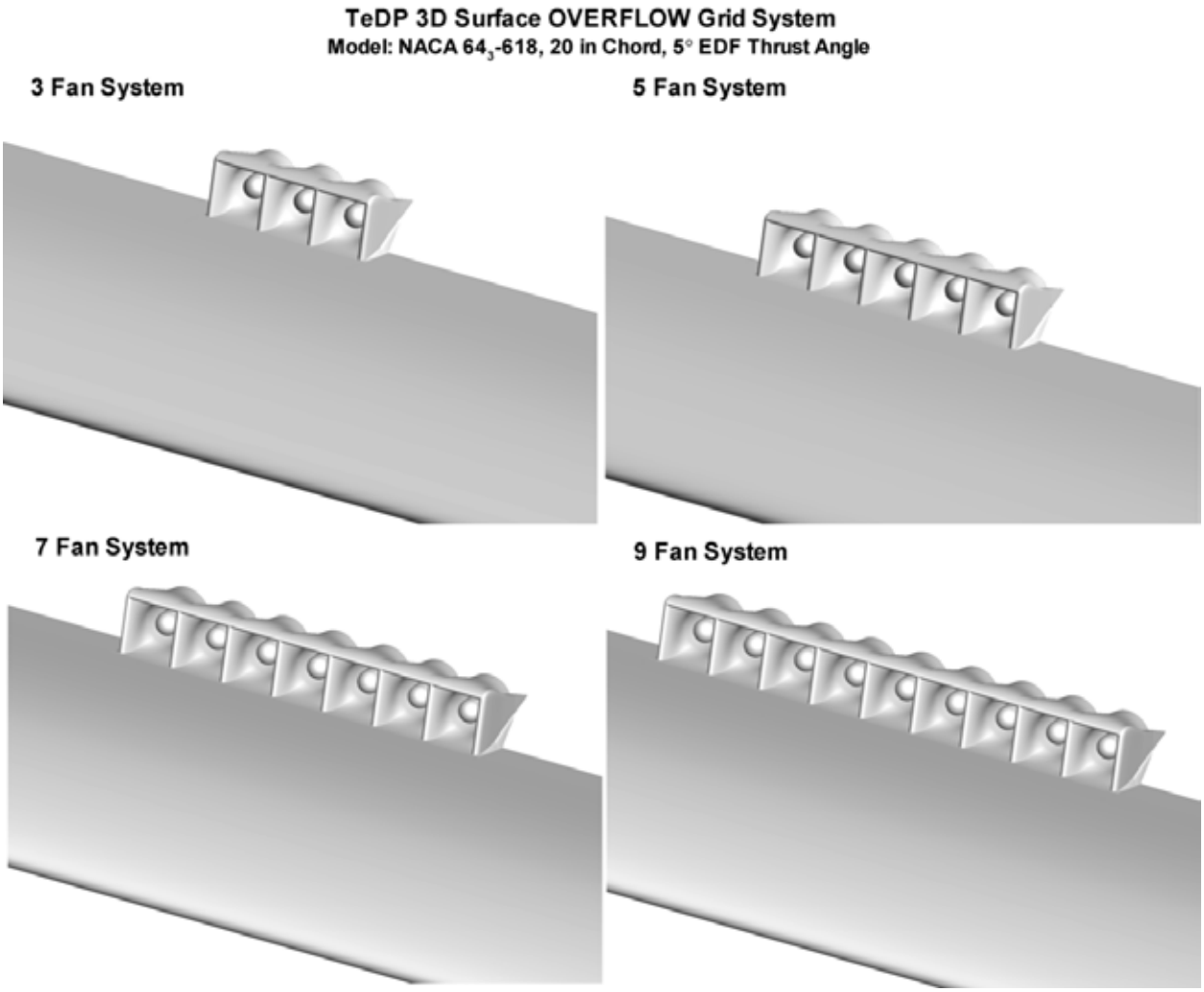

Figure 29: Effect of varying the number of fans for the TeDP surface grid system.

From Figure 29, varying the number of fans is a rather straight forward modification of the basic 5 fan system. The ability to change the number of fans, however, could be useful to estimate the effect different thrust levels have upon adjacent fans and the spanwise extent to which the effect is felt. Figure 30 shows the effect of varying the inlet width. The baseline inlet width was set at 2.6 inches. This inlet width was then varied to 2.3 inches and 2.9 inches. The surfaces shown in Figure 30 show how a change in inlet width filters into all of the surrounding geometry. Other than the basic width of the overall EDF layout, the cowl and rear fairings are also affected. Figure 31 shows the effect of varying the cowl to fan blend height. The cowl to fan blend height sets the distance the cowl will follow the contour of the fan at the fan exit. A small cowl blend height will create deep recesses between the fans and reduce the size of the rear teardrop fairings. The blend height is specified as a percentage of the fan radius. The baseline blend height is 45%. Blend heights of 20% and 70% were also generated. From the surfaces shown in Figure 31, changing a single parameter can have a large effect upon the geometry as a whole.

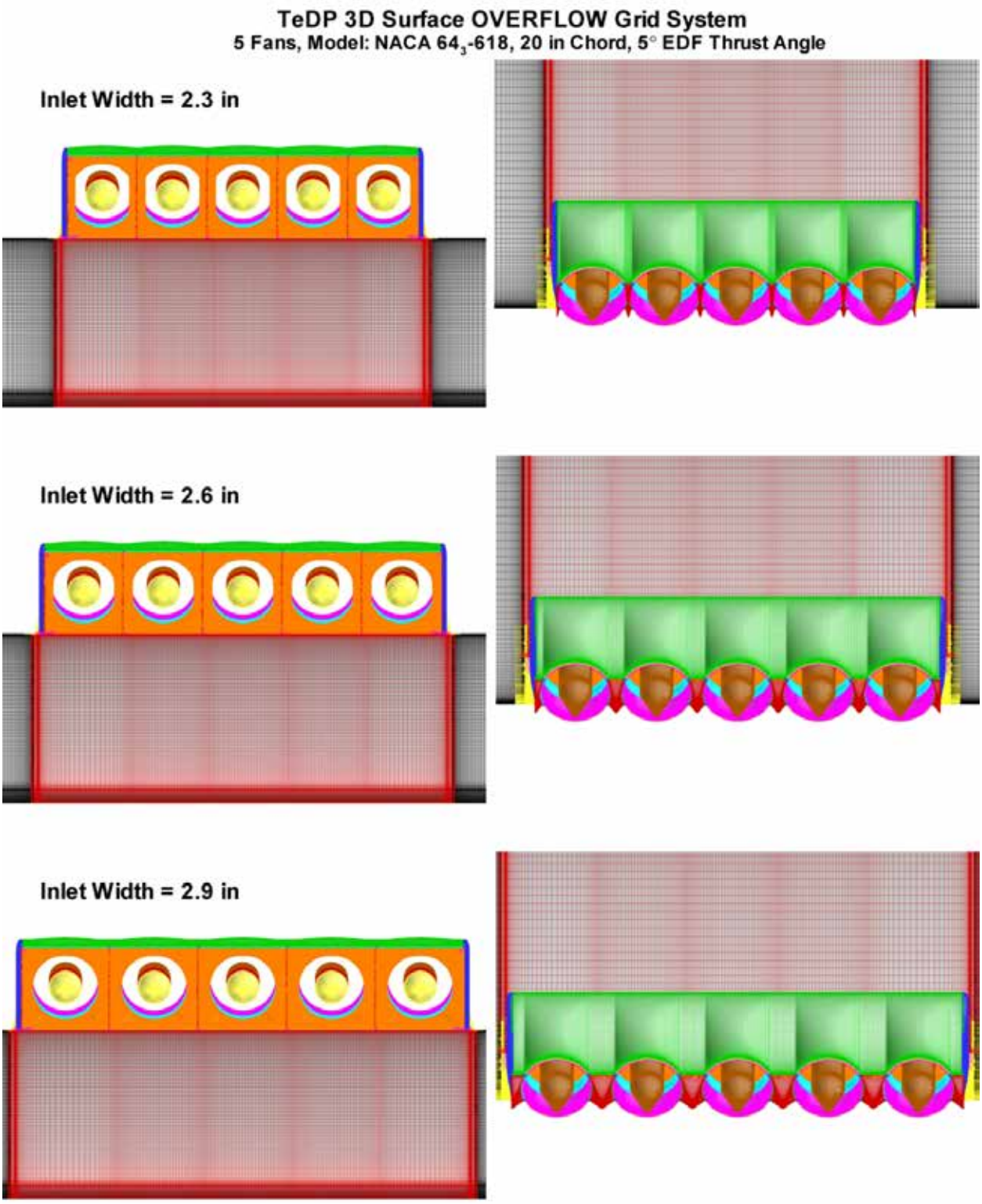

Figure 30: Effect of varying inlet width on the 5 fan TeDP surface grid system.

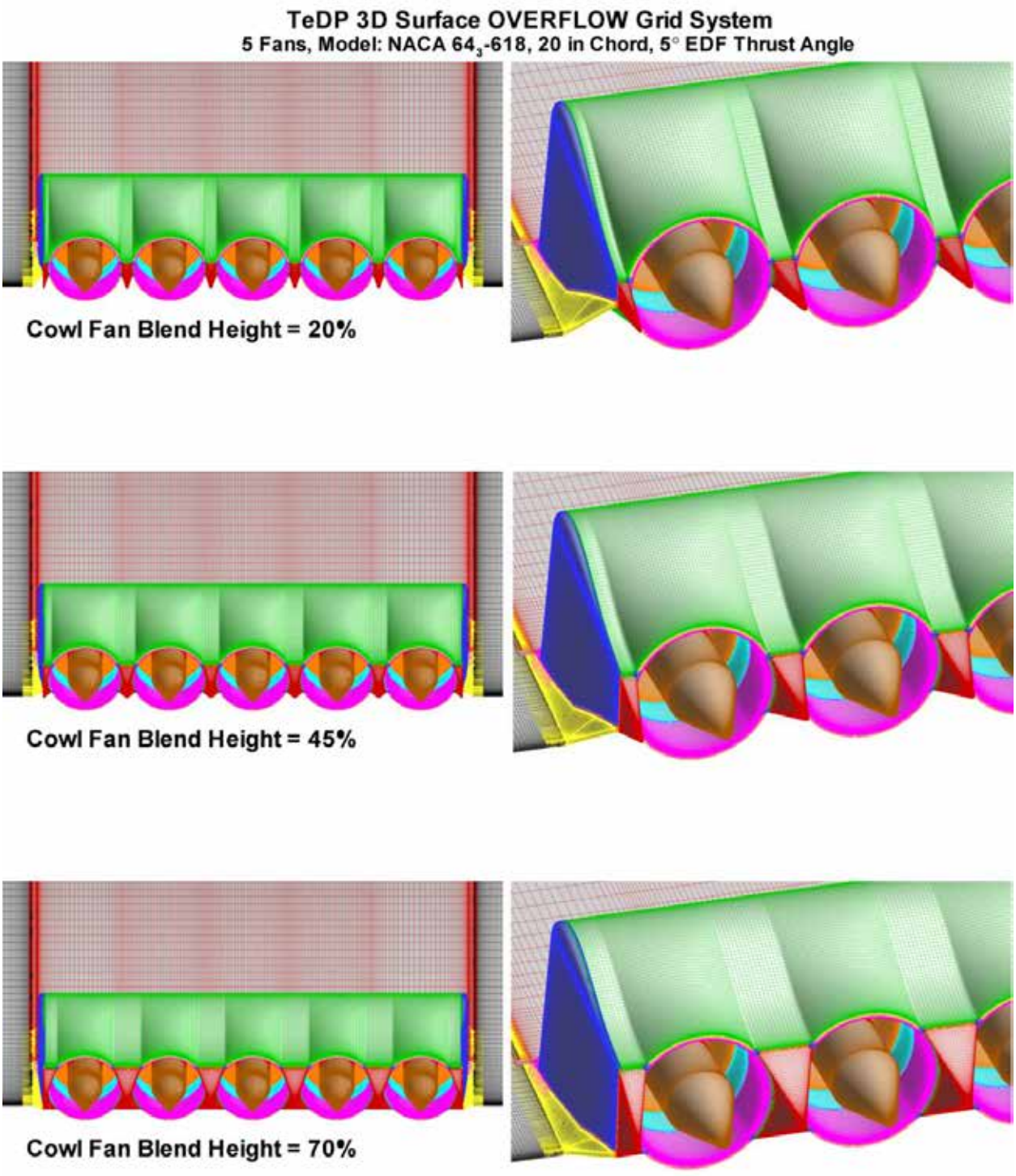

Figure 31: Effect of varying to fan blend height on the 5 fan TeDP surface grid system.

During the course of the 3D design, several fan parameters were investigated. These included varying the inlet height, inlet width, cowl lip shape, upper cowl surface contour, the cowl-to-fan

blend height (as shown in Figure 31), the chordwise location of the inlet, the length of the inlet, the chordwise location of the fan, the aft duct length downstream of the fan, and the thrust angle. After changing a parameter in the design script, new grids and volumes could be generated within 10 minutes. After generating new grids and volumes, Pegasus would need to be re-run to re-cut holes and generate the new interpolation stencils. Generally, a new design could be run within 2 hours of a design parameter change.

6.1. 3D Inlet Design Considerations

The design of the 3D inlet for the TeDP configuration is complicated by the fact that not only is the inlet a boundary-layer ingesting inlet, but also by the fact that the multiple fans and inlets sit side-by-side. The primary function of an inlet is to provide mass flow to the fan/engine. A good inlet design minimizes losses due to distortion and pressure loss. As thrust levels change, the mass flow through the fan/engine changes and as a result the capture area changes. For a traditional round nacelle, this capture area can be thought of as a stream tube supplying mass flow to the engine through the inlet. The inlet is usually sized to accommodate the flight condition requiring the largest mass flow. At lower mass flows, the diameter of the capture stream tube decreases. For very low mass flows, the possibly of spillage around the nacelle inlet exists. For the traditional under wing, forward mounted nacelle, the capture area has 360° of relief, or freedom to adjust the size of the stream tube to match the required mass flow rate. For a BLI ingesting, multi-fan, side-by-side distributed propulsion configuration, however, the capture area stream tube is significantly constrained. Unlike the traditional nacelle with 360° of relief, the BLI side-by-side multi-fan stream tube is constrained on three sides. First, the stream tube is constrained due to the fact that the inlet resides on a surface with the flow following the contour of that surface. Secondly, for a side-by-side fan/engine configuration, the stream tube is constrained on either side of the fan by the neighboring fan's capture stream tube. As a result, the only relief for the stream tube as a function of changing mass flow is the area above the inlet. As compared to the traditional nacelle, this conceptually limits the area available to the stream tube to adjust for changes in mass flow to just 90°. A schematic illustrating the differences in the capture areas for changes in required mass flow between a traditional nacelle and the BLI distributed propulsion configuration is shown in Figure 32.

From Figure 32, as the required mass flow for the fan reduces, the size of the capture stream tube decreases. As the stream tube capture area becomes smaller than the inlet area, spillage around the inlet can occur. For the case of the BLI inlet, as the mass flow is reduced below the design mass flow for the inlet area, the flow sees an increasing pressure as it approaches the inlet. This has several compounding effects for the BLI distributed propulsion inlet. First, the pressure distribution upstream of the inlet becomes more positive as the flow decelerates, reducing the overall C_l of the section. Some of this C_l is recovered by the more negative pressures created at the trailing-edge due to the flow accelerating through the inlet and over the cowl. Secondly, since the flow is retarded approaching the inlet, the inlet velocity decreases. Since the fan thrust is a function of the difference between the inlet and exit velocities, the reduced inlet velocity produces an increased fan thrust. If required to maintain a given thrust, the mass flow through the fan should be reduced, which would further exacerbate the problem by creating more back

pressure and further reducing the thrust. At mass flows above the design mass flow for the inlet, due to the constrained capture stream tube, the flow will accelerate into the inlet, creating a velocity greater than the design inlet velocity, reducing the thrust, requiring a further increase in mass flow to maintain that thrust. The increased velocity will also create more negative pressures on the aft portion of the airfoil approaching the inlet, increasing the sectional C_l. The pressure distribution and resulting aerodynamics of the section, inlet velocity, and thrust are a coupled system.

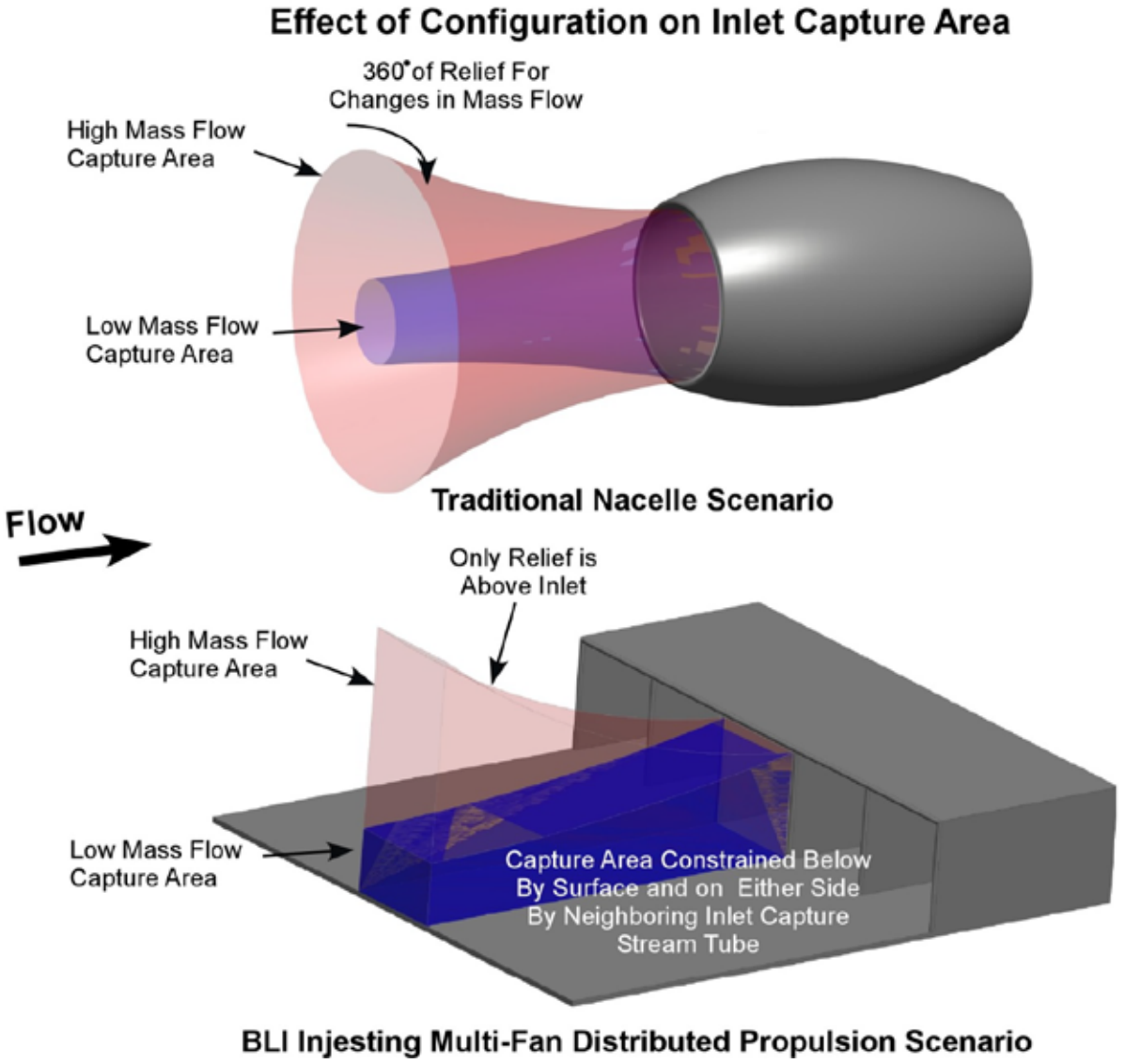

Figure 32: Schematic showing the effect of the configuration on the required inlet capture area due to changes in fan mass flow.

6.2. Initial Inlet Sizing

The inlet for the EDF was sized based on an estimation of the mass flow through the fan. From continuity, the free-stream capture area mass flow, inlet mass flow, and fan exit mass flow must be equal $\dot{m} = \rho v A$, or $\dot{m} = \dot{m}_{Inlet} = \dot{m}_{Fan} = \dot{m}_{Exit}$. Assuming that the fan exit pressure is equal to free-stream pressure, the fan thrust is related to the mass flow and the difference in velocity between the free-stream and fan exit as given by:

$$T = \dot{m}(v_{exit} - v_{\infty})$$

Equation 6-1

Knowing the thrust, free-stream velocity, and fan exit area, an estimate of the required mass flow can be calculated:

$$\dot{m} = \frac{\rho A_{exit}}{2}\left\{v_{\infty} + \sqrt{{v_{\infty}}^2 + \frac{4T}{\rho A_{exit}}}\right\}$$

Equation 6-2

After an estimate of the required mass flow has been obtained, an estimate of the inlet area can be derived. Since the inlet is a boundary-layer ingesting inlet, the inlet velocity is made up of the external edge flow and the variation of the velocity through the boundary-layer. A schematic of the inlet and boundary-layer is shown in Figure 33.

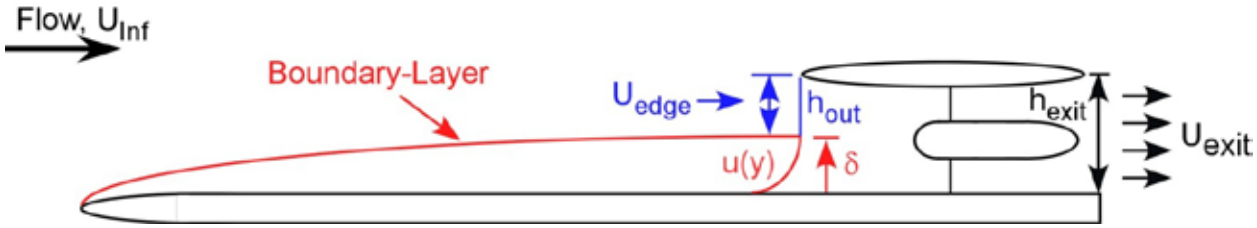

Figure 33: Schematic of boundary-layer ingesting inlet.

From Figure 33, at the inlet the mass flow is the sum of the contribution from the boundary-layer and the relatively constant edge velocity. Assuming a 2D width w, and a constant density, the inlet mass flow is equal to:

$$\dot{m}_{Inlet} = \rho_{Inlet} u_{Inlet} h_{Inlet} w = \rho_{Inlet} w \left(u_{edge} h_{out} + \int_0^{\delta} u(y)dy\right)$$

Equation 6-3

From Equation 6-3, the inlet mass flow is a function of the edge velocity and the integral of the velocity up through the boundary-layer thickness at the inlet. The inlet height can be solved for knowing the mass flow, boundary-layer thickness, and the shape of the velocity profile. Since

the flow for the current investigation is subsonic and incompressible, a mean flow integral approximation developed by Moses using a Cole's wake solution for an attached turbulent boundary-layer with pressure gradient can be used for the shape of the profile[10]:

$$\frac{u}{U_{edge}} = 1 + \frac{\sqrt{C_f/2}}{\kappa} ln\left(\frac{y}{\delta}\right) - \frac{2\Pi}{\kappa}\sqrt{\frac{C_f}{2}}\left[1 - 3\left(\frac{y}{\delta}\right)^2 + 2\left(\frac{y}{\delta}\right)^3\right]$$

Equation 6-4

Where P is Cole's wake parameter $\Pi = \kappa\frac{\delta^*}{\delta}\sqrt{\frac{C_f}{2}} - 1$, and k is a universal constant, usually taken to be k≈0.41.[11] Estimates for the boundary-layer thickness, displacement thickness, and skin friction can be obtained from an XFOIL analysis. XFOIL outputs skin friction, displacement, and momentum thickness as a function of chord for the airfoil. The boundary-layer thickness for turbulent profiles can be calculated from Drela and Giles[12] using:

$$\delta = \theta\left(3.15 + \frac{1.72}{H_k - 1}\right) + \delta^*$$

Equation 6-5

Equation 6-5 is based on the same boundary-layer formulation used in XFOIL. H_k in Equation 6-5 is the kinematic shape factor. Integrating Equation 6-3 using the relationship in Equation 6-4 and solving for h_{out} yields:

$$h_{out} = \frac{\dot{m}}{\rho w U_{Edge}} - \delta\left[1 - \frac{\sqrt{C_f/2}}{\kappa} - \frac{\Pi}{\kappa}\sqrt{C_f/2}\right]$$

Equation 6-6

From Equation 6-6, knowing the local boundary-layer thickness d, displacement thickness d^*, and skin friction C_f, along with an estimate of the mass flow $\dot{m}$ (Equation 6-2), an estimate of the inlet height, and area can be calculated.

Using the derivations above shown in Equation 6-1 through Equation 6-6, the first step in calculating an estimation for the inlet sizing is to calculate a mass flow based on the fan thrust. At cruise conditions, the TG-14A thrust available is T_a=270 lbs, with a thrust required of T_r=120 lbs. Scaled to the wind tunnel test conditions, the thrust available becomes T_a=13.35 lbs with a T_r=5.9 lbs. Since there are 18 fans in the proposed TG-14A configuration, the thrust available per fan at the wind tunnel scale is T_a=0.742 lbs, with the thrust required being T_r=0.330 lbs. Based on a free-stream velocity of U_∞=100 ft/s, the estimated mass flows for the thrust available and required cases are $\dot{m}_{Ta}$ = 0.0084 slugs/s and $\dot{m}_{Tr}$ = 0.0067 slugs/s. A table showing estimated inlet heights as calculated using Equation 6-6 for the two thrust cases is shown in Table 6. The width of the inlet is based on the minimum distance between fans for mounting of 2.6 inches.

Xfoil (x/c=0.90)	
C_l	0.328
Re	1.06E+06
Ue/V_∞	0.987
δ^*/c	0.00653
θ/c	0.00380
H_k	1.72
δ (in)	0.552

Model Scale Estimation	T_a = 0.742 (lbs)	T_r = 0.330 (lbs)
$\dot{m}$ (slug/s)	0.0084	0.0067
h_{out} (in)	1.57	1.16
h_{total} ($h_{out}+\delta$) (in)	2.12	1.71
h_{final} (in)	**1.84**	

* $hfinal=h_{out,Ta} - (0.33x\Delta h_{out}(T_a-T_r)$

** Estimations based on inlet width of 2.6 in

Table 6: Model scale estimations for mass flow and inlet height.

The final inlet height value shown in Table 6 is a weighted average of the thrust available and thrust required heights. The estimated inlet area is 4.79 in^2, as compared to the fan swept area of the Hyperflow fan of 2.71 in^2.

It should be noted that the predicted inlet height is less than the inner diameter of the fan. The inner diameter of the Hyperflow 56 fan is 2.146 inches. Since low subsonic inlets should be converging, this inlet height below the diameter of the fan is a function of both the chosen inlet width and also the fan swept area. Since the fan has a plug center body containing the motor and fan hub, it is the fan swept area, FSA, or the area between the plug and fan diameter that determines the area used to compute the mass flow. The FSA for the Hyperflow 56 fan is 2.71 in^2. For an inlet width of 2.6 inches, the inlet height is 1.84 inches for an inlet area of 4.79 in^2, yielding an as expected converging inlet. Reducing the inlet width will increase the height of the inlet.

Based on the weighted average of the thrust available and thrust required heights, at the thrust required mass flow, the mass flow will be below the design capture area for the inlet, producing a back pressure upstream of the inlet and an inlet velocity below the baseline section edge velocity at that same x/c location. At the thrust available mass flow, the mass flow will be above the design capture area for the inlet, accelerating the flow into the inlet and producing an inlet velocity above the baseline section edge velocity at that same x/c location. For a fixed inlet configuration, the inlet design is a compromise between the low and high mass flow conditions. If a movable inlet lip were used, the inlet area could be optimized for changing mass flow requirements.

6.3. Fan BCs and Force and Moment Calculations

As was done for the 2D simulations discussed in Section 5, the fan thrust was simulated using an actuator disk boundary condition in OVERFLOW. The actuator disk BC imposes a prescribed

static pressure jump at a specified location. The actuator disc BC was used at the fan face location. The Dp was set initially based on a desired thrust given by T=DPA. The Dp was then adjusted to achieve the desired thrust. The desired thrust for the individual fans included the cowl and plug forces in the integration.

$$T = \dot{m}_{fan}(v_{exit} - v_{Inlet}) + (P_{exit} - P_{\infty})A_{exit} - Drag_{Cowl} - Drag_{Plug}$$

Equation 6-7

Similarly, the fan thrust effects were included in the overall calculated lift, drag, and moment.

$$T_{Fan} = \dot{m}_{fan}(v_{exit} - v_{Inlet}) + (P_{exit} - P_{\infty})A_{exit}$$

$$C_{LTotal} = C_{LPress} + C_{LVisc} + T_{Fan}sin(Thrust\ Angle + \alpha)/(q_{inf}A)$$

$$C_{DTotal} = C_{DPress} + C_{DVisc} - T_{Fan}cos(Thrust\ Angle + \alpha)/(q_{inf}A)$$

$$C_{MTotal} = C_{MPress} + C_{MVisc} - \frac{z_T T_{Fan} cos(Thrust\ Angle)}{q_{inf}Ac} - \frac{x_T T_{Fan} sin(Thrust\ Angle)}{q_{inf}Ac}$$

Equation 6-8

The Fan thrust T_{Fan} is the basic mass flow velocity differential and pressure thrust, where *A* and *c* are the reference area and length. The inlet and exit velocities were obtained by computing an area weighted average for each fan inlet and exit. The mass flow for each fan was computed at the fan face. The thrust angle is the set angle of the fan on the model trailing edge and is assumed positive trailing-edge down. The distances z_T and x_T are the x and z locations of the resultant thrust location at the fan exit. Force and moment results were only computed for the center TeDP 5 fan section of the semi-infinite wing. As was discussed in Section 6.1, rotation of the fan thrust angle produced slightly different chord lengths. The chord length for the model was defined in the traditional manner as the distance between the model leading-edge and the trailing-edge, where for the TeDP fan configuration the trailing-edge is defined as the bottom of the fan aft most location. As the thrust angle increases and the trailing-edge rotates down, the chord is decreased slightly. For each different thrust angle, each as run chord was used for the force and moment computations for that given thrust angle geometry.

6.4. Inlet Design Results

Due to a sign error in an excel spreadsheet for Equation 6-6, initial inlet designs were based on an overly large inlet height. The initial runs used an inlet height of 2.69 inches with an inlet width of 2.6 inches. A blend height of 20% for the rear fairings was also used. This low blend height (see geometry in Figure 31) creates a small rear teardrop fairing and large scalloped upper surface cowl. This deep recess between the fans led to significant separation in this area. The inlet height was then reduced to 2.55 inches and then 2.35 inches while reducing the inlet width from 2.6 inches to 2.45 inches and increasing the blend height to 75% before the sign error was discovered in the inlet height estimation discussed in Section 6.2. After discovering the error in the inlet height estimation routine, the inlet height was first reduced to 2.25 inches with a width

of 2.45 inches. This inlet height corresponds to the correct capture area for the Thrust available case. For the Phase I effort, the inlet was sized for the maximum mass flow expected thrust available case. The inlet face was also moved forward to x/c=0.85 from x/c=0.90 while keeping the fan face at x/c=98.72. At x/c=0.85, the baseline C_p is slightly negative at approximately C_p»-0.1. The inlet face was moved forward to provide area for the duct to converge slightly while leaving a short straight section upstream of the fan face. Based on the 2D results reported in Section 2D Thrust Angle Study, the baseline thrust angle chosen was 5° as this appeared to best match the clean NACA 64_3-618 lift curve. Contours of Mach number for a cut down the centerline of the model for a thrust matching the thrust required at α=0° for the wind tunnel test conditions, $V_{¥}$=100 ft/s, Re=1.06x10^6 are shown in Figure 34. The fans are labeled 1 to 5 from left to right, –span to + span. The centerline cut is therefore through fan #3.

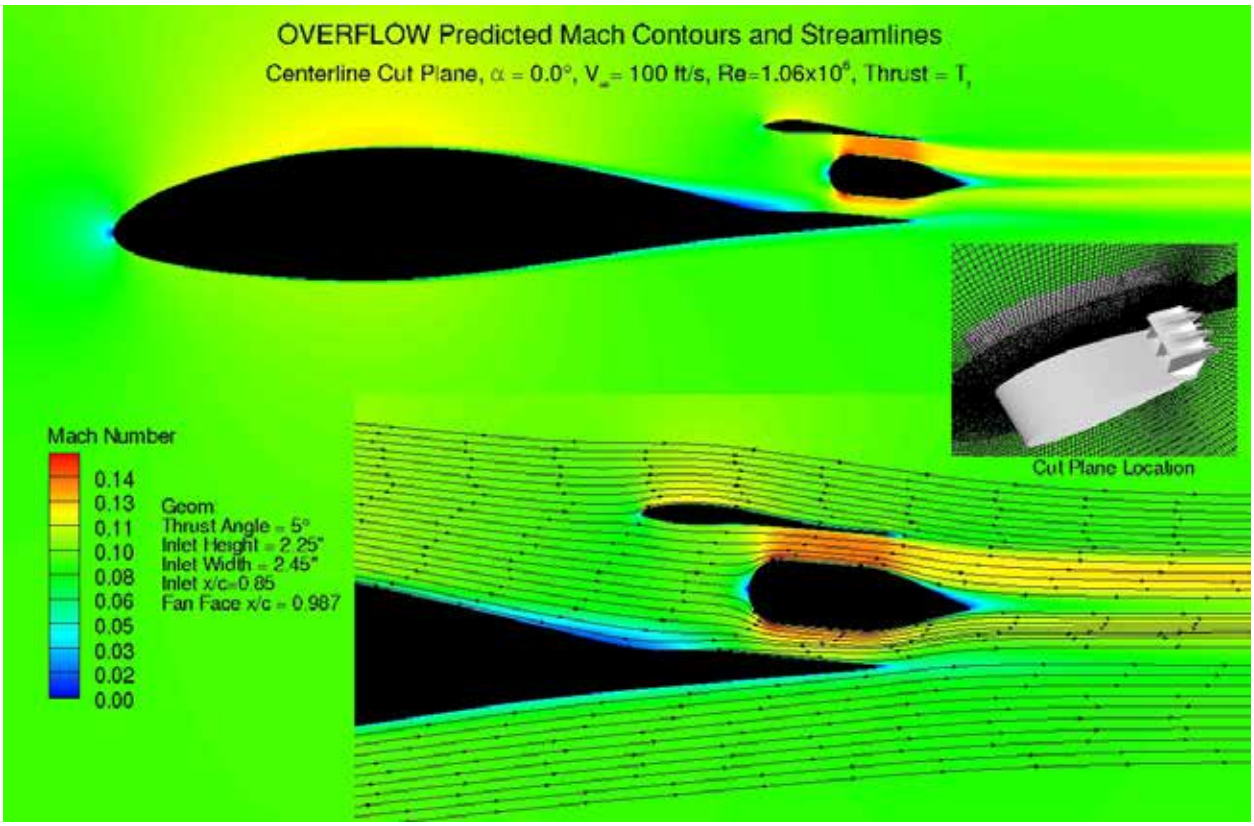

Figure 34: Contours of Mach number and streamlines for a model centerline cut plane (fan #3) for a thrust required mass flow, 5° thrust angle ,α=0°, $V_{¥}$=100 ft/s, Re=1.06x10^6.

From Figure 34, flow appears to be fairly well behaved with no separation on the cowl, the plug, or upstream of the fan. The boundary-layer thickness upstream of the inlet is clearly visible. The presence and effect of the low-speed boundary-layer flow is observed to continue through the fan to the exit. Since the thrust for this case is based on the thrust required value and the inlet was sized for the thrust available mass flow, the inlet is operating below the design mass flow, creating blockage upstream of the inlet. The Mach contours near the wall upstream and at the inlet location show a rapidly thickening boundary-layer as the upstream flow encounters the back

pressure created by inlet and the low mass flow condition. The average velocity for the inlet for this case is 0.72 $V_{¥}$. Based on the inlet location, the edge velocity of the baseline airfoil is approximately 1.05 $V_{¥}$. Since the inlet is oversized for this thrust/mass flow, it is expected that the inlet velocity is well below the baseline edge velocity. Contours of Mach number at the fan face for each of the fans is shown in Figure 35.

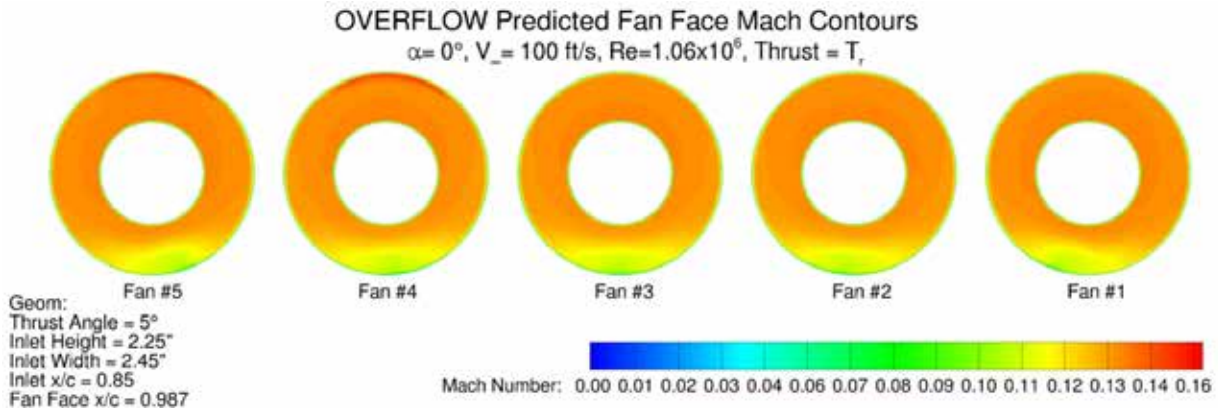

Figure 35: Contours of Mach number at the fan faces for a thrust required mass flow, 5° thrust angle, α=0°, $V_{¥}$=100 ft/s, Re=1.06x10^6.

From Figure 35, the presence of the low speed flow at the fan face due to the ingested boundary layer is again clearly evident. From Figure 35, however, the low-speed flow remains fairly confined to the bottom of the fan duct. While the Mach contours for the centerline fan (fan #3) are symmetric from left the right, the adjacent fan Mach contours become increasingly less symmetric as the outer fans are approached. The asymmetry is due to the fact that the inlets are operating at a mass flow below their design mass flow, T_r versus T_a mass flow, causing blockage. The blockage felt by the oncoming flow forces the flow to attempt to move out of the way of the inlet structure to either side. Again, as discussed in Section 6.1, the only relief for the multi-fan BLI configuration is above the fans, or on either end(side) of the fan system. It should be noted that the boundary condition used for the fan thrust is the actuator disk BC. The actuator disk BC imposes a static pressure jump at the BC location, but does not impart any swirl to the flow. OVERFLOW does not have a BC for swirl. Although the fans have flow straightening stators, one would expect some of the low-speed flow near the bottom of the fan ducts to be mixed due to swirl. Contours of static pressure for the centerline cut plane are shown in Figure 36.

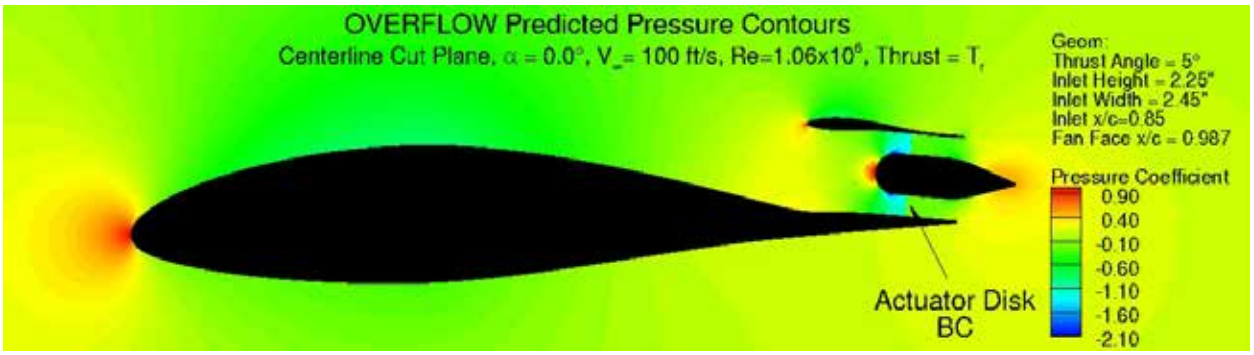

Figure 36: Contours of static pressure for a model centerline cut plane (fan #3) showing effect of the actuator disk BC for a thrust required mass flow, 5° thrust angle ,α=0°, V_{∞}=100 ft/s, Re=1.06x10^6.

The static pressure contours shown in Figure 36 illustrate the jump in static pressure at the fan face location due to the actuator disk boundary condition. Contours of Mach number and streamlines for a cut plane through the #3 rear fairing at the same conditions are shown in Figure 37.

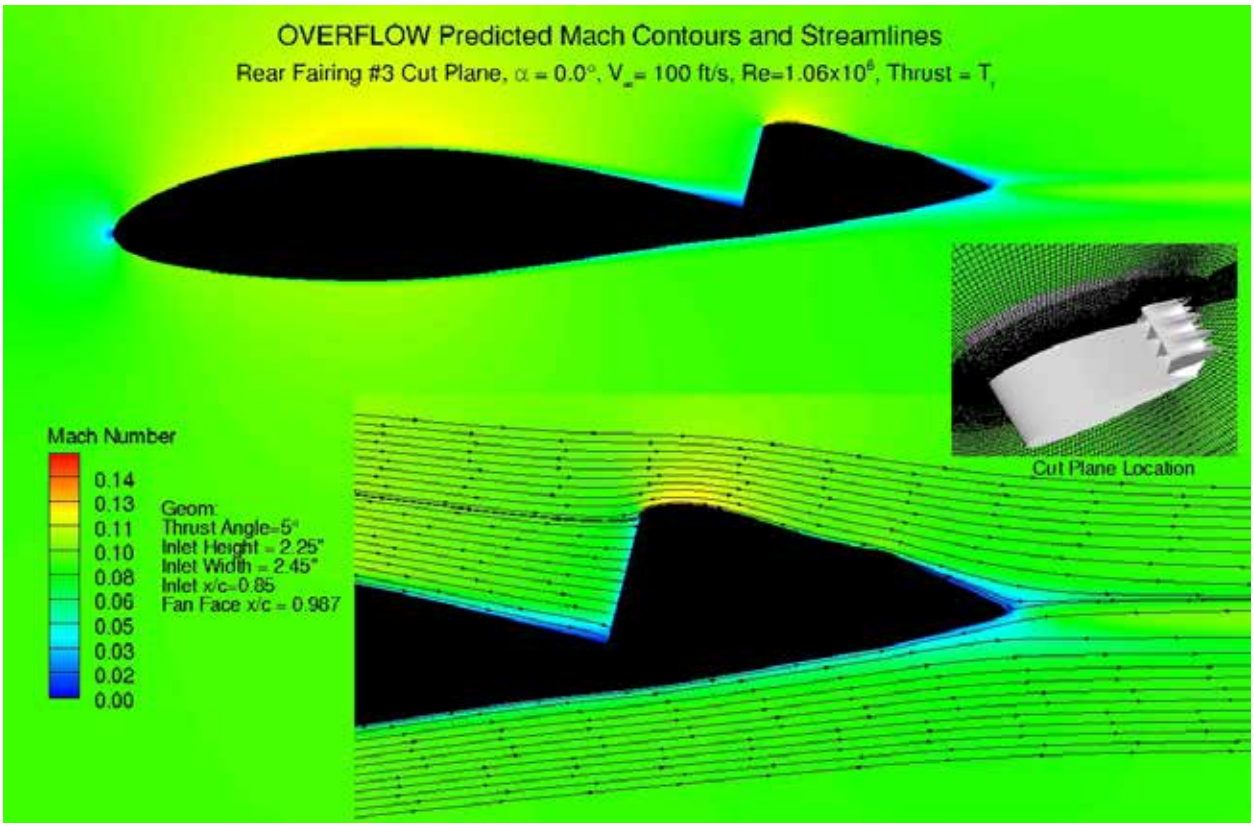

Figure 37: Contours of Mach number and streamlines for a centerline cut plane thought the #3 rear fairing for a thrust required mass flow, 5° thrust angle, α=0°, V_{∞}=100 ft/s, Re=1.06x10^6.

The rear teardrop fairings between the individual fans were included in the geometry in an attempt to mitigate the large rear facing surfaces present between the fans at the back of the

model to reduce/eliminate the pressure drag created by these surfaces. Since the fairings are to the sides of the fans, the reduction in aft facing pressure or base drag must be weighed against the scrubbing drag created by the fan exhaust. From Figure 37, this cut plane is down the middle of the fairing adjacent to the centerline fan. From the Mach contours and streamlines, flow over the teardrop fairing is attached. These rear teardrop fairings were included in the Phase I wind tunnel investigation, but not in the Phase I computational model. A plot showing streamlines just off the surface and pressure contours for the geometry is shown in Figure 38. From Figure 38, as was observed in the cut plane contours in shown in Figure 34 and Figure 37, the flow looks well behaved with no obvious areas of separation on the model surface or cowl top. The blockage created by the presence of the inlets due to the below design mass flow thrust is evident in the higher surface pressure contours upstream of the inlets. The middle fan surface streamlines are symmetric into the inlet. The # 2 and #4 inlets, however, show some asymmetry as the flow experiences an increasing back pressure due to the presence of the inlets. The outer fans (#1 and #5), show the largest asymmetry in the surface streamlines as the flow searches for the path of least resistance to the outside of the fans, creating a seemingly significant local flow angle to the cowl side lips. This asymmetry was also observed in the fan face Mach contours shown in Figure 35.

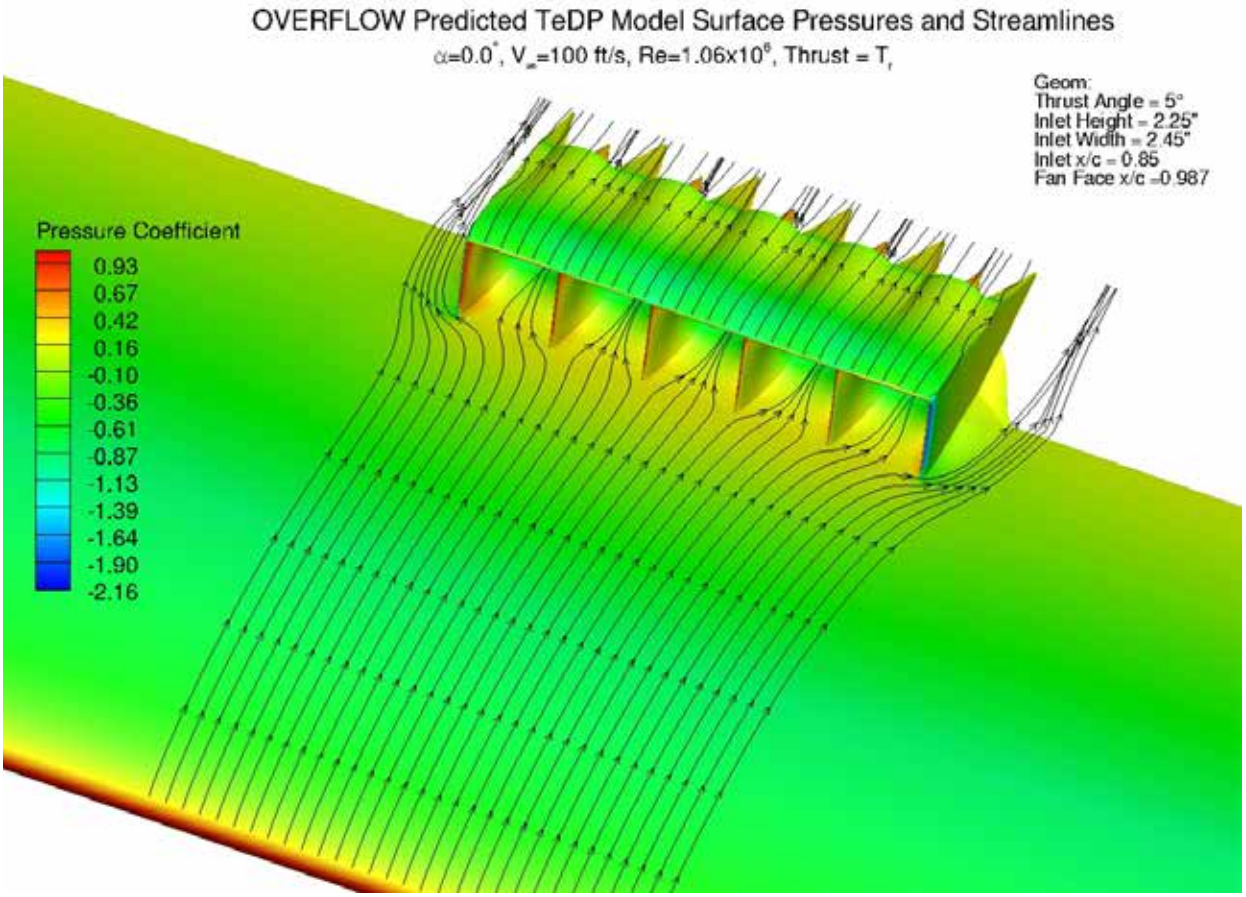

Figure 38: Contours of surface pressure coefficient and streamlines just off the surface for the thrust required mass flow, 5° thrust angle, α=0°, V_∞=100 ft/s, Re=1.06x10^6.

The results for the 2.25 inch height inlet with a width of 2.45 inches with a 5° thrust angle show that for an overly large inlet, the cowl and rear fairings can be designed to alleviate separation on the cowl top and on the rear fairings. As previously discussed, initial designs used a deeper scallop between the fans to reduce the size of the rear teardrop shape. The deeper scallop created larger adverse pressure gradients on the cowl top which produced large amounts of separation between the fans and on the rear fairings. A blend height of 75% of the fan radius proved to provide a separation free cowl top surface.

After finding a set of parameters to design a separation free cowl top surface, the inlet height was reduced to 2.15 inches. This reduced inlet height increased the average inlet velocity only slightly from 0.72 $V_{¥}$ to 0.76 $V_{¥}$. Since the Hyperflow fan FSA is 2.71 in^2, and the fan casing inner diameter is 2.145 inches, an inlet height below 2.145 inches means that the inlet will initially be converging, then slightly diverge in order to match up with the contour of the fan casing. This is not the ideal subsonic converging inlet, but an initially converging inlet, followed by a slightly diverging section until the fan casing is reached, where the flow will converge to the fan FSA. Reducing the inlet width would allow a larger inlet height. The current width of 2.45 inches, however, is the minimum width which will allow fastening hardware to be used to attach the fans to the model in a side-by-side configuration. If a constant area inlet up to the fan face were desired to avoid this converging, diverging, converging inlet, a serpentine type surface on the inlet floor could be developed. This serpentine surface would initially ramp up away from the inlet bottom then back down again as the fan face/hub is reached. A schematic showing the basic concept is shown in Figure 39.

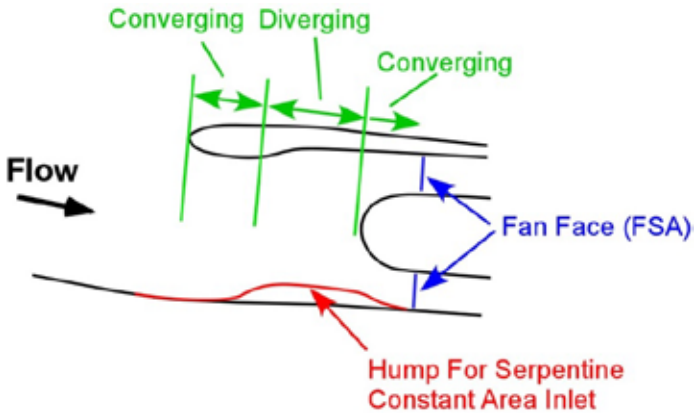

Figure 39: Inlet height and duct schematic for basic and serpentine geometries.

From Figure 39, results from Phase I showed that for the low speed, essentially incompressible flow experienced by the proposed model and test bed aircraft that other than the presence of the ingested boundary-layer, very little distortion was introduced to the fan due to the inlet geometry. As a result, it was decided to explore the converging, diverging, converging (CDC) geometry and avoid the overly complicated flow path presented by the serpentine duct.

After deciding to go with the CDC duct geometry, the duct height was further reduced to 1.95 inches. The 1.95 inch height is a weighted average between the thrust required and thrust

available mass flow heights, 1.81 inches versus 2.24 inches respectively. Although the 1.95 inch inlet height is 15% less than 2.25 inch height shown in Figure 34 through Figure 38, the value is still above the thrust required mass flow height of 1.81 inches. As a result, the 1.95 inch inlet is still oversized and will produce some back pressure.

Contours of Mach number for a centerline cut of the model for the thrust required mass flow at α=0° for the wind tunnel test conditions, $V_{¥}$=100 ft/s, Re=1.06x10^6 are shown in Figure 40 for the 1.95 inch height geometry.

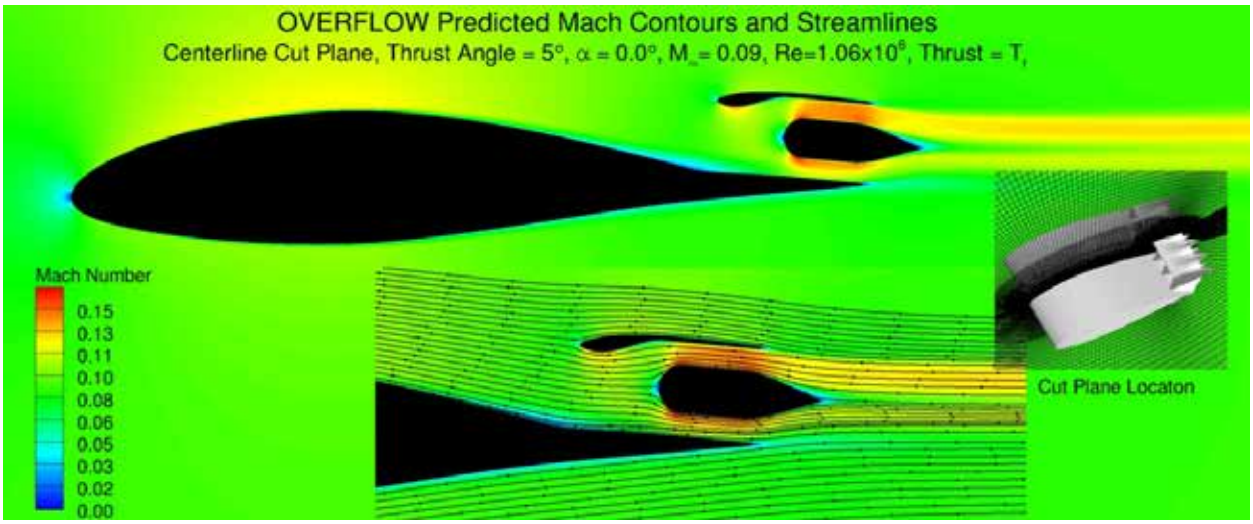

Figure 40: Contours of Mach number and streamlines for a model centerline cut plane (fan #3) for a thrust required mass flow, 5° thrust angle ,α=0°, $M_{¥}$=0.09, Re=1.06x10^6.

From Figure 40, the converging, diverging, converging aspect of the cowl lip and inlet are visible. The flow appears to be well behaved with no separation on the cowl, plug, or upstream of the fan. The boundary-layer thickness upstream of the inlet is clearly visible. At the inlet location, the boundary-layer thickness is 30% of the overall inlet thickness. Again, as was observed for the larger inlet in Figure 34, the presence of the low-speed boundary-layer flow is observed to continue through the fan to the exit. Since the thrust for this case is based on the thrust required value and the inlet was sized for a mass flow between the thrust required and thrust available cases, the inlet is operating below the design mass flow, creating blockage upstream of the inlet. The Mach contours near the wall upstream of and at the inlet location show a rapidly thickening boundary-layer as the upstream flow encounters the back pressure created by inlet and the low mass flow condition. The average velocity for the inlet for the thrust required case at a=0° is 0.85 V_∞, up from 0.72 V_∞ for the 2.25 inch inlet geometry.

Contours of Mach number and total pressure ratio at the fan face for each of the fans is shown in Figure 41. From Figure 41, the presence of the low speed flow at the fan face due to the ingested boundary layer is clearly evident in the Mach contours. The low speed flow, however, remains confined to the bottom of the fan duct. The asymmetry observed for the larger duct in Figure 35 is still present, but significantly reduced. The reduced height inlet has reduced the blockage felt by the oncoming flow. The stagnation pressure ratio contours show very little

distortion even though the boundary-layer thickness to fan diameter ratio at the fan face is 18%. This ratio of boundary-layer thickness to fan diameter of d/d=18% is down from the value of 30% at this inlet face due to the converging inlet geometry accelerating the flow up to the fan face. The loss in stagnation pressure is less than 1.5%, producing a very low distortion level. The low distortion level is a result of the converging duct and the low free-stream Mach number.

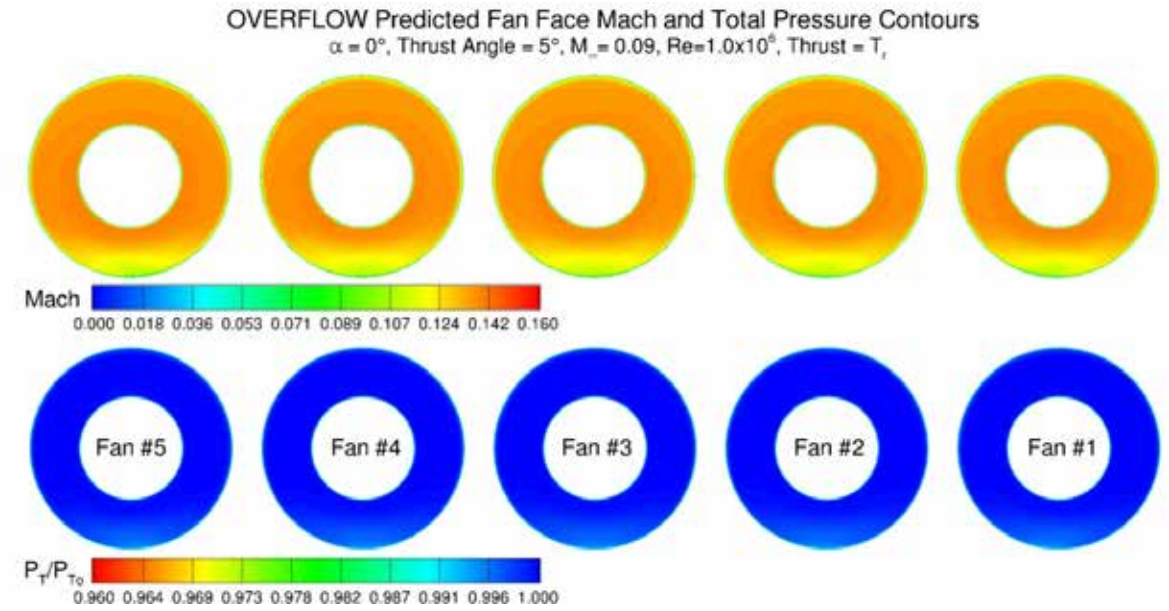

Figure 41: Contours of Mach number and stagnation pressure ratio at the fan faces for a thrust required mass flow, 5° thrust angle, α=0°, M_∞=0.09, Re=1.06x10^6.

A plot showing Mach contours and streamlines for a centerline cut plane through fan #3 for the thrust required mass flow at angles-of-attack of 0°, 4°, and 8° for an inlet height of 1.95 inches is shown in Figure 42. For the three angles-of-attack shown, the flow looks very well behaved with no separation present on the cowl, plug, or either upstream or in the inlet. The growth of the boundary-layer with increasing angle-of-attack is clearly visible in the increased extent of the low Mach number region just upstream of the inlet. The vertical extent of the lower Mach number flow below the plug is also observed to increase with increasing angle-of-attack. This increase in the thickness of the boundary-layer is most easily observed in the fan face Mach contours for these angles-of-attack which are shown in Figure 43.

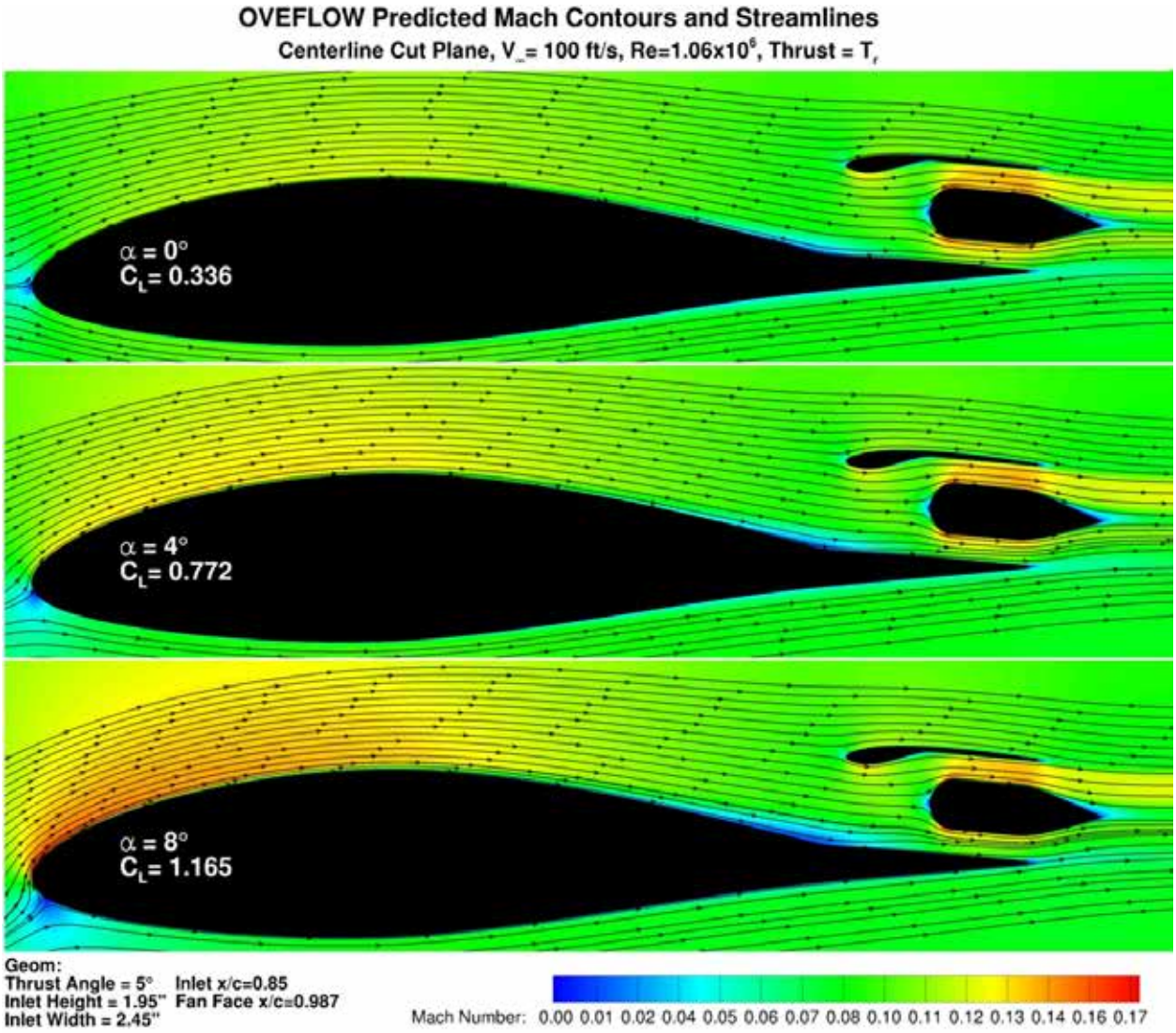

Figure 42: Contours of Mach number and streamlines for a model centerline cut plane (fan #3) for a thrust required mass flow, 5° thrust angle ,α=0°, 4°, and 8°, V_{∞}=100 ft/s, Re=1.06x10^6.

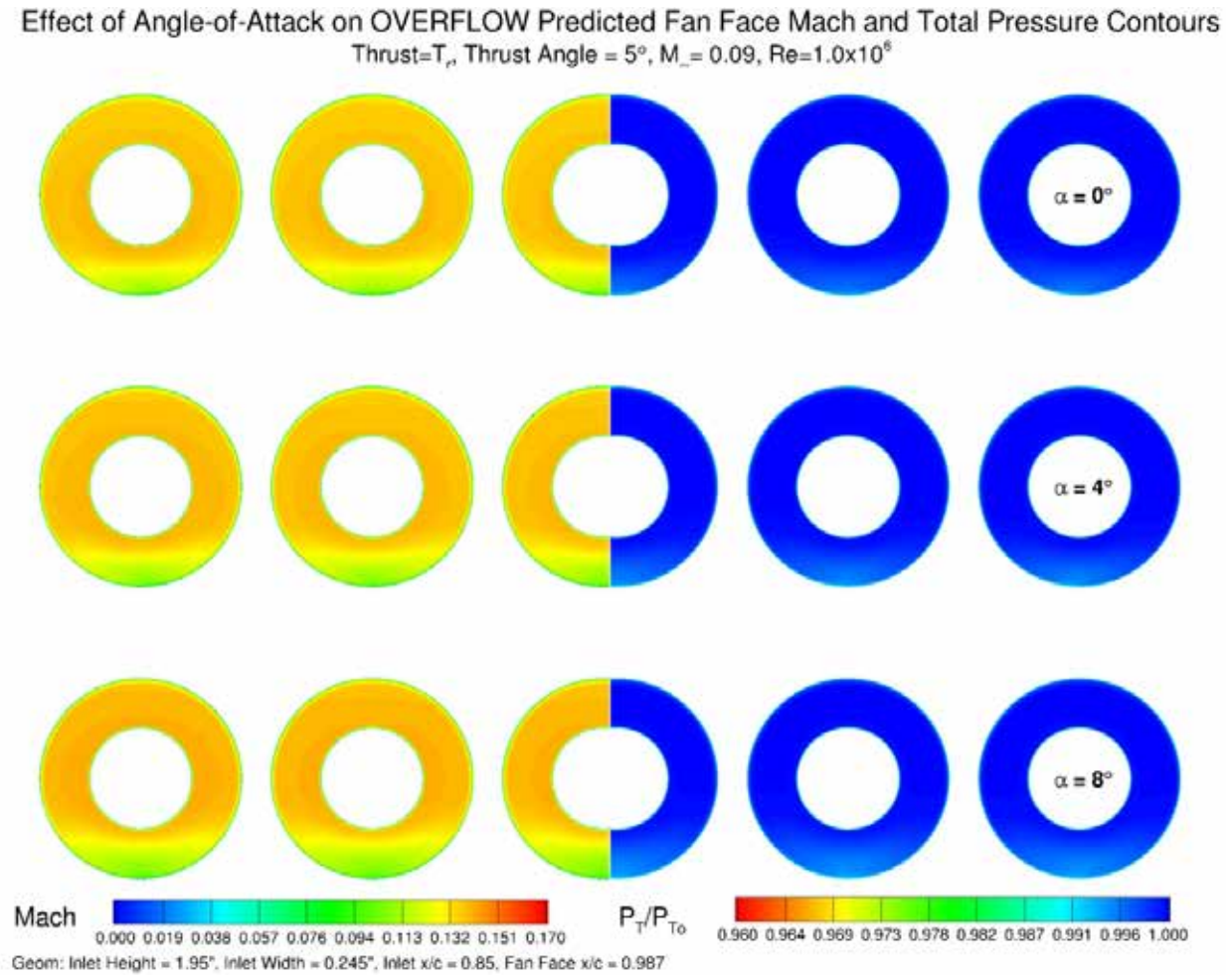

Figure 43: Contours of Mach number at the fan faces for a thrust required mass flow, 5° thrust angle, α=0°, 4°, and 8°, V_∞=100 ft/s, Re=1.06x10^6.

Also included in Figure 43 are total pressure ratio contours. Since the flow is symmetric about the center fan, total pressure ratio contours are shown for fans #1, #2, and half of fan #3. The other half of fan #3, #4, and #5 show contours of Mach number. From Figure 43, the increasing growth of the boundary-layer with angle-of-attack is clearly visible in the fan face Mach contours. The magnitude of the asymmetry does not appear to increase significantly with increasing angle-of-attack. The contours of total pressure show very little distortion as the angle-of-attack increases. Even with the relatively thick ingested boundary layer, there is very little distortion present in the total pressure contours.

Contours of Mach number and streamlines for a cut plane through the #3 rear fairing at the same angles-of-attack are shown in Figure 44. From Figure 44, the flow again appears to be well behaved. At a=0° and 4°, the rear fairing appears to be attached with no separated flow. At a=8°, however, a small separation bubble is present on the upper surface of the rear teardrop fairing. The aft extent of the fairing was increased to alleviate this separation in a later design iteration. Although the increased fairing length did eliminate the separation, the overall drag of

the cowl increased due to the increase in scrubbed area. While the pressure drag was reduced, the increased area produced a larger viscous drag due to the fact that the fairing sides are scrubbed by the fan exhaust. As a result, the baseline geometry shown in Figure 44 was retained for the 5° thrust angle geometry. Overall, results for the 1.95 inch inlet with a 5° thrust angle were greatly improved over previous designs and heights.

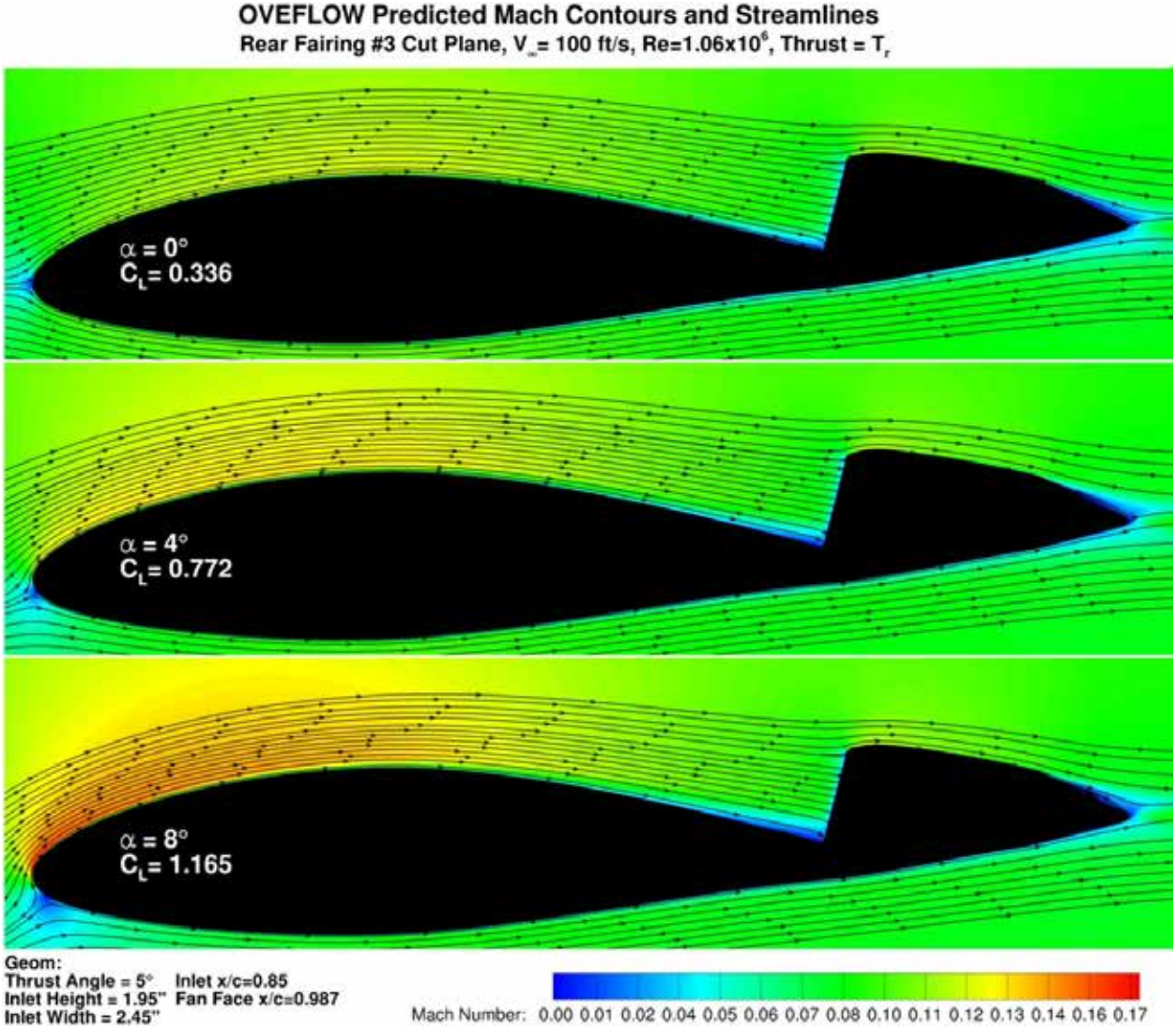

Figure 44: Contours of Mach number and streamlines for a centerline cut plane thought the #3 rear fairing for a thrust required mass flow, 5° thrust angle, α=0°, 4°, and 8°, V_{∞}=100 ft/s, Re=1.06x10^6.

6.5. **Thrust Angle Effects**

The effect of varying the fan thrust angle was investigated. Since the airfoil/fan system is closely coupled, varying the fan thrust angle will affect sectional lift, drag, and pitching moment. The baseline trailing-edge angle for the NACA 64_3-618 section is 14.5°. Since the fan extends slightly beyond the trailing-edge of the baseline airfoil, the thrust angle of the fan sets the

trailing-edge angle for the TeDP section. As would be expected, changing the fan thrust angle will change the section's camber, affecting lift, drag, and moment. Additionally, since the fan thrust is included in the force and moment results, increasing the fan thrust angle increases the thrust's lift contribution and decreases the actual thrust used for propulsion. Additionally, increasing the thrust angle will increase the nose down moment of the section. Thrust angles of 5°, 7.5°, and 11.4° were investigated.

Contours of Mach number and streamlines for a centerline cut plane through fan #3 for the thrust required mass flow for thrust angles of 5°, 7.5°, and 11.4° at a= 4° is shown in Figure 45. From Figure 45, the slight rotation of the trailing-edge with increasing thrust angle is visible. The Mach contours and streamlines show well behaved flow with no separation for any of the three thrust angles for either the cowl or plug. Upon close inspection, the low velocity region just upstream of the inlet appears to be slightly smaller for the 11.4° thrust angle case.

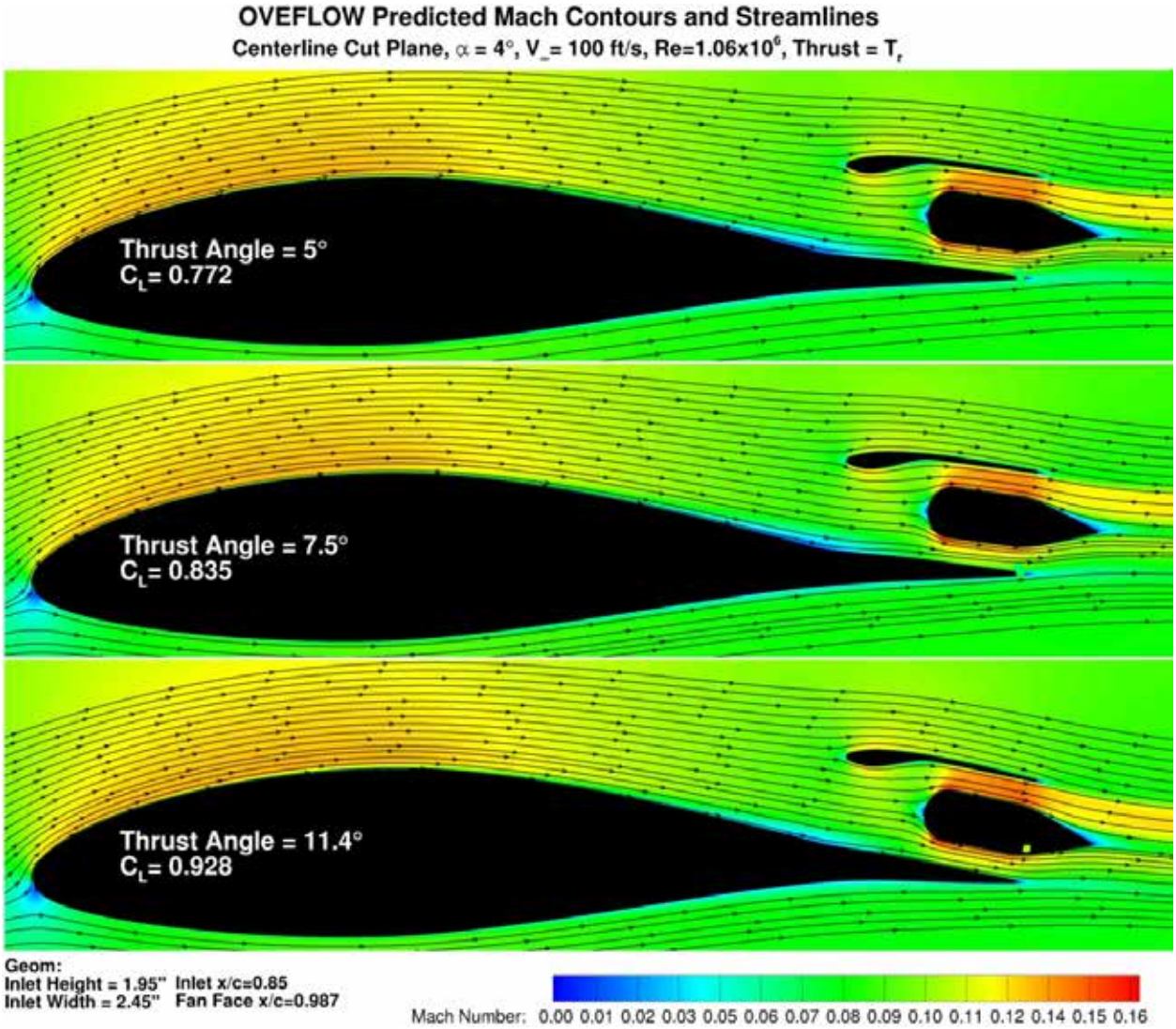

Figure 45: Contours of Mach number and streamlines for a model centerline cut plane (fan #3) for a thrust required mass flow, 5°, 7.5°, and 11.4° thrust angles, α=4°, V¥=100 ft/s, Re=1.06x10^6.

Contours of Mach number for the fan faces at a=4° for the 5°, 7.5°, and 11.4° thrust angle geometries at the thrust required mass flow are shown in Figure 46. From Figure 46, as was observed for the 5° thrust angle case as a function of angle-of-attack shown in Figure 43, the Mach contours for the various thrust angles show a small amount of asymmetry for the outer fan faces. The slight reduction in the low speed flow near the wall observed in the 11.4° thrust angle geometry shown Figure 45 is also visible in the fan face Mach contours for the 11.4° geometry in Figure 46. This slight reduction in low speed flow near the wall is most likely a result of the slight increase in mass flow required to overcome an increase in cowl drag due to the higher fan angle deflection which will be discussed shortly.

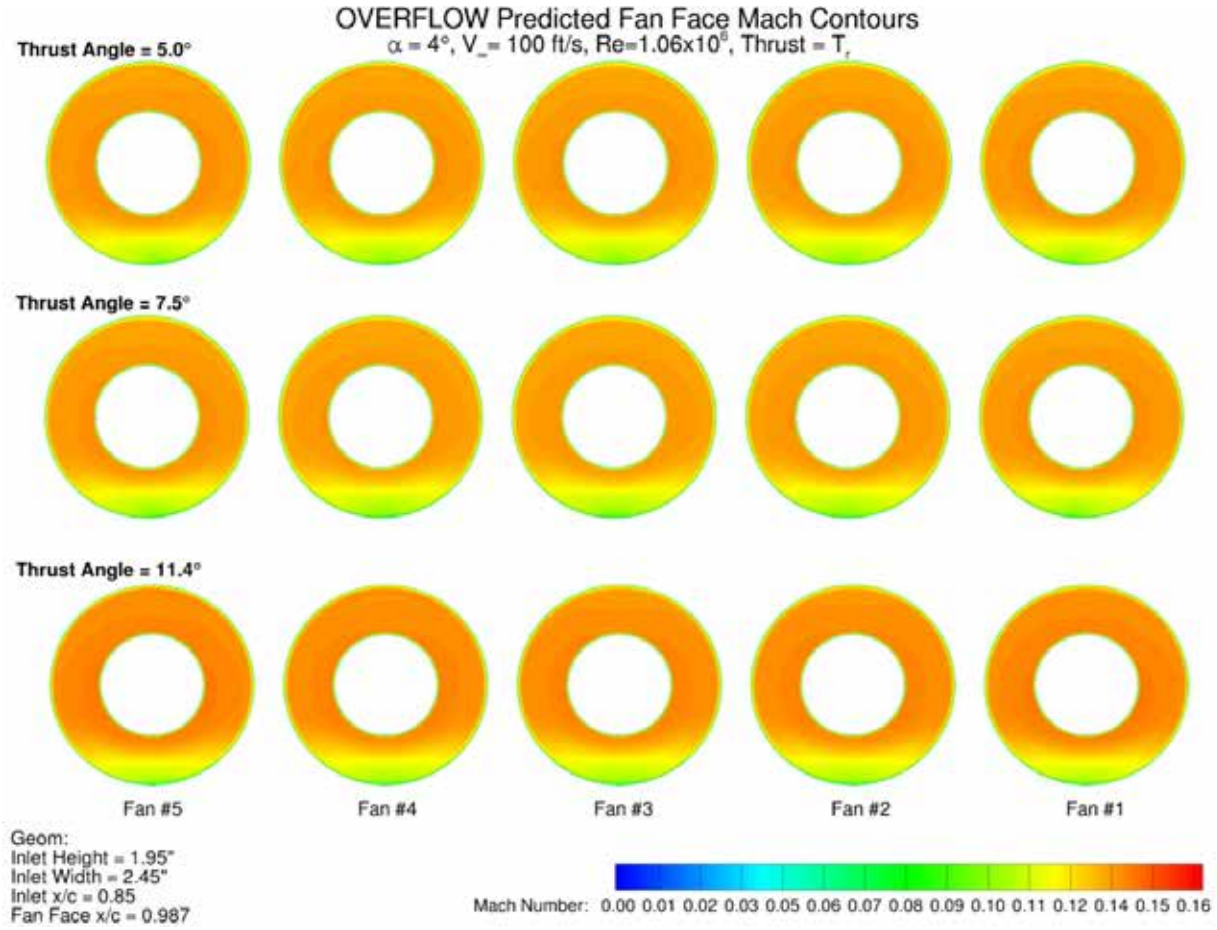

Figure 46: Contours of Mach number at the fan faces for a thrust required mass flow, 5°, 7.5°, and 11.4° thrust angles, α=4°, V_∞=100 ft/s, Re=1.06x10^6.

Contours of surface pressure and streamlines for the 5°, 7.5°, and 11.4° thrust angle geometries at a=4° the thrust required mass flow case are shown in Figure 47. From Figure 47, as was observed for the fan face Mach contours shown in Figure 46, the symmetry of the surface streamlines entering the inlets does not vary significantly for the different thrust angles. Outward movement of the surface streamlines away from the center is observed in the outer most fans (fan #1 and fan #5)

.

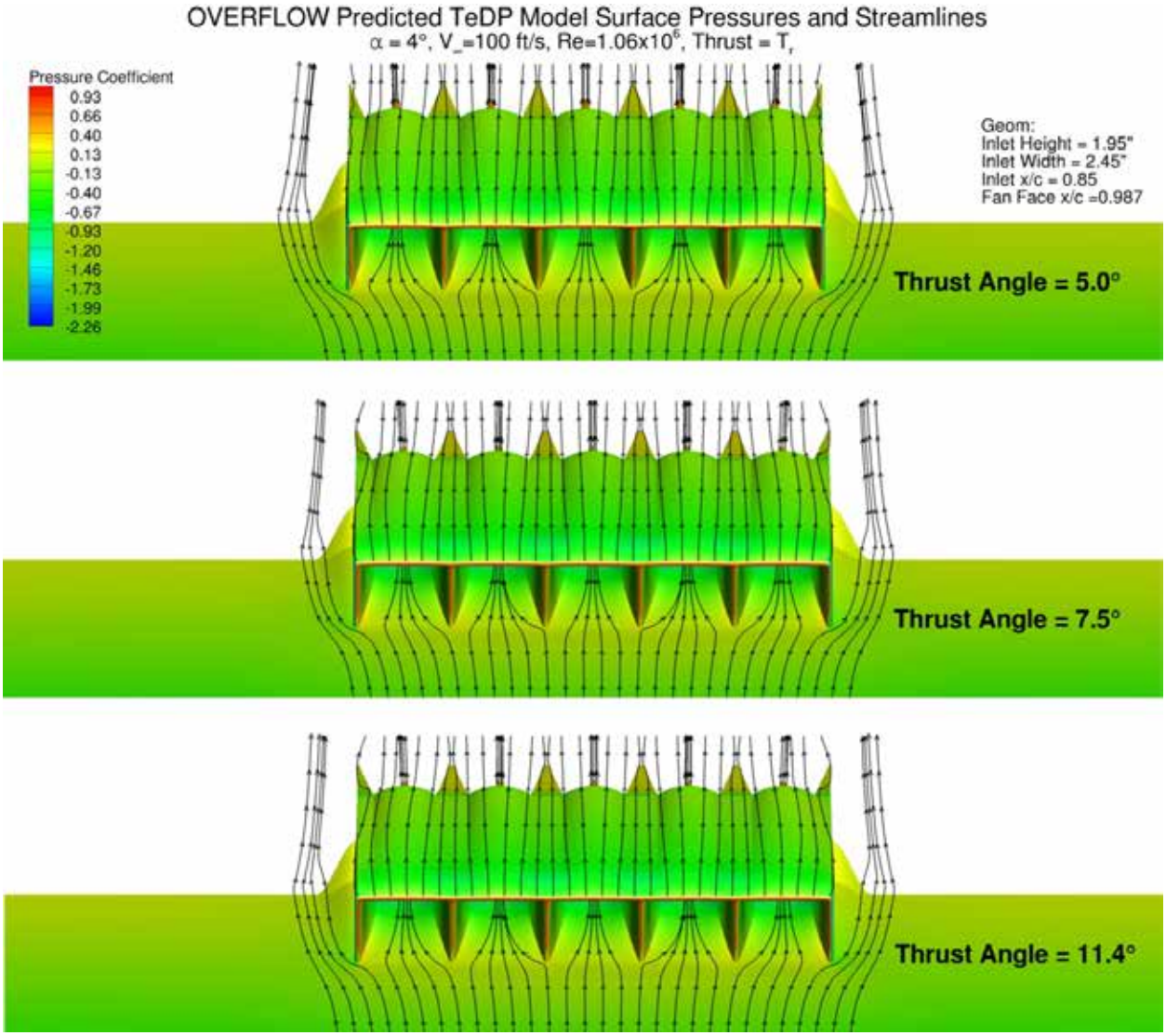

Figure 47: Contours of surface pressure coefficient and streamlines just off the surface for the thrust required mass flow, 5°, 7.5°, and 11.4° thrust angles, α=4°, V¥=100 ft/s, Re=1.06x10^6.

Force and moment results for the baseline NACA 64_3-618 and the 5 fan TeDP model with a thrust angle of 5°, 7.5°, and 11.4° degrees are shown in Figure 48. Figure 48 contains lift, drag, and moment polars. Also included in Figure 48 is a graph showing the thrust ratio ($T/T_{a=0°}$) as a function of lift coefficient. For the angle-of-attack polars, the fan mass flow was set at a=0° to match the desired thrust. This mass flow was then held constant for all other angles-of-attack in the polar. From Figure 48, the effect of increasing the fan thrust angle is to shift the lift curve to the left. This shift to the left is due to a change in the section's camber with thrust angle and a slight increase in the lift due to an increasing thrust vector in the lift direction. The increased effective camber also produces a higher maximum lift coefficient. The shift is fairly consistent in the linear range of the lift curve. All of the thrust angles have a lift curve slope similar to the

baseline NACA 64_3-618 section. The 5° thrust angle case produces a lift coefficient approximately ΔC_L= -0.13 low for a given angle-of-attack as compared to the baseline NACA 64_3-618 section. The 7.5° thrust angle case produces a lift coefficient approximately ΔC_L= -0.07 low. The 11.4° thrust angle results compare well to the baseline NACA 64_3-618 results. Whereas the basic trailing edge angle for NACA 64_3-618 is 14.5°, the 11.4° thrust angle geometry coupled with the thrust effect mimic the camber of the baseline section. The 11.4° thrust angle geometry also produces an increase in C_{Lmax} (ΔC_{Lmax}=8.5%) over the baseline section for the thrust required mass flow at the highest angle-of-attack investigated. The increase in thrust angle, however, did not come without a cost. Increasing the thrust angle also reduced the thrust component in the axial direction and increased the drag and moment of the section requiring a 3.7% increase in mass flow in order to achieve the same thrust at α=0°.

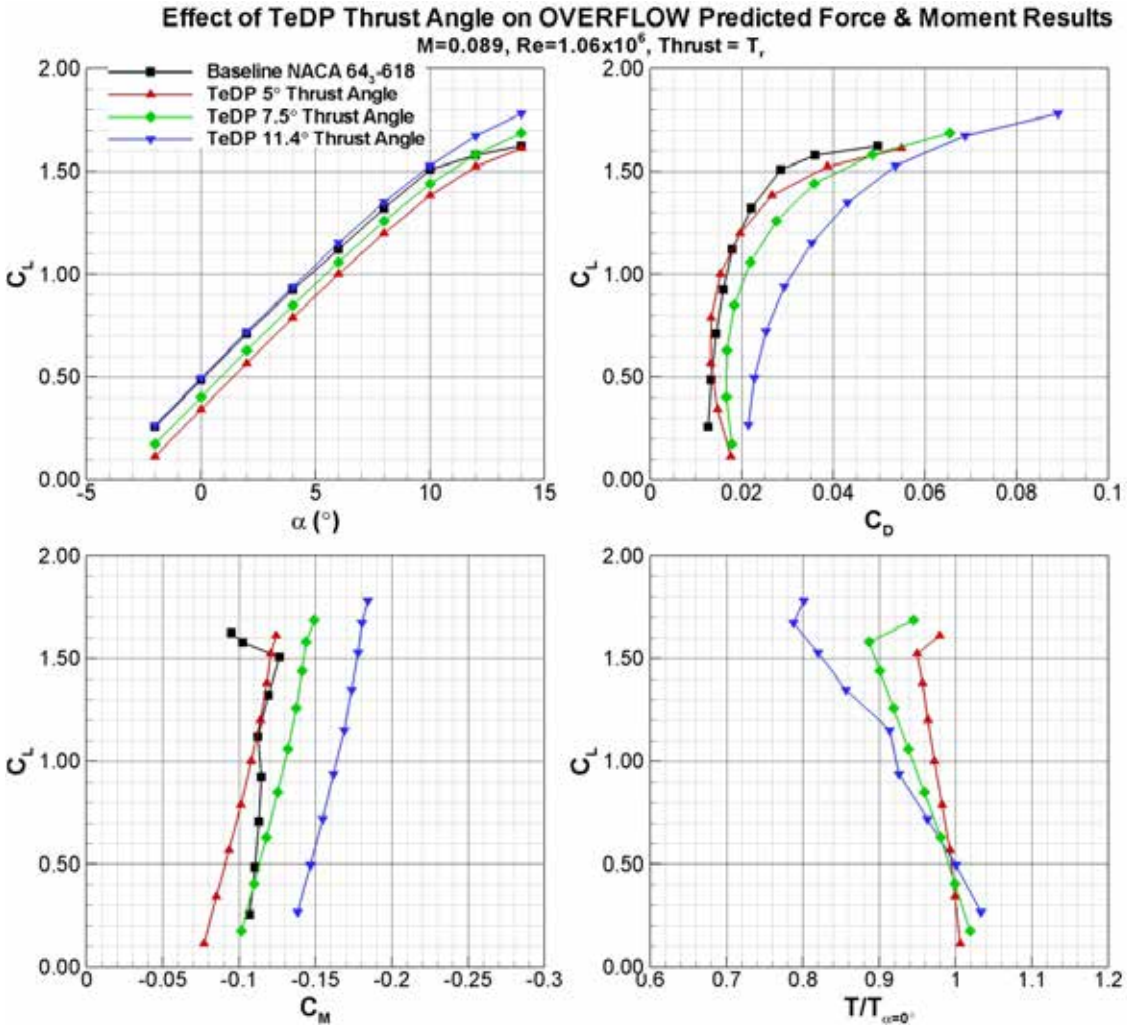

Figure 48: OVERFLOW predicted force and moment results for the baseline NACA 643-618 section and the 5 fan TeDP configuration at thrust angles of 5°, 7.5°, and 11.4° degrees at M_∞=0.09, Re=1.06x10^6.

The C_D values in Figure 48 for the C_L versus C_D plot include drag for the airfoil, cowl, and inlet/fan geometry and does not include the mass flow based thrust or the plug. From Figure 48, at low lift coefficients, the drag of the 5° and baseline NACA 64_3-618 section compare fairly well across the polar. The change in camber and the addition of the cowl geometry do not add a significant drag penalty to the 5° TeDP model. At high C_Ls, however, the drag of the 5° TeDP geometry increases beyond that of the baseline NACA 64_3-618 section. The drag of the 11.4° thrust angle geometry, however, is significantly greater than both the baseline NACA 64_3-618 section and the 5° thrust angle geometry. As would be expected the drag of the 7.5° thrust angle geometry lies between the 5° and 11.4° results. At C_L=0.5, the drag of the 7.5° geometry is 22% greater than the 5° geometry, increasing to 32% at C_L=1.0. The drag of the 11.4° geometry is 65% greater than the 5° geometry at C_L=0.5, increasing to 102% at C_L=1.0. After scrutinizing the drag of the individual components, the large increase in drag for the 7.5° and 11.4° geometry is primarily a result of the cowl top. Since the fan mass flow ejects at the cowl trailing-edge, the upper surface of the cowl sees a Coanda effect, producing a low pressure over the top of the cowl. This low pressure does not recover at the cowl trailing-edge due to the presence of the jet. As compared to the 5° geometry, the further trailing-edge down rotation of the 7.5° and 11.4° geometries means that more of the cowl upper surface is an aft facing surface. This aft facing surface for the increased thrust angles produces a higher pressure drag. The effect of this increase in drag for the cowl for the higher thrust angle geometries as compared to the 5° geometry is also observed in the thrust ratio as a function of C_L. Recall that the fan mass flow was set at α=0° to match the desired thrust. This mass flow was then held constant for all other angles-of-attack in the polar. As discussed in Section 6.3, in addition to the mass flow based thrust, the thrust calculation includes the plug drag and the cowl drag to account for installation penalties. Since the fan mass flow was held constant, changes in thrust level with angle-of-attack would then be due to changes in the drag of the plug, cowl, or inlet velocity. For all of the thrust angles, the plug drag and inlet velocity remained relatively constant with angle-of-attack. For the 5° geometry, the thrust level decreases by approximately 5% between α=0° to α=12°. For the 7.5° and 11.4° geometry, however, the thrust level decreases by 12% and 22% between α=0° to α=12°, respectively. This reduction in thrust with C_L is primarily due to the increase in cowl drag.

Moment results are also shown in Figure 48. As would be expected, increasing the thrust angle produces a more negative pitching moment. The reduction in camber of the 5° geometry as compared to the baseline NACA 64_3-618 section produces a slightly more positive pitching moment at low C_Ls. As C_L increases, the 5° geometry and the NACA 64_3-618 section produce similar moments. For the 5° geometry, the reduction in camber is balanced by the lower pressures over the cowl surface at the airfoil trailing-edge and the addition of the jet thrust effect upon the moment. The 7.5° geometry increases the nose down moment by 21% as compared to the 5° thrust angle. The 11.4° geometry further increases this negative moment, ΔC_M = -50% as compared to the 5° geometry. These increases in nose down moment are a result of the increased camber of the section, the increased jet thrust effect, and more negative cowl pressures.

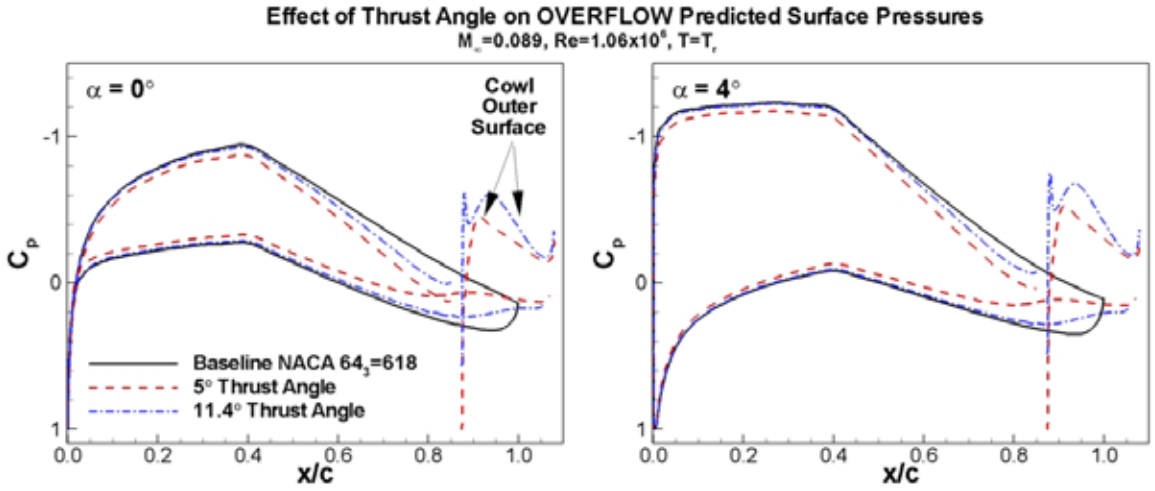

Figure 49: OVERFLOW predicted surface pressures for the baseline NACA 64_3-618 section and the 5° and 11.4° thrust angle at a thrust required mass flow, α=0°, 4°, M_∞=0.089, Re=1.06x10^6.

Surface pressures for the baseline NACA 64_3-618 section and the 5° and 11.4° geometry at α=0° and α=4° are shown in Figure 49. The pressures in Figure 49 for the TeDP configuration are for a cut through the center of the #3 fan. The pressures are for the main airfoil and the external cowl. The internal fan pressures are not shown. Since the polars were generated at a constant mass flow, the internal fan pressures do not change with angle-of-attack and do not significantly contribute to the force/moments due to the axisymmetric nature of the fan. From Figure 49, the higher pressure (more positive pressures) upstream of the inlet due to the retarding effect of the oversized inlet for the thrust required mass flow are clearly evident in both the α=0° and 4° pressures. The back pressure of the oversized inlet is felt up to the max thickness of the airfoil at x/c≈0.40. The acceleration of the flow over the upper surface cowl is also evident. The reduced camber of the 5° geometry and lower lift for a given angle-of-attack is clearly depicted in the pressures as compared to the baseline section. The pressures upstream of x/c≈0.40 on the upper surface and the lower surface pressures for the 11.4° thrust angle case compare much better to the baseline section pressures, as would be expected from the lift curve comparison shown in Figure 48. The increased negative pitching moment of the TeDP section due to the increased aft cowl pressures is also evident.

Compared to the 2D results shown in Section 5, the 3D geometry produces significant 3D relieving effects. From the 2D results, the 5° thrust angle best matched the baseline lift curve. From the 3D results, the 11.4° thrust angle best matches the baseline lift curve. It is believed that the plug surface in the 2D results is primary reason for the difference between the 2D and 3D thrust angle results. For the 2D case, the plug acts as another lifting surface. In the actual 3D flowfield, the plug is circular, with a significant 3D relieving effect as the flow moves up and around the plug at angle-of-attack.

The results from the thrust angle investigation showed that the fan thrust angle has a large effect upon the lift, moment, and performance of the section. Due to the far aft location of the fan, the fan thrust angle directly affects the section's camber. It was initially expected that the fan thrust angle which matched the baseline NACA 64_3-618 section lift curve would be the preferred

geometry. The results presented here, however, indicate that although the 11.4° thrust angle geometry does match the baseline lift curve well and increase the high angle-of-attack lift of the section, the increased drag and more negative moment are significant drawbacks. It was found that the large drag increase of the 11.4° geometry was primarily a result of increased pressure drag on the upper surface cowl due to the increased rotation of the thrust angle. Since the performance and efficiency of the TeDP configuration is of primary importance, the 5° geometry would appear to be a more optimal configuration. As a result, the 5° geometry was chosen for the remaining CFD studies and for the wind tunnel model.

6.6. **Effect of Thrust Level**

The 5° thrust angle geometry was used to investigate the effects of varying the fan thrust level. Three thrust levels were run, including a windmilling, thrust required (T_r=0.33 lb/fan), and thrust available cases (T_a=0.74 lb/fan). For the windmilling case, the fan actuator disk Δp was set to zero. Recall that the inlet capture area was sized for a mass flow between the thrust required and thrust available cases. As was observed in Section 6.4, the thrust required mass flow produced an inlet velocity 15% below the local edge velocity due to the blockage induced by the oversized inlet. For the thrust available mass flow, the inlet is undersized, which should produce an inlet velocity above the edge velocity. A comparison of the Mach contours and streamlines for a centerline cut through the #3 fan is shown in Figure 50 for the three cases at α=0°.

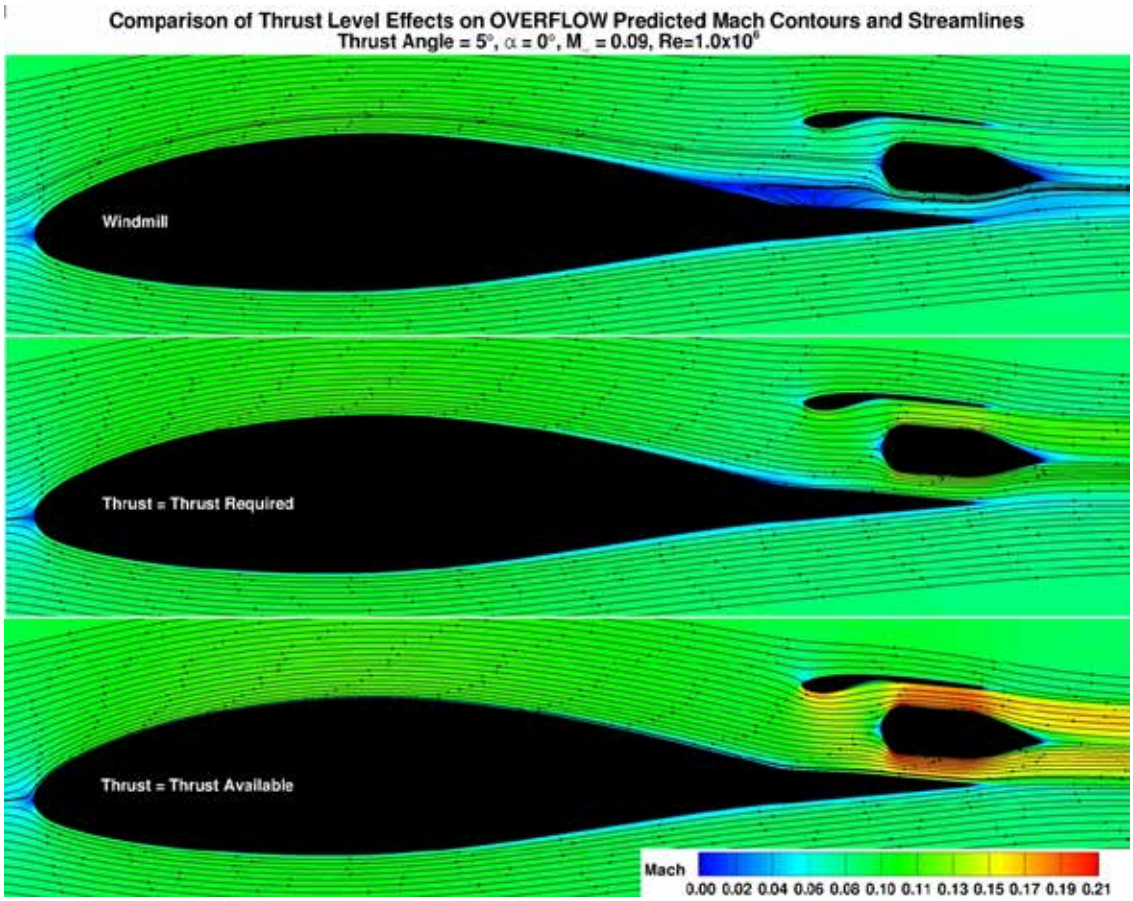

Figure 50: Contours of Mach number and streamlines for a model centerline cut plane (fan #3) for the windmill, thrust required, and thrust available mass flow cases, 5° thrust angle, α=0°, M_{∞}=0.09, Re=1.06x10^6.

From Figure 50, the blockage created by the windmill case creates a large separated region upstream of the inlet. The separation upstream of the inlet for the windmill case is not unexpected. The cowl surface, however, remains attached. The results for the windmill case are optimistic. The presence of the fan blades in the actual windmill case would produce increased blockage, increasing the amount of separation. For the thrust available case, the difference in the higher Mach number flow through the fan due to the increased mass flow is evident. The undersized inlet for the thrust available case has accelerated the flow upstream of the inlet, reducing the incoming boundary-layer thickness. Both thrust available and thrust required cases show well behaved flow with no separation upstream of the inlet or on the cowl or plug surface. The average inlet velocity for the thrust required case is 0.85 V_{∞}, whereas the average inlet velocity for the thrust available case is 1.10 V_{∞}. The boundary layer thickness for the thrust required case is 30% of the inlet height, reducing to 23% for the thrust available case. Contours of Mach number and total pressure ratio at the fan face for fans at the three different thrust levels are shown in Figure 51.

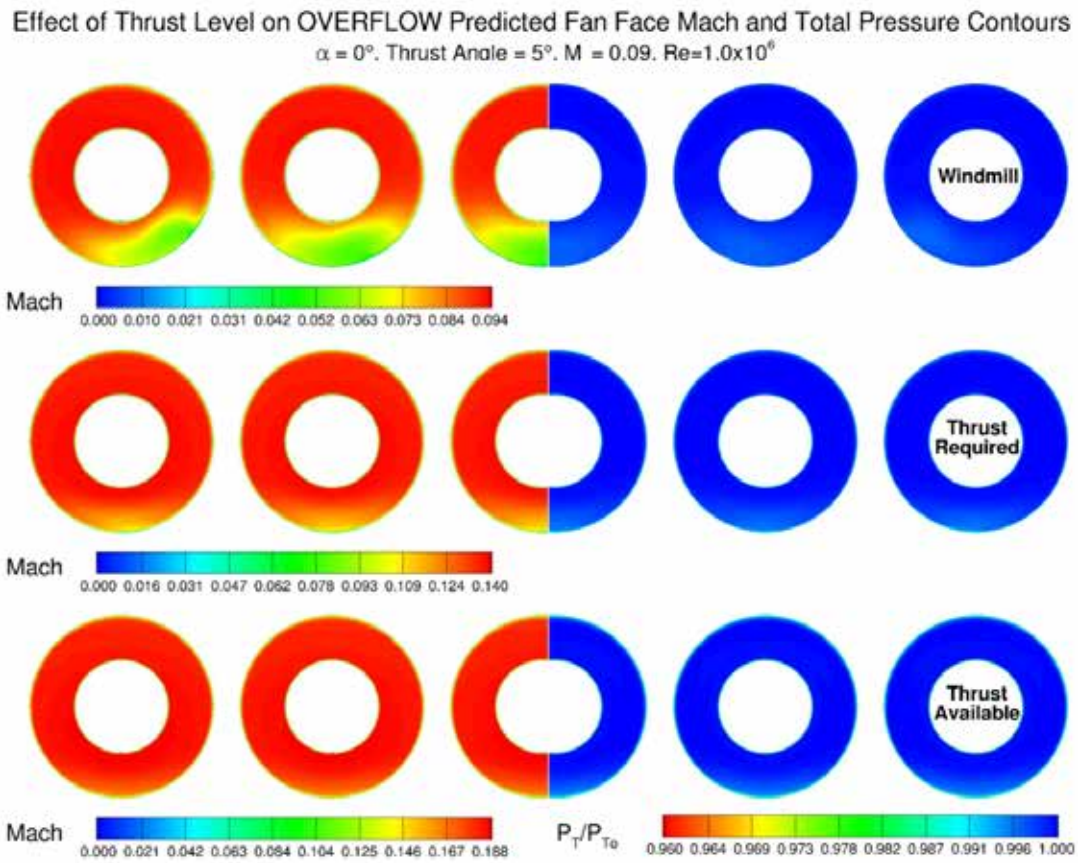

Figure 51: Contours of Mach number and stagnation pressure ratio at the fan faces for the windmill, thrust required, and thrust available mass flows, 5° thrust angle, α=0°, M_{∞}=0.09, Re=1.06x10^6.

The Mach and total pressure ratio contours shown in Figure 51 are split between the fans with fan #1, #2, and half of fan #3 showing total pressure ratio contours and the other half of fan #3, fan #4 and fan #5 showing Mach contours. The Mach contours of each thrust setting have been set to the maximum for each thrust level so as to highlight the ingested boundary-layer. The total pressure ratio contour bounds are equivalent for the three different cases. From Figure 51, the Mach contours for the three different cases show decreasing boundary-layer height and increasing symmetry with increasing thrust level/mass flow rate through the fan. Since the thrust available case is above the inlet's designed mass flow, the flow should be the most symmetric with the smallest boundary-layer percentage. Even with the large percentage of boundary-layer ingestion by the windmill case and visible asymmetry, the total pressure ratio contours show negligible total pressure loss. As was previously discussed in Section 6.4 and Section 6.5, this low total pressure loss is primarily a result of the low Mach number flowfield. A plot of surface streamlines and pressure contours for the three thrust levels at a = 0° is shown in Figure 52.

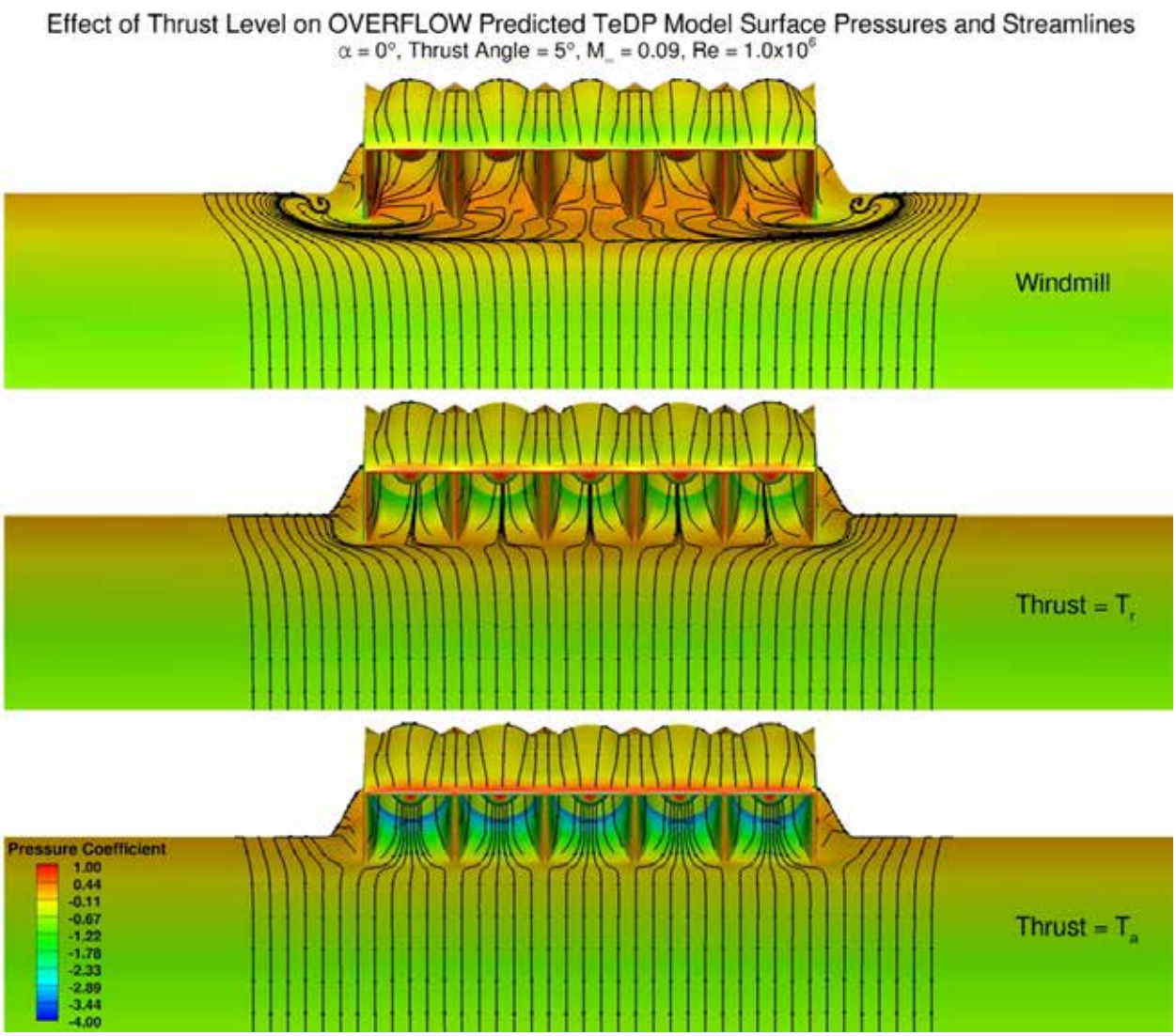

Figure 52: Contours of surface pressure coefficient and streamlines as a function of thrust level, 5° thrust angle, α=0°, M_{∞}=0.09, Re=1.06x10^6.

From Figure 52, the flow looks well behaved with no obvious areas of separation on the model surface or cowl top. Again, for the thrust required case the middle fan surface streamlines are symmetric into the inlet. The # 2 and #4 inlets, however, show a slight asymmetry as the flow experiences an increasing back pressure due to the low mass flow condition. The outer fans (#1 and #5), show the largest asymmetry in the surface streamlines as the flow searches for the path of least resistance to the outside of the fans. The windmill case shows significant separation upstream of the inlets, as was observed in the cut plane Mach contours shown in Figure 50. For the windmill case, the fans simply present an obstacle for the flow to negotiate. The flow primarily moves to the outside of the fans/inlets. The cowl top surface remains attached at this angle-of-attack for the windmill case. For the thrust available case, where the mass flow through the fan is above the design mass flow, excellent inlet symmetry is observed for all of the five

fans as the flow is accelerated into the inlet. For either the thrust required or thrust available cases, no large local flow angles are observed at the inlet sides. No separation is observed on the cowl upper surface, and although not discernable from the angle shown in the figure, no separation is present on the rear teardrop fairings.

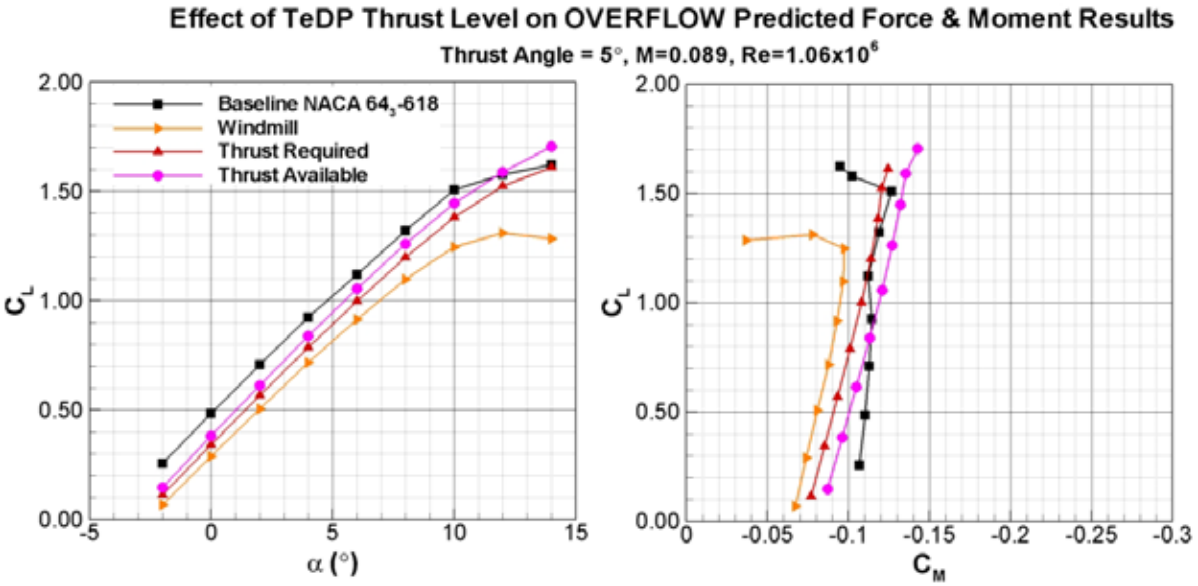

Figure 53: OVERFLOW predicted force and moment results for the baseline NACA 643-618 section and the 5 fan TeDP configuration as a function of thrust level, 5° thrust angle, M_∞=0.09, Re=1.06x10^6.

Force and moment results for the baseline NACA 64$_3$-618 and the 5 fan TeDP model for the three different thrust levels are shown in Figure 53. From Figure 53, the thrust available and thrust required cases show similar lift curves with the thrust available case being shifted to the left. At α=0°, the increase in C_L from the thrust required to the thrust available mass flow is ΔC_L=0.04 increasing to ΔC_L=0.05 (5%) at α=8°. At α=14°, the increase in C_L between the thrust available and thrust required increases to ΔC_L=0.09 (5.8%). The increase in C_L between the thrust required and thrust available cases is due to a combination of the increased thrust vector in the lift direction and the increased circulation caused by the higher thrust level. At α=10°, the difference in C_L between the thrust required and thrust available cases is ΔC_L=0.065. The thrust vector only accounts for ΔC_L=0.015 of this C_L difference, implying that the remaining increase in lift is due to increased circulation caused by the increased fan mass flow. The increase in effective camber at the thrust available mass flow, however, is not enough to match the baseline NACA 64$_3$-618 lift curve. Whereas the baseline NACA 64$_3$-618 lift breaks above α=10°, the thrust required and thrust available lift curves only show a slight rounding above α=10°. Close inspection of the baseline NACA 64$_3$-618 results show a near wall trailing-edge separation beginning at α=8° and growing rapidly above α=10°. The rounding in the lift curve above α=10° for the thrust required and thrust available cases will be discussed shortly. The loss in lift for the windmill case is more significant than the difference between the thrust required and thrust available cases. At α=0°, the decrease in C_L from the thrust required to the windmill case is ΔC_L=-0.05, increasing to ΔC_L=-0.10 (10%) at α=8°. As would be expected, the lift for the windmill case drops off significantly at higher angles-of-attack as compared to the powered

cases. Above α=10°, the lift curve rounds over as the separation upstream of the inlet grows to a size where it extends over the cowl top surface. The moment results shown in Figure 53 indicate an increase in nose down moment with an increase in thrust level as would be expected. The thrust available case produces a fairly consistent 10% increase in nose down moment with increasing lift coefficient, with both the thrust required and thrust available overall moment level comparing well to the baseline NACA 64_3-618 moment level.

Surface pressures for the baseline NACA 64_3-618 section and the 5° thrust angle geometry at the three different thrust levels are shown in Figure 54 for angles-of-attack of α=0°, 4°, 8°, 12°. The pressures in Figure 54 for the TeDP configuration are for a cut through the center of the #3 fan. As was done for the pressures shown in Figure 49, the pressures are for the main airfoil and the external cowl. From Figure 54 at α=0°, the reduced camber of the 5° geometry and lower lift for a given angle-of-attack is clearly depicted in the pressures as compared to the baseline section for the thrust required case. Both the windmill and thrust required cases generate mass flows below the design inlet mass flow, and as a result the pressures upstream of the inlet are more positive than the baseline due to the blockage effect of the oversized inlet, with the windmill case being more severe. The local separation upstream of the inlet for the windmill case is also visible. Also of interest is the fact that the external cowl pressures for the windmill case are more negative with a higher cowl suction peak than the thrust required case. This increase in the cowl pressures is a result of the lower mass flow condition moving the stagnation point on the cowl lip into the cowl, creating a larger effective angle-of-attack on the cowl lip. The thrust available case compares much better to the baseline section pressures on the upper surface. Due to the fact that the thrust available mass flow is above the inlet's design mass flow, the flow accelerates into the inlet, creating more negative pressures upstream of the inlet as compared to the baseline section pressures. Also, since the flow is accelerating into the inlet, the stagnation point for the cowl moves out and around the cowl lip, effectively lowering the cowl lip angle-of-attack and reducing the cowl pressures below that observed for thrust required or windmill case. The increased mass flow and exit velocity, however, create more negative pressures at the cowl trailing-edge for the thrust available case. These observations are mimicked in the α=4° and α=8° pressures, with the separated region upstream of the windmill case moving forward on the section with increased angle-of-attack. At α=12°, the lift for the thrust required case is above that of the baseline NACA 64_3-618 section as the baseline section begins to separate at the trailing-edge. The increased lift of the thrust required case as compared to the baseline NACA 64_3-618 is reflected in the thrust required pressures.

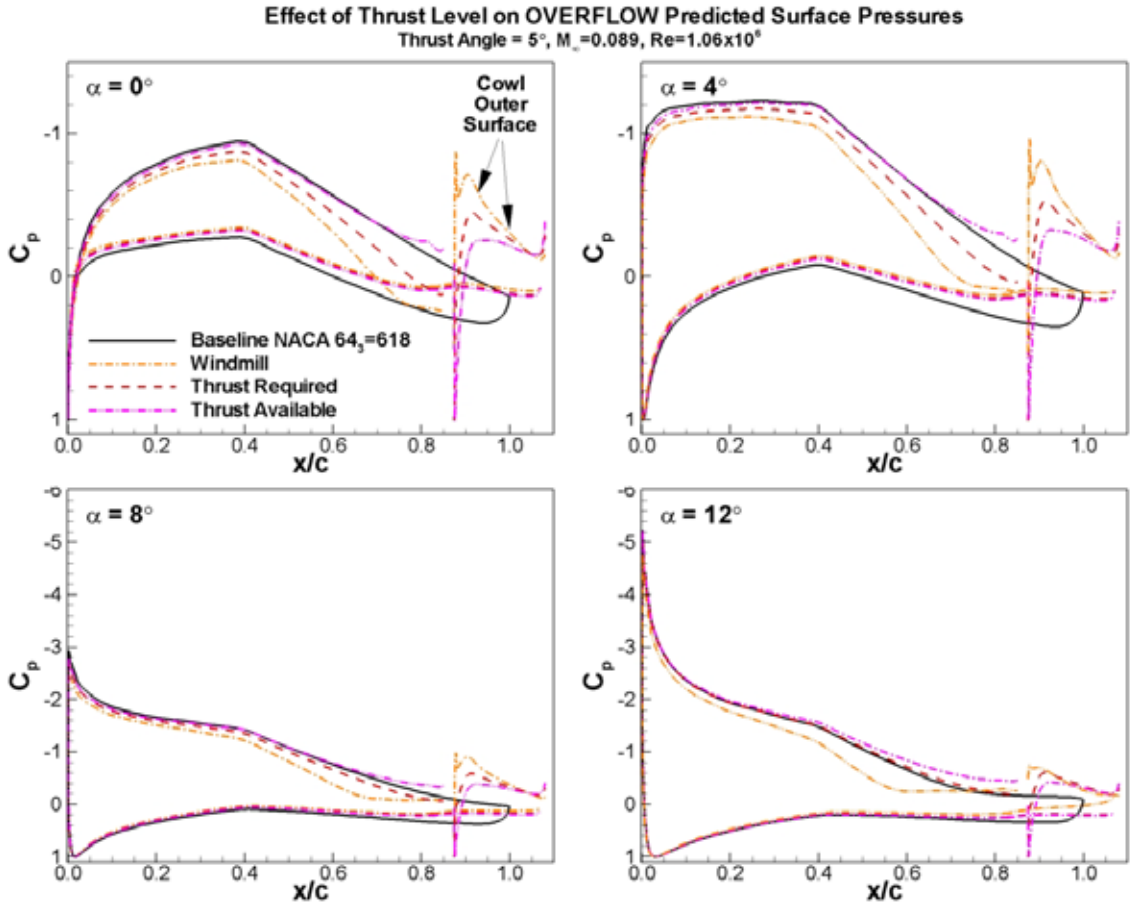

Figure 54: Effect of thrust level on OVERFLOW predicted surface pressures for the baseline NACA 64$_3$-618 section, 5° thrust angle, a=0°, 4°, 8°, 12°, M_∞=0.089, Re=1.06x10^6.

The surface pressure contours and streamlines results shown in Figure 52 for the thrust required and thrust available cases at a=0° show no separation and only minor asymmetry for the thrust required case. At higher angles-of-attack, one might expect increased asymmetry in the inlet fan flowfields. One would also expect that as the baseline NACA 64$_3$-618 section on either side of the 5 fan middle section begins to experience trailing-edge separation around a=10°, that the separation would have an effect upon the outboard fans (fan #1 and fan #5). Surface pressure contours and streamlines at a=4°, 8°, and 12° for the thrust required and thrust available cases is shown in Figure 55. From Figure 55, for the thrust required case at a=4° the outer fan inlet asymmetry has become more apparent as compared to the a=0° shown in Figure 52. The thrust available streamlines a=4° show no inlet asymmetry. At a=8°, the inlet asymmetry has become more pronounced for the thrust required case, especially for the outboard #1 and #5 fans. Some asymmetry in the outer fans is also observed for the thrust available case at a=8°. Most notable in the a=8° results for both of the thrust required and thrust available cases is the interaction between the middle #5 fan section and the outer baseline NACA 64$_3$-618 section. At a=8°, the baseline NACA 64$_3$-618 section results exhibit a small, near-wall trailing-edge separation. This separation is apparent in both the thrust available and thrust required streamlines at a=8°. The outboard fan asymmetries for both cases are affected by the outer baseline wing separation. At

a=12°, beyond the break in the lift curve for the baseline NACA 64_3-618 section (see Figure 54), both the thrust required and thrust available cases show significant interaction with the baseline NACA 64_3-618 outer wing section. The baseline NACA 64_3-618 section trailing-edge separation has moved forward on the airfoil chord. The surface streamlines for the #1 and #5 fans show large interactions with the outer wing separated region. Flow from these outer regions is being drawn into the outboard #1 and #5 inlets. At a=12°, the #2 and #4 inlet surface streamlines appear to be more symmetrical than at a=8°. From Figure 54, above a=10°, both the thrust required and thrust available lift curves show a 50% reduction in lift curve slope. The force and moment integration for the TeDP model only includes the center 5 fan section. The center section area of integration includes the cowl sides. The change in lift curve slope above 10° is a result of the interaction of the center fan section with the outer baseline NACA 64_3-618 section. While the fan flowfield is able to remain attached locally, the separation generated by the outer wing section interacts with and affects the outer inlet flowfields and center fan section forces.

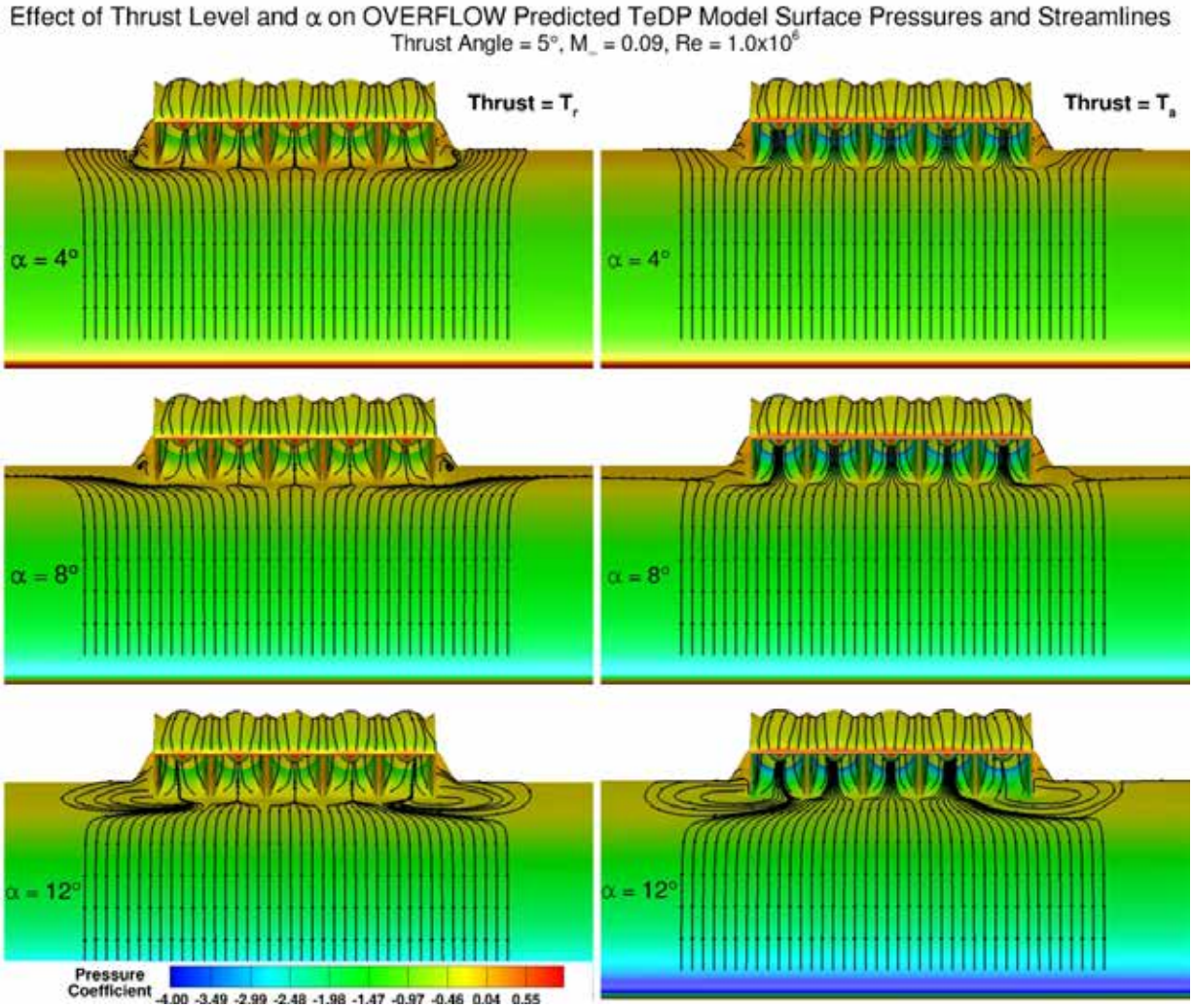

Figure 55: Contours of surface pressure coefficient and streamlines as a function of angle-of-attack and thrust level, 5° thrust angle, M_{∞}=0.09, Re=1.06x10^6.

The pressure contours and surface streamlines shown in Figure 55 show that significant asymmetries in the inlet surface streamlines exist with increasing angle-of-attack. It would be reasonable to assume that these asymmetries would significantly impact the individual fan flowfield and thrust level. The individual fan thrust ratio as a function of angle-of-attack for the thrust required and thrust available cases are shown in Figure 56. The thrust ratio in Figure 56 is the fan thrust at angle-of-attack divided by the prescribed thrust at a=0°. From Figure 56, for the thrust required case, the there exists a 2% difference in thrust between the #1 and #5 fans and the centerline #3 fan. The #2 and #4 fans show 0.5% difference in thrust from the centerline #3 fan. The centerline #3 fan has the lowest thrust, with the outer fans producing slightly higher thrust levels. These differences in thrust level are a result of differences in the average inlet velocities. The asymmetries observed in the outboard inlet flowfields translate into small reductions in the inlet velocities, producing small increases in individual fan thrust. As the asymmetries become smaller for the #2 and #4 fans, the differences in thrust between the #2 and #4 fans and the centerline #3 become smaller. The thrust levels for the individual fans are symmetric about the centerline fan. At the thrust available case, where the outer fan asymmetries are greatly reduced, the spanwise fan thrust differences are less than 0.30% and only become significant at higher angles-of-attack as the baseline NACA 64_3-618 section separation begins to influence the center TeDP section flowfield.

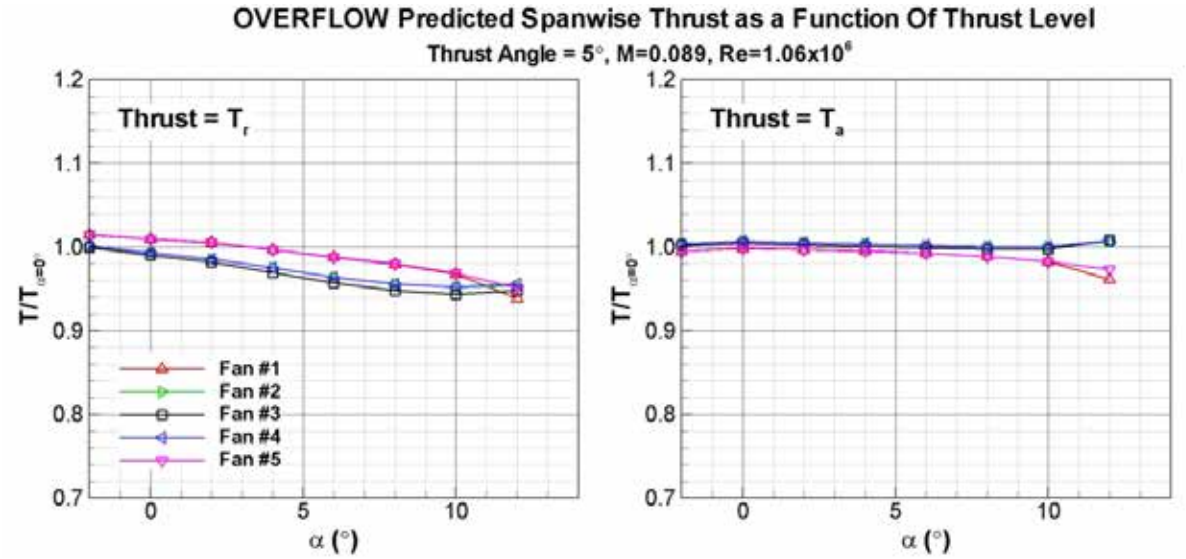

Figure 56: OVERFLOW predicted spanwise thrust as a function of thrust level, 5° thrust angle, M_{∞}=0.09, Re=1.06x10^6.

Results from the thrust level investigation have shown that for the 5° thrust angle geometry, while differences in force and moment results exist with thrust level, they are generally small, with changes in lift around 5-6% between the thrust required and thrust available mass flows. The pitching moment showed a larger 10% difference between the thrust required and thrust available cases. The windmill case produced slightly larger differences on the order of 10% in lift as compared to the thrust required case. The windmill case results, however, are optimistic since the fan blades are not modeled and would produce increased blockage if present. The force and moment differences with thrust level also showed that the differences in force and moment

results were a result of changes in circulation caused by the increased fan thrust in addition to the non-zero thrust vector effect. At higher angles-of-attack, increased asymmetries in the fan inlet flowfields were found to be a result of the baseline NACA 64_3-618 outer wing section separation influencing the outboard fan inlets. These asymmetries produced spanwise thrust variations of up to 2% depending upon the thrust level. While the fan flowfield is able to remain attached locally at angles-of-attack beyond the baseline NACA 64_3-618, the separation generated by the baseline outer wing section interacts with and affects the outer inlet flowfields and center fan section forces.

6.7. Differential Thrust

In addition to the thrust angle and thrust level studies, differential thrust effects were also investigated. The differential thrust runs were investigated to determine the effect a neighboring fan's mass flow rate has upon the distortion and flow characteristics of the adjacent fan, and how far those effects propagate. Significant differential thrust effects were observed during the Phase I three fan wind tunnel test. Part of the reason for increasing the Phase II model from 3 fans to 5 fans was to gain a better understanding of the spanwise propagation effect an individual fan's mass flow has upon neighboring fan flowfields.

Three different differential thrust settings were investigated. These included a thrust required case with fan #1 at the windmill condition with fans #2 through #5 at the thrust required mass flow. A thrust available case where fan #1 was at the windmill condition with fans #2 through #5 at the thrust available mass flow was also investigated. Finally, a mixed thrust available/thrust required case was run. For the mixed case, fan #1 was set at the thrust required mass flow with fans #2 though #5 at the thrust available mass flow. Angles-of-attack of 0°, 4°, 8°, and 12° were run.

For the differential thrust cases, the runs were performed using the fan BC settings from the continuous thrust cases, and also with slightly modified DPs at the BC location. When running the initial cases with the baseline BCs, it was found that the fan adjacent to the windmilling fan experienced a slight drop in mass flow. The case was then rerun with a slightly increased DP in the adjacent fan to return the mass flow to its original value. Both force and moment and pressure results for these two cases showed very little difference. As a result, it was decided to present the runs with the baseline fan BC DPs.

6.7.1. Thrust Required Differential Results

The first differential thrust case examined was the thrust required differential case. For this case, Fan #1 was set at the windmill condition with Fans #2-#5 set to the thrust required mass flow. Angles-of-attack of 0°, 4°, 8°, and 12° were run. Force and moment results for the thrust required differential case as compared to the baseline thrust required case at M=0.09, $Re=1.06x10^6$ are shown in Figure 57.

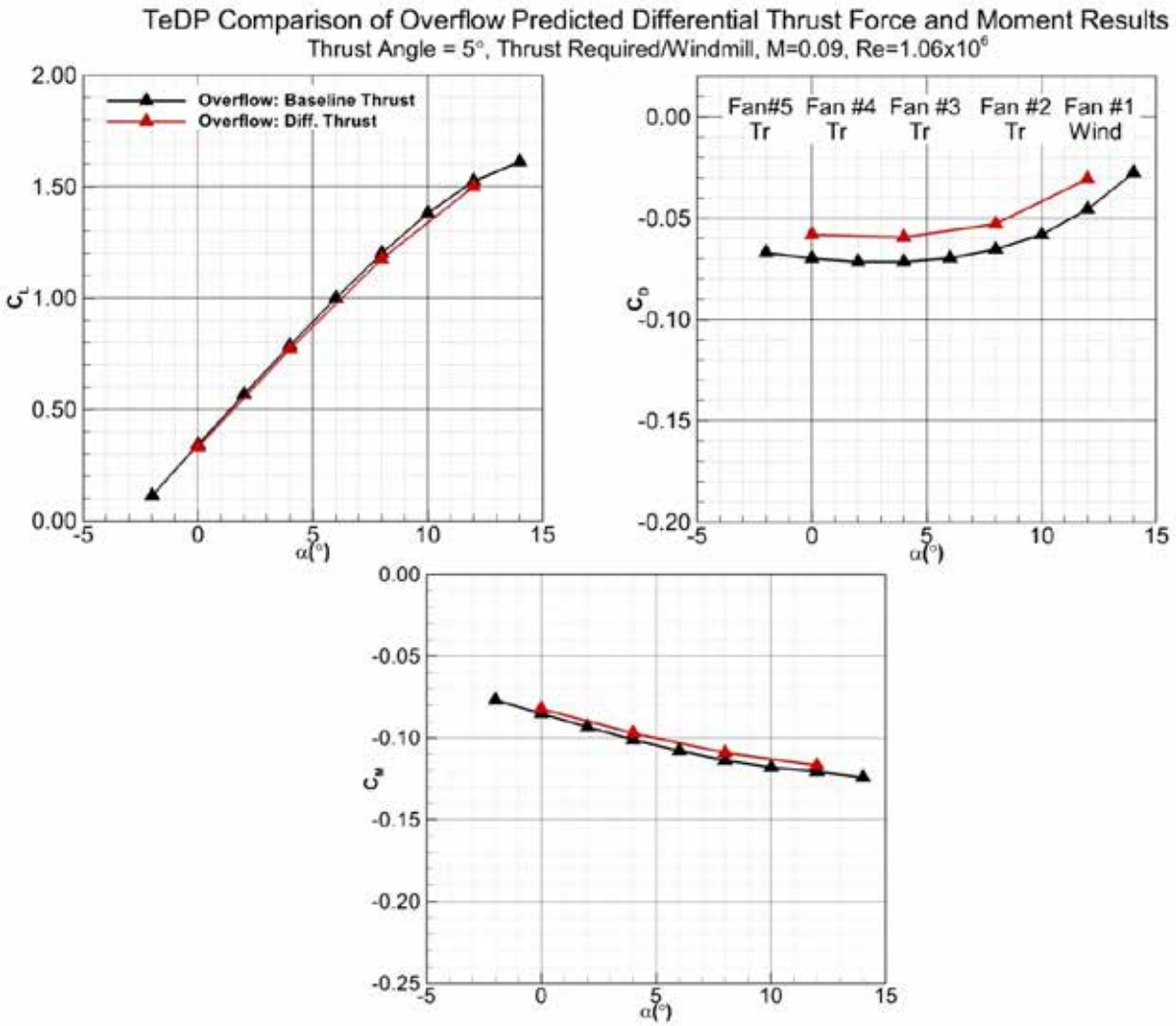

Figure 57: OVERFLOW predicted force and moment results for the baseline thrust required mass flow and the thrust required differential set-up for the 5 fan TeDP configuration as a function angle-of-attack, 5° thrust angle, M_{∞}=0.09, Re=1.06x10^6.

From Figure 57, the effect of the differential thrust setting on the force and moment results is relatively small. At low angles-of-attack, the loss of the single fan does little to change the lift curve. At higher angles-of-attack, the loss of the outboard fan produces a slight loss in lift. As previously discussed, since the windmilling fan does not model the presence of the fan blades, this slight loss in lift at the higher angles-of-attack is optimistic. The single windmilling fan also produces a slightly less negative pitching moment as would be expected. This lower pitching moment is a result of a combination of thrust/mass flow based moment and a reduction of the low pressure region on the cowl upper surface over the windmilling fan. The drag results shown in Figure 57 include the thrust based component. As a result, the overall drag is negative, indicating a net thrust. Recall that for the CFD results shown in this section, the results are for the center 5 fan section only. The drag results in Figure 57 show an increase in drag of approximately 17% to 18% with the windmilling engine. One might expect a minimum 20%

increase in drag with the loss of 1 of the 5 fans. Again, since the windmilling fan does not model the fan blades, the fan still creates some thrust due to the presence of the plug producing a converging geometry which accelerates the flow through the fan. The thrust loss is most likely under predicted. Contours of pressure coefficient and surface streamlines for the baseline thrust required case and the differential thrust required case at angles-of-attack of 0°, 4°, and 8° are shown in Figure 58.

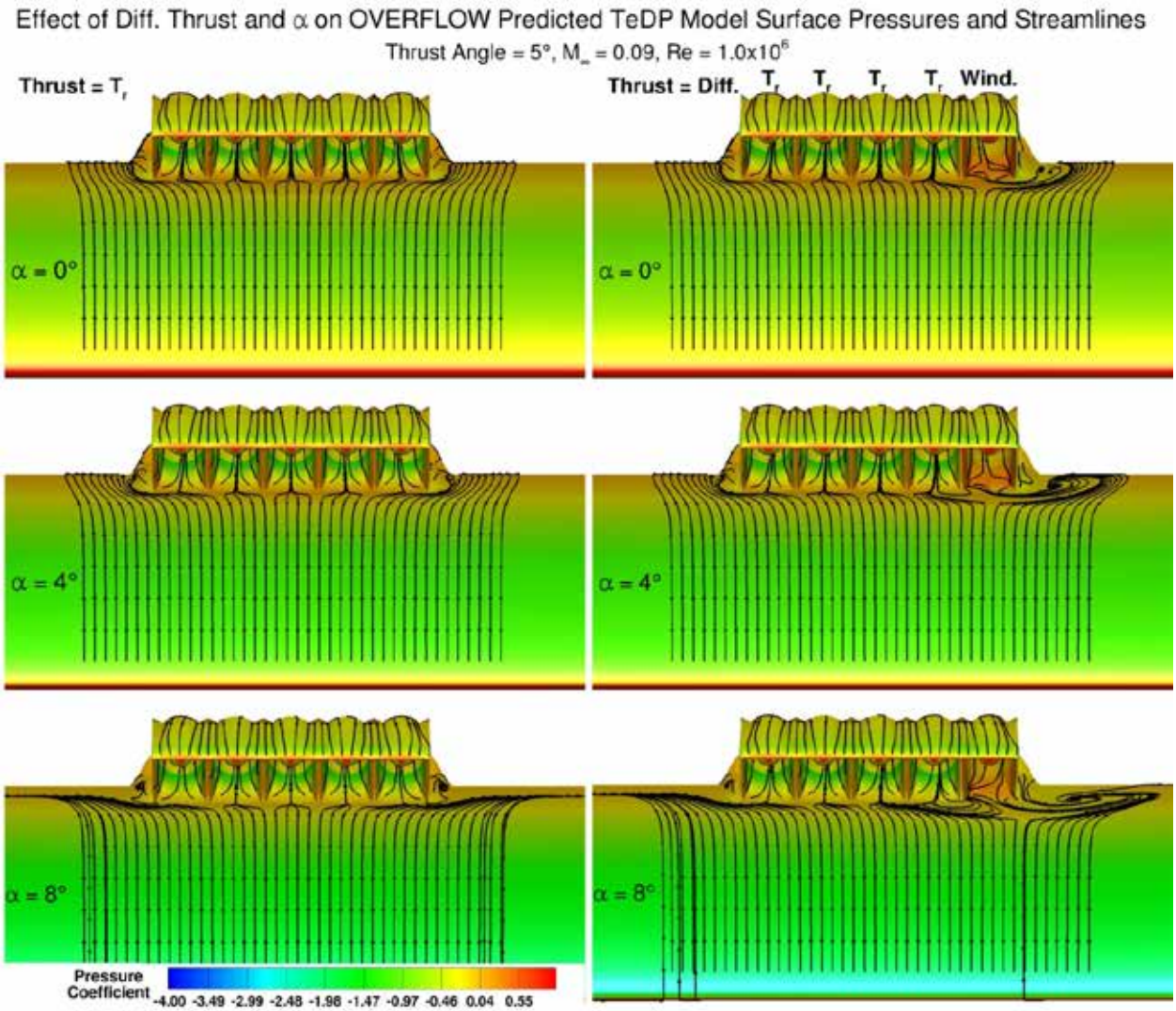

Figure 58: Contours of surface pressure coefficient and streamlines as a function of angle-of-attack for the baseline thrust required and the differential thrust required cases, M_{∞}=0.09, Re=1.06x10^6.

From Figure 58, the presence of the windmilling fan is clearly visible in the surface pressures and surface streamlines. The increased back pressure created by the windmilling fan creates a separated region upstream of the fan as would be expected. The increased back pressure is also observed to affect the neighboring fan. For the a=0° and 4° cases, the fan adjacent to the

windmilling fan is primarily effected, with the center fan surface streamlines showing minor asymmetries. At a=8°, however, the center fan surface streamlines appear to be effected to a larger extent. The baseline separated region to the outside of the fan section is also affected by the windmill separation, increasing in extent as a result of the windmilling fan's increased back pressure and blockage. Contours of Mach number and stagnation pressure ratio at a=0° for the baseline thrust required and the differential thrust case are shown in Figure 59 and Figure 60.

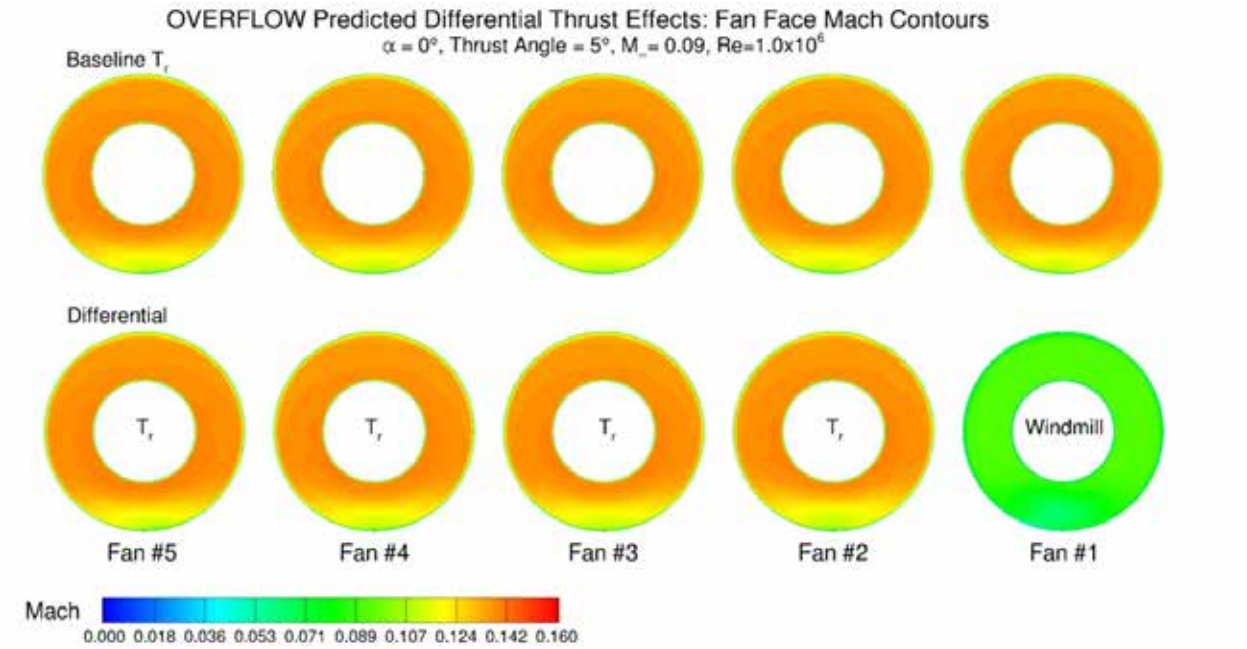

Figure 59: OVERFLOW predicted contours of Mach number at the fan faces for the baseline thrust required and the differential thrust required mass flows, 5° thrust angle, α=0°, M_{∞}=0.09, Re=1.06x10^6.

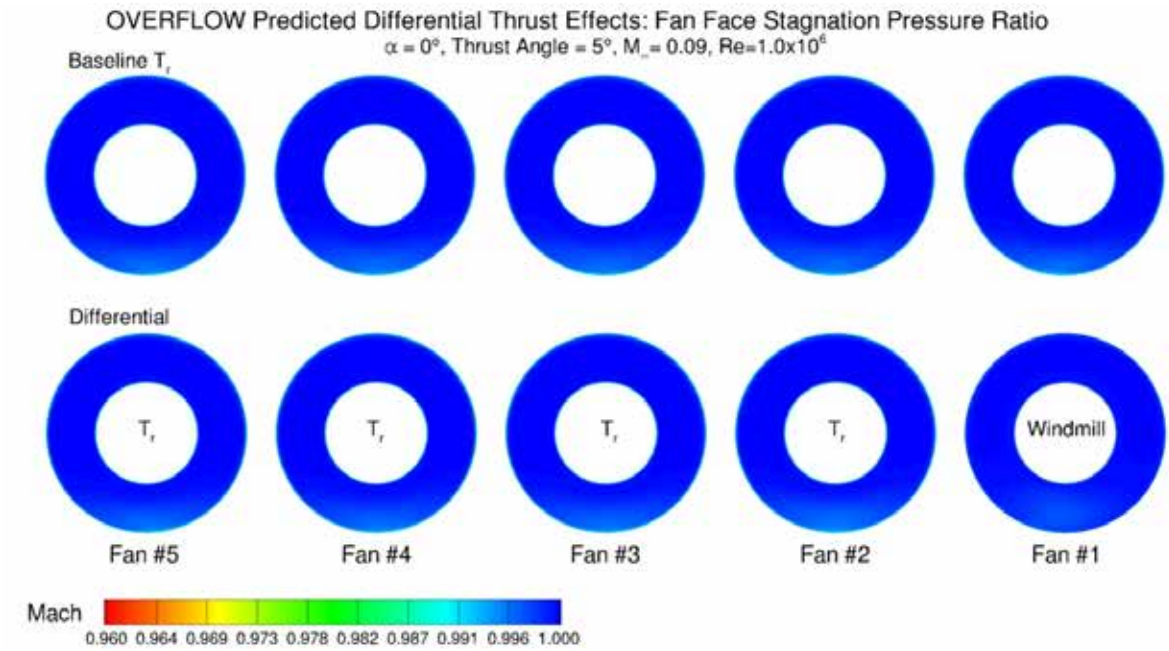

Figure 60: OVERFLOW predicted contours of stagnation pressure ratio at the fan faces for the baseline thrust required and the differential thrust required mass flows, 5° thrust angle, α=0°, M_{∞}=0.09, Re=1.06x10^6.

From Figure 59, the presence of the windmilling fan is clearly visible in the fan face Mach contours for the #1 fan. At the fan face, however, the neighboring fan #2 Mach contours compare well to the baseline thrust required Mach contours. Although not shown, the fan face Mach contours at a=8° show similar results. As compared to the surface streamlines shown in Figure 58, the fan face Mach contours show little effect upon the neighboring fan, even at the higher angles-of-attack. The stagnation pressure ratio contours in Figure 60 also show very little distortion. This lack of distortion, even for separated flowfields upstream of the fan, has been observed throughout the project and is primarily as result of the low Mach number condition. Surface pressures for a centerline cut through Fan #1, Fan #2, and Fan #3 for angles-of-attack of 0°, 4°, and 8° are shown for the baseline thrust required and the differential thrust mass flow cases in Figure 61.

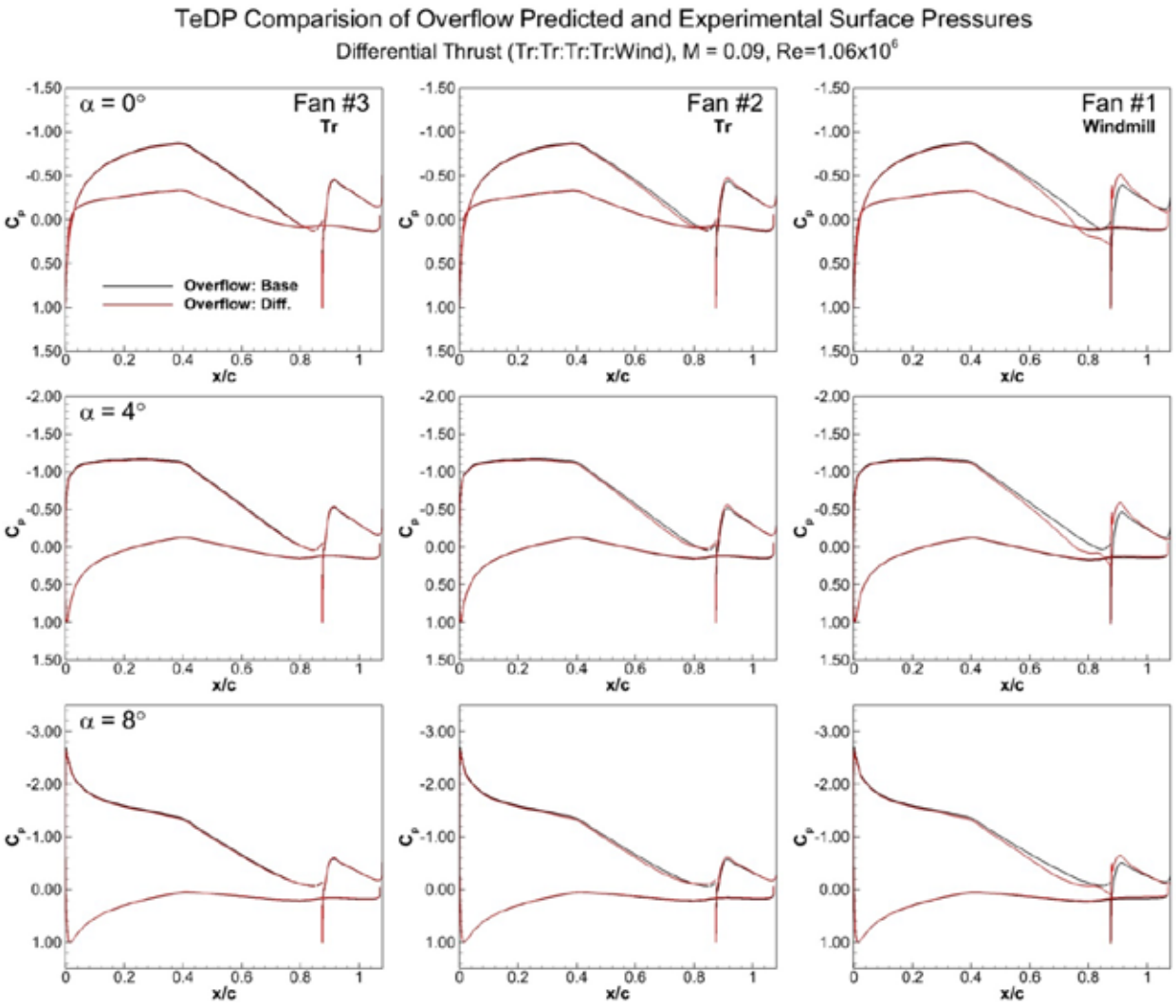

Figure 61: OVERFLOW predicted surface pressures for a centerline cut for Fans #1 to #3 for the baseline thrust required and differential thrust required mass flow cases, 5° thrust angle, α=0°, 4°, 8°, M_{∞}=0.09, Re=1.06x10^6.

From Figure 61, the increased back pressure caused by the windmilling #1 fan is clearly evident in the increased (more positive) pressures upstream of the fan inlet for the differential thrust cases. The extent of the upstream influence does not appear to change with increasing angle-of-attack for the #1 fan. Increased separation upstream of the fan is visible, however, with increasing a. The centerline pressures for the #2 fan are also affected by the neighboring fans reduced mass flow. The #2 fan pressures are slightly more positive for the differential thrust case, indicating increased back pressure on the #2 fan as a result of the #1 fan. These differences are not observed in the #3 center fan, indicating that the influence of the #1 fan is confined to the adjacent fan. These results compare well to those observed in the fan face Mach contours shown in Figure 59. Whereas the surface streamlines shown in Figure 58 show a larger spanwise influence, the fan face Mach contours and fan centerline surface pressures show that the overall effect is limited to the adjacent fan.

In order to further explore the differential thrust effect upon each fan's thrust component build up, individual fan thrust producing components were compiled. The OVERFLOW predicted individual thrust components for the thrust required differential mass flow case at a=0° is shown in Figure 62.

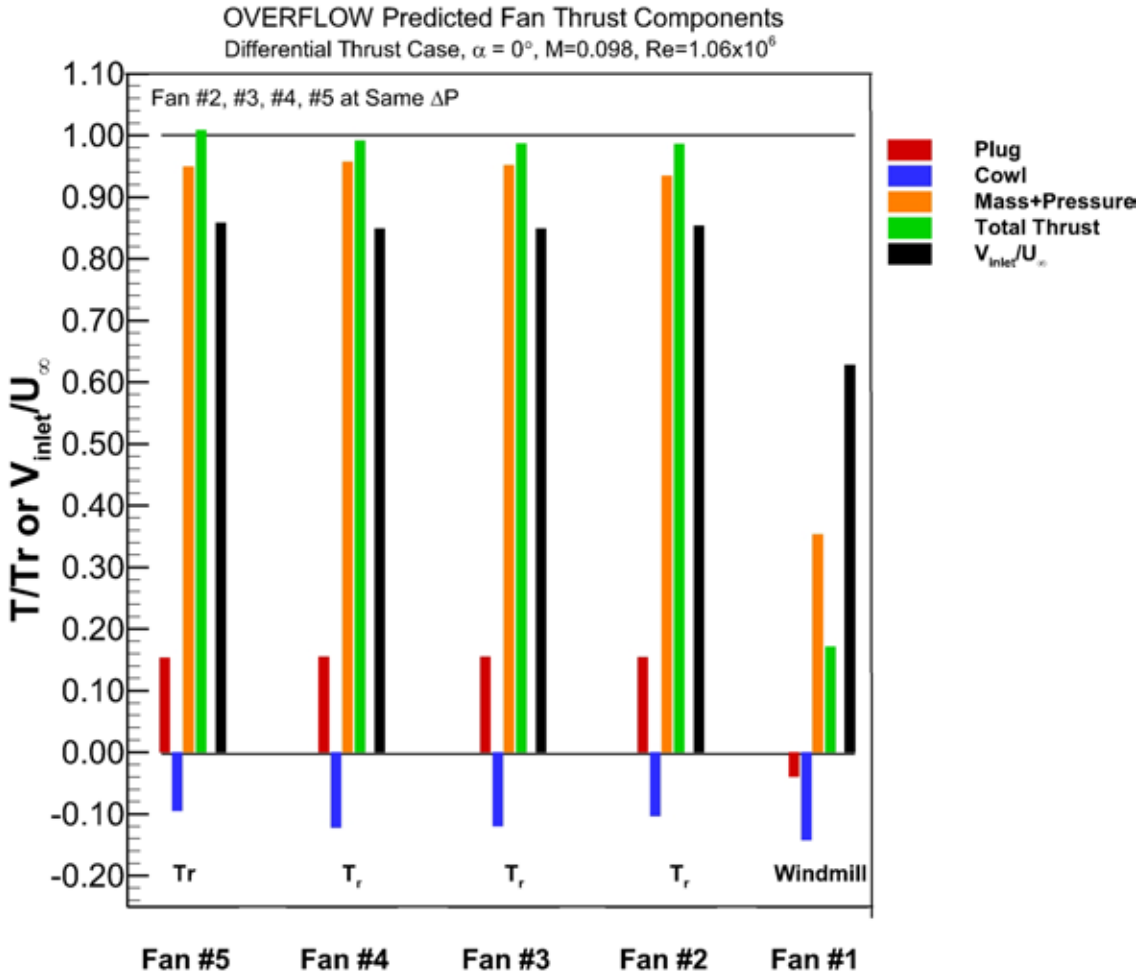

Figure 62: OVERFLOW predicted differential thrust component breakdown for the differential thrust required mass flow case, 5° thrust angle, α=0, M_{∞}=0.09, Re=1.06x10^6.

Included in Figure 62 are each fan's total thrust, cowl and plug drag, mass flow and pressure based thrust, and the average inlet velocity. During the Phase I experimental investigation, it was found that due to the increased back pressure and spillage from the neighboring fan, the fan adjacent to the windmilling or lower thrust setting fan saw an increased thrust (2% up to 8%, depending upon the differential thrust level). It was speculated that this increased thrust was due to an effective lower inlet velocity caused by the neighboring fan spillage. For the Phase I effort, the centerline fan thrust was recorded using a thrust balance. The metric surfaces for the thrust balance took the mass flow and pressure based thrust, and also the plug based thrust into account. The cowl drag was not included in the thrust measurement. From Figure 62, the neighboring fan thrust (#2 fan), compares well to the #4 fan, indicating that the windmilling fan reduced mass

flow is not producing an increased thrust in the adjacent #2 fan. The thrust shown in Figure 62 includes the cowl drag. The mass flow and pressure based thrust is actually ≈ 2% lower than that for the #4 fan. The loss in mass flow and pressure based thrust is made up for by a slight reduction in cowl drag for the #2 fan as compared to the #4 fan. This lack of an increased thrust in the CFD results is curious. As compared to the other fans, the windmilling fan has an increased cowl drag, and the plug becomes a drag producing element. For the baseline fans, the increased pressure aft of the fan face integrates to a pressure thrust on the plug. The inlet velocity of the adjacent #2 fan does not appear to be lower than the other neighboring fans. For the windmilling fan, the inlet velocity is still 60% of the free-stream velocity, as compared to 85% for the baseline fans. This high inlet velocity for the windmilling fan is a result of an unrealistically low blockage in the computational model due to the lack of the presence of the fan blades. As previously discussed, the presence of the fan blades in the actual windmill case would produce increased blockage, increasing the amount of separation, and most likely significantly reducing the windmilling fan's inlet velocity. This increased local blockage would then increase the spillage and blockage to the neighboring fan. Even though the fan DP is set to zero for the windmilling fan, the fan still produces thrust due to the low blockage coupled with the converging duct geometry accelerating the flow through the duct. It is believed that the unrealistically low blockage of the windmilling fan is the primary reason an increased thrust is not observed in the #2 adjacent fan in the CFD model. The slightly increased thrust observed for the #5 fan as compared to the centerline fans is due to the fan's interaction with the baseline model flowfield outside of the fan section, and was shown and discussed in Figure 56, Section 6.6.

6.7.2. Thrust Available Differential Results

The second differential thrust case examined was the thrust available differential case. For this case, Fan #1 was set at the windmill condition with Fans #2-#5 set to the thrust available mass flow. Angles-of-attack of 0°, 4°, 8°, and 12° were run. Force and moment results for the thrust available differential case as compared to the baseline thrust available case at M=0.09, Re=1.06x10^6 are shown in Figure 63.

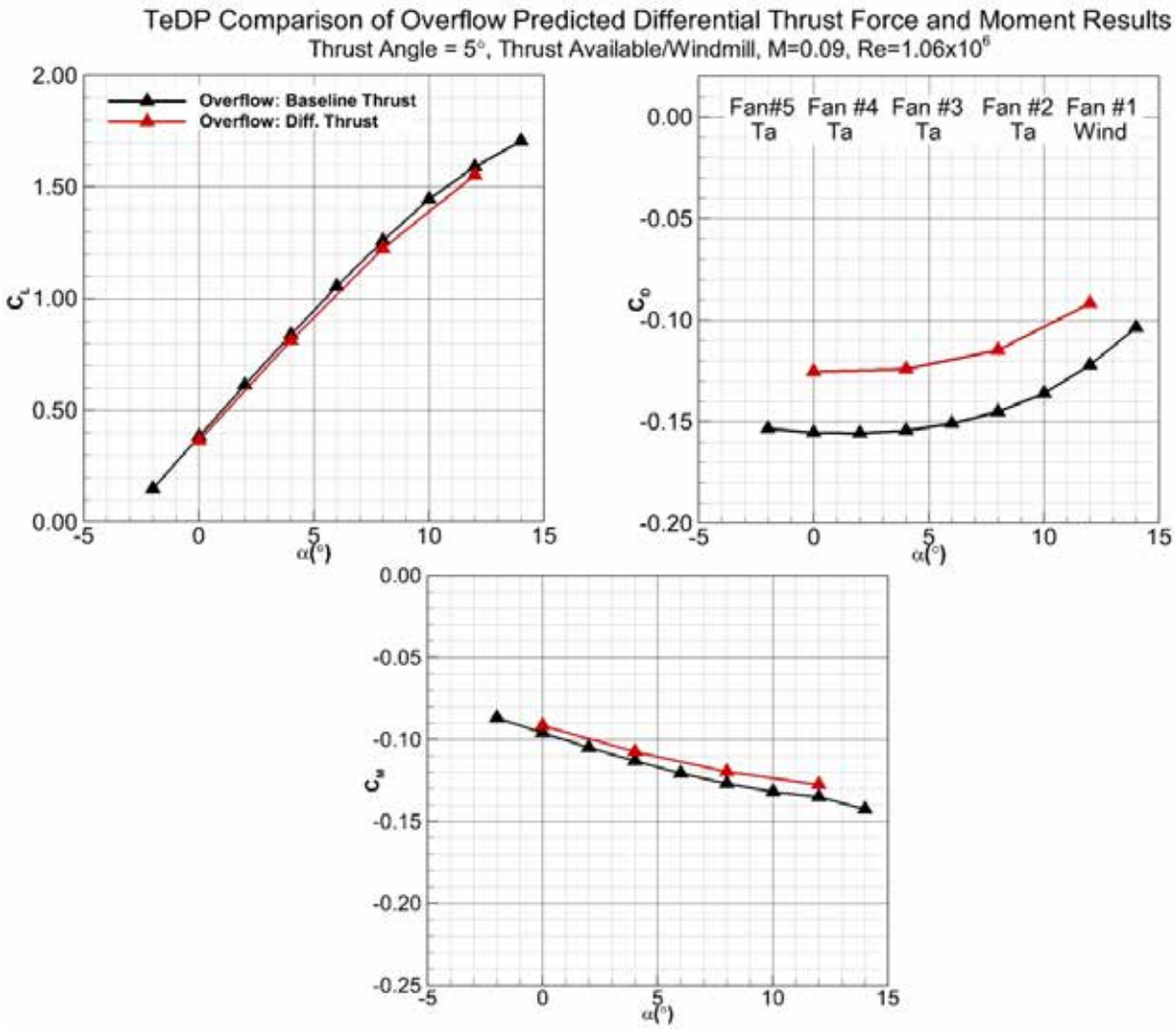

Figure 63: OVERFLOW predicted force and moment results for the baseline thrust available mass flow and the thrust available differential set-up for the 5 fan TeDP configuration as a function angle-of-attack, 5° thrust angle, M_{∞}=0.09, Re=1.06x10^6.

The difference between the thrust available and thrust required settings should increase the amount of blockage/spillage felt by the neighboring #2 fan for the thrust available case. From Figure 63, however, much like that observed for the thrust required differential results shown in Figure 57, the effect of the differential thrust setting on the force and moment results is relatively small for the thrust available case. At low angles-of-attack, the loss of the single fan does little to change the lift results. At higher angles-of-attack, the loss of the outboard fan produces a slight loss in lift, similar to that observed in the thrust required differential results. At a=12°, the difference in C_L between the baseline and differential results is 1.5% for the thrust required differential case, as compared to 2.3% for the thrust available differential results. The change in moment results for the thrust available differential results show a similar trend. The differential

results produce a more positive C_M as would be expected, with the difference between the baseline and differential results slightly larger for the thrust available differential results as compared to the thrust required differential results. This increased effect of the thrust available differential results carries over to the drag. For the thrust required differential results, the drag increased by 17% to 18% with the windmilling fan. For the thrust available differential results, the drag increases by 19% to 20%. Again, the drag results are optimistic since the actual windmilling fan would produce a higher drag value due to the presence of the fan blades. Contours of pressure coefficient and surface streamlines for the baseline thrust available case and the differential thrust available case at angles-of-attack of 0°, 4°, and 8° are shown in Figure 64.

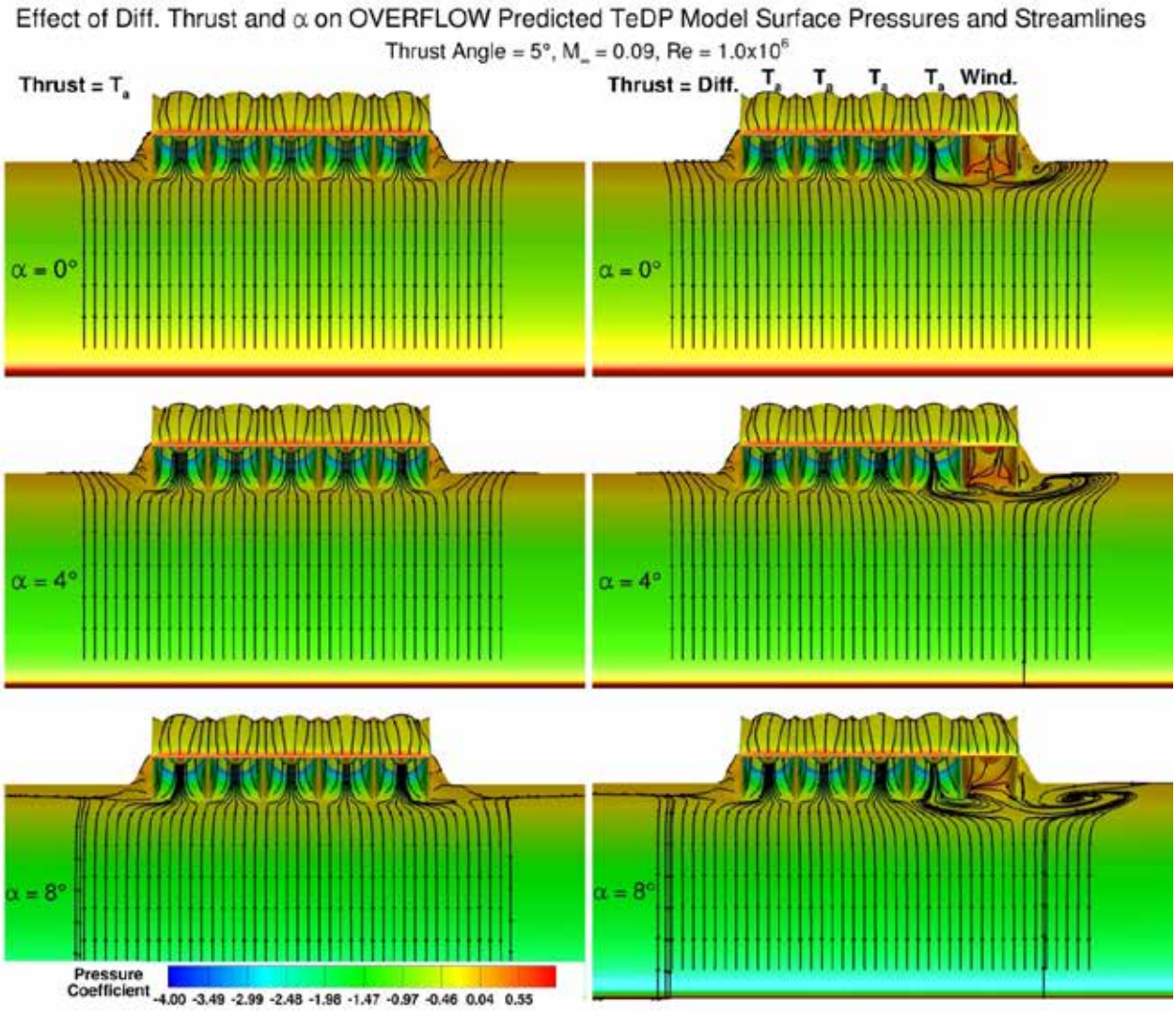

Figure 64: Contours of surface pressure coefficient and streamlines as a function of angle-of-attack for the baseline thrust available and the differential thrust available cases, M_{∞}=0.09, Re=1.06x10^6.

The results shown in Figure 64 also include the baseline thrust available results. As was discussed in Section 6.6, the increased mass flow for the thrust available case produces very symmetric surface streamlines into the fan inlets as compared to the thrust required results. Due

to the increased mass flow of the thrust available case, the effect of the windmilling #1 fan increases the effect on the adjacent fan. The effect is observed to increase with increasing angle-of-attack. Unlike the reduced mass flow thrust required differential results, however, the centerline #3 fan surface streamlines to not appear to be affected by the windmilling #1 fan. Contours of Mach number at a=0° for the baseline thrust available and the differential thrust case are shown in Figure 65.

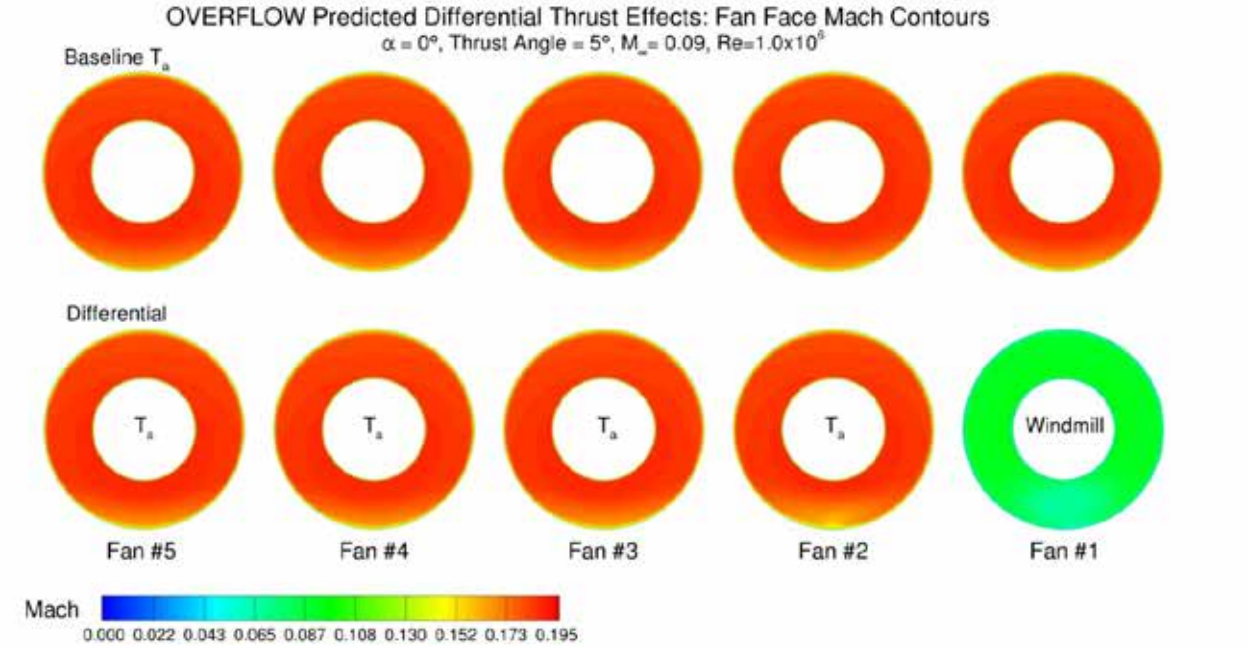

Figure 65: OVERFLOW predicted contours of Mach number at the fan faces for the baseline thrust available and the differential thrust available mass flows, 5° thrust angle, α=0°, M_∞=0.09, Re=1.06x10^6.

From Figure 65, as with the surface streamlines shown in the previous figure, the increased fan-to-fan symmetry of the thrust available results is evident. The blockage and spillage of the windmilling #1 fan, however, can be seen in the Mach contours of the #2 fan. While confined to the wall region, the effect is clearly discernable. Also, as was observed in the surface streamlines shown in Figure 64, the effect of the windmilling #1 fan does not extend beyond the adjacent #2 fan. Contours of stagnation pressure ratio at a=0° for the baseline thrust available and the differential thrust available case are shown in Figure 66.

From Figure 66, the stagnation pressure ratio contours mimic the effects seen in the Mach number contours. Only the #2 fan is affected by the windmilling #1 fan. Of note, however, is the increase in stagnation pressure loss in the #2 fan as compared to the lower mass flow, and lower Mach number, thrust required case. Again, as with the Mach contours, the stagnation pressure loss is confined to the fan bottom. Although larger than that observed for the thrust required case, the maximum stagnation pressure loss is only 2.5%. Surface pressures for a centerline cut through Fan #1, Fan #2, and Fan #3 for at angles-of-attack of 0°, 4°, and 8° are shown for the baseline thrust available and the differential thrust available mass flow cases in Figure 67.

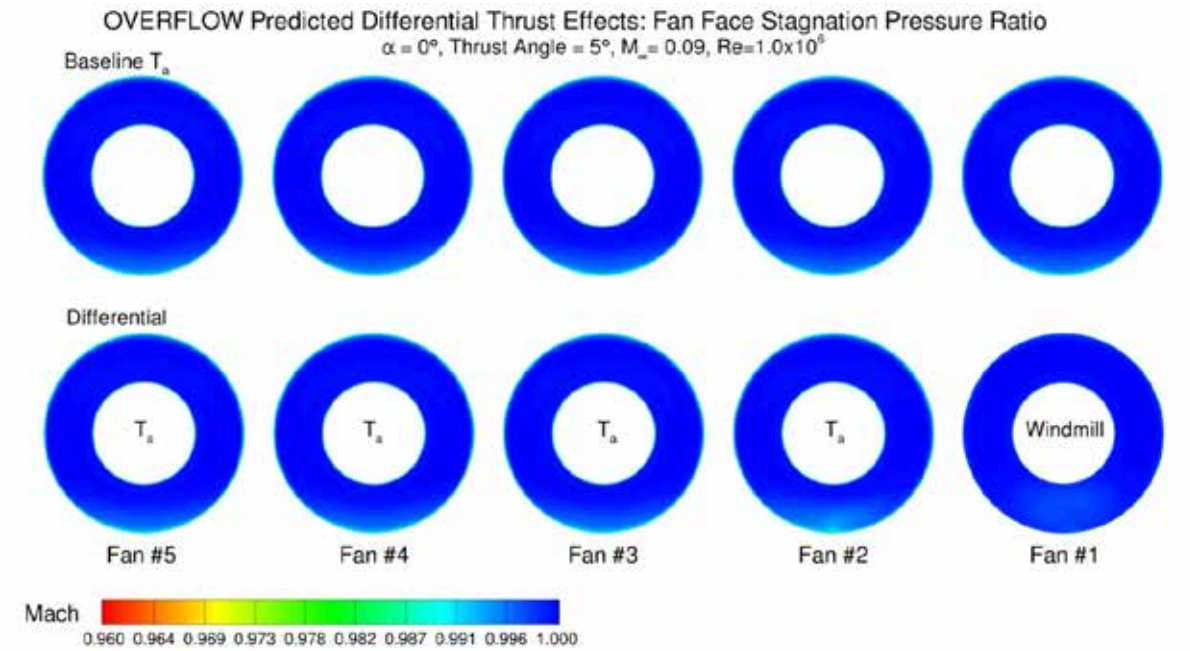

Figure 66: OVERFLOW predicted contours of stagnation pressure ratio at the fan faces for the baseline thrust available and the differential thrust available mass flows, 5° thrust angle, α=0°, M_{∞}=0.09, Re=1.06x10^6.

From Figure 67, the increased spillage produced by the windmilling #1 fan is clearly evident in the increased pressures (more positive) upstream of the #1 fan inlet for all of the angles-of-attack shown. The level of spillage and back pressure, and the effect upon the pressures upstream of the fan, are larger than those observed for the thrust required case shown in Figure 61. The effect upon the #2 fan is also larger than that observed for the thrust required case. The extent of the increased back pressure effect, however, does not extend upstream of the section's maximum thickness (x/c≈0.40). As was observed for the surface streamlines shown in Figure 64 and the fan face Mach contours shown in Figure 65, the effect of the windmilling #1 fan does not extend beyond the adjacent #2 fan. The centerline #3 fan pressures appear essentially unaffected.

As was observed for the thrust required differential results, the thrust available differential results do not show an increased thrust in the adjacent #2 fan for the mass flow and pressure based thrust component. The inlet velocity of the windmilling fan is still 60% of the free-stream velocity. The differential between the baseline fans and the windmilling fan is more than the thrust required case, but is still far less than if the computational model of the windmilling fan were able to include the presence of the fan blades.

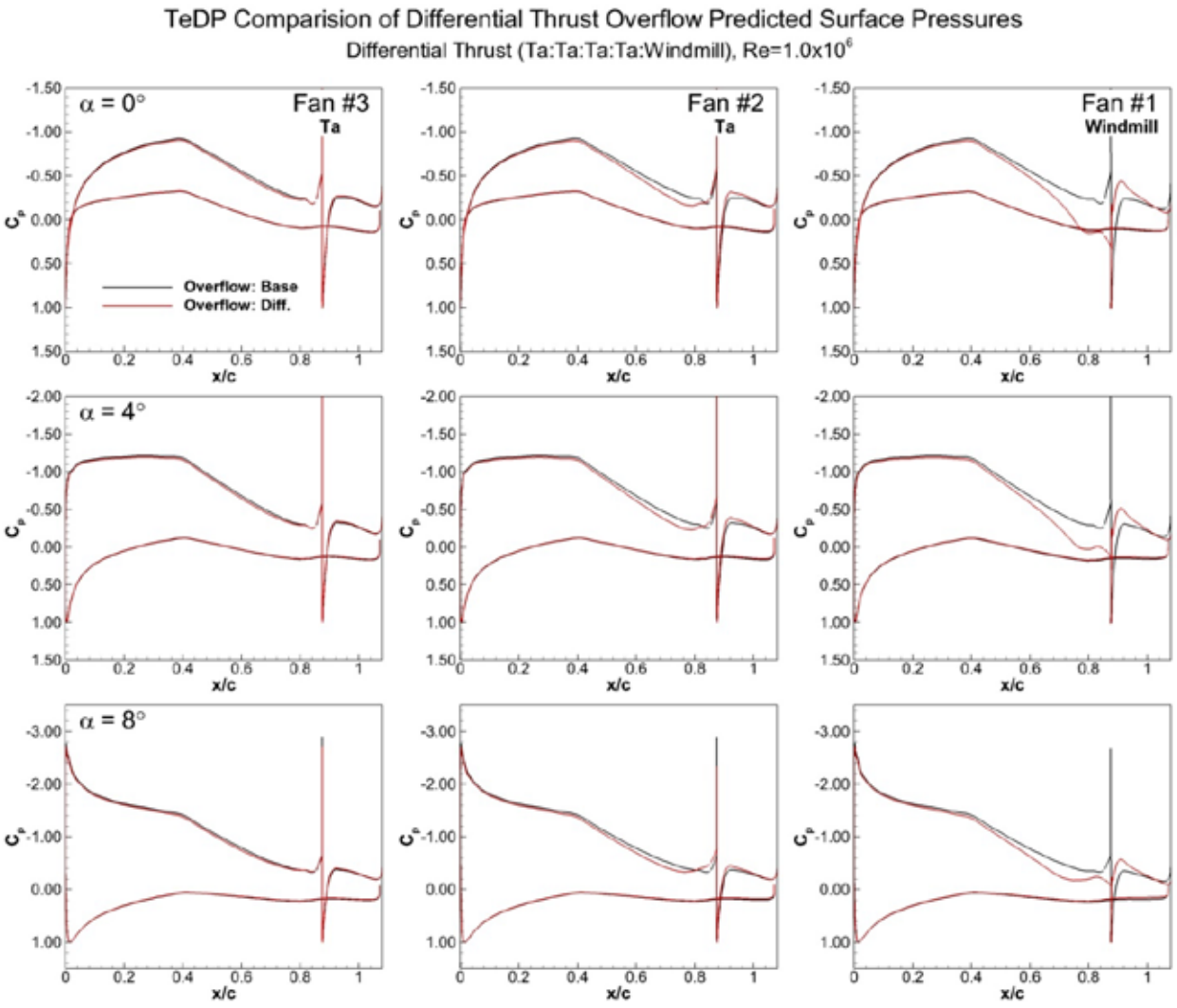

Figure 67: OVERFLOW predicted surface pressures for a centerline cut for Fans #1 to #3 for the baseline thrust available and differential thrust available mass flow cases, 5° thrust angle, α=0°, 4°, 8°, M_{∞}=0.09, Re=1.06x10^6.

6.7.3. Thrust Available/Thrust Required Differential Results

The final differential thrust case examined was the mixed thrust available/thrust required differential case. For this case, Fan #1 was set at the thrust required mass flow condition with Fans #2-#5 set to the thrust available mass flow. Angles-of-attack of 0°, 4°, 8°, and 12° were run. Force and moment results for the mixed thrust available/required differential case as compared to the baseline thrust available case at M=0.09, Re=1.06x10^6 are shown in Figure 68. Also included in Figure 68, for comparative purposes, are the thrust available differential case results discussed in Section 6.7.2.

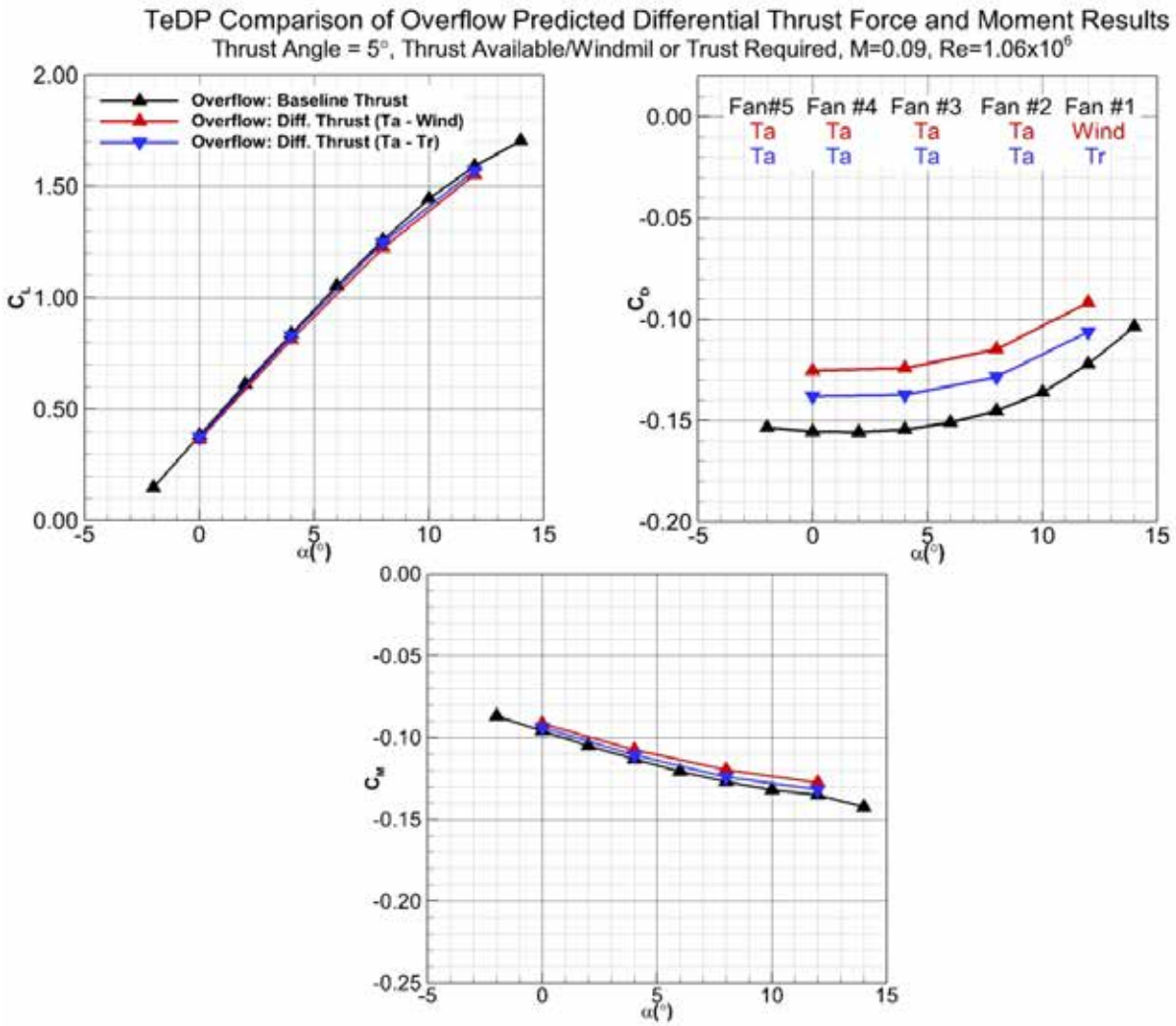

Figure 68: OVERFLOW predicted force and moment results for the baseline thrust available mass flow and the mixed thrust available/required differential case for the 5 fan TeDP configuration as a function angle-of-attack, 5° thrust angle, M_{∞}=0.09, Re=1.06x10^6.

From Figure 68, as would be expected, the mixed thrust available/required differential case results lie between the baseline thrust available and the differential thrust available results. For the drag results, the mixed differential thrust available/required results produce a drag increase of approximately 11.5%, as opposed to the 19% to 20% for the thrust available differential results. There are no significant surprises in the mixed thrust available/required differential force and moment results. Contours of pressure coefficient and surface streamlines for the differential thrust available case and the differential mixed thrust available/required case at angles-of-attack of 0°, 4°, and 8° are shown in Figure 69.

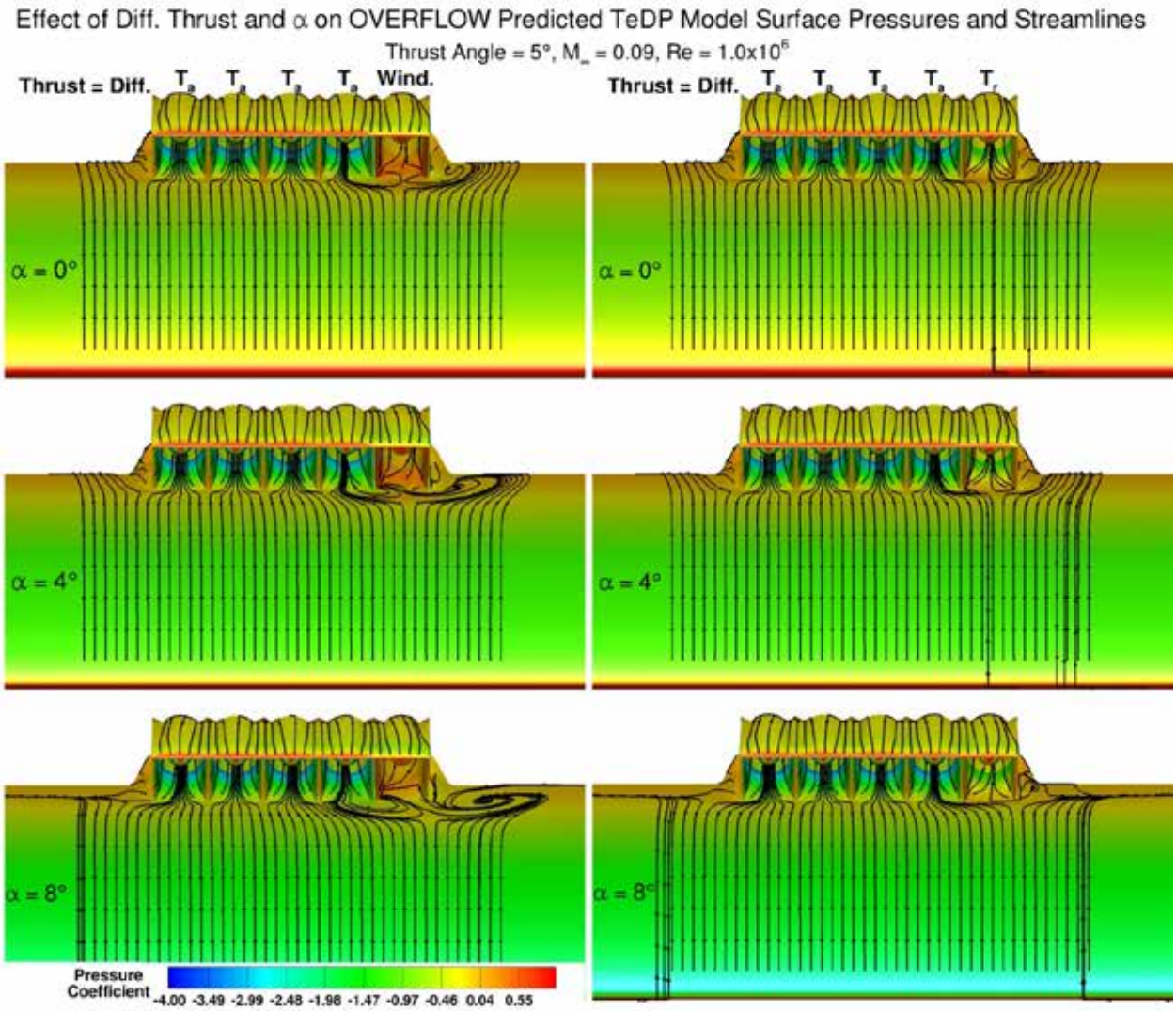

Figure 69: Contours of surface pressure coefficient and streamlines as a function of angle-of-attack for the differential thrust available and the differential thrust available/required cases, M_{∞}=0.09, Re=1.06x10^6.

From Figure 69, the reduced blockage produced by the thrust required mass flow for the #1 fan as compared to the windmill mass flow case is clearly evident. The thrust required surface streamlines show a much more benign flowfield as compared to the windmill/thrust available case. Whereas the #2 fan is significantly affected by the windmilling #1 fan for the thrust available differential case, the #2 fan appears to be only slightly affected by the adjacent #1 fan thrust required mass flow for the mixed differential case. The effect does not appear to grow significantly with angle-of–attack. The flowfield outside of the fan section is also not greatly affected. These results are mimicked in the fan face Mach number and stagnation pressure ratio contours shown in Figure 70 and Figure 71.

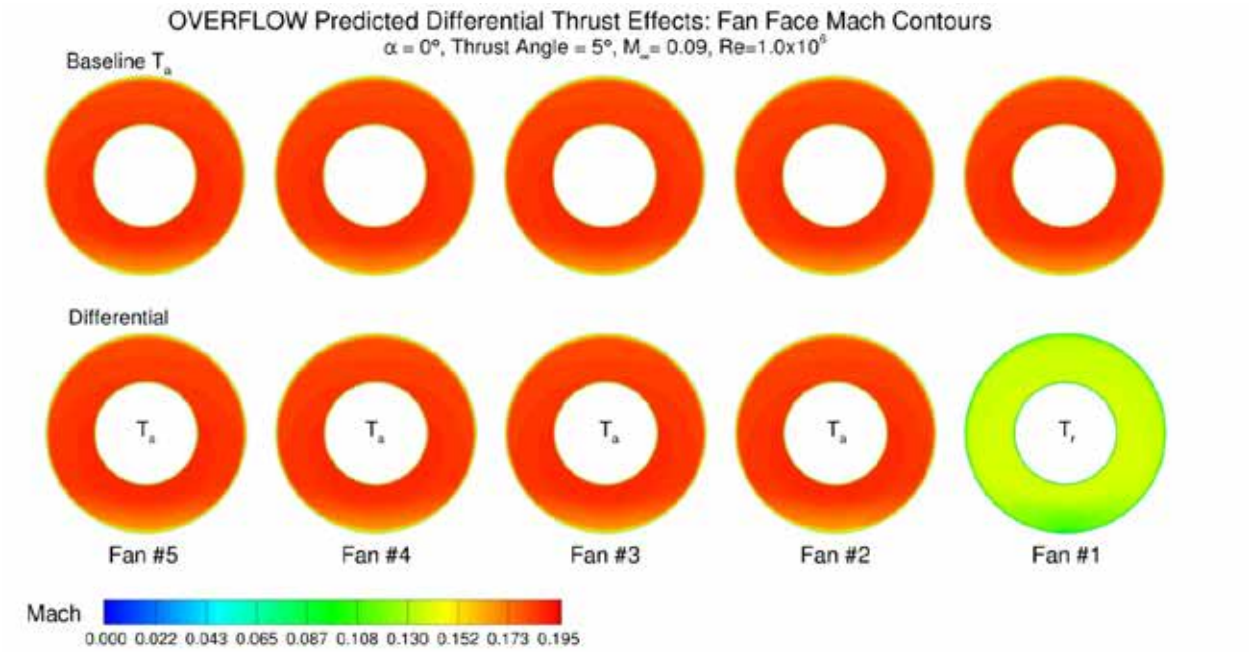

Figure 70: OVERFLOW predicted contours of Mach number at the fan faces for the baseline thrust available and the differential thrust available/required mass flows, 5° thrust angle, α=0°, M_{∞}=0.09, Re=1.06x10^6.

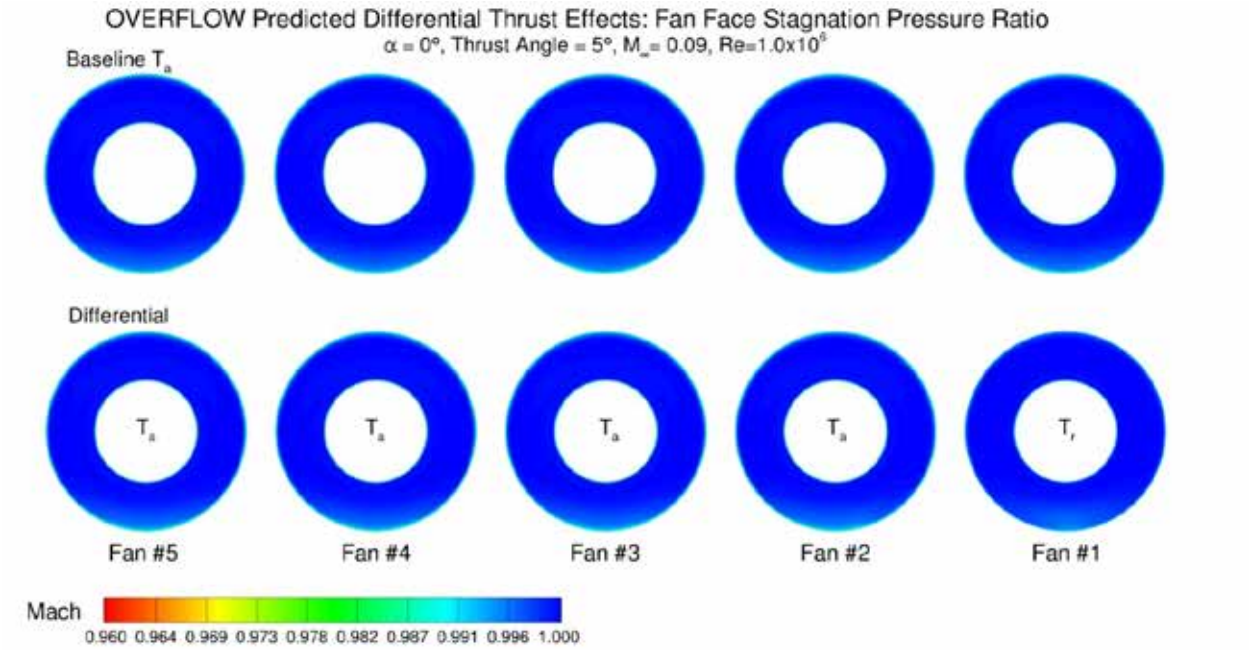

Figure 71: OVERFLOW predicted contours of stagnation pressure ratio at the fan faces for the baseline thrust available and the differential thrust available/required mass flows, 5° thrust angle, α=0°, M_{∞}=0.09, Re=1.06x10^6.

The fan face Mach number and stagnation pressure ratio contours for the mixed thrust available/required case are compared against the baseline thrust available results in Figure 70 and Figure 71. From Figure 70 and Figure 71, the reduced mass flow thrust required setting for the #1 fan appears to have little effect on the #2 fan, with the center #3 fan flowfield essentially unaffected. Surface pressures for a centerline cut through Fan #1, Fan #2, and Fan #3 for at angles-of-attack of 0°, 4°, and 8° are shown for the baseline thrust available and the differential mixed thrust available/required mass flow case in Figure 72. Also included in Figure 72 for comparison are the differential thrust available results.

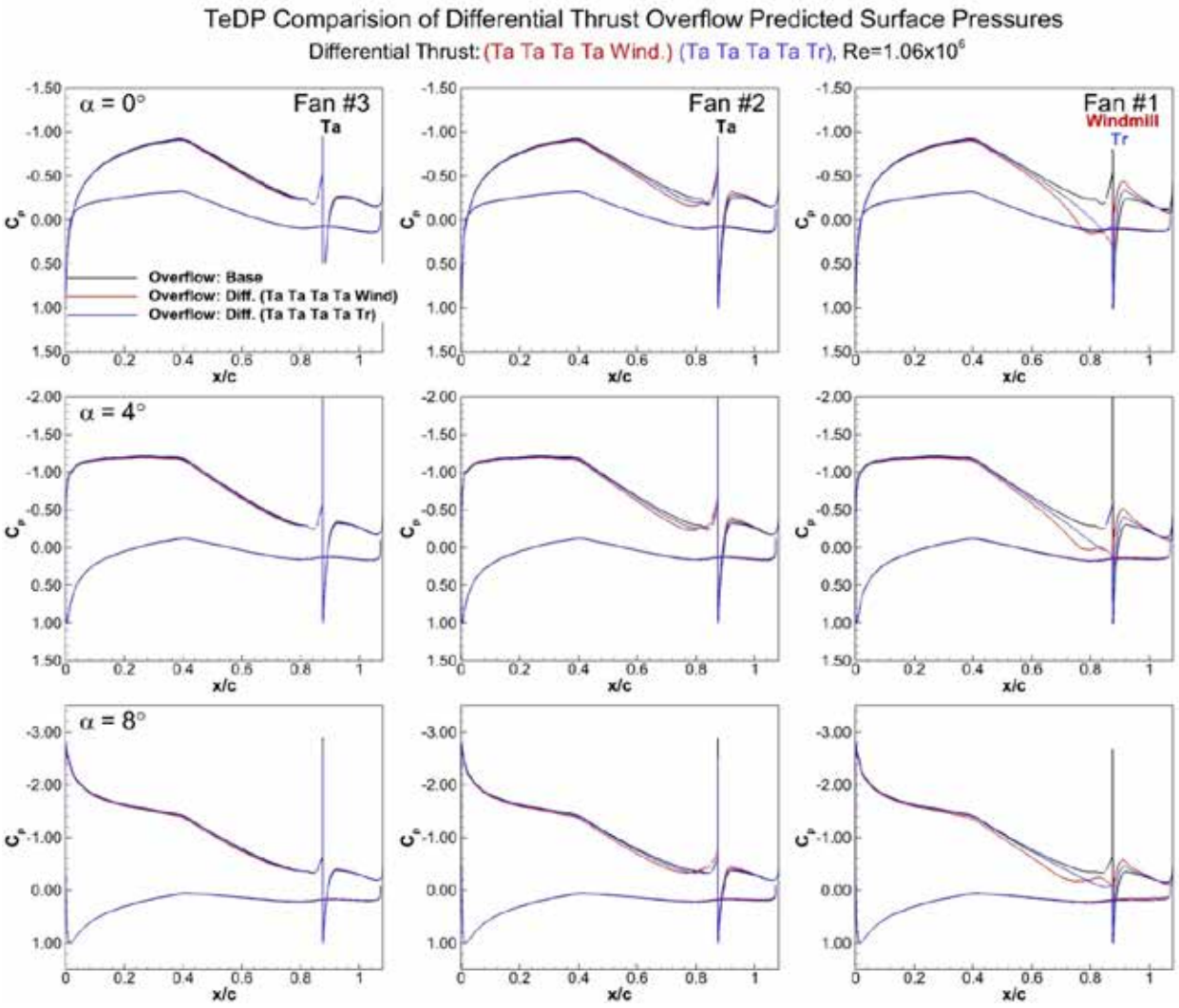

Figure 72: OVERFLOW predicted surface pressures for a centerline cut for Fans #1 to #3 for the baseline thrust available and differential thrust available/required mass flow cases, 5° thrust angle, α=0°, 4°, 8°, M_{∞}=0.09, Re=1.06x10^6.

From Figure 72, again, as would be expected, the pressures for the differential mixed thrust available/required case lie between the baseline thrust available and the differential thrust available cases. As was observed for the surface streamlines and fan face Mach and stagnation pressure ratio contours, the effect of the reduced mass flow #1 fan on the adjacent #2 fan is

significantly reduced for the mixed thrust available/required case. Also, as was observed for all of the differential thrust cases, only the adjacent fan flowfield is affected, with the effect dying out by the #3 centerline fan.

6.7.4. Differential Thrust Results Summary

The differential thrust results showed that the windmilling, or reduced thrust fan can have a significant effect upon the adjacent fan flowfield. The blockage and spillage produced by the reduced mass flow can affect the adjacent fan pressures, surface streamlines, and the fan face flowfield. The effects are greatly exaggerated for the windmill cases as opposed to a reduced thrust case. For all of the differential cases investigated computationally, the effect of the reduced mass flow fan was confined to the adjacent fan, and did not affect the 2nd fan from the reduced mass flow fan. The primary effect of the differential thrust results was to increase the drag of the section, while small reductions in lift and moment were observed.

The computational results in the current study did not predict the increased adjacent fan thrust observed during the Phase I experimental investigation. It is believed that the unrealistically low blockage of the windmilling fan is the primary reason an increased thrust is not observed in the adjacent fan in the CFD model.

6.8. 3D Design and CFD Summary

The 3D inlet design results have shown interesting differences between the 2D and 3D results. The 2D results showed much larger thrust super circulation affects than the 3D results. Although an oversized inlet can be designed such than no flow separation is observed on the cowl, plug, or inlet geometry, and also upstream of the inlet, the effect of the added blockage can create large asymmetries between the various fan inlets. These asymmetries can be significantly reduced by reducing the inlet height and resulting apparent blockage. A 1.95 inch inlet height with a 2.45 inch inlet width was converged upon that computationally produced an efficient, low blockage design. The inlet mass flow was sized using a weighted average of the thrust required and thrust available mass flows.

The results from the thrust angle investigation showed that the fan thrust angle has a significant effect upon the lift, moment, and performance of the section. The fan thrust angle was found to directly affect the section's camber. Of the three thrust angles investigated, the 11.4° thrust angle was found to best match the lift curve of the baseline NACA 64_3-618 section. While it was initially expected that the fan thrust angle which matched the baseline section lift curve slope would be the preferred geometry, the results of thrust angle investigation showed that while the 11.4° thrust angle geometry does match the baseline lift curve well and increase the C_L of the section at higher angles-of-attack, the higher thrust angle geometries also produced a significantly increased drag and more negative moment as compared to the lower thrust angle cases. It was found that the large drag increase of the higher thrust angle geometries was primarily a result of increased pressure drag on the upper surface cowl due to the increased rotation of the cowl surface. While not matching the baseline NACA 64_3-618 section lift curve

as well as the 11.4° geometry, the 5° geometry produced a drag and moment comparable to the baseline NACA 64_3-618 section. Since the performance and efficiency of the TeDP configuration is of primary importance, the 5° geometry was chosen as the more optimal configuration and was used for the thrust level investigation and for the final wind tunnel investigation.

A thrust level investigation was performed using the 5° thrust angle geometry. Results from the thrust level investigation showed that while differences in force and moment results exist with thrust level, they are generally smaller than were anticipated. Changes in lift of 5-6% between the thrust required and thrust available mass flows were observed. The pitching moment showed a larger 10% difference between the thrust required and thrust available cases. The force and moment differences with thrust level also showed that the differences in force and moment results were a result of changes in circulation caused by the fan thrust in addition to the non-zero thrust vector effect. Asymmetries in the inlet flowfields as a function of angle-of-attack were also observed. While the fan flowfield is able to remain attached locally at angles-of-attack beyond the baseline NACA 64_3-618, the separation generated by the baseline outer wing section was observed to interact with the outer inlet flowfields and affect the center fan section forces. This interaction increased asymmetries in the outer fan inlet flowfields, producing spanwise thrust variations of up to 2% depending upon the thrust level and angle-of-attack.

Results from the differential thrust study showed that while the blockage and spillage produced by a reduced mass flow fan can have significant effects upon the adjacent fan flowfield, those effects are confined to the adjacent fan and do not extend beyond the adjacent fan. The primary effect of the differential thrust on the section's force and moment results was to increase the drag of the section, with small reductions in lift and moment also observed.

7. Final Verification Wind Tunnel Test

After completion of the CFD study, a final verification wind tunnel test was performed. The wind tunnel test was conducted in the University of Illinois at Urbana-Champaign's (UIUC) Aerodynamics Research Laboratory (ARL) low-speed wind tunnel. The low-speed wind tunnel at ARL is a 3 ft x 4 ft open return type tunnel with a maximum free-stream speed of approximately 140 mph (200 ft/s). A schematic of the wind tunnel is shown in Figure 73.

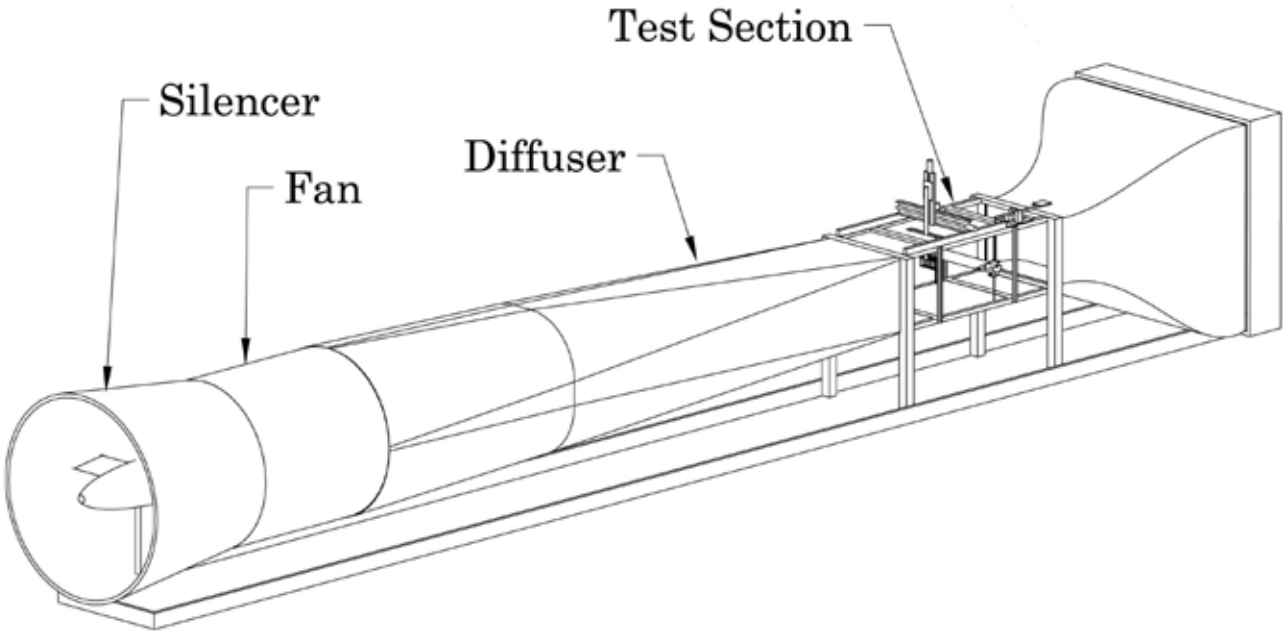

Figure 73: Schematic of UIUC ARL low-speed 3 ft x 4 ft wind tunnel.

The model for the final wind tunnel verification test mimicked the pseudo 3D CFD model developed in Section 6. The pseudo 3D model spanned the tunnel floor to ceiling with a height of 33.563 inches and a chord of 20 inches. The model has 5 BLI electric ducted fans mounted on a 2D straight wing. The test examined multi-fan effects on aerodynamic/propulsive coupling, BLI, circulation effects, and reenergizing the wake with the thrust stream. Specifically, the effect of thrust levels and mass flow on both the overall wing and sectional aerodynamic characteristics including lift, drag, and pitching moment were investigated. As with the CFD, the test also focused on the effect of spanwise differential thrust, specifically the effect of changing mass flow and spillage on adjacent fan flowfield was also studied.

7.1. Fan Set-Up and Experimental Static Thrust Testing

Prior to the wind tunnel investigation, the 5 individual fan units which make up the pseudo 3D model distributed propulsion system were bench tested under static thrust conditions to verify fan function and fan-to-fan repeatability. As was discussed in the scaling section (Section 4), the Hyperflow 56 EDF was chosen as the commercially available fan which best matched the scaled flying test bed configuration, providing the best combination of thrust and required low input power/amperage.

7.1.1. Fan/Motor Set-Up

The Hyperflow 56 fan is manufactured by Great Planes. According to the manufacturer, the Hyperflow 56 EDF will produce approximately 1.9 lbs static thrust at 50,000 RPM. Photographs of the Hyperflow 56 fan are shown in Figure 74.

Figure 74: Photographs of the Hyperflow 56 EDF.

Several motor options are available for the Hyperflow 56 body. In order to achieve the rated 1.9 lbs thrust, however, the Great Planes 24-45-3790 brushless motor is required. A great planes silver series SS-35 electronic speed control (ESC) was used. Since the Hyperflow 56 fan is significantly smaller, and cheaper than the Schuebeler fans used during the Phase I investigation, the overall quality of the fans was also lower. Several fans were purchased to obtain a set of 5 dimensionally accurate/repeatable fans. The biggest difference between the smaller Hyperflow fans and the larger Schuebeler fans is the tail cone and motor power routing. The Schuebeler fans were purchased with an integrated motor and tail cone. The power routing for the Schuebeler motors was very compact and aerodynamically non-intrusive, with the motor power lines routed through the stator vanes. Due to the small size of the Hyperflow fan, the motor power lines cannot be routed through the fan stator vanes, but are instead allowed to hang aft of the motor and need to be routed into the model body. Another issue with the Hyperflow fan is the fan tail cone. While a tail cone is provided for the fan, for the high power 24-45-3790 brushless motor required to meet the maximum rated thrust, the tail cone does not fully fit over the motor. Also, for high power/thrust operation, the manufacturer recommends not using the tail cone to provide adequate cooling to the motor. A no tail cone geometry would be a significant departure from the CFD model. As a result, the tail cone was fitted to the motor such that an open gap was left between the fan end and the tail cone beginning, allowing cooling air access to the aft motor body. While the presence of the motor wires and partial tail cone represent differences between the CFD and experimental flowfield, these differences should be limited to drag differences, and should not significantly affect the inlet or airfoil flowfield.

7.1.2. Power Supply

During the Phase I investigation, run times were severely limited due to the required use of lithium/polymer batteries to run the fans. Batteries were required since the fans used required a power input of 52 Volts at 190 Amps. The power required to achieve the maximum static thrust

and RPM of the Hyperflow 56 fan is 14.8 V at 32.6 A. This power input is small enough to be able to run the fan from a DC power supply instead of batteries. Due to the significantly lower power requirement of the Hyperflow 56 fan, a relatively small power supply was found which could replace the batteries and hopefully allow for significantly longer run times. The power supply chosen was a regulated 50 Amp compact power supply with an adjustable voltage from 9 to 15 Volts (750 Watts) manufactured by QJE (model PSW50SWIII). A photograph of the power supply is shown in Figure 75.

Figure 75: Regulated power supply used to power Hyperflow 56 fans.

The power supply is regulated with variable noise reduction. The power supply is popular with amateur ham radio operators due to its filtered, low noise operation. Each fan was run with its own power supply.

7.1.3. Static Thrust Stand Results

Prior to the wind tunnel test, the individual fans were tested in a static thrust test stand to document their performance and repeatability. The individual Hyperflow 56 fans were mounted in a thrust test stand designed and built during the Phase I effort. The test stand originally used a 25 lb Transducer Techniques load cell. For the current investigation, the 25 lb load cell was replaced with a Transducer Techniques 10 lb load cell. The motor ESC is controlled using a computer generated pulse width modulated (PWM) signal. Motor control and data acquisition were accomplished using a National Instruments LabVIEW based data acquisition and control system. Motor RPM was monitored in real time by the pulsed control signal generated by the ESC to drive the motor using a sensor manufactured by Eagle Tree Systems (model # RPM-BRS-V2). Photographs of the Hyperflow 56 fan mounted in the thrust test stand are shown in Figure 76.

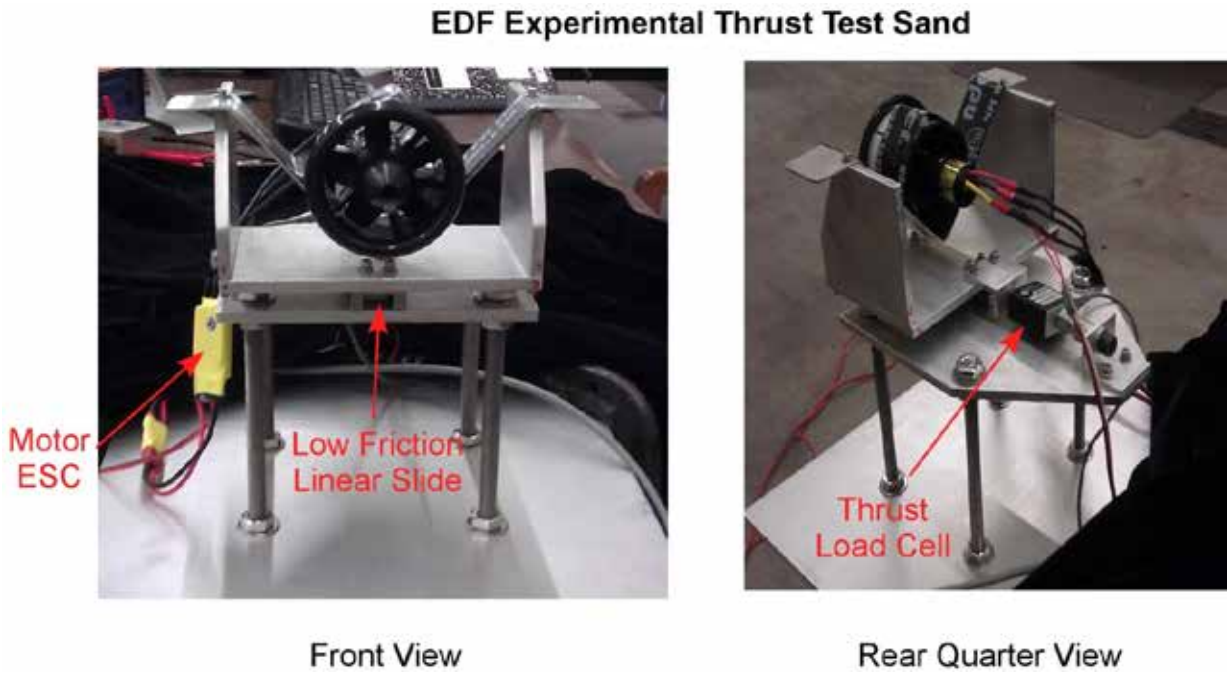

Figure 76: Photographs showing the Hyperflow 56 EDF mounted in the experimental thrust test stand.

The photographs shown in Figure 76 do not show the tail cone mounted to the motor. For the static thrust measurements, the manufacturer supplied bell mouth was used. Prior to mounting the fan in the test stand, the test stand thrust load cell was calibrated to a value slightly higher than the maximum expected thrust of 1.9 lbs. A plot showing the thrust test stand calibration results is given in Figure 77. From Figure 77, the thrust test stand results have excellent linearity.

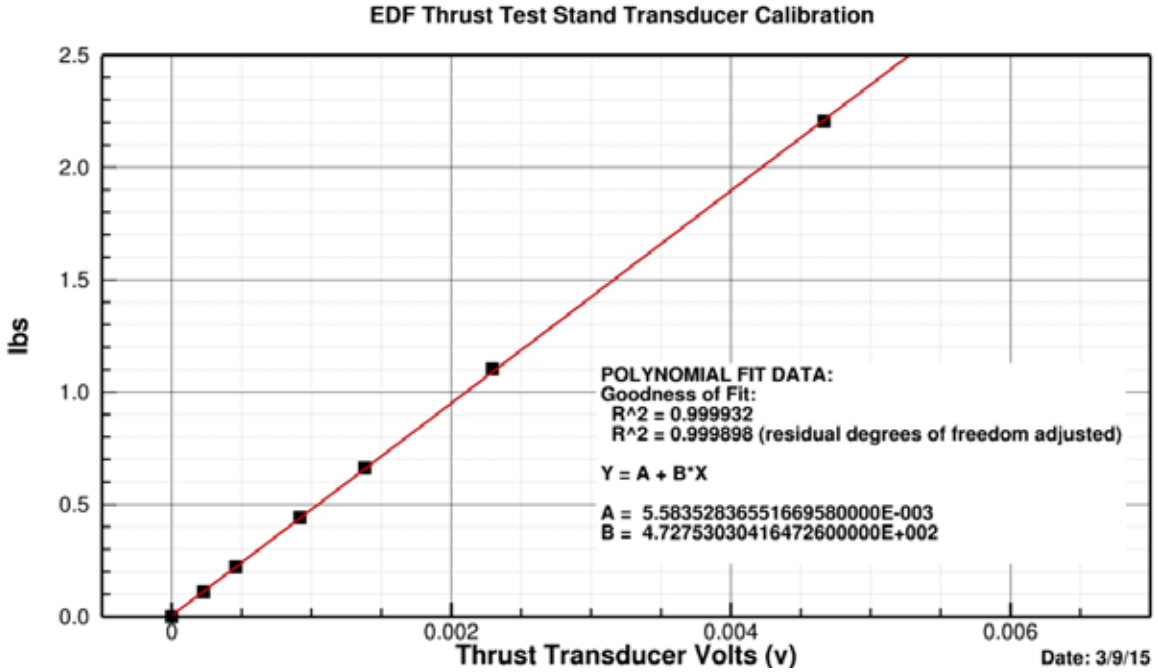

Figure 77: EDF thrust test stand transducer calibration.

Test stand results for the Hyperflow 56 fans are shown in Figure 78. From Figure 78, thrust data were obtained up to an RPM of approximately 44,000. The thrust data for the individual fans is relatively consistent with RPM and shows good agreement between the fans. The maximum thrust observed was approximately 1.75 lbs, 0.15 lbs below the manufacturers quoted 1.9lbs. The manufacturers quoted maximum thrust value of 1.9 lbs was achieved at an RPM of 48,000. In order to place the motor ESCs outside of the model during testing (due to space constraints within the model and cooling issues to be discussed shortly), wire lengths between the motors and the motor controllers had to be on the order of 48 inches. This long line length had the effect of limiting the maximum RPM of the motor to approximately 44,000 RPM, producing the slightly lower maximum static thrust value. The 1.75 lbs of static thrust, however, should be sufficient to reach the required thrust available mass flow required during testing.

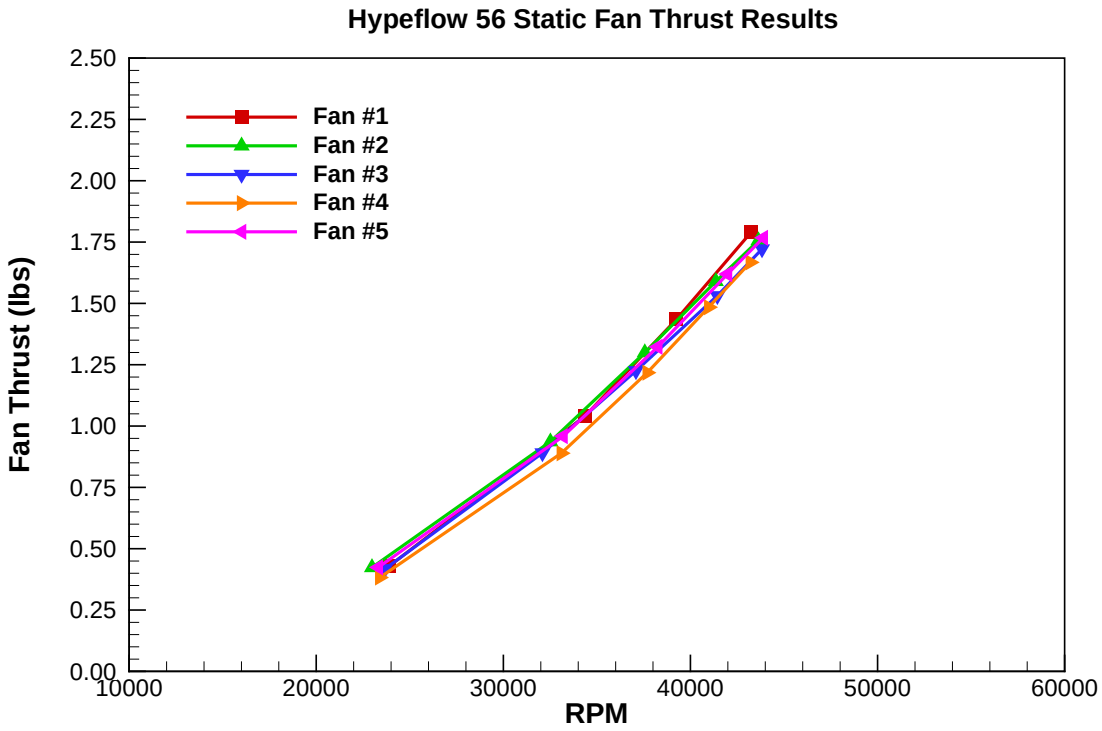

Figure 78: Static thrust test stand results for the Hyperflow 56 EDF.

7.1.4. Motor and ESC Cooling

During the initial static testing of the fans it was found that the motor and the motor ESC controller would very quickly get extremely hot, particularly the motor ESC. RTD temperature sensors were mounted on the motor body and also on the motor ESC to be able to continuously monitor the motor and controller temperature. The ESC has an automatic cut-off above an ESC temperature of 220 °F. This cut-off temperature would be reached after about 40 seconds of testing at high power levels. After speaking with the manufacturer, it was noted that the ESC does require some cooling during operation. The very short run time however, pointed to other

possible issues. Consultation with other researchers attempting to use power supplies to run high power brushless R/C motors using R/C hobbyist type hardware have also experienced higher than normal temperatures. These higher than normal temperatures are somehow related to the use of a DC power supply instead of the as-designed for battery. The root cause of the increased temperature/power supply combination is currently unknown. In order to achieve the desired long run times, however, battery usage to power the fans was not an option. As a result, alternative, active cooling schemes were investigated. While the motor will be cooled by the tunnel airstream during testing, due to space constraints within the model the ESC needed to be placed outside of the model, below the tunnel floor.

The arrived at cooling scheme for the motor controller was water cooling. The basic ESC has an aluminum plate mounted on either side of the ESC. The aluminum plate is in direct contact with several ICs on the ESC. Thermally conductive grease is also present between the aluminum place and the ICs. Water cooling jackets were added on either side of the aluminum plate, with thermal grease applied between the plate and the water cooled jackets. Water cooling the ESC is often used for R/C boats. A schematic and photograph of the set-up is shown in Figure 79.

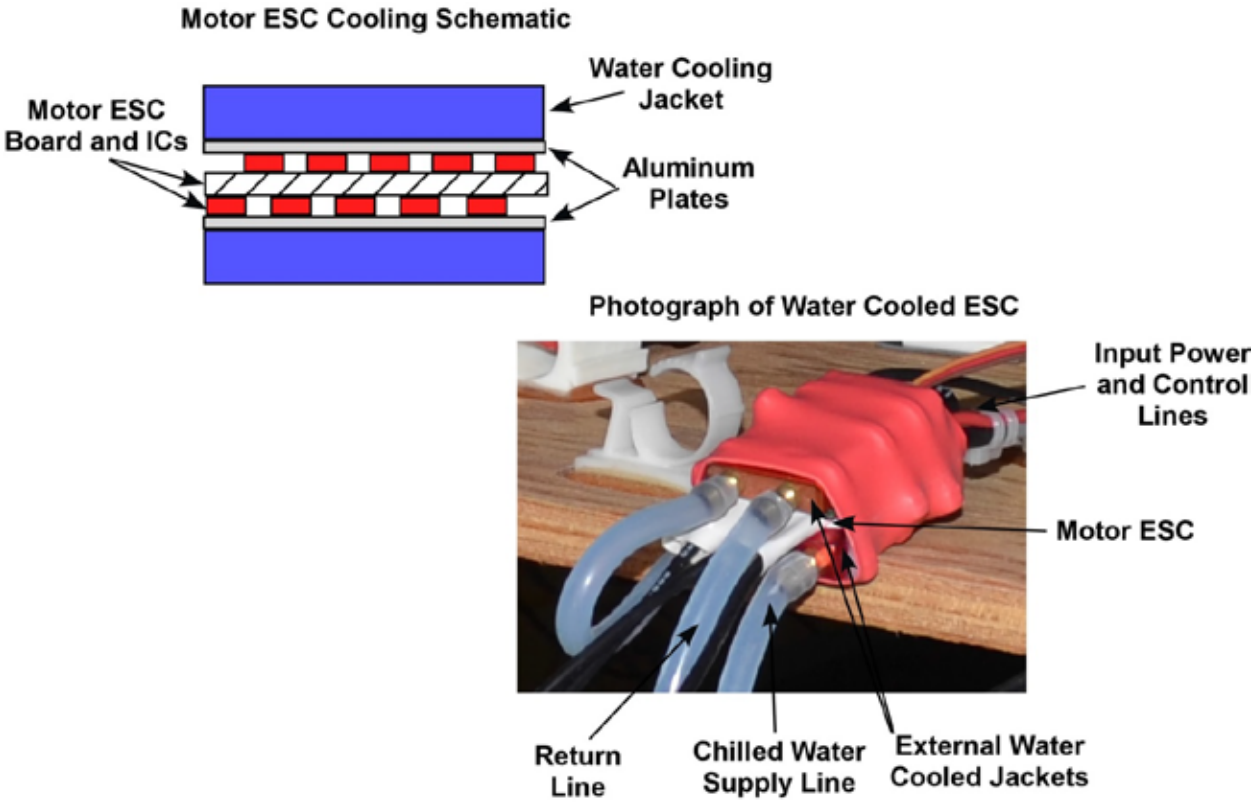

Figure 79: Schematic and photograph of motor ESC water cooling.

Water entering the cooling jacket was chilled in an ice bath. The lower jacket water was then routed to the upper jacket, and then back to the ice bath. The 5 individual cooling jackets were fed from a single pump through a manifold. The pump was capable of supplying 560 GPH. For testing purposes, an individual ESC was cooled to 55 °F and run in the static test stand until the motor temperature reached a high enough level to warrant stopping before damaging the motor.

This test lasted approximately 5 minutes. The ESC temperature during this time did not rise above 65 °F. As previously stated, during actual runs in the tunnel, the motor body will be cooled by the free-stream flow. Due to the small temperature rise over 5 minutes, it was thought that the water cooled set-up would provide adequate cooling to the motor ESC to allow for extended run times.

7.2. Wind Tunnel Model Design

The wind tunnel model is a 2D NACA 64_3-618 with the 5 BLI ingesting fans mounted on the model centerline. The model span is 33.563 inches with a nominal chord of 20 inches. The model mimics the 3D CFD model discussed in Section 6. The model was constructed using stereo lithography for the model body, with an internal spar and rib system of stainless steel. The model was designed to span the wind tunnel ceiling to floor. The basic model design and layout was built up in ProE from the CFD generated surfaces. The main airfoil body wrapped around the leading-edge. A lower surface cover plate allowed access to the model interior. A schematic of the 3D ProE model is shown in Figure 80.

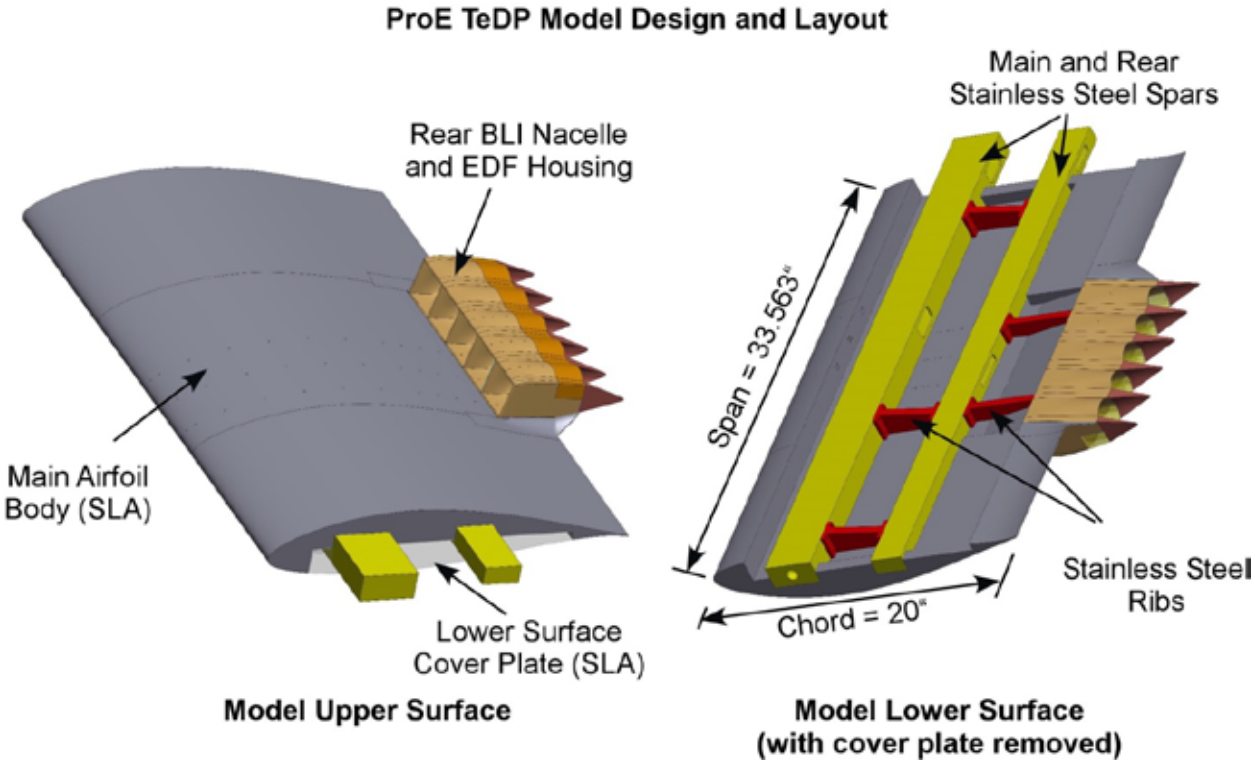

Figure 80: TeDP model ProE design and layout.

Since the motor ESCs were located below the tunnel floor, the motor wiring was routed out of the motor tail cone to the underside of the model and through a slot cut in the lower surface SLA cover plate. The wires were then routed out of the tunnel through the rear spar. The model also contained three rows of surface static pressure taps. The static pressure taps were located on the fan centerlines of fans #1, #2, and #3. The tap lines were routed directly in the SLA. Four

surface static pressure taps were also located in the fan #1, #2, and #3 ducts. The four internal surface static pressure taps in the ducts were used to correlate fan mass flow to the CFD fan mass flow. The tubes for the surface static pressure taps were routed out of the model through the main spar. Photographs showing the TeDP model mounted in the wind tunnel are shown in Figure 81. Since the CFD simulations were run fully turbulent, a distributed roughness grit boundary-layer trip (#50 grit) was placed on the model upper and lower surface at x/c=0.03. The trip was sized for a critical roughness Reynolds number of $Re_{k,crit}$=600.[13]

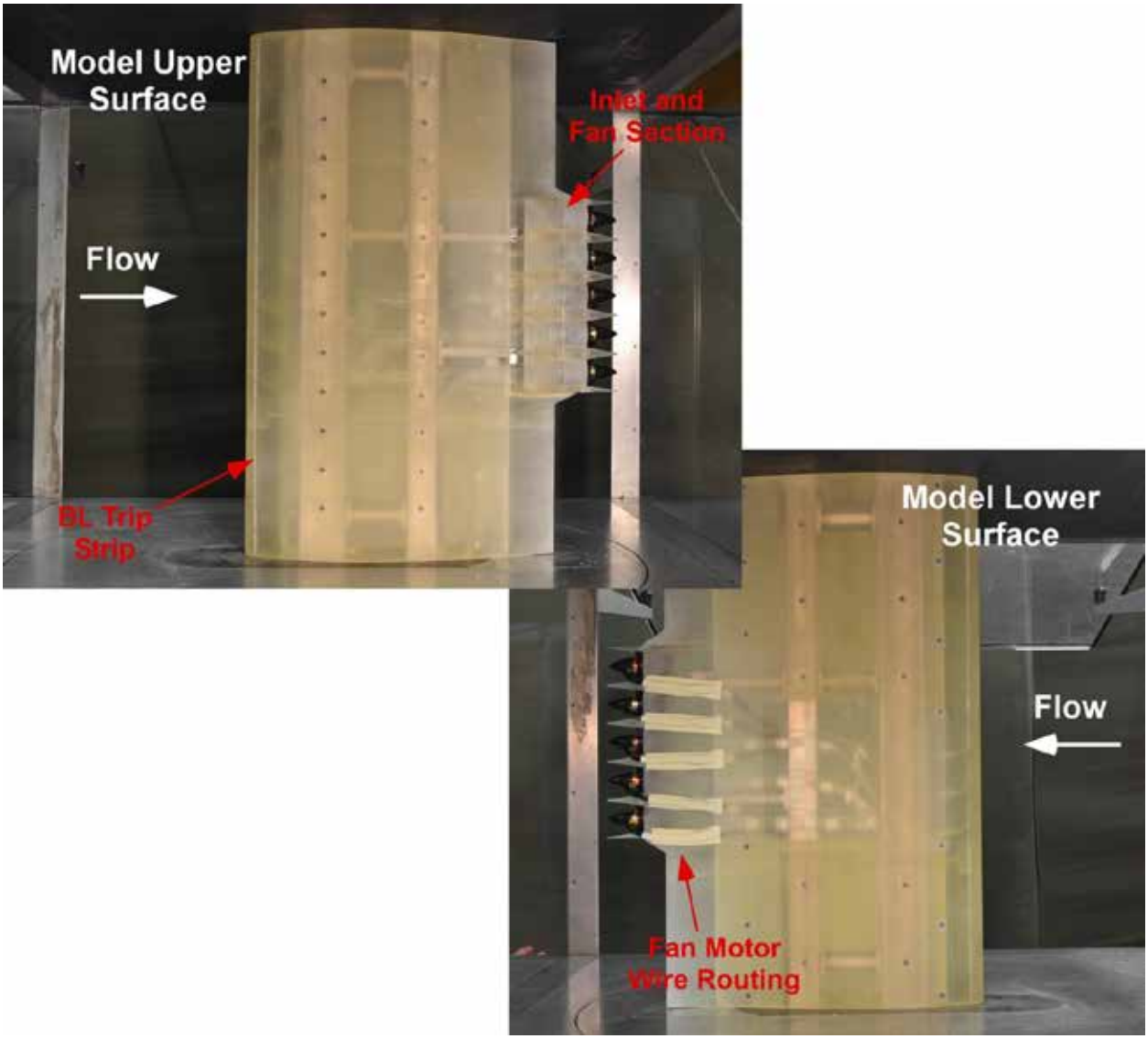

Figure 81: Photographs of TeDP model mounted in tunnel.

A close-up of the nacelle inlet/exit and fans is shown in Figure 82. The wire routing for the EDF fans from the fan tail cone to underneath the model is also shown. The tail cone opening for motor cooling is also highlighted in Figure 82, as are several of the surface static pressure taps.

As previously discussed in Section 7.1.1, the tail cone opening and routing of the fan motor wires on the model lower surface represent differences between the wind tunnel model and the CFD model. These differences should be limited to the drag of the wind tunnel model and should not affect the airfoil or nacelle/inlet flowfield.

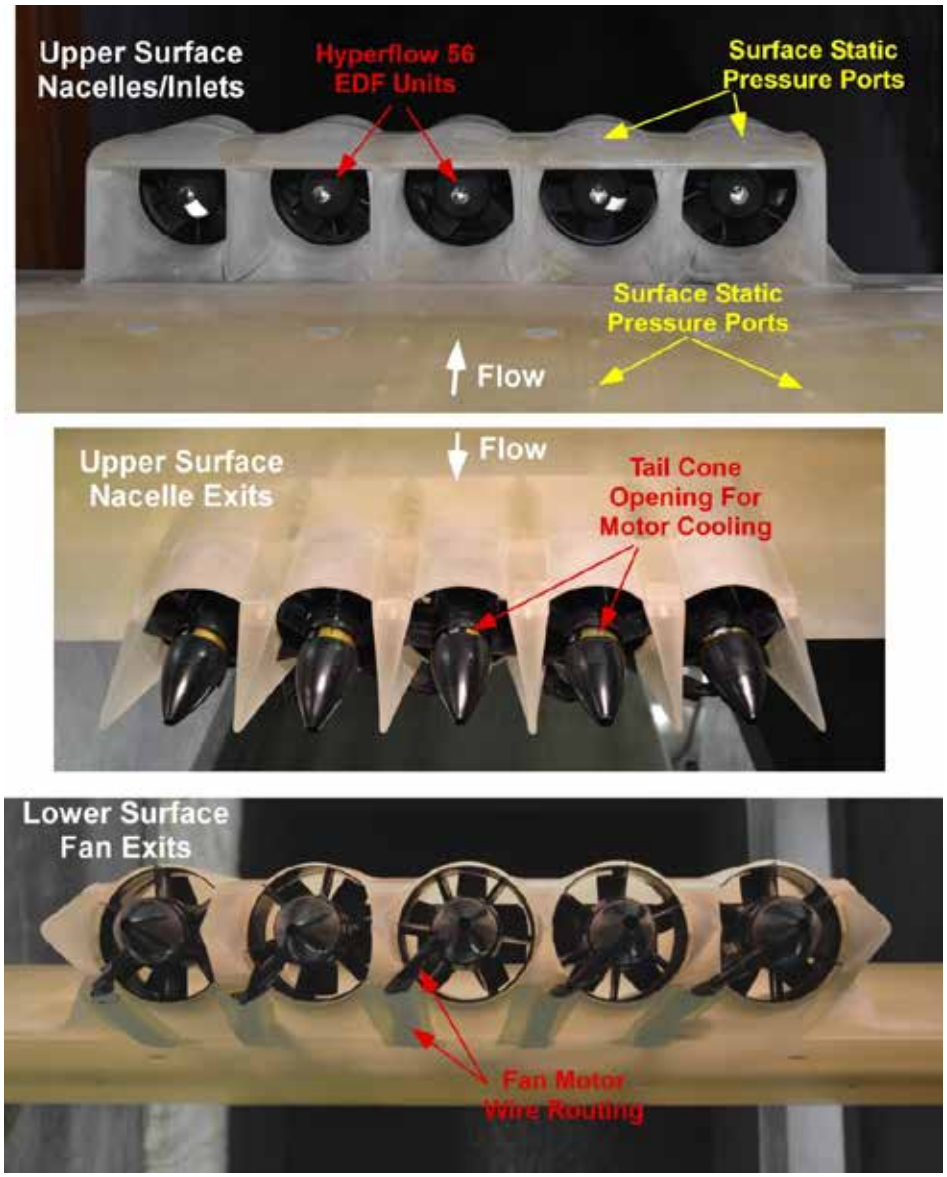

Figure 82: Close-up photographs showing TeDP model fan nacelle inlets/exits.

7.3. Model Instrumentation and Acquisition

The TeDP wind tunnel model primary force and moment measurement system was a three-component force balance mounted below the tunnel floor. The three-component force balance measured lift, drag, and pitching moment. Force and moment data were corrected for both solid and wake blockage using the standard 2D methods from Barlow et al.[14] In addition to the three-

component force balance data, surface static pressures were also obtained as discussed in Section 7.2. Three spanwise rows of surface static pressures were measured. The rows corresponded to centerline cuts through fans #1, #2, and #3. The individual tap rows contained 29 taps on the model upper and lower surface. In addition to the external taps, 4 taps were located in the inlet duct for fans #1, #2, and #3 at x/c=0.96, just upstream of the fan nose cone. The taps are spaced a 90° increments around the duct. With the main taps rows and the nacelle taps, the model has a total of 103 surface static pressure taps. The static pressures were acquired using a DTC Initium system. A schematic of the model pressure tap layout is shown in Figure 83.

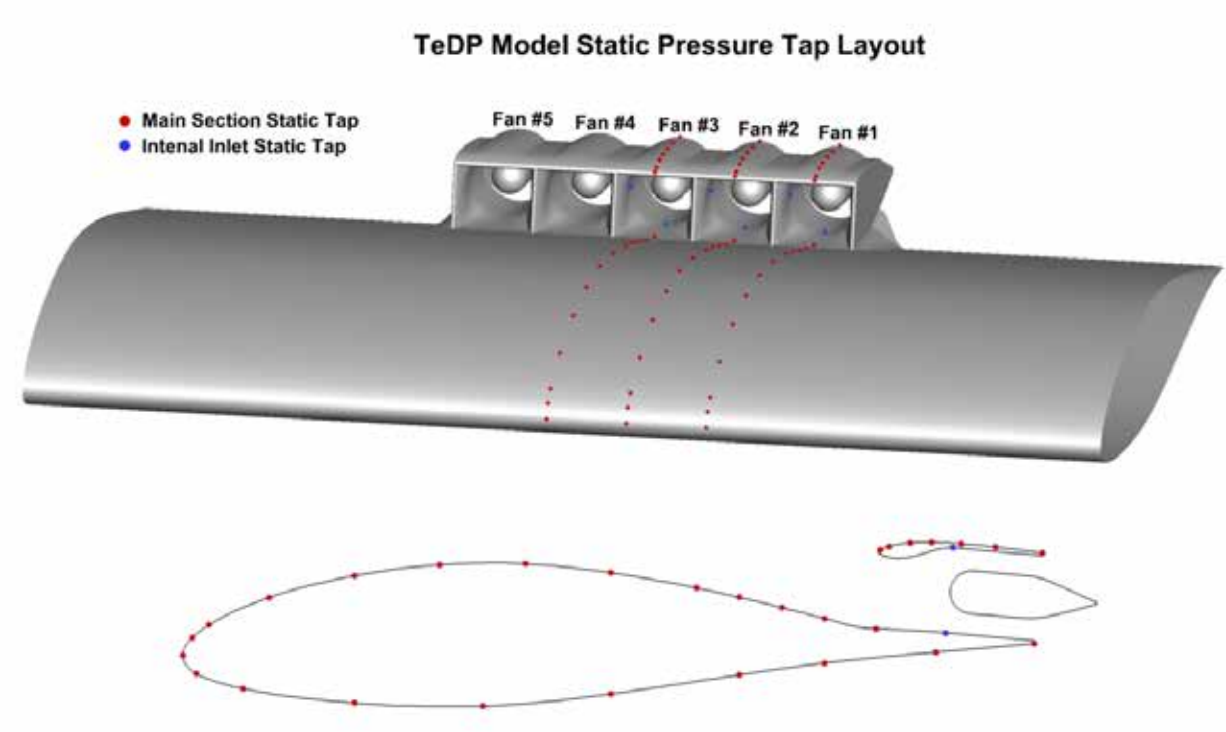

Figure 83: TeDP wind tunnel model static pressure tap layout.

The static tap locations shown in Figure 83 were arrived at by integrating the CFD pressures at various angles-of-attack to determine the minimal number of tap locations to generate a reasonably accurate sectional C_l representation from a tap row. A National Instruments LabVIEW routine was written to integrate both the CFD and proposed tap location data in order to minimize the C_l difference. Only the outer cowl pressures are used for the integration. Since the inner cowl pressures are mostly symmetric, their effects tend to cancel upon integration. A screen capture of the integration routine used to determine the tap locations is shown in Figure 84. From the integration results shown in Figure 84 for the thrust available case at α=8°, the difference between the CFD and tap line integrated lift coefficient is approximately 1%, with a 3% difference in pitching moment.

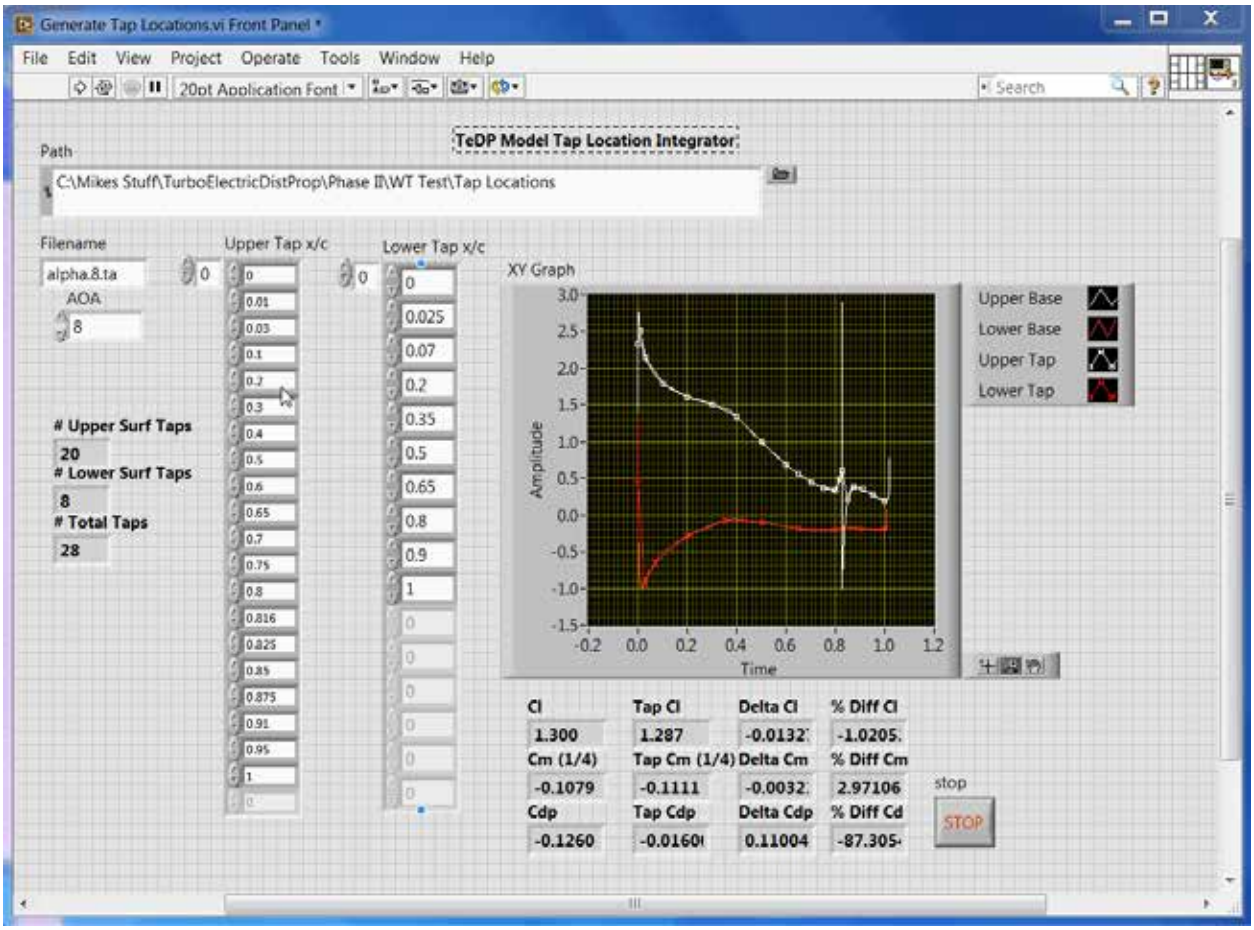

Figure 84: LabVIEW integration routine used to determine surface static tap locations.

In addition to the balance force and moment and surface static pressure data, individual fan/motor RPM, amperage, motor, and controller temperatures were acquired. The fan RPM was acquired using the Eagle Tree systems brushless motor RPM sensor (model # RPM-BRS-V2). Motor amperage was acquired using a hall effect current sensor between the power supply and the motor ESC and was manufactured by Tamura (model # L03S050D15). The motor and controller temperatures were measured using RTDs. The motor RTD was mounted to the fan motor case with the controller RTD mounted to one of the aluminum heat-sink plates on the controller between the controller and the heat-sink plate. With the motor/fan parameters, balance and tunnel parameters, a total of 28 individual parameters were recorded during testing. All acquisition, tunnel, and EDF control was performed using routines written in National Instruments LabVIEW. A screen capture of the acquisition routine is shown in Figure 85. During the data acquisition process, all fan RPM, motor amperages, and temperatures were monitored continuously.

Fan thrust settings were set by adjusting the width of the PWM signal sent to the motor controller. This allowed a throttle setting between 0% and 100% throttle. The RPM set

repeatability was approximately 1%-2% at the lower throttle settings and less than 1% for the higher throttle settings.

Figure 85: National Instruments LabView based data acquisition and reduction routine.

Finally, it was planned to map the wake of the model using a 5-hole probe system. Previously the tunnel had set-up a single 5-hole probe on a traverse to map the wake behind a 3D model.[15] Using this system, spanwise lift and drag values could be extracted. For a semi-span model, the single 5-hole probe wake survey method would require approximately 5 to 6 hours to acquire data for a single angle-of-attack. For the R/C hobby based EDF fans and controllers, this run time was unacceptably long. As a result, the tunnel acquired two additional 5-hole probes to make a rake of 3 5-hole probes. It was thought that the rake of 3 probes would reduce run times to between 1 to 2 hours. The additional probes were purchased and a multi-probe mount was designed and tested in the March/April 2015 time frame. Unfortunately, due to calibration issues, the multi-probe rake provided inconsistent results. Basically, small differences between the individual probe calibrations, or probe-to-probe interference were producing different readings from each individual probe in a uniform flowfield. At the time of this report writing, these calibration or probe interference issues had not yet been resolved. As a result, a single probe set-up would be required to obtain the desired wake measurements, with run times on the order of 5-6 hours for an individual point.

As discussed in Section 7.1.4, great strides were taken to provide cooling to the motor and motor controller. These included leaving an opening between the rear of the EDF and the tail cone to allow for motor cooling and adding water cooled jackets to the motor controller. Data for the individual force/moment and pressure polars and differential thrust results were obtained before an attempt was made to acquire the wake data. For the baseline force and moment data, run times were short. After acquiring the baseline data, extended runs of the motors/controllers were made to determine if the extremely long run times required by the wake probe measurement system could be achieved. As previously stated, the water used to cool the motor controllers was drawn from an ice bath. After cooling the motor controllers down to approximately 55 degrees, the tunnel was brought up to speed to cool the motors and the motors run at the thrust required RPM. Unfortunately, it was found that the controllers would not run beyond several minutes. While some controllers would run longer than others, they were inconsistent from controller to controller. The RTD temperature probe on the motor controller never got above 65 °F before the motor RPM would begin to fluctuate. The controllers have an internal cut-off when the

controller temperature reaches 220 °F. It is speculated that while most of the pertinent components were being adequately cooled by the water cooling, some components were not, leading to the fluctuating RPM. What role the use of a power supply to power the motor and controller plays in the overheating of the controllers is not fully known, though a connection is suspected. The R/C hobby based electric motors and controllers are simply not designed to run continuously for extended periods of time.

The primary purpose of obtaining the wake data was to determine the spanwise lift and drag of the model, and to study the effect of the fans re-energizing the model wake, especially for differential thrust cases. Since multiple pressure tap rows are present on the model, the spanwise effect on sectional lift can still be determined. Unfortunately, the spanwise drag cannot. While the wake data could not be obtained, RHRC still feels that all of the other proposed test points were obtainable with the as tested set-up, and that the data set produced is a very unique and valuable data set for distributed propulsion configurations.

7.4. Experimental Results

All data were obtained for a chord based Reynolds number of 1.06×10^6, at a tunnel speed of approximately 100 ft/s. This Reynolds number/tunnel speed was arrived at, along with the choice of fans, from the scaling study discussed in Section 4, as they provided the combination of inlet face boundary layer thickness to fan diameter, and fan diameter to model chord, which best matched the proposed flying test bed at reasonable tunnel blockage ratios.

Data were obtained first for the windmilling case, followed by the baseline thrust required and thrust available polars. After the continuous thrust polars were obtained, differential thrust polars were run. Prior to running the active fan cases, the fan throttle level for the thrust required and thrust available mass flows was determined to match those run for the CFD cases.

After model build up, installation, and check out, of the 29 surface static taps per row, one tap was lost on the model lower surface near the leading edge due to an internal connection in the SLA routing, with an upper surface cowl tap lost for the same reason. Additionally, due to the ultra-thin surface of the rear upper nacelle cowl, the upper cowl trailing-edge tap did not build properly. While the loss of these taps affects the sectional lift coefficient integration absolute accuracy, it should not affect the ability to compare the section lift characteristics between the fan rows.

7.4.1. Fan Thrust Level Determination

As previously discussed, prior to any active fan runs where the thrust required or thrust available mass flows were desired, the fan throttle setting was calibrated so that the internal nacelle duct pressures matched the CFD duct pressures and the model surface pressures at those conditions to ensure that the wind tunnel model and the CFD model results would be compared at similar fan mass flows. The CFD results were run at both the thrust required and thrust available mass

flows, where the fan mass flows were set at a=0° and then held constant at different angles-of-attack. The experimental model was run at Re=1.06x10^6, a=0°, at throttle settings of 25%, 40%, 60%, 80%, and 90%. A plot of the average internal duct C_{ps} for the three fans as compared to the CFD thrust required and thrust available internal duct C_ps is shown in Figure 86.

From Figure 86, as would be expected, as the throttle percentage increases, the duct C_ps drop as the flow is accelerated through the duct. The trend is fairly linear with increasing throttle position. From the duct pressures, it would appear that a 30% throttle setting would best match the CFD thrust required duct pressures, with a 90% throttle setting matching the thrust available pressures. The duct mass flow, however, are not the only indication of the correct fan mass flow for comparison.

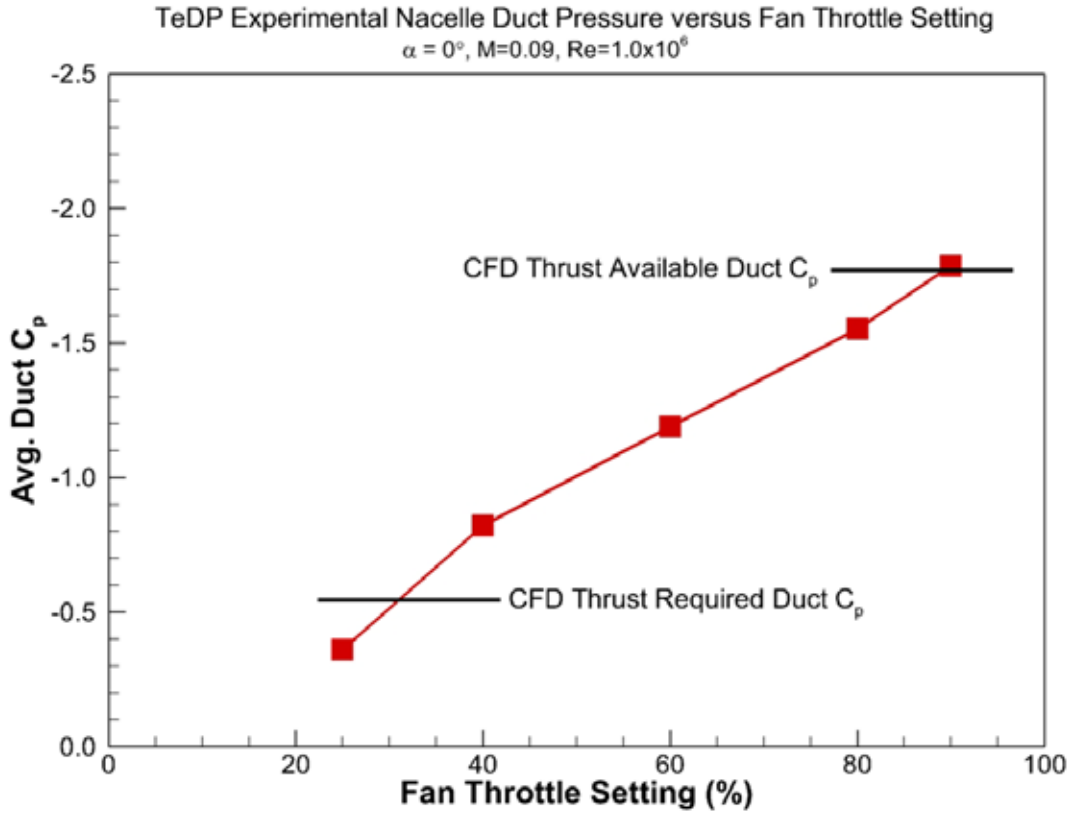

Figure 86: Effect of experimental TeDP model throttle level on average nacelle duct static pressure, a=0°, M=0.09, Re=1.06x10^6.

Since the CFD fan mass flows were set to achieve a desired thrust, and the thrust book keeping included the cowl drag, if the cowl drag were over, or under predicted by the CFD, the mass flow set to achieve the desired thrust would also be over or under predicted, which would affect the duct pressures. As a result, the model surface pressures upstream of the duct can also be used to calibrate the fan throttle setting.

Surface pressures for the centerline fan at α=0° as a function of throttle setting are shown in Figure 87. Also included in Figure 87 are the OVERFLOW predicted surface pressures for the thrust required and thrust available mass flow cases. From Figure 87, the effect of increasing the fan throttle is to create more negative pressures upstream of the duct as the fan draws more mass flow. This increase in mass flow accelerates the flow into the duct, lowering the pressure upstream of the duct. From the surface pressures, the 25% throttle setting pressures compare relatively well to the OVERFLOW predicted pressures at the thrust required mass flow. This compares well to the duct pressures shown in Figure 86, indicating that a 30% throttle setting for the thrust required case is a reasonable throttle setting for comparison of the experimental and computational results. For the thrust available case, however, the 80% throttle setting pressures compare best to the OVERFLOW predicted pressures at the higher mass flow. This is slightly below the 90% throttle setting implied by the duct pressures shown in Figure 86. As previously discussed, since the duct pressures for the CFD are reliant on the accurate prediction of the cowl drag, a combination of the duct pressures and surface pressures are most likely a more accurate method of setting the throttle level. It should be noted that while the baseline model pressures appear to be well predicted by the CFD, the upper surface cowl pressures appear to be under predicted, further lending credence to the choice of a throttle setting based on a combination of the duct and model surface pressures. Based on the results shown in Figure 86 and Figure 87, a throttle setting of 30% was used to compare the experimental results to the CFD thrust required predictions, and a throttle setting of 80% was used to compare the experimental results to the CFD thrust available predictions.

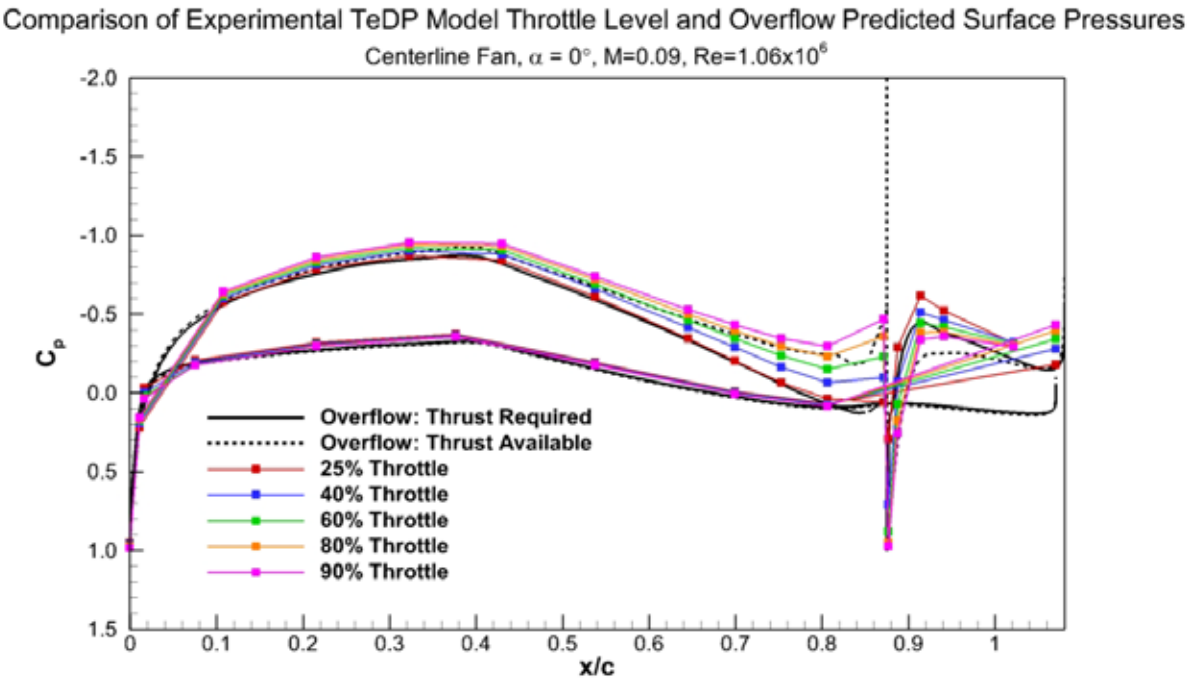

Figure 87: Effect of experimental TeDP model throttle level on centerline fan surface pressures, α=0°, M=0.09, Re=1.06x10^6.

7.4.2. Thrust Required Results

The first active thrust case investigated was the thrust required case. As discussed in Section 7.4.1, for the thrust required case, the throttle setting was set to 30%. A 30% throttle setting produced a fan RPM of approximately 33,000. For the thrust required case, an angle-of-attack polar from a=-2° to a=14° was run at M=0.09, Re=1.06x10^6. A plot showing a comparison between the experimental and OVERFLOW predicted force and moment results is shown in Figure 88.

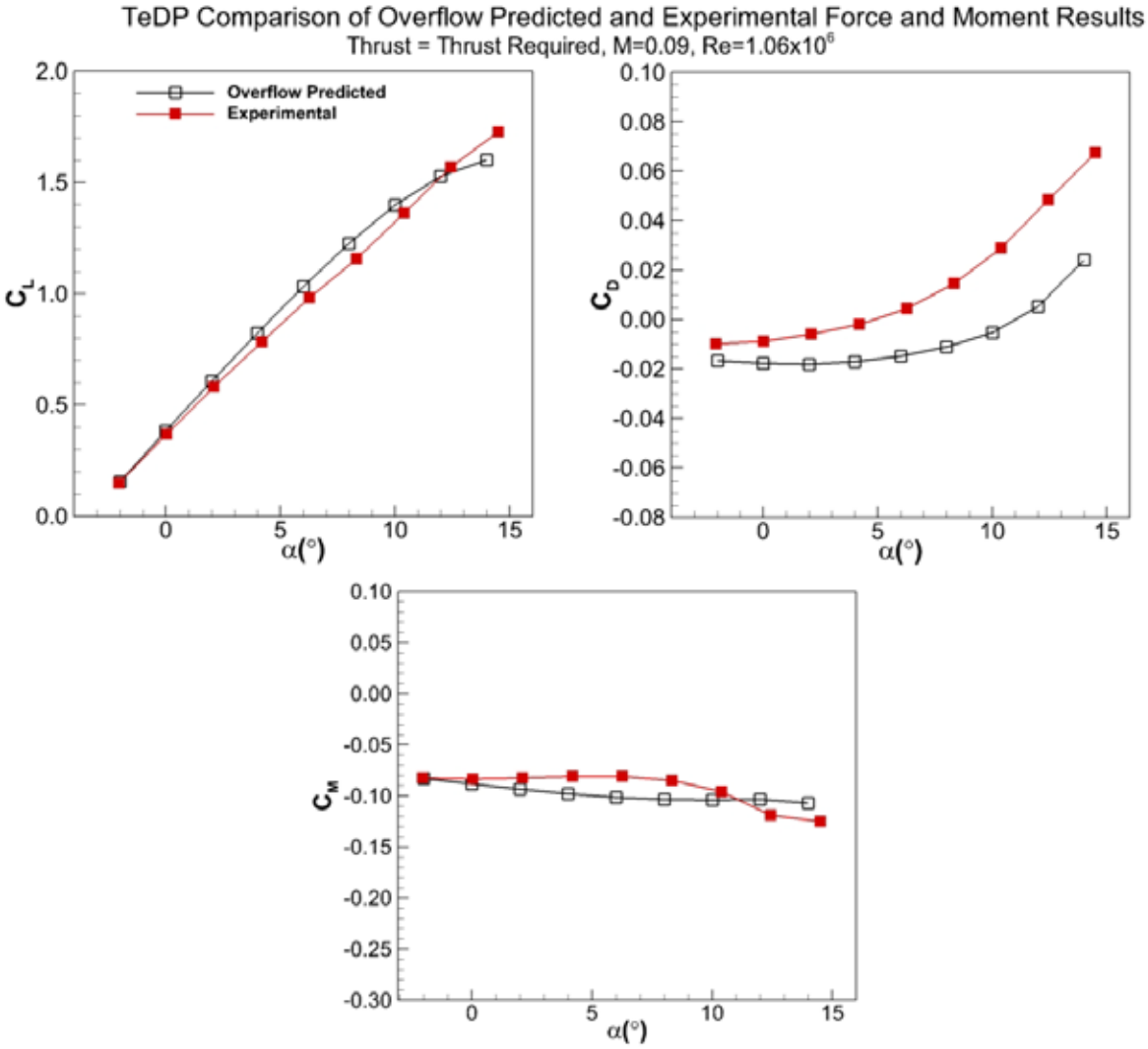

Figure 88: Comparison of TeDP model experimental and OVERFLOW predicted force and moment data for the thrust required mass flow case, M=0.09, Re=1.06x10^6.

It is important to note that the results shown in Figure 88 differ from those shown in Section 6 by the baseline model area of integration. For the results shown in Section 6, the force and moment integration is only over the 5 fan section of the model. The computational results shown in the experimental section, however, are integrated over a spanwise area which mimics the wind tunnel model, but do not include the side wall effects. From Figure 88, the lift curve results for the experimental data show a slightly reduced lift curve slope as compared to the CFD. At α=-2° and α =0°, the experimental and OVERFLOW predicted lift coefficients compare well. Above α=4°, the experimental lift coefficient under predicts the computational. At α=4°, the the computational results over predict the experimental by ΔC_L= 0.05, increasing to ΔC_L= 0.10 at α=8°, before the experimental lift coefficient increases above that of the computational. The loss in lift in the mid polar region might be due to several reasons, including the presence of local separation, the baseline model to either side of the TeDP center section, or sidewall effects. The drag results shown in Figure 88, as discussed above, are for the whole model span, and as a result show a less negative drag number than shown in Figure 57. At low angles-of-attack, the experimental drag is approximately 50% higher than the CFD predicted drag, with the discrepancy increasing with increasing angle-of-attack. The difference in drag can be attributed the presence of a combination of the motor wires present in the thrust stream and their routing on the lower surface of the model, and the tail cone opening to allow for motor cooling. The increase in discrepancy with increasing angle-of-attack would tend to indicate an increasing pressure or separation based drag. Again, some of the drag discrepancy might be due to the baseline section on either side of the TeDP center section. The moment results shown in Figure 88 compare well in overall level, but differ in shape with the experimental moment having a shallower slope with increasing angle-of-attack as compared to the computational predictions. Surface pressures for the centerline fan (#3 fan) as a function of angle-of-attack for the thrust required polar are shown in Figure 89.

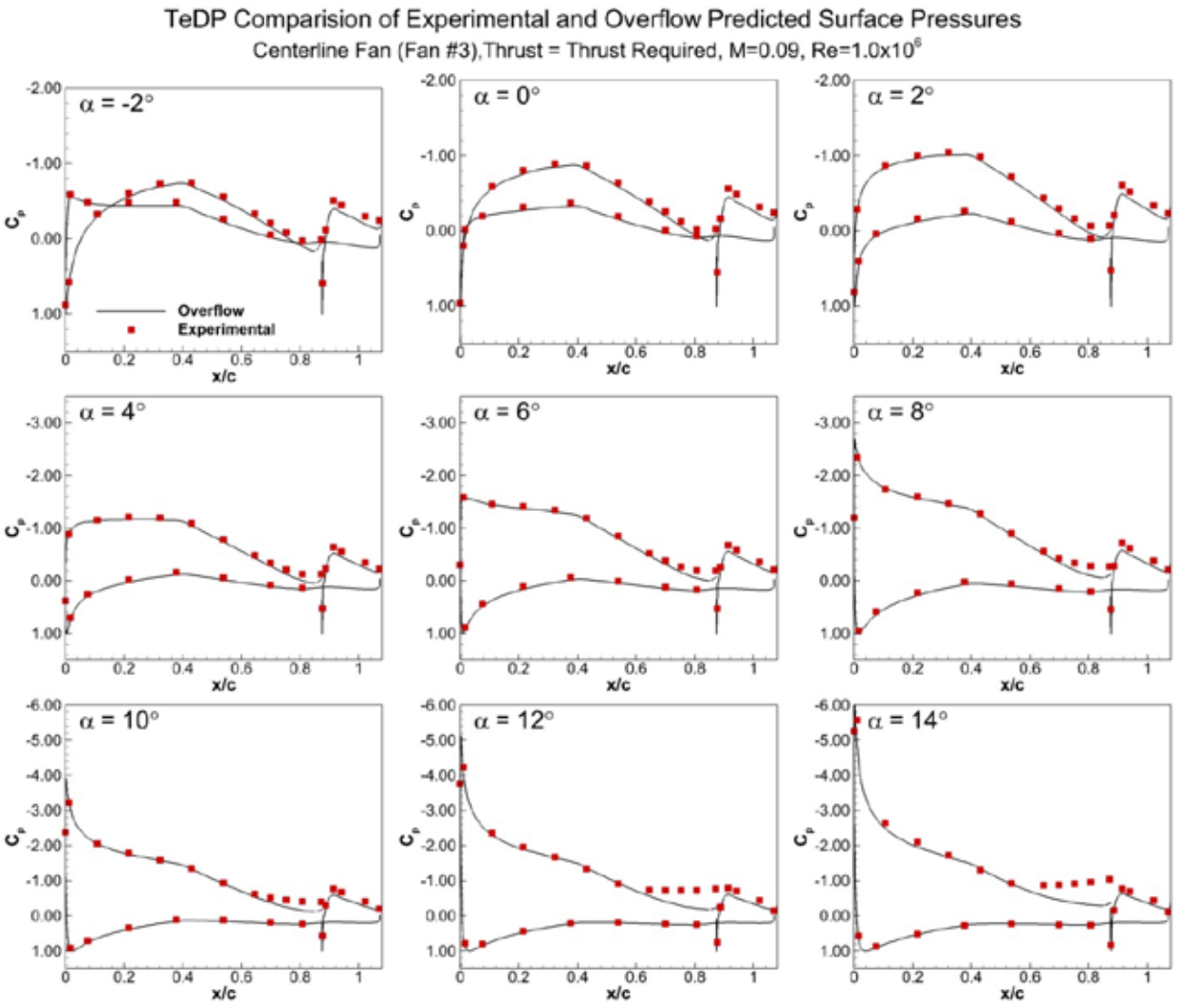

Figure 89: Comparison of TeDP model experimental and OVERFLOW predicted surface pressures as a function of a, thrust required mass flow, M=0.09, Re=1.06x10^6.

From Figure 89, the experimental and computational surface pressures compare relatively well, especially at the lower angles-of-attack. The main airfoil body pressures compare especially well. The upper surface cowl pressures are slightly more negative than the OVERFLOW predicted pressures. Beginning at a=4°, it appears that there is a growing area of local separation just upstream of the inlet that is not predicted by the CFD. Recall that for the thrust required case, the inlet is operating at below its design mass flow, creating back pressure and a more adverse pressure gradient upstream of the fan. This increased adverse gradient appears to be promoting some premature separation upstream of the fan at higher angles-of-attack. The inlet was designed for a combination of the thrust required and thrust available mass flows at a=0°. At a=8° and above, this separation upstream of the inlet is clearly apparent. This separation upstream of the inlet might be responsible for the differences in the lift curve and large increase in drag at higher angles-of-attack shown in Figure 88. It is interesting to note,

however, that the cowl upper surface appears to remain attached, even at high a. The cowl most likely remains attached due to the fan jet Coanda effect upon the cowl. It is also interesting to note that since the separation does not extend to the trailing-edge, it does not appear to affect the leading-edge suction peak. For a traditional airfoil with trailing-edge separation, the suction peak would also be reduced. Surface pressures for the three individual fans at angles-of-attack of 0°, 4°, and 8° are shown in Figure 90 for the thrust required polar.

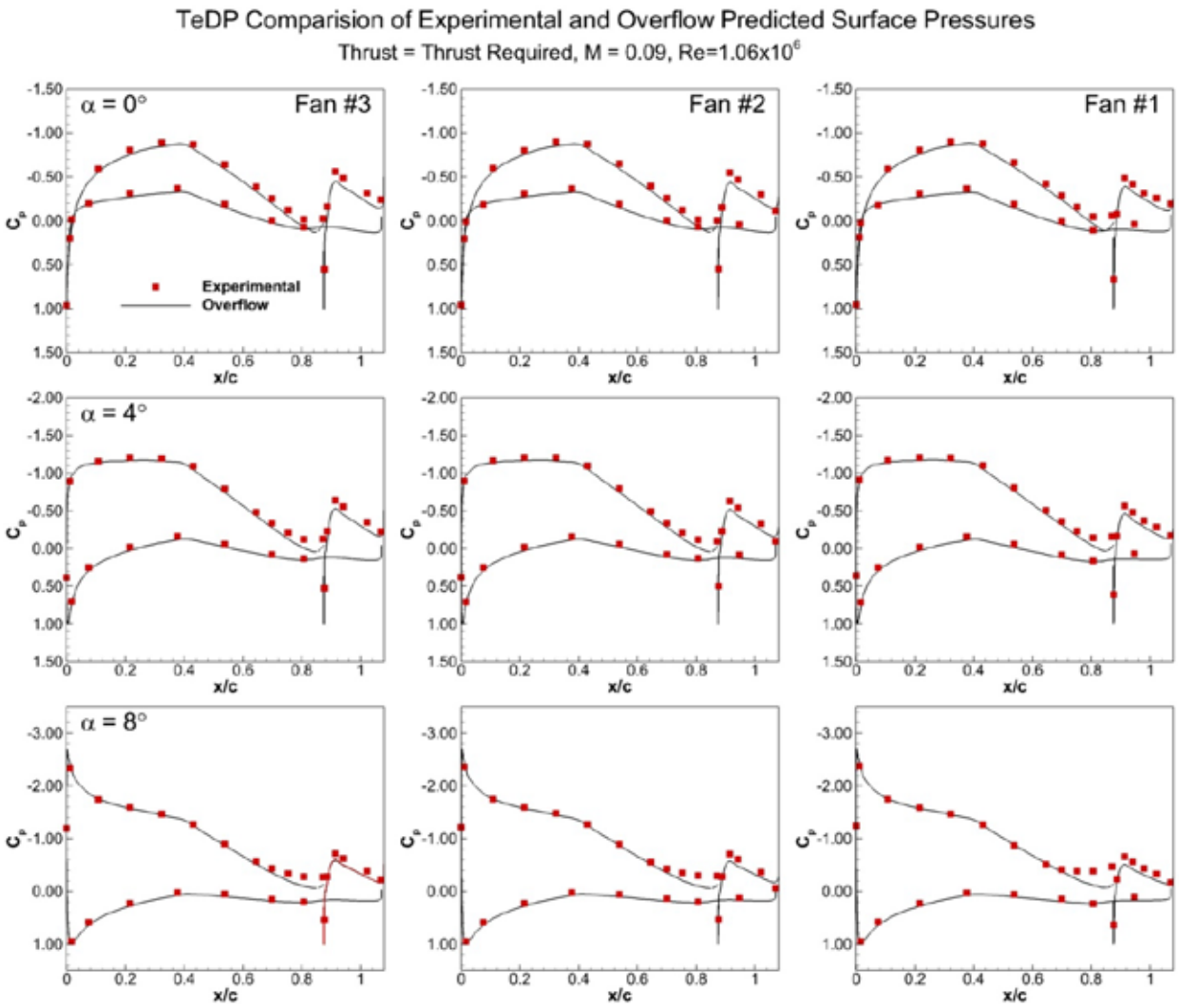

Figure 90: Comparison of TeDP model experimental and OVERFLOW predicted fan to fan surface pressures at a=0°, 4°, 8°, thrust required mass flow, M=0.09, Re=1.06x10^6.

From Figure 90, no large spanwise differences in the surface pressures are observed. Again, the experimental and computational surface pressures compare well. The mild separation upstream of the inlet is present for each of the three fans shown. For the #1 fan which borders the baseline airfoil section which is known to exhibit trailing-edge separation beginning at a=8°, the separated region upstream of the inlet appears to be slightly larger at 8°, as compared to the #2

and #3 fans. This increase in separation is a result of the inlet flowfield interacting with the baseline airfoil section flowfield. This interaction was also observed in the computational results.

For the thrust required case, the average fan power consumption was approximately 150 Watts. A plot showing the fan power consumption as a function of angle-of-attack for the #1, #2, and #3 fans is shown in Figure 91. From Figure 91, a slight power consumption increase of approximately 2% was observed between the low and high angles-of-attack. This power increase also appears to be fairly linear. This increase in power may be attributed to the thickening of the boundary-layer and separation growth upstream of the inlet lowering the effective inlet velocity, resulting in a higher fan power to obtain a given throttle setting/RPM.

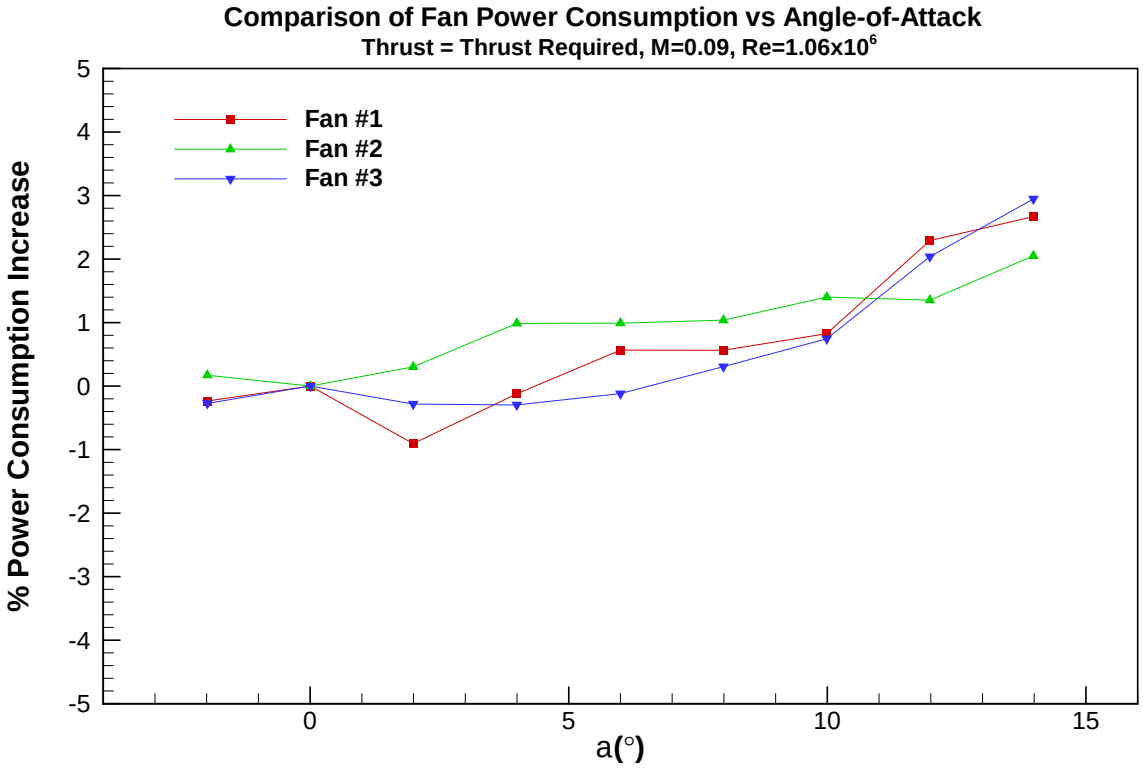

Figure 91: Comparison of fan power consumption as a function of angle-of-attack for the thrust required mass flow, M=0.09, Re=1.06x10^6.

Overall, noting the complexity of the CFD model, the experimental and computational results compare relatively well. The CFD does not predict the separation upstream of the inlet. Noting the performance of the CFD in predicting the baseline airfoil separation in Figure 15, this is not wholly unexpected. It should be noted, that in an actual flying aircraft, as the angle-of-attack is increased, the throttle, and fan mass flow, would also be increased to maintain level flight due to the increase in drag. This increase in mass flow would most likely significantly reduce, or eliminate the presence of the separation. A moveable inlet lip would also eliminate the separation.

7.4.3. Thrust Available Results

After running the thrust required mass flow case, the thrust available case was investigated. As discussed in Section 7.4.1, the throttle setting was set to 80% for the thrust available case. An 80% throttle setting produced a fan RPM of approximately 42,500. As was done for the thrust required case, an angle-of-attack polar from α=-2° to a=14° was run at M=0.09, Re=1.06x10^6 was run for the thrust available case. A plot showing a comparison between the experimental and OVERFLOW predicted force and moment results for the thrust available case is shown in Figure 92. Also included in Figure 92 are the experimental and computational thrust required results from Figure 88 for comparison.

From Figure 92, the lift drag and moment results for the thrust available setting mimic those observed for the thrust required case. For the lift curve results, however, the experimental thrust available results compare better to the CFD predictions. At α=-2° and α =0°, the experimental and OVERFLOW predicted lift coefficients compare very well. Above α=4°, the computational lift coefficient again over predicts the experimental, but by a significantly smaller level. At α=4°, the computational results over predict the experimental by ΔC_L= 0.03, increasing to ΔC_L= 0.055 at α=8°, before the experimental lift coefficient again increases above that of the computational. The decrease in discrepancy in the mid polar region between the thrust required and thrust available cases is clearly tied to the fan mass flow. The increased fan mass flow for the thrust available case might be reducing the separation upstream of the inlet or having a more positive interaction with the baseline section on either side of the TeDP fan section. The difference between the CFD lift coefficients at α=4° is ΔC_L=0.04 for the thrust available and thrust required cases. This difference remains relatively constant with angle-of-attack for the computational data. The difference between the experimental lift coefficients for the thrust required and thrust available cases at α=4° is ΔC_L=0.06, growing to ΔC_L=0.09 at α=8°.

The drag results shown in Figure 92 follow the same trends as for the thrust required case. At low angles-of-attack, the thrust available experimental drag compares better to the computational predictions, with the computational results predicting a only a 9% lower drag at α=-2° to 0°. As was seen with the thrust required data, as the angle-of-attack increases the drag increases at a quicker rate than the computational prediction. The increased drag for the experimental results can be partially attributed to the presence of the motor wires in the thrust stream and their routing on the lower surface of the model, and the tail cone opening to allow for motor cooling. The thrust available moment results compare as well to the computational predictions as the thrust required results did, and show similar trends. Surface pressures for the centerline fan (#3 fan) as a function of angle-of-attack for the thrust required polar are shown in Figure 93.

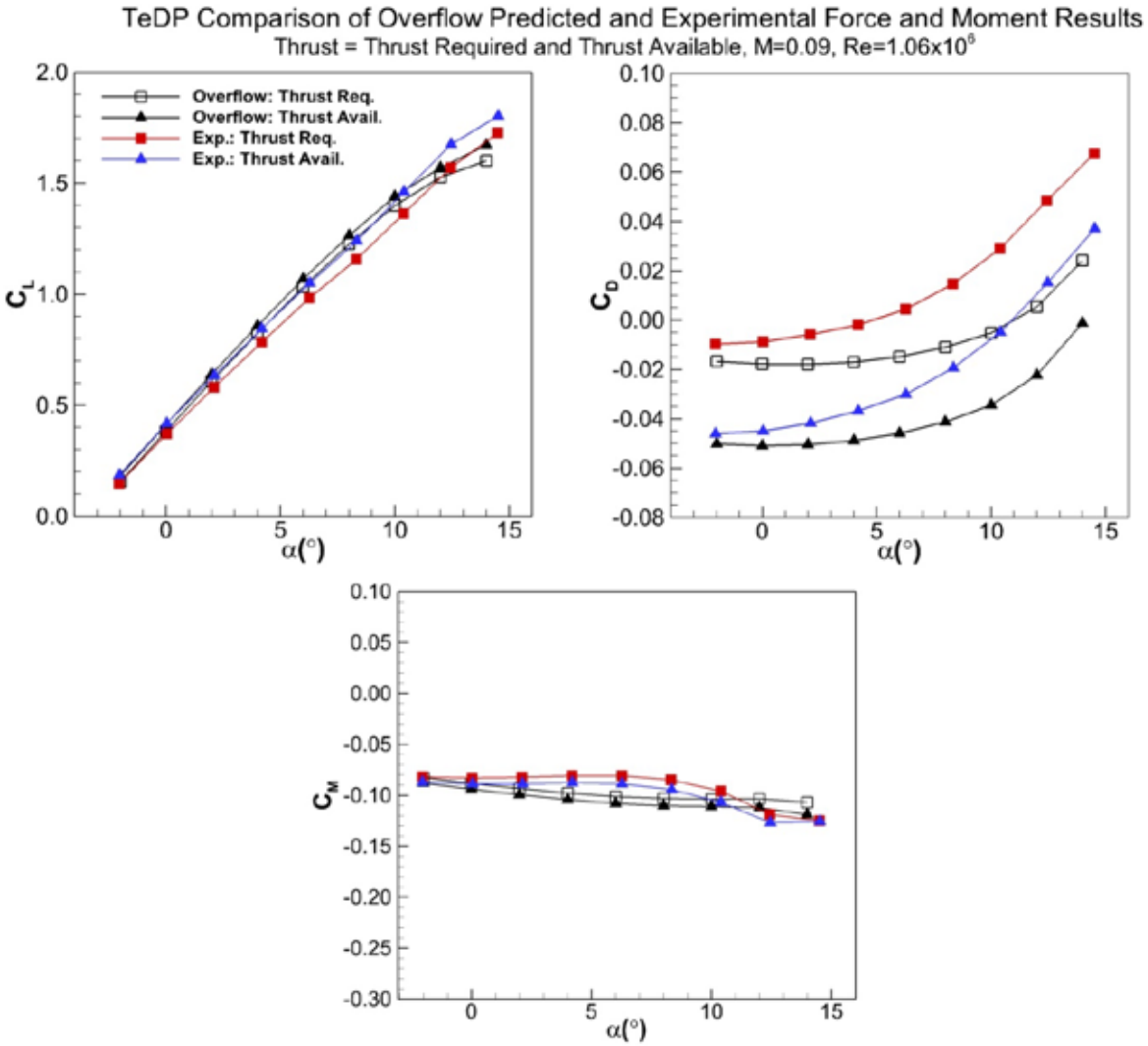

Figure 92: Comparison of TeDP model experimental and OVERFLOW predicted force and moment data for the thrust required and thrust available mass flow cases, M=0.09, Re=1.06x10^6.

From Figure 93, as was observed for the thrust required pressures shown in Figure 89, the experimental and computational surface pressures for the thrust available case compare relatively well. Again, the main airfoil body pressures compare especially well with the upper surface cowl pressures being slightly more negative than the OVERFLOW predicted pressures. The small separated region just upstream of the inlet beginning at a=4° for the thrust required data is not present in the thrust available results up through a=8°, and is not clearly discernable to a=12°. The increased mass flow of the thrust available case is accelerating the flow into the duct, reducing the magnitude of the adverse pressure gradient experienced at the lower mass flow thrust required case. Again, the cowl upper surface appears to remain attached up though a=14°.

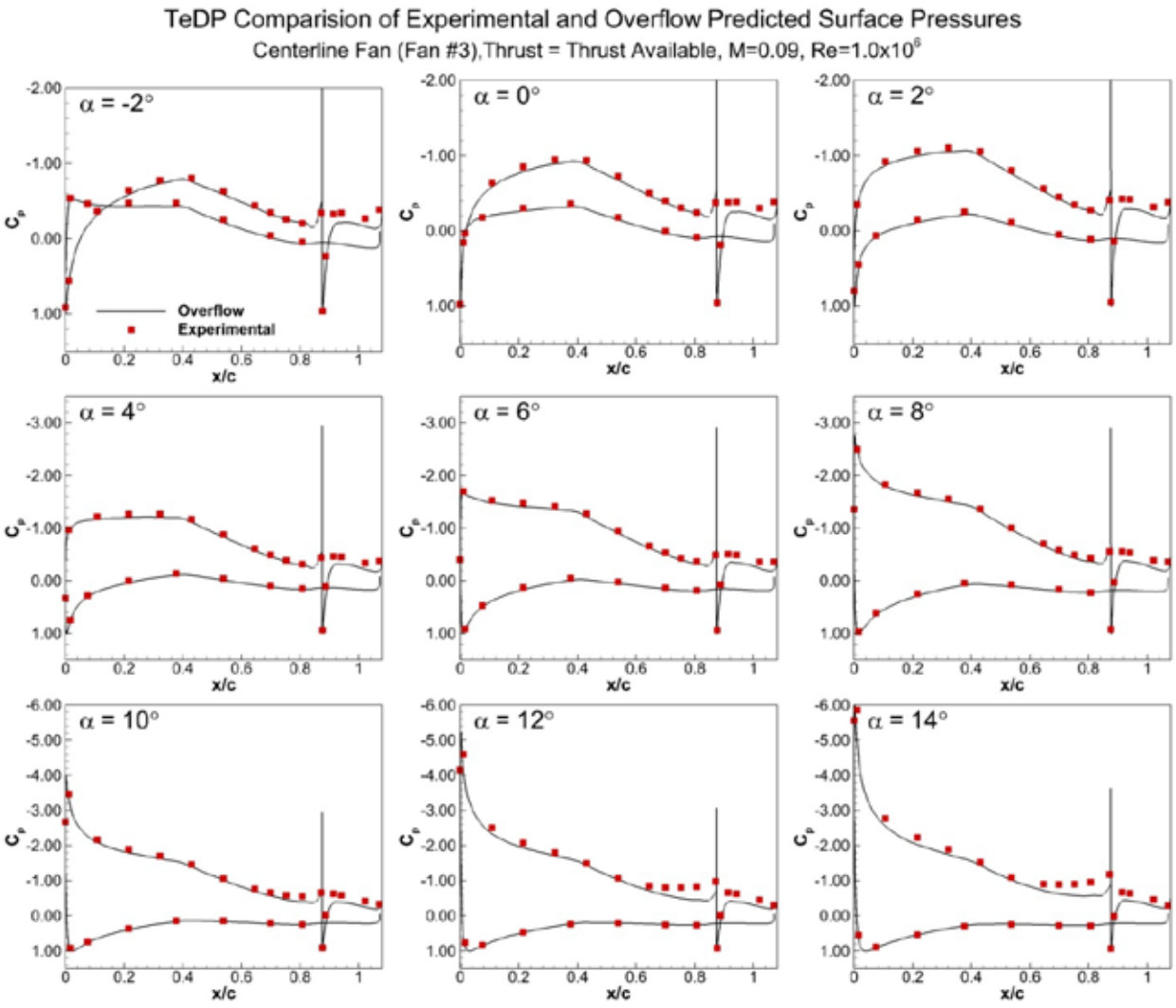

Figure 93: Comparison of TeDP model experimental and OVERFLOW predicted surface pressures as a function of a, thrust available mass flow, M=0.09, Re=1.06x10^6.

Surface pressures for the three individual fans at angles-of-attack of 0°, 4°, and 8° are shown in Figure 94 for the thrust available polar. The thrust available fan-to-fan pressures compare well to the computational predictions. No significant fan-to-fan differences are evident in the pressures. As was observed for the thrust required pressures, at a=8°, the #1 fan separation upstream of the inlet is slightly larger than for the #2 or #3 fans. This slight increase in the separation for the #1 fan is due to its interaction with the baseline section trailing-edge separation which begins to appear at a=8°.

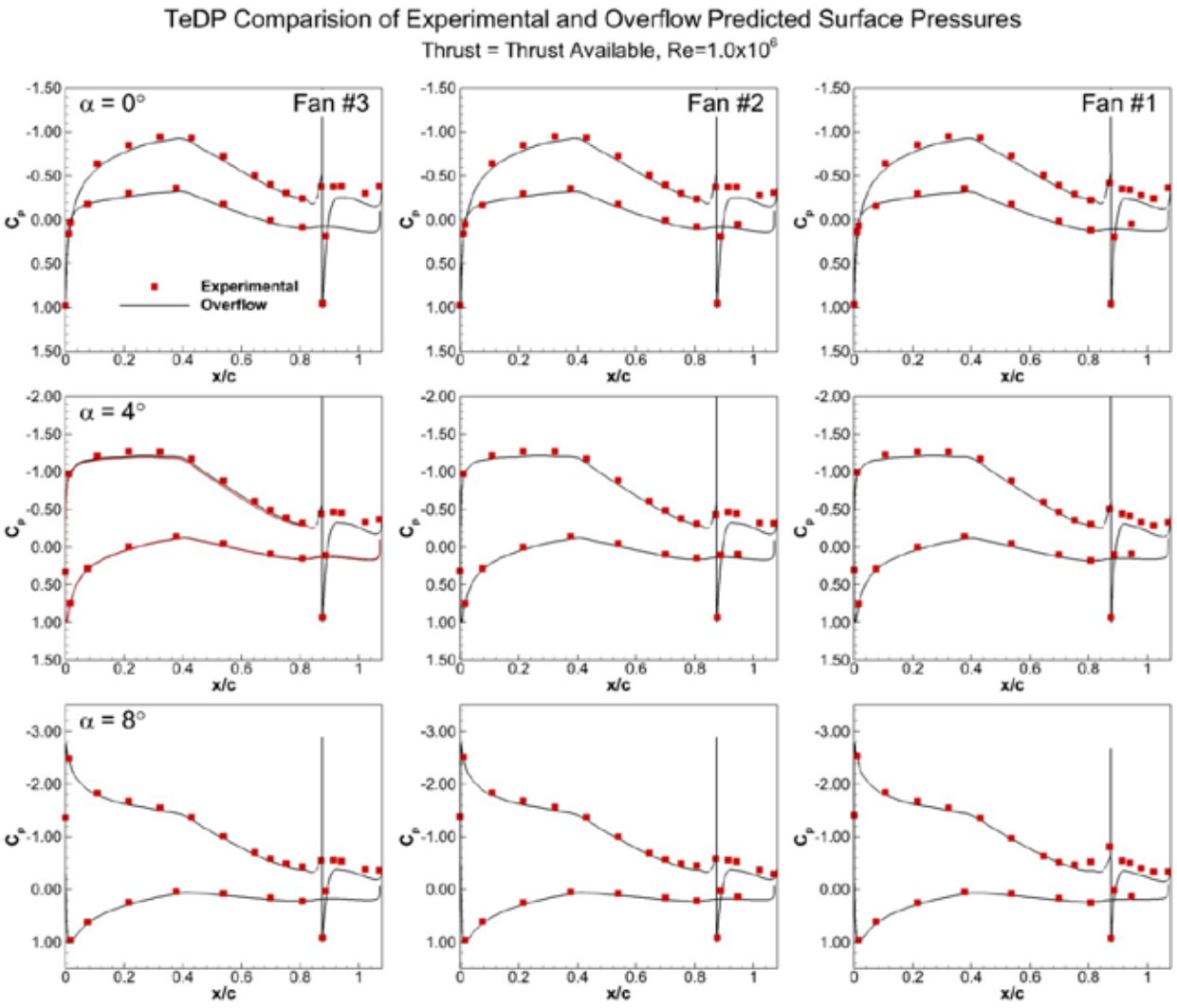

Figure 94: Comparison of TeDP model experimental and OVERFLOW predicted fan-to-fan surface pressures at a=0°, 4°, 8°, thrust required mass flow, M=0.09, Re=1.06x10^6.

For the thrust required case, the average fan power consumption was approximately 290 Watts. A plot showing the fan power consumption as a function of angle-of-attack for the #1, #2, and #3 fans is shown in Figure 95. The results shown in Figure 95 show a different trend than that observed for the thrust required case. Unlike the thrust required case, there appears to be a different behavior between the #1 and #2 fans, and the #3 fan. The behavior of the #3 fan mimics that observed for the thrust required case, but to a lesser extent. The #3 fan power only increases by 1.4%, with a shallower slope at lower angles-of-attack. The #1 and #2 fans, however, show an opposite behavior, with decreasing power at angles-of-attack above a≈8°. Below 10°, no separation is apparent upstream of the ducts for the thrust available case. Above 10°, a slight separation is present, with a larger separation present for the #1 fan at a=14°, which shows the largest drop off in fan power. If separation upstream of the duct results in a lower average inlet velocity, causing the fan to work harder to maintain a given RPM, this would seem

to be at odds with the data shown Figure 95 for the thrust available case as compared to the results shown in Figure 91 for the thrust required case. Based solely on the flowfield, the biggest difference between these two cases is the fact that the thrust required case produces blockage upstream of the fan with the thrust available case accelerating the flow into the fan. This difference in blockage affects the amount of separation upstream of the duct, with the thrust required case having a significantly larger amount.

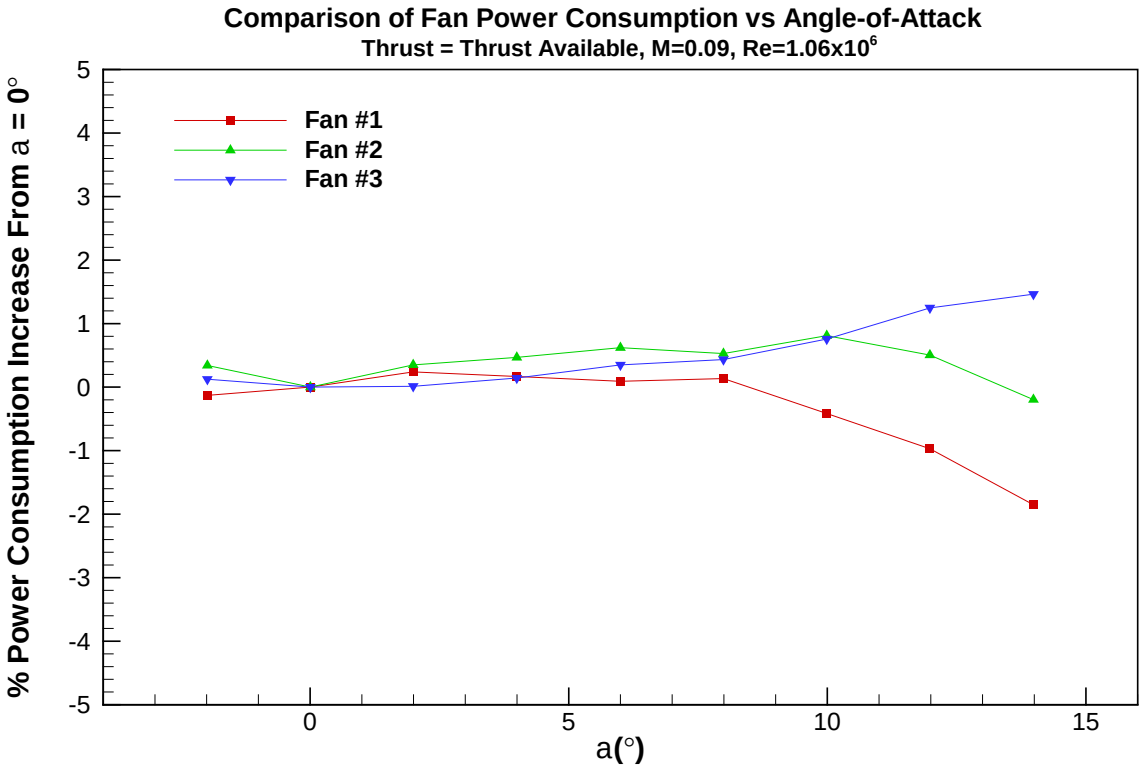

Figure 95: Comparison of fan power consumption as a function of angle-of-attack for the thrust available mass flow, M=0.09, Re=1.06x10^6.

Results observed for the experimental thrust available data compare relatively well to the computational results. The lift curve results for the thrust available data compare better to the computational predictions than the thrust required results. This is also true for the surface pressures. The better comparison between the thrust available data can be attributed to the increased fan mass flow creating a less severe adverse pressure gradient into the fan, significantly reducing the amount of local separation upstream of the fan.

7.4.4. Windmill Results

Polar data were also taken with the fans allowed to windmill at a zero power setting. As discussed in the CFD results Section 6, the windmill results for the computational predictions are most likely optimistic due to the fact that the fan blades are not modelled in the CFD. For the experimental data, the free-stream speed of 100 ft/s did not provide sufficient dynamic pressure

to cause the fans to rotate. As a result, the blockage created by the windmilling fans is significantly larger than that modelled computationally. This was somewhat unexpected as the Phase I Schuebeler fans were observed to rotate at the windmill condition. A plot showing the windmilling force and moment results as compared to the CFD predictions is shown in Figure 96.

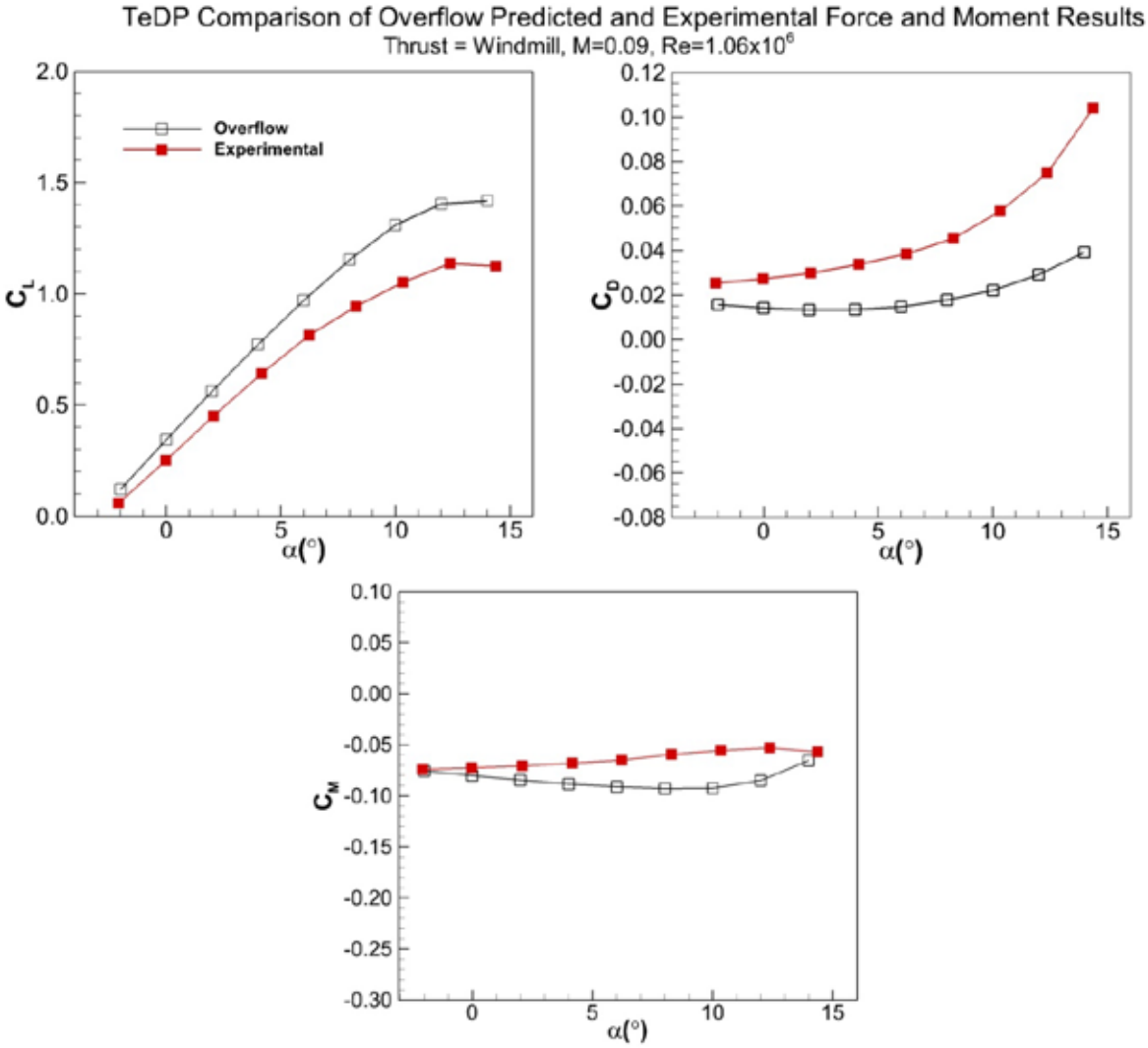

Figure 96: Comparison of TeDP model experimental and OVERFLOW predicted force and moment data for the windmill case, M=0.09, Re=1.06x10^6.

From Figure 96, the increased blockage for the experimental data is evident in both the significantly reduced lift results and the almost 100% increase in drag at low angles-of-attack as compared to the computational predictions. This large increase in blockage for the windmill case should make the differential thrust settings interesting. Surface pressures for the three individual fans at angles-of-attack of 0°, 4°, and 8° are shown in Figure 97 for the windmill polar.

From Figure 97, the large blockage created by the windmill fans is evident in the large amount of separation upstream of the fans. Considering the amount of separation, the experimental and computational results compare well. It is interesting to note that the upper surface cowl pressures are better predicted for the separation dominated windmill case than for either the thrust required or thrust available cases discussed in Section 7.4.2 and Section 7.4.3. It is also interesting to note the leading-edge suction pressures at a=8°. For the thrust required and thrust available cases, at higher angles-of-attack were separation was present upstream of the duct, no drop in leading-edge suction pressure was observed. For the windmill case, this loss of leading-edge suction typically present for sections with significant trailing-edge separation is clearly present. The jet mass flow effect for the thrust required and available cases is keeping the upper cowl attached due to the fan jet Coanda effect, allowing the leading-edge suction pressures to remain high.

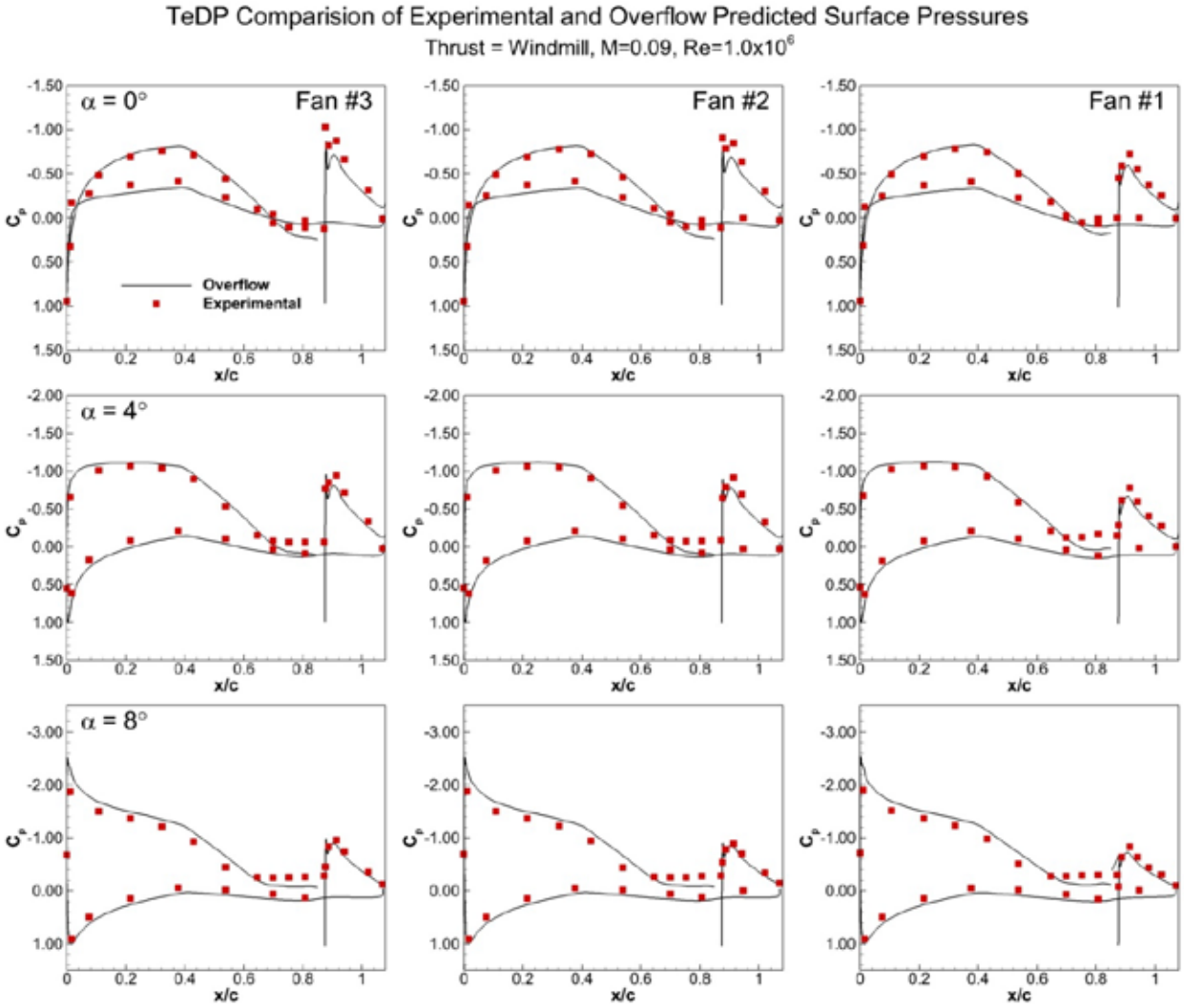

Figure 97: Comparison of TeDP model experimental and OVERFLOW predicted fan-to-fan surface pressures at a=0°, 4°, 8° for the windmill case, M=0.09, Re=1.06x10^6.

7.4.5. Differential Thrust Results

After completing the baseline thrust required and thrust available tests, differential thrust runs were made. Five individual differential thrust configurations were investigated. The different differential thrust cases run are shown in Table 7. All of the differential thrust cases were run at an abbreviated polar schedule of α=0°, 4°, 8°, and 12°, M=0.09, Re=1.06x10^6.

	Fan #5	Fan #4	Fan #3	Fan #2	Fan #1
Thrust Level	T_r	T_r	T_r	T_r	Windmill
	T_a	T_a	T_a	T_a	Windmill
	T_a	T_a	T_a	T_a	T_r
	T_r	T_r	T_r	Windmill	Windmill
	T_r	T_r	Windmill	T_r	T_r

Table 7: Differential thrust cases investigated.

7.4.5.1. T_r T_r T_r T_r Windmill Results

The first differential thrust case investigated was the baseline thrust required case where the #1 fan was set to the windmill condition, with fans #2-#5 set at the thrust required setting. Force and moment results for the thrust required/windmill case at M=0.09, Re=1.06x10^6 are shown in Figure 98.

Also shown in Figure 98 are the computational predictions and the baseline thrust required results discussed in Section 7.4.2. From Figure 98, the lift curve results show a small loss in C_L between the baseline thrust required data and the differential thrust results. The CFD predicted loss is ΔC_L=-0.015, whereas the experimental loss is ΔC_L=-0.030. The increased loss due to the windmilling fan for the experimental data is a result of the significantly increased blockage provided by the fan blades that were not present in the CFD simulation. The loss in C_L appears to be relatively constant with increasing angle-of-attack, growing slightly at α=8°.

The drag results show a similar trend between the CFD and the experimental data with an as expected increase in drag with the windmilling fan. The experimental drag increases by a fairly constant increment of approximately 100 counts. The moment results show a negligible effect for the differential thrust case. For the force and moment results, other than a slight loss in lift for the model, the most significant impact is a large increase in drag. Surface pressures for the three individual fans at angles-of-attack of 0°, 4°, and 8° are shown in Figure 99 for the differential thrust required results. Also included in Figure 99 are the computational predictions and the baseline thrust required pressures for comparison.

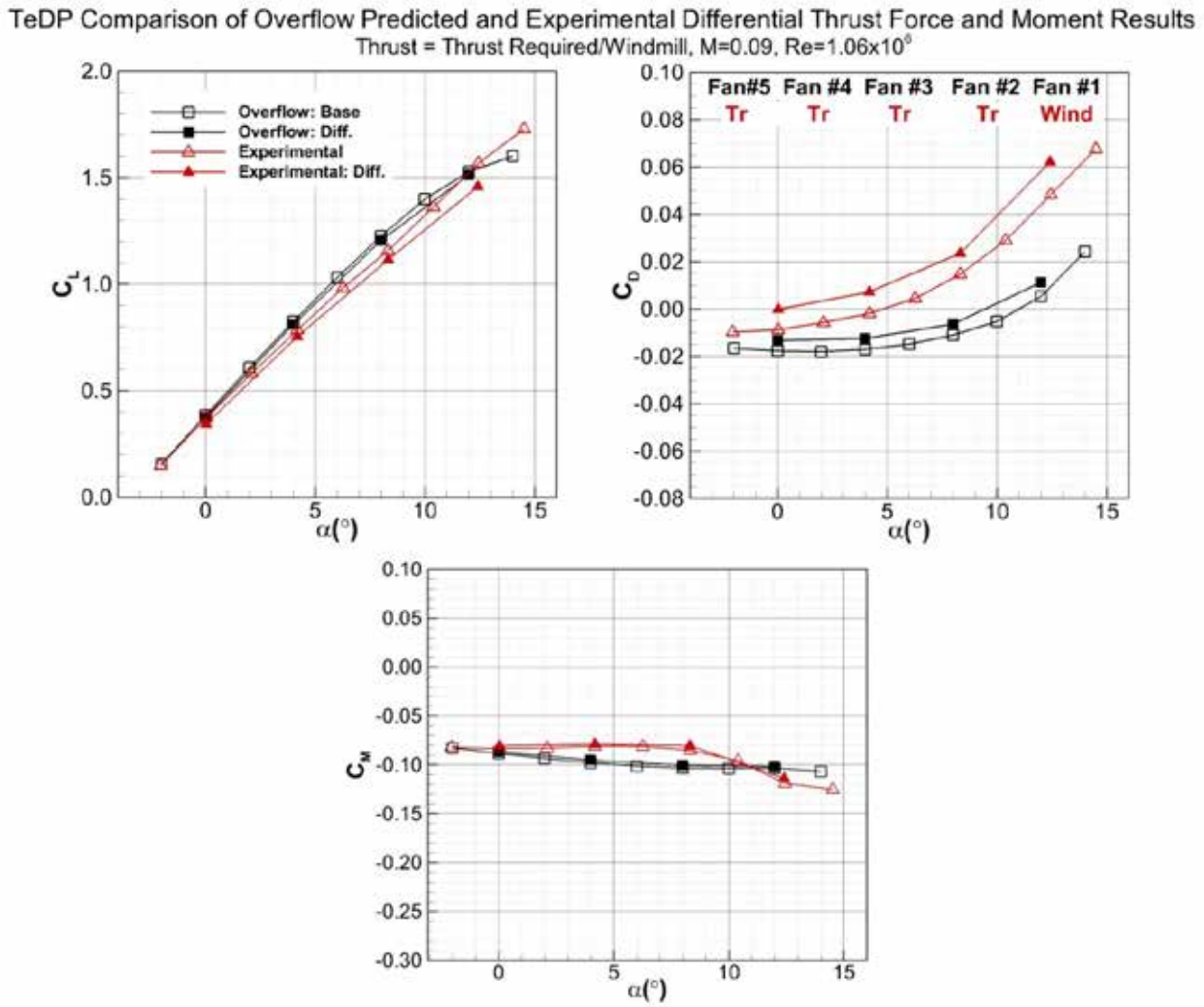

Figure 98: Comparison of TeDP OVERFLOW predicted and experimental differential thrust force and moment results for the thrust required/windmill case, M=0.09, Re=1.06x10^6.

From Figure 99, as with the baseline thrust required case, the computational results compare well to the differential pressures with the exception of the under prediction of the level of separation upstream of the windmilling #1 fan. Pressures for the #2 and #3 fans are well predicted by the CFD. The #2 fan pressures upstream of the inlet are clearly affected by the windmilling #1 fan blockage. The separation upstream of the #2 fan is increased by the #1 fan spillage. Of significant note, however, is that the effect of the #1 windmilling fan only affects the adjacent #2 fan. The presence of the windmilling #1 fan does not appear to have an effect upon the centerline #3 fan. As evidenced by the computational pressures and discussed in Section 6.7, both the experimental and CFD predictions indicate that the effect of the blockage produced by the windmilling fan is confined to the adjacent fan. For the thrust required mass flow, the effect of the windmilling fan on the #2 fan is limited to the flow just upstream of the inlet. A plot showing the fan power consumption as a function of angle-of-attack for the #1, #2, and #3 fans for the differential thrust required case is shown in Figure 100.

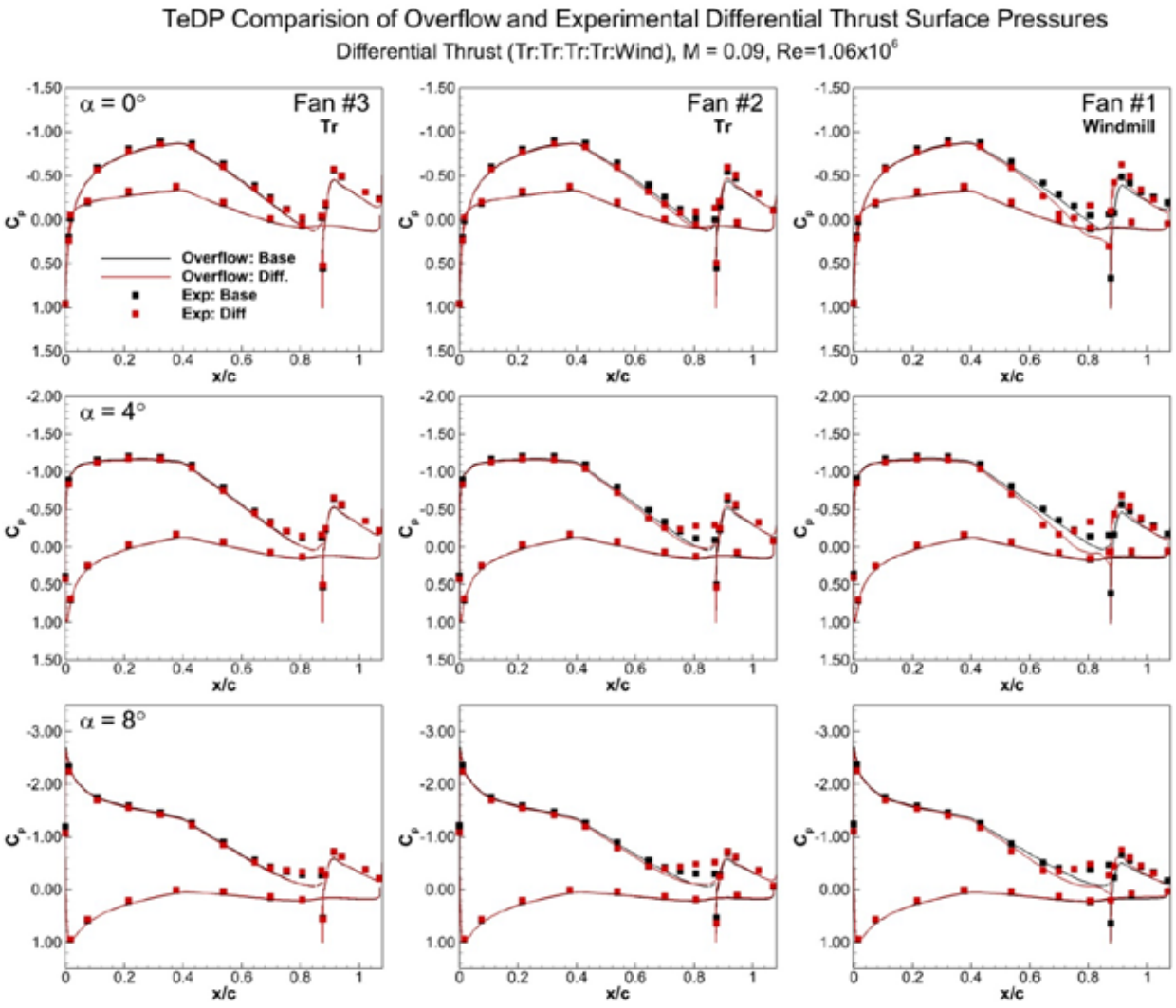

Figure 99: Comparison of OVERFLOW and experimental surface pressures for a centerline cut for Fans #1 to #3 for the baseline thrust required and differential thrust required/windmill case, α=0°, 4°, 8°, M_{∞}=0.09, Re=1.06x10^6.

Also included in Figure 100 are the power consumption results for the baseline thrust required case. Since the #1 fan is windmilling and not consuming any power, only power consumption results for the #2 and #3 fans are shown. From Figure 100, no noticeable effect on the power consumption for the windmilling fan is discernable in the neighboring #2 fan. The absolute magnitude of the change in power consumption is small for both cases, and any change in power consumption might be buried within the overall measurement noise for the amperage sensor. Sectional lift coefficients integrated from the surface pressures for the differential thrust case are shown in Figure 101.

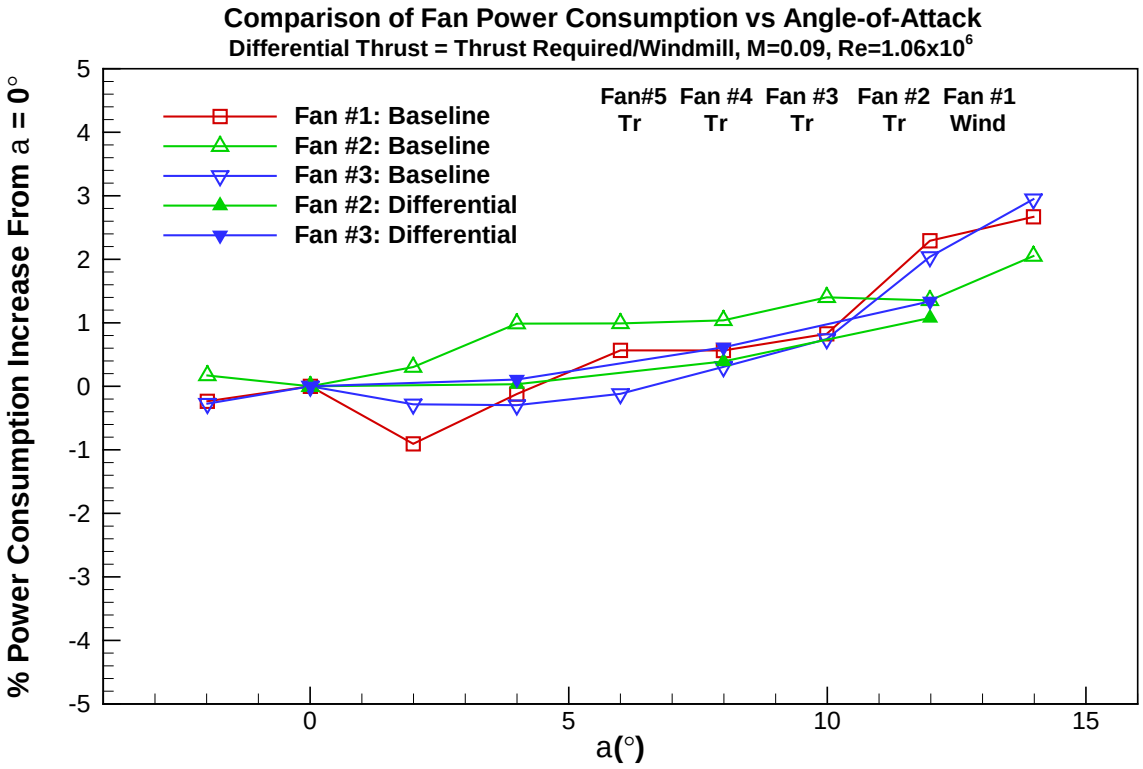

Figure 100: Comparison of fan power consumption as a function of angle-of-attack for the differential thrust required/windmill case, M=0.09, Re=1.06x10^6.

From Figure 101, no significant difference in sectional lift coefficient is observed at the lower angles-of-attack. At α=12°, the sectional lift coefficient for the windmilling #1 fan is observed to drop. The loss in C_l for the windmilling fan is ΔC_l = -0.130. This loss in lift coefficient is confined to the windmilling fan. Although differences in the pressures are observed in the #2 fan results shown in Figure 99, the differences are small. These small differences, combined with the limited number of taps to integrate, make the small changes in pressures hard to distinguish after integration.

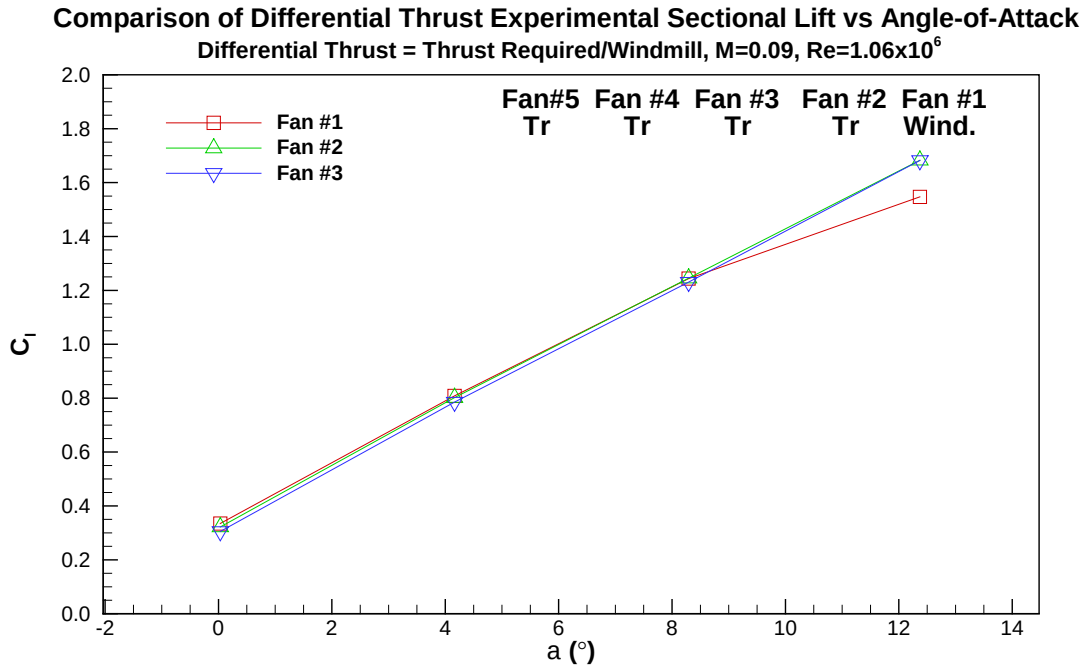

Figure 101: Comparison of differential thrust experimental sectional lift versus angle-of-attack for the thrust required/windmill case, M=0.09, Re=1.06x10^6.

7.4.5.2. T_a T_a T_a T_a Windmill Results

After completing the thrust required differential thrust runs, the thrust available differential case was run. For the thrust available differential case the #1 fan was set to the windmill condition, with fans #2-#5 set at the thrust available setting. Force and moment results for the thrust required/windmill case at M=0.09, Re=1.06x10^6 are shown in Figure 102.

Also shown in Figure 102 are the computational predictions and the baseline thrust available results discussed in Section 7.4.3. The differential thrust results for the thrust available case mimic those observed for the thrust required case. From Figure 102, the lift curve results show a small loss in C_L between the baseline thrust available data and the differential thrust results. This loss is slightly larger for the thrust available case than was observed for the thrust required results. The CFD predicted loss is ΔC_L=-0.030, whereas the experimental loss is ΔC_L=-0.050. The increased loss between the thrust required and thrust available cases is due to the increase in the blockage delta between the thrust required and windmill fan and the thrust available and windmill fan. Unlike the thrust required results, the loss in C_L appears to increase slightly with increasing angle-of-attack.

The drag results shown in Figure 102 also mimic those observed for the thrust required results. The drag delta between the baseline thrust available data and the differential case has increased from ≈100 counts for the thrust required case to ≈150 counts for thrust available case. Again, the

delta between the baseline thrust available data and the differential data remains fairly constant with angle-of-attack. As with the thrust required results, the differential thrust setting has no effect upon the moment. Surface pressures for the three individual fans at angles-of-attack of 0°, 4°, and 8° are shown in Figure 103 for the differential thrust available results. Also included in Figure 103 are the computational predictions and the baseline thrust available pressures for comparison.

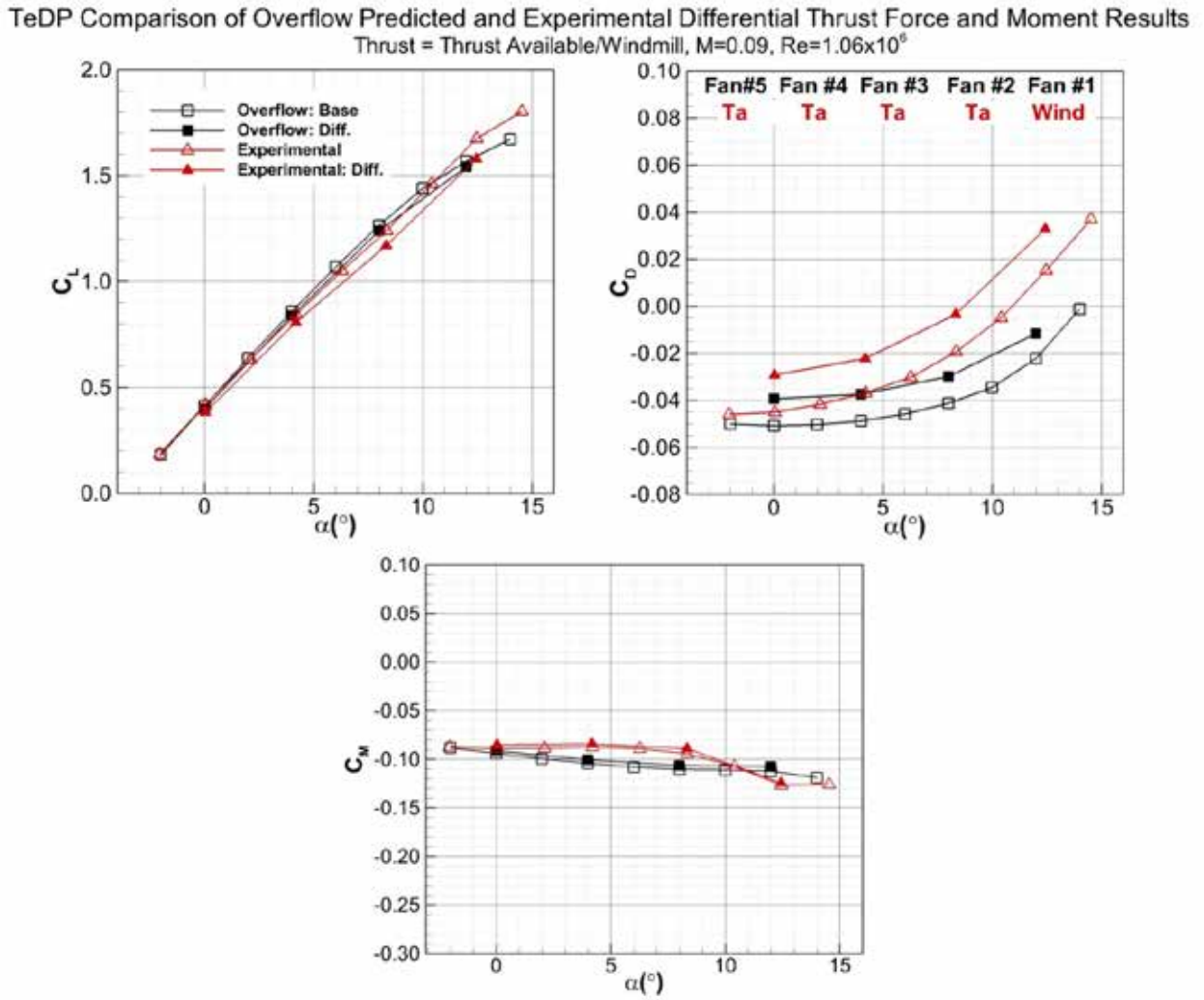

Figure 102: Comparison of TeDP OVERFLOW predicted and experimental differential thrust force and moment results for the thrust available/windmill case, M=0.09, Re=1.06x10^6.

From Figure 103, again the computational results compare well to the differential run pressures, especially for the lower angles-of-attack. The amount of separation upstream of the inlet is under predicted by the CFD, as has been observed throughout this study. As was observed in the thrust required results, the #2 fan pressures upstream of the inlet are clearly affected by the windmilling #1 fan blockage for the thrust available data. The separation upstream of the #2 fan is increased by the #1 fan spillage to an extent greater than that seen in the thrust required results. Again, the

effect of the #1 fan windmilling only affects the adjacent #2 fan. The presence of the windmilling #1 fan does not have an effect upon the centerline #3 fan. The effect of the blockage produced by the windmilling fan is confined to the adjacent fan. Also, the effect of the windmilling fan on the #2 fan is limited to the flow just upstream of the inlet. A plot showing the fan power consumption as a function of angle-of-attack for the #1, #2, and #3 fans for the differential thrust available case is shown in Figure 104.

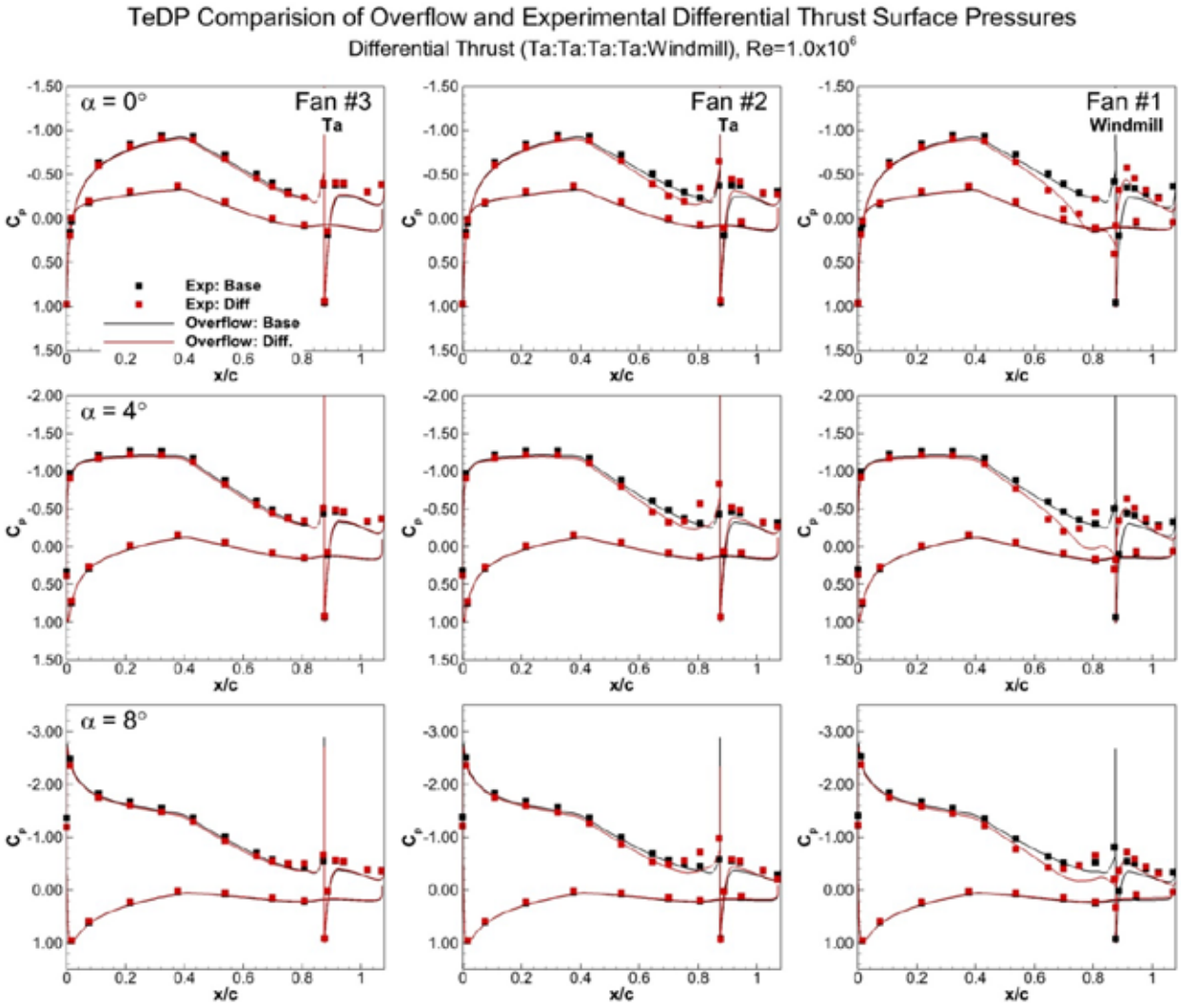

Figure 103: Comparison of OVERFLOW and experimental surface pressures for a centerline cut for Fans #1 to #3 for the baseline thrust available and differential thrust available/windmill case, α=0°, 4°, 8°, M_{∞}=0.09, Re=1.06x10^6.

Also included in Figure 104 are the power consumption results for the baseline thrust available case. Again, since the #1 fan is windmilling and not consuming any power, only power consumption results for the #2 and #3 fans are shown. From Figure 104, the power consumption for the #2 fan is reduced at a=12° as compared to the baseline thrust available results. While the trend is similar between the baseline thrust available and the differential results with the power

consumption dropping for the #2 fan at a=12°, the drop in the differential power consumption would appear to be above the noise level for the measurement. Again, the absolute magnitude of the change in power consumption is small for both cases. The difference in the rise in consumption for the thrust required case and drop in consumption for the thrust available case is not well understood at this point. Sectional lift coefficients integrated from the surface pressures for the differential thrust available case are shown in Figure 105.

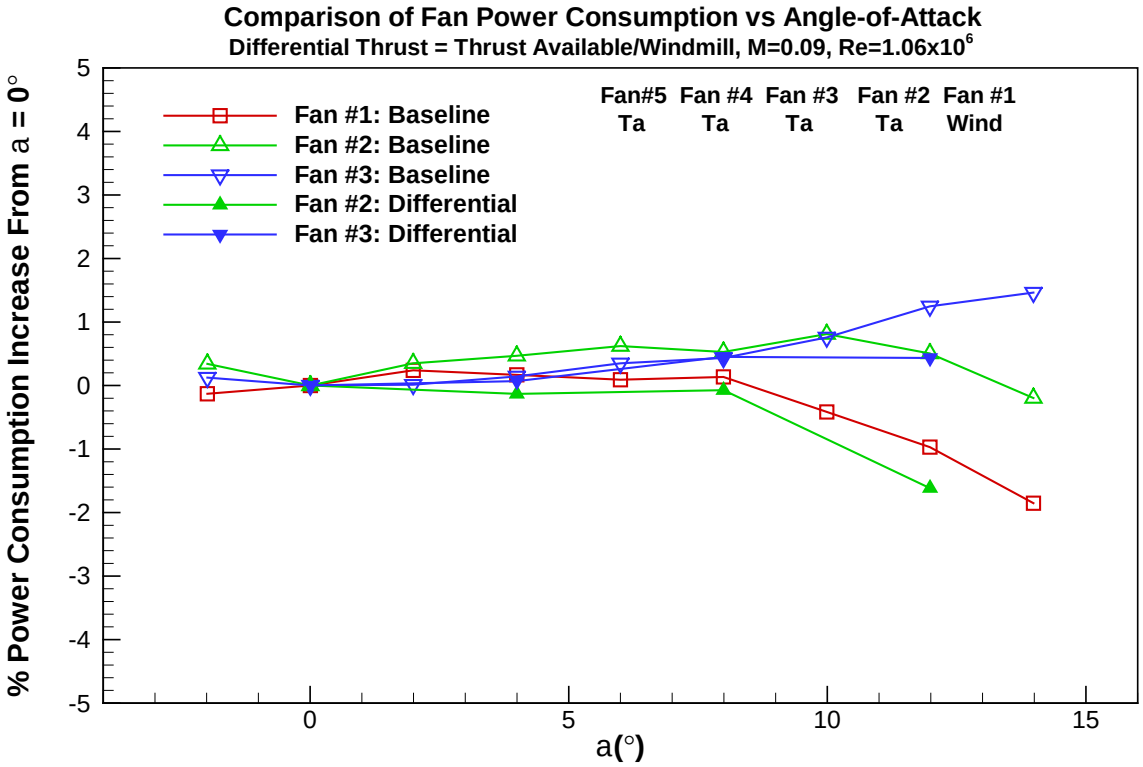

Figure 104: Comparison of fan power consumption as a function of angle-of-attack for the differential thrust available/windmill case, M=0.09, Re=1.06x10^6.

As was observed for the force and moment and surface pressures, the results shown in Figure 105 for the sectional lift characteristics for the differential thrust available results mimic those observed for the thrust required case. No significant difference in sectional lift coefficient is observed at the lower angles-of-attack. At a=12°, the sectional lift coefficient for the windmilling #1 fan is observed to drop, with a loss in C_l for the windmilling fan is ΔC_l = -0.15. This loss in the lift coefficient is not substantially higher than that observed for the thrust required case. Again, the loss in lift coefficient is confined to the windmilling fan. No effect of the windmilling fan is observed in the #2 or #3 fan integrations.

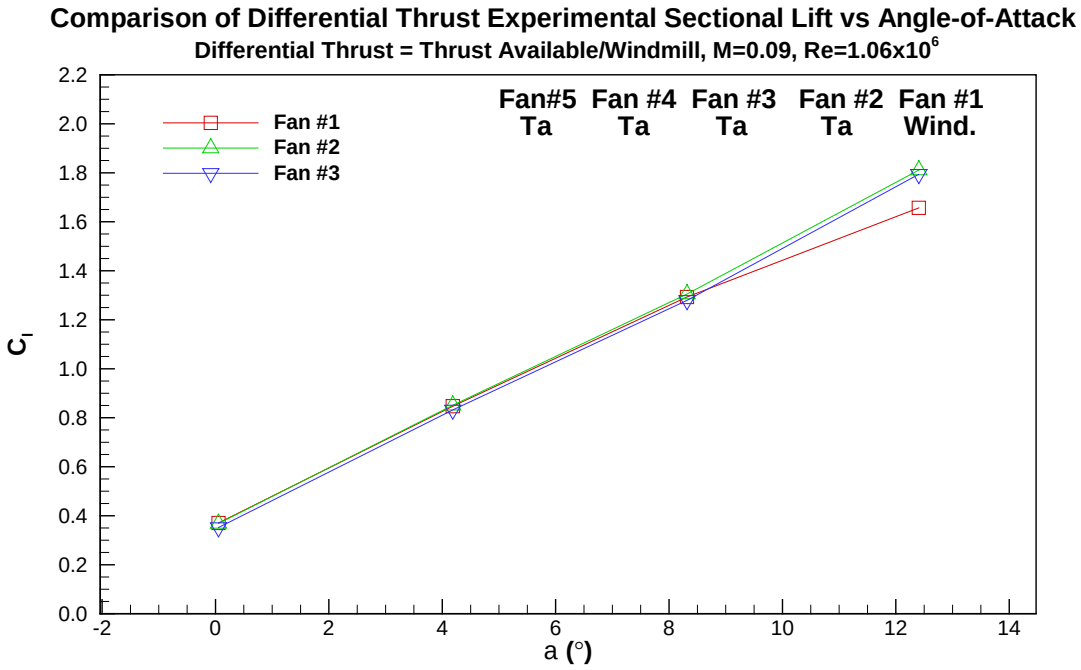

Figure 105: Comparison of differential thrust experimental sectional lift versus angle-of-attack for the thrust available/windmill case, M=0.09, Re=1.06x10^6.

7.4.5.3. T_a T_a T_a T_a T_r Results

The next differential thrust case investigated was the mixed thrust available/thrust required case. For the mixed thrust available differential case the #1 fan was set to the thrust required condition, with fans #2-#5 set at the thrust available setting. Force and moment results for the thrust required/windmill case at M=0.09, Re=1.06x10^6 are shown in Figure 106.

Also shown in Figure 106 are the computational predictions, the baseline thrust available results discussed in Section 7.4.3, and the thrust available/windmill differential results discussed in Section 7.4.5.2. Since the thrust required setting for the #1 fan lies between the thrust available and windmill setting, one would expect the mixed thrust available/thrust required results to lie between the baseline thrust available and thrust available/windmill differential results. From Figure 106, the lift curve results show that the mixed thrust available/thrust required differential results show only a negligible loss on overall C_L. The mixed differential results essentially lie on the baseline thrust available lift curve.

The drag results shown in Figure 106 for the mixed differential thrust available/thrust required case lie between the baseline thrust available and the thrust available/windmill results as expected. The drag delta between the baseline thrust available data and the differential thrust available/windmill case is ≈150 counts. This difference reduces to ≈65 counts for the mixed thrust available/thrust required case. The delta between the three cases remains fairly constant

with angle-of-attack. As would be expected, based on the previous differential results, the differential thrust setting has no effect upon the moment. Surface pressures for the three individual fans at angles-of-attack of 0°, 4°, and 8° are shown in Figure 107 for the mixed differential thrust available/thrust required results. Also included in Figure 107 are the computational predictions and the baseline thrust available pressures for comparison.

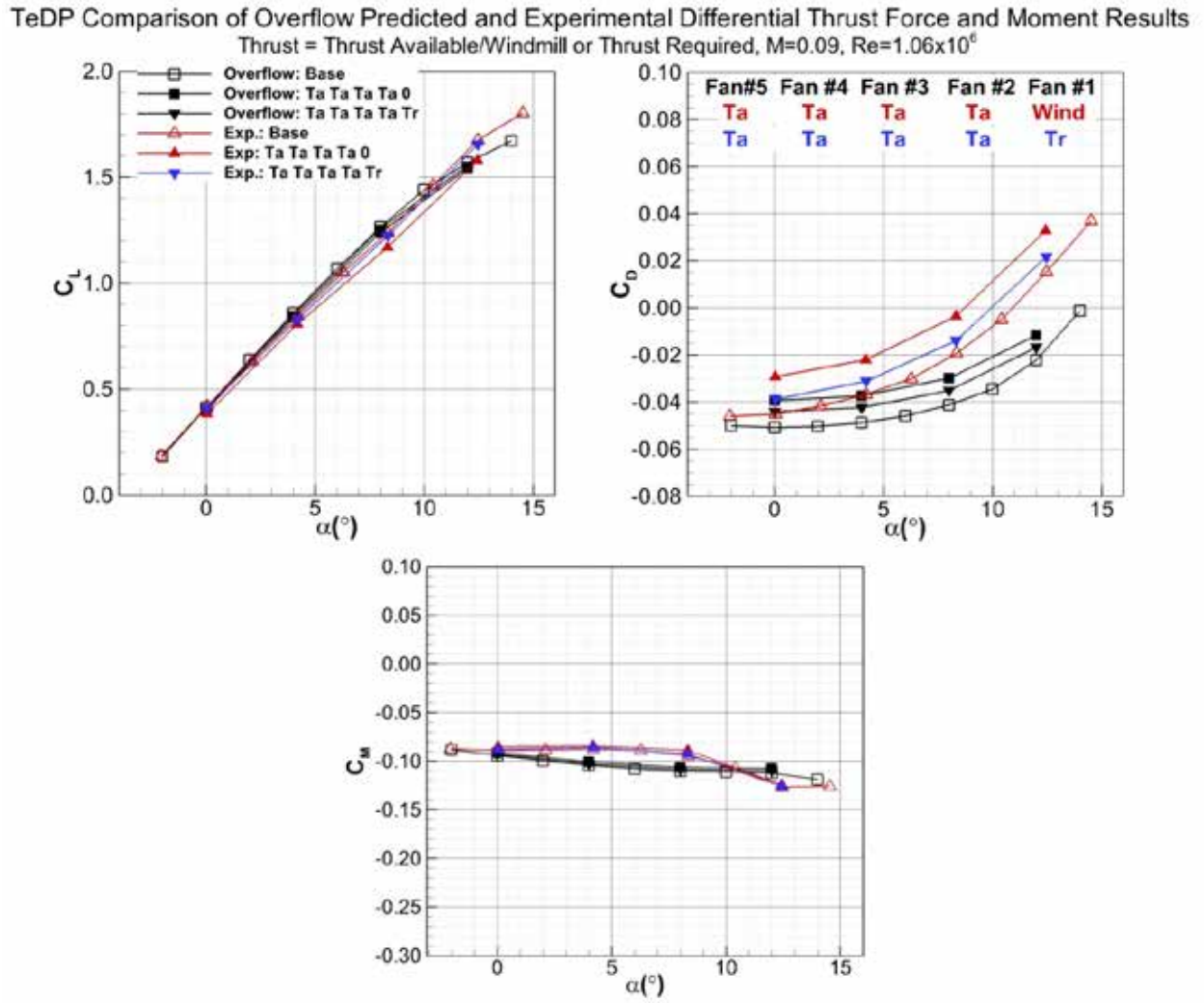

Figure 106: Comparison of TeDP OVERFLOW predicted and experimental differential thrust force and moment results for the thrust available/thrust required case, M=0.09, Re=1.06x10^6.

From Figure 107, as would be expected, the differences between the mixed differential results and the baseline thrust available results shown in Figure 103 are less for the mixed case as compared to the basic differential thrust available/windmill results. While differences are observed in the #1 fan between the baseline thrust available results and the mixed differential results, very little difference is observed in the #2 fan pressures, with no discernable differences observe in the centerline #3 fan. Again the computational results compare well to the differential pressures. As was observed for the previous two differential thrust cases, the effect of the #1 fan differential mass flow only affects the adjacent #2 fan. The influence of the reduced mass flow

fan is limited to the adjacent fan. A plot showing the fan power consumption as a function of angle-of-attack for the #1, #2, and #3 fans for the mixed differential thrust available/thrust required case is shown in Figure 108.

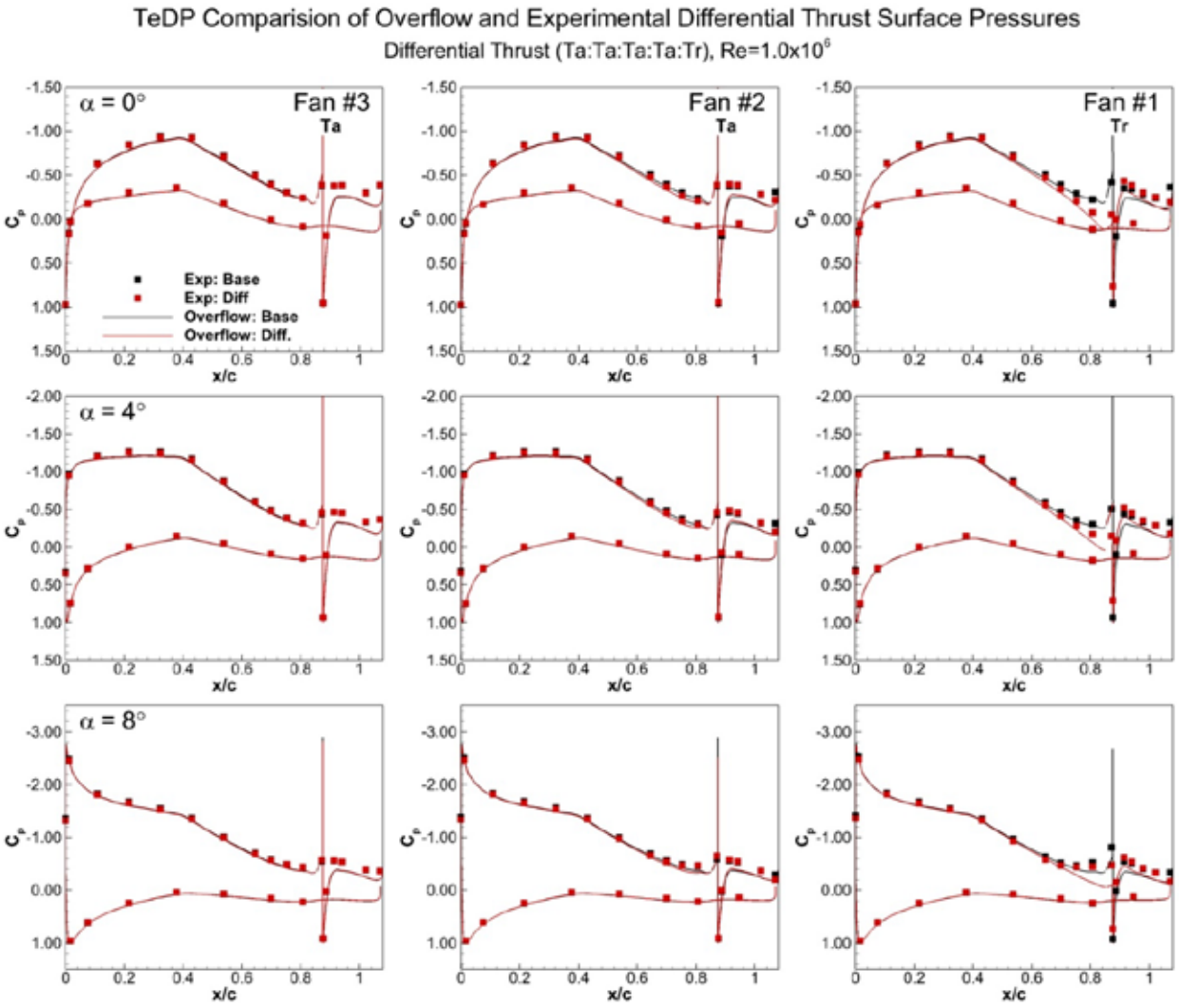

Figure 107: Comparison of OVERFLOW and experimental surface pressures for a centerline cut for Fans #1 to #3 for the baseline thrust available and differential thrust available/thrust required case, α=0°, 4°, 8°, M_{∞}=0.09, Re=1.06x10^6.

Also included in Figure 108 are the power consumption results for the baseline thrust available case. From Figure 108, the power consumption for the mixed differential thrust available/thrust required results compares well to the baseline thrust available results up through a=8°. Some differences are observed at a=12°. The mixed differential results remain at relatively the same levels for the #1 and #3 fans, and increase slightly #2 fan. These differences are small enough to

be a result noise or repeatability. Sectional lift coefficients integrated from the surface pressures for the differential thrust available case are shown in Figure 109.

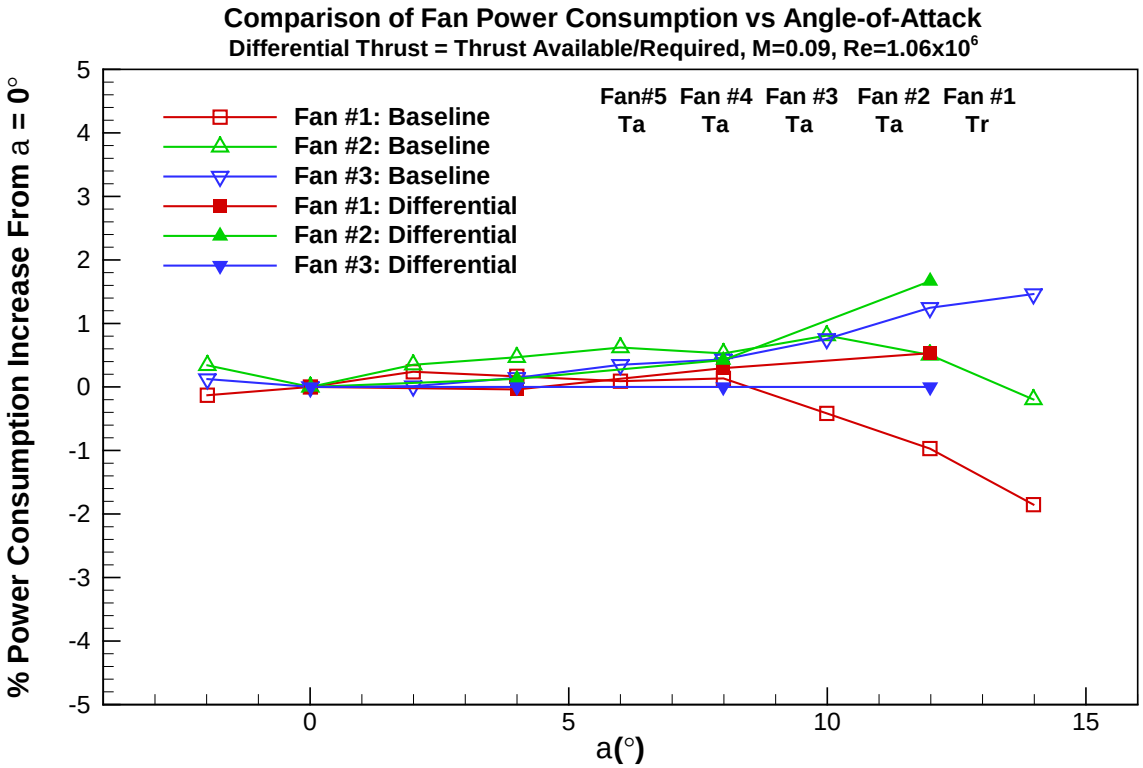

Figure 108: Comparison of fan power consumption as a function of angle-of-attack for the differential thrust available/thrust required case, M=0.09, Re=1.06x10^6.

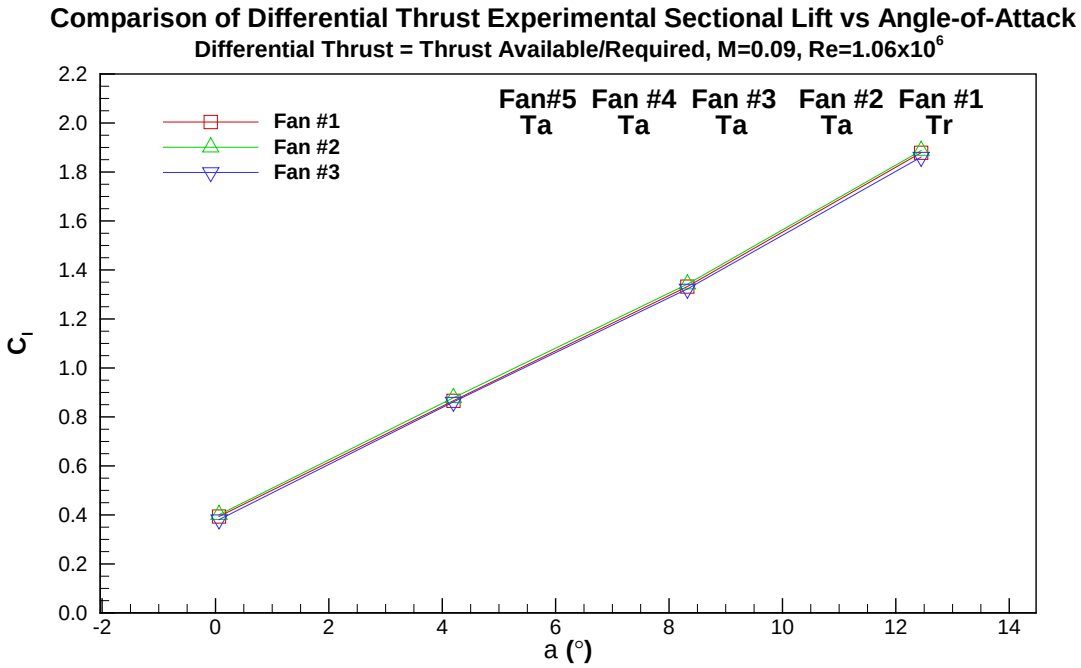

Figure 109: Comparison of differential thrust experimental sectional lift versus angle-of-attack for the thrust available/thrust required case, M=0.09, Re=1.06x10^6.

From Figure 109, no effect of the mixed differential thrust available/thrust required setting is observed in the sectional lift results. Based on the lift curve results shown in Figure 106, any effect would be small. The small relative change in mass flow between the thrust available and thrust required mass flows between the #1 and #2 fan do not produce effects large enough to be discernable in the integration for the limited number of taps available.

7.4.5.4. T_r T_r T_r Windmill Windmill Results

After completing the mixed differential thrust available/thrust required case, a thrust required dual windmill case was run. For the thrust required dual wind mill case the #1 and #2 fan were set to the windmill condition, with fans #3-#5 set at the thrust required setting. Force and moment results for the thrust required dual windmill case at M=0.09, Re=1.06x10^6 are shown in Figure 106.

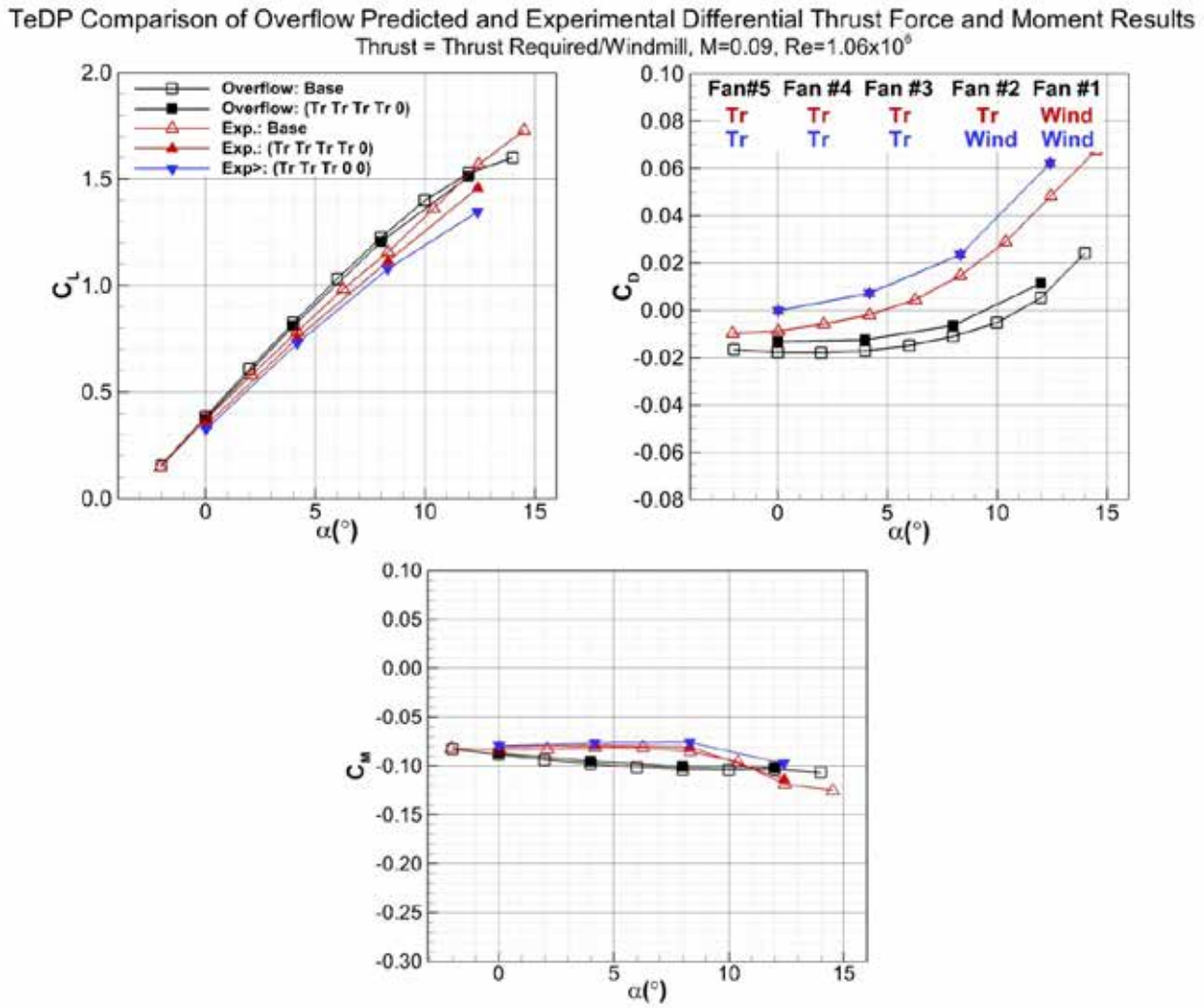

Figure 110: Comparison of TeDP OVERFLOW predicted and experimental differential thrust force and moment results for the thrust required/windmill/windmill case, M=0.09, Re=1.06x10^6.

No direct computational data is available for comparison to the thrust required dual windmill case. Also shown in Figure 110 are the computational predictions and experimental data for the baseline thrust required results discussed in Section 7.4.2, and the thrust required/windmill differential results discussed in Section 7.4.5.1. Since the thrust required dual windmill doubles the blockage of the basic differential thrust required/windmill a larger reduction in lift and increase in drag would be expected. From Figure 110, the lift curve results show an increased loss of lift as compared to the basic differential thrust required/windmill results. At α=6° the difference between the baseline thrust required lift coefficient and the differential thrust required/windmill lift coefficient is ΔC_L = -0.05. This loss in lift increases to ΔC_L = -0.08, slightly less than double the basic single fan windmill case. The difference between the basic single fan windmill and the dual fan windmill lift loss also appears to increase with increasing angle-of-attack.

The drag results shown in Figure 110 for the differential dual thrust required/windmill case show a higher drag for the dual windmill case as compared to the single windmill results as expected. The drag delta between the baseline thrust required data and the differential thrust required/windmill case is ≈100 counts. This difference increases to ≈150 counts for the dual thrust required/windmill case. As was observed for the other differential thrust cases, the delta between the three cases remains fairly constant with angle-of-attack. Unlike the previous differential thrust cases, however, a slight reduction in the moment is observed for the differential dual thrust required/windmill case at higher angles-of-attack. Surface pressures for the three individual fans at angles-of-attack of 0°, 4°, and 8° are shown in Figure 111 for the dual differential thrust required/windmill results. Also included in Figure 111 are the computational and experimental results for the baseline thrust required results and the basic thrust required/windmill differential results.

From Figure 111, as would be expected, the dual thrust required/windmill results show increased separation upstream of the windmilling fans. It is interesting to note that the separation upstream of the #1 fan is slightly increased as compared to the single windmilling fan results. Since the #2 fan is also now windmilling, increased separation is observed upstream of the #2 fan as compared to the single windmilling case. Finally, since the #2 fan is now windmilling, the #3 fan also shows separation upstream of the inlet due to the increased blockage from the #2 fan. The level of increased separation in the #3 fan, however, appears to not be any greater than that would be observed between the #1 and #2 fan for the single windmilling case, indicating that the separation, or spanwise effect is not additive. A plot showing the fan power consumption as a function of angle-of-attack for the #1, #2, and #3 fans for the dual differential thrust required/windmill case is shown in Figure 112.

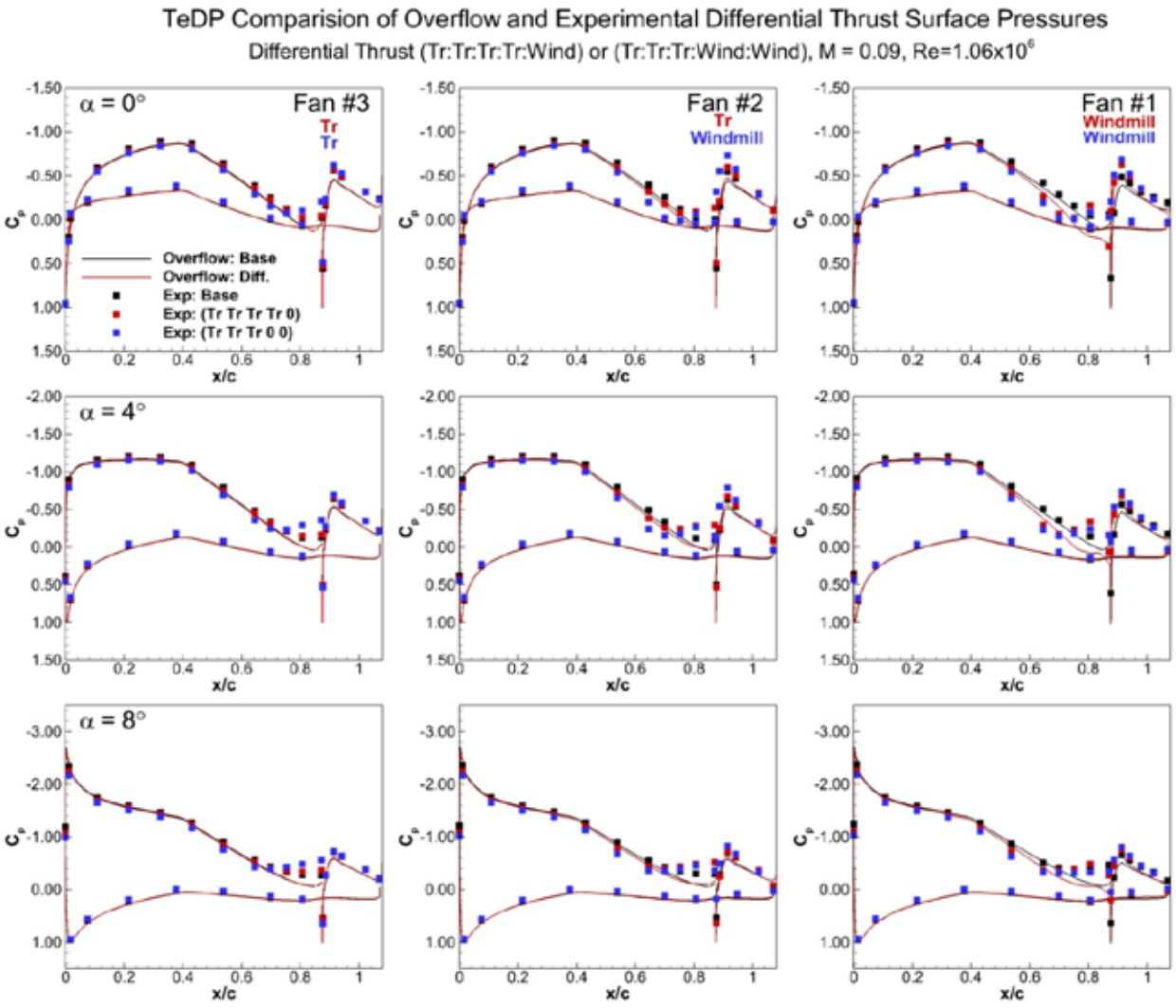

Figure 111: Comparison of OVERFLOW and experimental surface pressures for a centerline cut for Fans #1 to #3 for the baseline thrust required and differential thrust required/windmill/windmill case, α=0°, 4°, 8°, M_{∞}=0.09, Re=1.06x10^6.

Also included in Figure 112 are the power consumption results for the baseline thrust required case and the basic differential thrust required/windmill results. Since only the #3 fan is operating for the dual differential thrust required/windmill case, only the #3 fan power consumption is shown. From Figure 112, the power consumption for the dual differential thrust required/windmill results compares well to the baseline thrust required results and the basic differential thrust required/windmill results. No significant differences are observed between the #3 fan for the single or dual windmilling cases. Sectional lift coefficients integrated from the surface pressures for the dual differential thrust required/windmill case are shown in Figure 113.

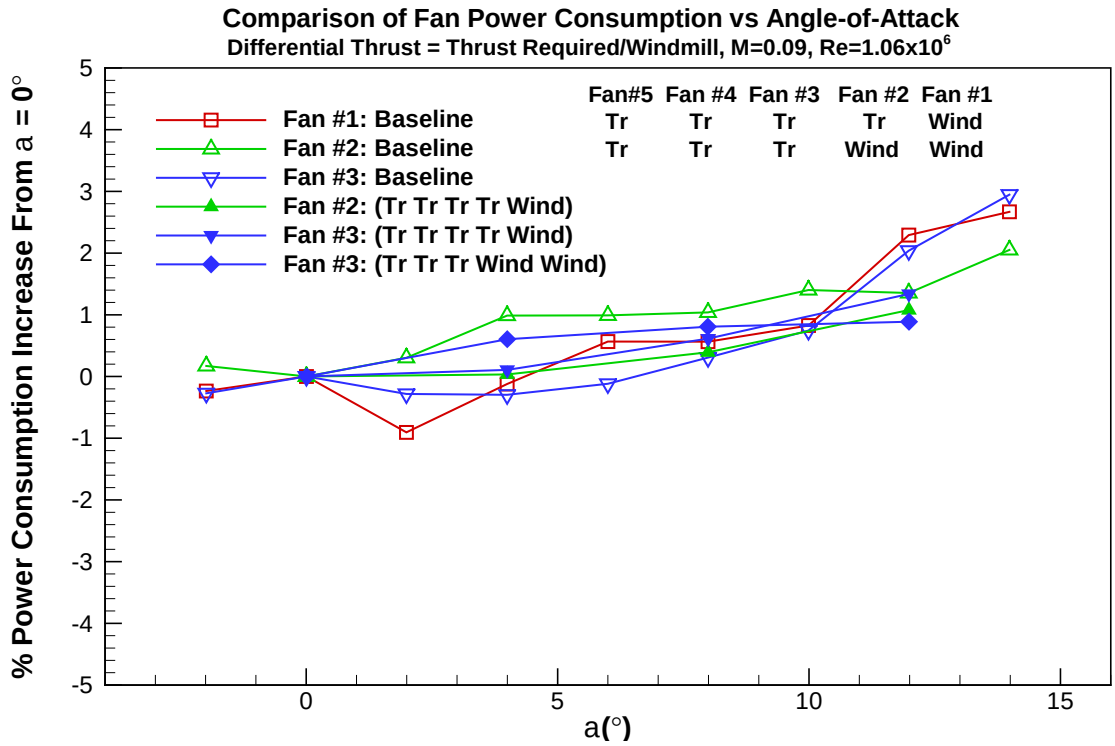

Figure 112: Comparison of fan power consumption as a function of angle-of-attack for the differential thrust required/windmill/windmill case, M=0.09, Re=1.06x10^6.

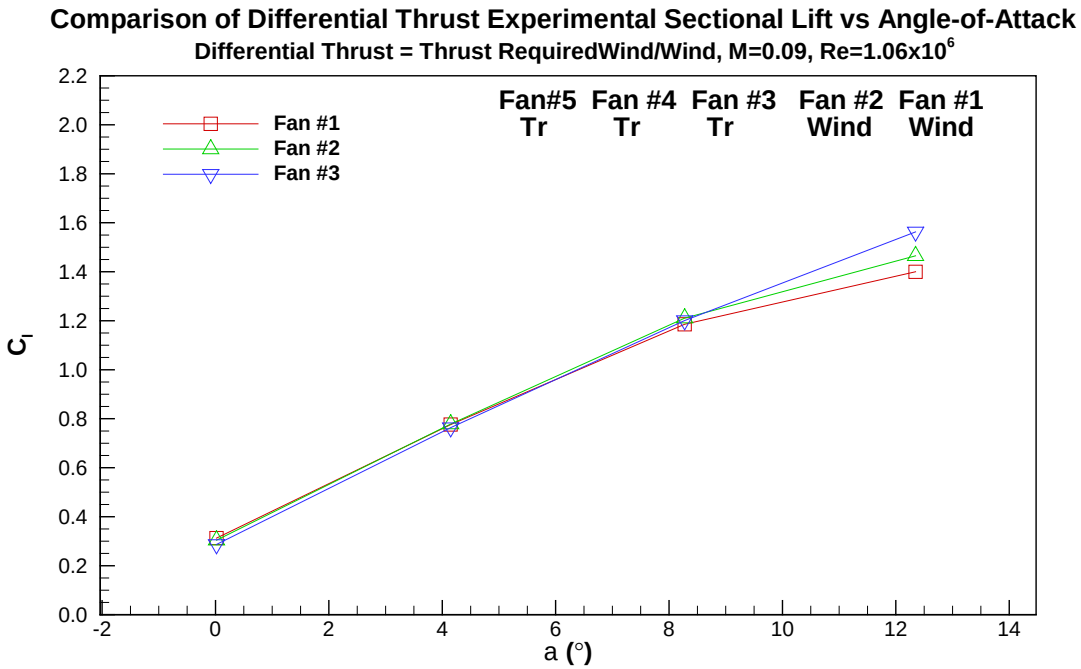

Figure 113: Comparison of differential thrust experimental sectional lift versus angle-of-attack for the thrust required/windmill/windmill case, M=0.09, Re=1.06x10^6.

As would be expected, the results shown in Figure 113 show an increasing loss in sectional lift coefficient from the #3 to the #2 fan, and then from the #2 to the #1 fan at higher angles-of-

attack. No significant difference in sectional lift coefficient is observed at the lower angles-of-attack. At a=12°, the sectional lift coefficient for the windmilling #1 fan is ΔC_l = -0.160, reducing to ΔC_l = -0.10 for the #2 fan. The ΔC_l = -0.160 loss in the lift for the #1 fan is slightly larger than that observed for the basic single windmill differential case shown in Figure 101, at ΔC_l = -0.130. This higher loss for the outboard fan is not unexpected as it is being effected on one side by the baseline airfoil section separation, and on the other side by the windmilling fan blockage.

7.4.5.5. T_r T_r Windmill T_r T_r Results

The final differential thrust case investigated was a thrust required/windmill case where fans #1, #2, #4 and #5 were set to the thrust required setting, with the centerline #3 fan at the windmill condition. Force and moment results for the thrust required center windmill case at M=0.09, Re=1.06x10^6 are shown in Figure 114.

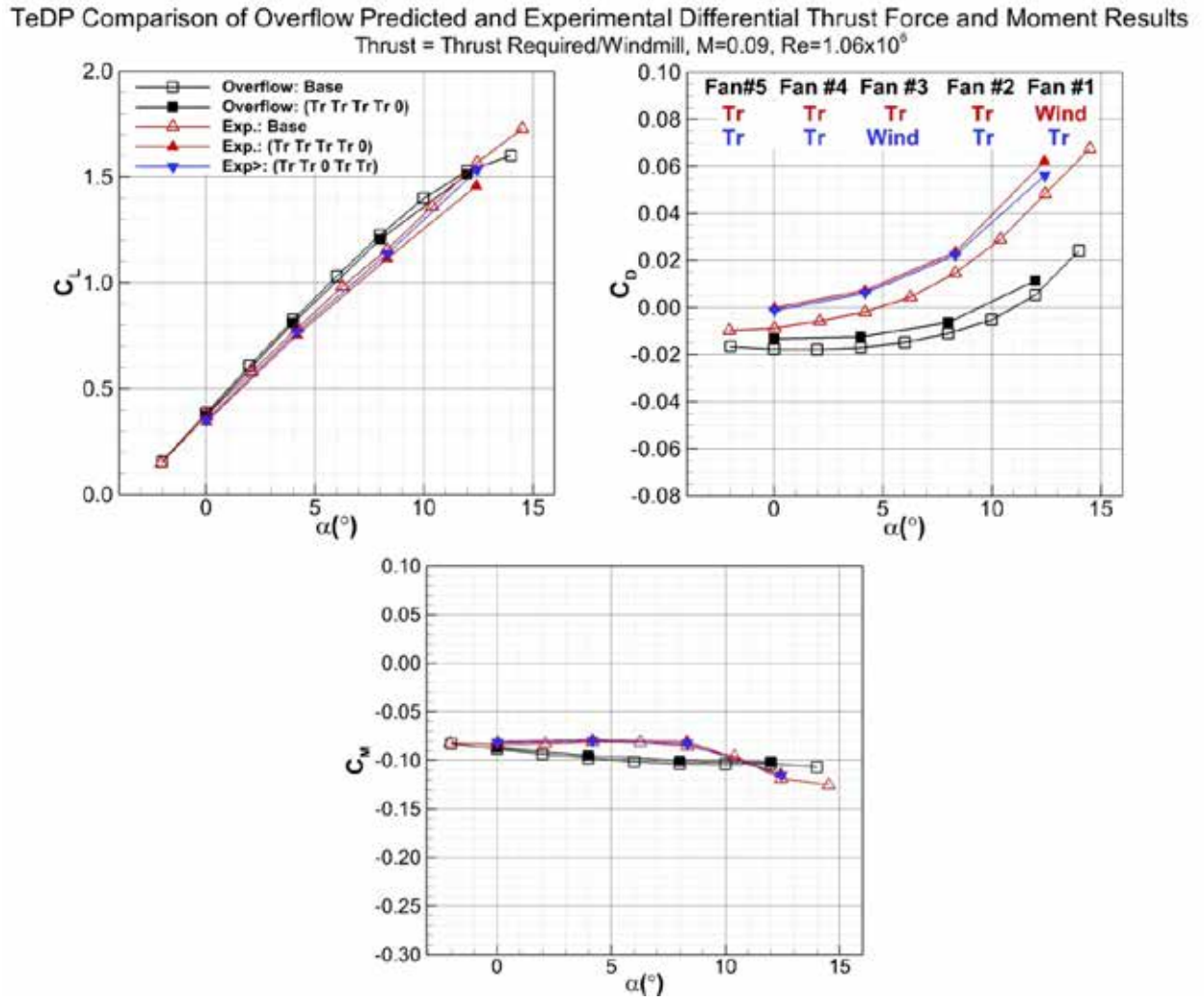

Figure 114: Comparison of TeDP OVERFLOW predicted and experimental differential thrust force and moment results for the thrust required/windmill/thrust required case, M=0.09, Re=1.06x10^6.

As with the dual differential thrust required/windmill case, no direct computational data is available for comparison to the thrust required centerline windmill case. Also shown in Figure 114 are the computational predictions and experimental data for the baseline thrust required results and the thrust required/windmill differential results. From Figure 110, the lift curve results show a negligible loss in lift between the baseline thrust required results and the differential thrust required centerline windmill case. These results are interesting and were only observed for the mixed differential thrust available/thrust required case. The centerline fan is isolated from the baseline airfoil by operating fans on either side. These operating fans appear to reduce the effect of the centerline fan windmill condition. The drag results, however, do show the effect of the windmilling centerline fan. Interestingly, at angles-of-attack up though a=8°, the drag results for the centerline windmill case compare well to the basic differential thrust/windmill case. At a=12°, the drag for the centerline windmill case is slightly lower than the basic differential thrust/windmill results. The drag for the basic differential thrust/windmill case is higher at a=12° since the #1 fan blockage induced separation is increased due to its interaction with the baseline outer airfoil separation. As would be expected for this case, no effect upon the moment is observed. Surface pressures for the three individual fans at angles-of-attack of 0°, 4°, and 8° are shown in Figure 115 for the differential thrust required centerline case. Also included in Figure 115 are the computational and experimental results for the baseline thrust required results and the basic thrust required/windmill differential results.

From Figure 115, as would be expected, the centerline windmill results are a mirror image to the basic differential thrust/windmill results where the outboard fan is set at the windmill condition. The effect upon the #2 fan is roughly equivalent for either the centerline #3 fan windmilling or the outboard #1 fan windmilling. A plot showing the fan power consumption as a function of angle-of-attack for the #1, #2, and #3 fans for the differential thrust required centerline windmill case is shown in Figure 116. Also included in Figure 116 are the power consumption results for the baseline thrust required case, the basic differential thrust required/windmill results, and the thrust required dual windmill case.

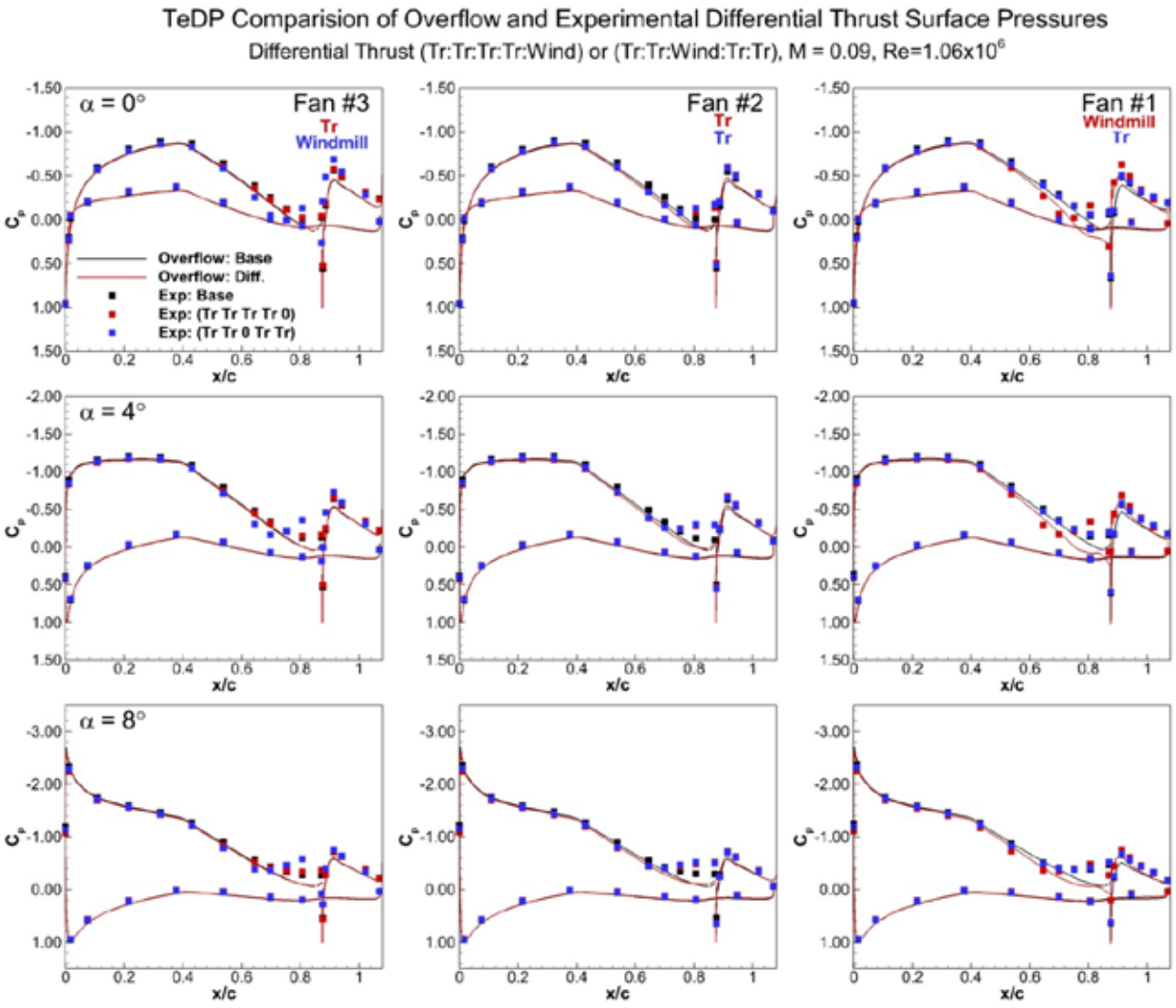

Figure 115: Comparison of OVERFLOW and experimental surface pressures for a centerline cut for Fans #1 to #3 for the baseline thrust required and differential thrust required/windmill/thrust required case, $\alpha=0°, 4°, 8°$, $M_\infty=0.09$, $Re=1.06x10^6$.

From Figure 116, as was observed for the basic differential thrust required and the dual windmill thrust required case, no significant differences are observed between the power consumption for the single, dual, or centerline windmilling cases. Sectional lift coefficients integrated from the surface pressures for the dual differential thrust required/windmill case are shown in Figure 117.

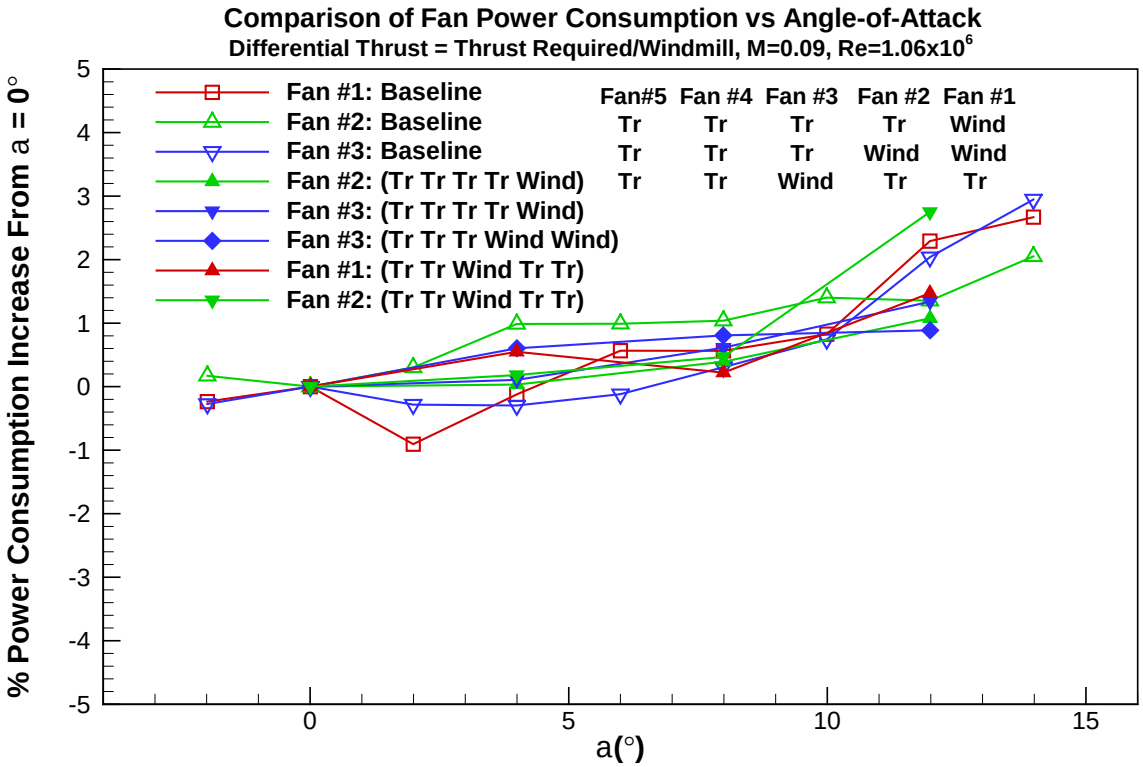

Figure 116: Comparison of fan power consumption as a function of angle-of-attack for the differential thrust required/windmill/thrust required case, M=0.09, Re=1.06x10^6.

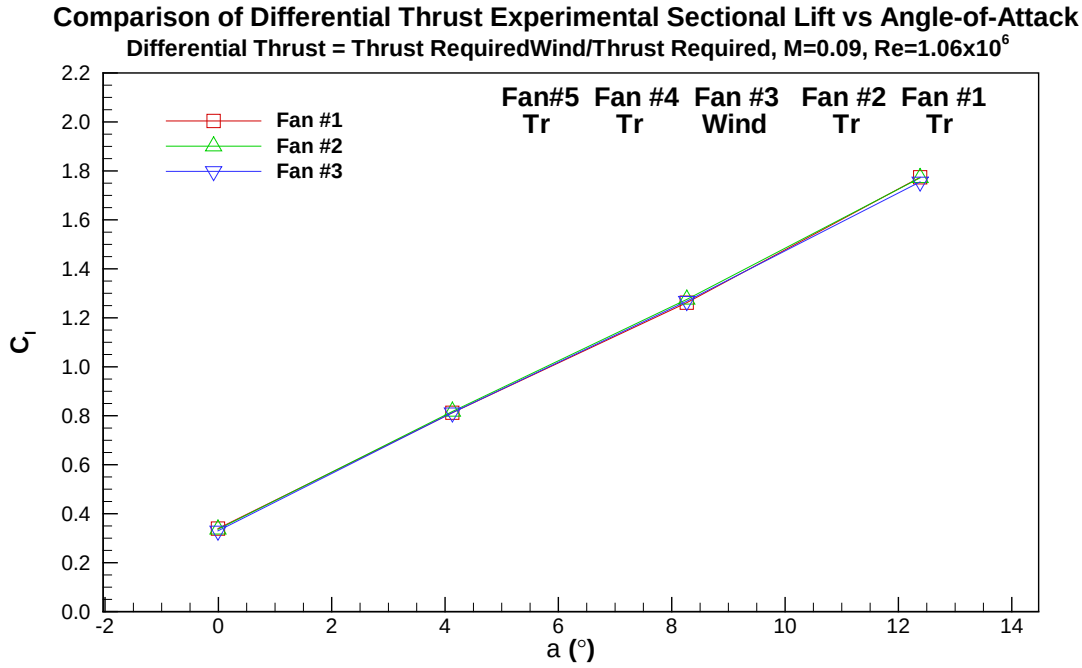

Figure 117: Comparison of differential thrust experimental sectional lift versus angle-of-attack for the thrust required/windmill/thrust required case, M=0.09, Re=1.06x10^6.

As was observed for the mixed differential thrust required/thrust available results, no effect of the differential thrust required centerline windmill setting is observed in the sectional lift results. Noting the lift curve results shown in Figure 114, any effect would be small.

7.4.5.6. Differential Results Summary

Results from the differential thrust study showed that other than the increased separation upstream of the inlets due to the presence of the fan blades that were not modelled in the CFD, the computational results compared well the experimental data. All of the major flowfield features present in the computational predictions were observed in the experimental results. The differential thrust data provided several important insights into the effect of differential thrust on the distributed propulsion flowfield. The most significant of these insights is that the blockage produced by a reduced mass flow fan only affects the adjacent fan, and does not extend beyond the adjacent fan. Also, increased blockage and spillage produced by a low mass flow condition in an outer fan that borders the baseline airfoil will interact with the separation of the baseline airfoil, increasing the effect upon the windmilling fan. A low mass flow fan that is shielded on either side by a higher mass flow fan will have a lower overall effect upon the force and moment results. Slight reductions in lift curve were observed for the majority of the differential thrust cases, with the most notable effect being increased drag as would be expected. Almost no effect upon the moment was observed.

7.4.6. Experimental Results Summary

A successful final wind tunnel verification test of the 5 fan pseudo 3D TeDP model was conducted in the UIUC ARL low-speed 3 ft x 4 ft facility. The tunnel entry measured overall model lift, drag, and pitching moment. Surface pressures were also obtained from multiple spanwise pressure rows, along with internal duct pressures. Unfortunately, due to heating issues with the motor controllers, no 5-hole probe wake data were obtained.

Overall, the experimental results compared well with the experimental data. All major flowfield features and trends present in the computational predictions were observed in the experimental results. Considering the complexity of the TeDP model, both computationally and experimentally, the comparison seems quite good. As was observed in the computational results, variations in thrust level between the thrust required and thrust available levels showed that while differences in force and moment results exist with thrust level, they are generally smaller than were anticipated. Changes in lift of 3%-4% between the thrust required and thrust available mass flows were observed in the CFD (for the wind tunnel model area), with 5%-6% observed in the experimental data.

Separation was observed upstream of the inlet for the thrust required case at moderate angles-of-attack, increasing in extent with increasing a. The CFD did not predict the separation upstream of the inlet. Noting the performance of the CFD in predicting the baseline airfoil separation, this is not wholly unexpected. The separation is a result of the fan operating at below its design mass

flow condition, creating a more severe adverse pressure gradient upstream of the inlet. It should be noted that in an actual flying aircraft, as the angle-of-attack is increased, the throttle and fan mass flow would also be increased to maintain level flight due to the increase in drag. This increase in mass flow would most likely reduce or eliminate the presence of the separation. The lift curve results for the thrust available data compare better to the computational predictions than the thrust required results. This is also true for the surface pressures. The better comparison between the thrust available data can be attributed to the increased fan mass flow creating a less severe adverse pressure gradient into the fan, significantly reducing the amount of local separation upstream of the fan.

Both the thrust required and thrust available cases showed increases in maximum lift for the section. While separation upstream of the inlets were observed at high angles-of-attack for both the thrust required and thrust available mass flows, no loss in suction peak pressures were observed for either case. For a traditional airfoil with trailing-edge separation, the suction peak is usually reduced, along with the magnitude of the upper surface pressures. This was not observed for the TeDP model. This maintaining of the suction peak pressures at higher angles-of-attack produced an increase in lift for the section. This behavior is attributed to the fan upper surface cowl remaining attached. The cowl most likely remains attached due to the fan jet Coanda effect upon the cowl.

Drag of the TeDP model was higher than that of the CFD predictions. The majority of this difference in drag can be attributed the presence of a combination of the motor wires present in the thrust stream and their routing on the lower surface of the model, and the tail cone opening to allow for motor cooling.

Several differential thrust cases were run. The differential thrust results provided several key insights into the effect of differential thrust on neighboring inlets for a distributed propulsion configuration. The most significant of these insights is that the blockage produced by a reduced mass flow fan only affects the adjacent fan, and does not extend beyond the adjacent fan.

8. Conclusions

The Phase II TeDP program focused on the detailed design and examination of a TeDP system for the proposed flying test bed aircraft. The overall objective of the Phase II program was to test a pseudo 3D wind tunnel model with a set of 5 BLI electric ducted fans mounted on a 2D straight wing. The test examined multi-fan effects on aerodynamic/propulsive coupling, BLI, and thrust based circulation effects. Specifically, the effect of thrust levels and mass flow on both the overall wing and sectional aerodynamic characteristics including lift, drag, and pitching moment were investigated. The test also focused on the effect of different thrust levels on the aerodynamics of higher angle-of-attack conditions. The effects of spanwise differential thrust, specifically the effects of changing mass flow and spillage on adjacent fan flowfield were also studied. Prior to the wind tunnel test, a detailed 2D and 3D computational fluid dynamics (CFD) study was performed to study thrust angle effects and to optimize the inlet and duct geometry.

The Phase II program has produced an extremely unique, first of its kind data set for multi-fan TeDP BLI configurations.

Prior to the CFD design and investigation of the TeDP model, a scaling study was performed to properly scale the wind tunnel model from the proposed flying test bed and to choose an appropriate commercially available ducted fan for use in the wind tunnel test model. Results from the scaling study show that multiple commercially available EDF units are capable of providing the thrust required to properly develop a sub-scale wind tunnel model capable of adequately representing the performance and characteristics of the full-scale vehicle. A Hyperflow 56 EDF was chosen with a 20 inch chord model for the NACA 64_3-618 section. This fan and model chord provided a good combination of thrust, boundary-layer to fan diameter ratio, and fan diameter to chord ratio at reasonable Reynolds numbers and acceptable wind tunnel blockage rations.

After completing the scaling study a 2D CFD study was performed to investigate thrust angle effects on aerodynamic/propulsive coupling in order to minimize coupling effects with changes in thrust/mass flow. Both thrust angle and thrust level were investigated in the 2D study. In several cases for the 2D study, separation was observed to occur on the fan plug. For the 2D geometry, the fan inlet, exit, and plug flowfield are rectangular. For the 3D geometry, the fan exit and plug flowfield are circular. It was believed that the circular aspect of the 3D plug flowfield would have a significant relieving effect, making the presence of the 2D separation questionable. As a result, no further optimization or study of the 2D geometry was performed in favor of moving to the 3D design.

For the 3D study, a design, optimization, and flowfield investigation of the multi-inlet TeDP configuration was undertaken. The 3D inlet design results showed interesting differences between the 2D and 3D results. The 2D results showed much larger thrust super circulation affects than the 3D results. The final 3D inlet area was sized using a weighted average of the thrust required and thrust available mass flows.

The results from the CFD thrust angle investigation showed that the fan thrust angle has a significant effect upon the lift, moment, and performance of the section. The fan thrust angle was found to directly affect the section's camber. Of the thrust angles investigated, an 11.4° thrust angle was found to best match the lift curve of the baseline NACA 64_3-618 section. While it was initially expected that this thrust angle would be the preferred geometry, the results of thrust angle investigation showed that higher thrust angle geometries also produced a significantly increased drag and more negative moment as compared to lower thrust angle cases. It was found that the large drag increase of the higher thrust angle geometries was primarily a result of increased pressure drag on the upper surface cowl due to the increased rotation of the cowl surface. While not matching the baseline NACA 64_3-618 section lift curve as well as some higher thrust angle geometries, a 5° thrust angle geometry was chosen as it produced a drag and moment comparable to the baseline section. Since the performance and efficiency of the TeDP configuration is of primary importance, the 5° geometry was chosen as the more optimal configuration.

After the CFD design, optimization, and flowfield study were performed, a wind tunnel model based of the design was constructed and tested. The final wind tunnel verification test was conducted in the UIUC ARL low-speed 3 ft x 4 ft facility. The tunnel entry measured overall model lift, drag, and pitching moment. Surface pressures were also obtained from multiple spanwise pressure rows, along with internal duct pressures. Unfortunately, due to heating issues with the motor controllers limiting run times, no 5-hole probe wake data were obtained.

Overall, the experimental results compared well with the computational predictions. All major flowfield features and trends present in the computational predictions were observed in the experimental results. Considering the complexity of the TeDP model, both computationally and experimentally, the comparisons were quite good. As was observed in the computational results, variations in thrust level between the thrust required and thrust available levels showed that while differences in force and moment results exist with thrust level, they are generally smaller than were anticipated based on previous 2D estimations. Changes in lift of 3%-4% between the thrust required and thrust available mass flows were observed in the CFD, with 5%-6% observed in the experimental data. These low thrust level/aerodynamic interactions are due to significantly 3D relieving effects coupled with the judicious choice of thrust angle for the geometry.

Both the thrust required and thrust available cases showed increases in maximum lift for the section. While separation upstream of the inlets were observed at high angles-of-attack for both the thrust required and thrust available mass flows, no loss in suction peak pressures were observed for either case. The ability to maintain a high leading-edge suction peak while experiencing separation upstream of the inlets at higher angles-of-attack produced an increase in lift for the section. This behavior is attributed to the fan upper surface cowl remaining attached. The cowl remains attached due to the fan jet Coanda effect upon the cowl.

Several differential thrust cases were run. The differential thrust results provided several key insights into the effect of differential thrust on neighboring fans for a distributed propulsion configuration. The most significant of these insights is that the blockage produced by a reduced mass flow fan only affects the adjacent fan, and does not extend beyond the adjacent fan. While small losses in lift were observed for individual fan differential cases, the most significant effect was an increase in drag. Larger lift losses were observed when an increasing number of fans were idled.

Overall, the results of the Phase II TeDP study were very successful. With the exception of not being able to obtain the 5-hole probe wake data, all program goals were met or exceeded. The program generated a very unique and valuable data set. Several key insights from the program are:

- While 2D results showed large coupling effects between fan mass flow and sectional characteristics, 3D relieving effects significantly reduced these effects.

- For the thrust required and thrust available fan mass flows investigated, changes in sectional characteristics of 5%-6% were observed in the experimental data. This lower than

expected coupling effect bodes well for a distributed propulsion configuration, lessening the effect of changing sectional characteristics with changing thrust level.

· High angle-of-attack results showed that the distributed propulsion section was able to maintain a high leading-edge suction peak even in the presence of significant separation upstream of the inlets. This ability to maintain a high suction peak produced increased lift at high angles-of-attack, delaying stall. This behavior is attributed to the fan upper surface cowl remaining attached. The cowl most likely remains attached due to the fan jet Coanda effect upon the cowl.

· Differential thrust results showed that the blockage produced by a reduced mass flow fan only affects the adjacent fan, and does not extend beyond the adjacent fan. While minor reductions in lift were recorded, the most significant effect was an increase in drag. Increasing the number of fans at idle or a lower mass flow condition increased the overall force and moment effect.

· While a fixed inlet lip geometry was shown to provide good performance for the current investigation, a movable inlet lip would provide a much wider range of separation free fan mass flow conditions.

9. Next Steps

Based on the results of the current investigation, a systems test bed and a larger scale wind tunnel test are recommended, using flight scale hardware. The larger scale test will not only develop and examine the full scale platform for the proposed flying test bed from both a structural and systems point of view, but a flight scale test will also provide an opportunity to develop the multi-fan control and battery management systems that would need to be developed in order to field a successful flying test bed aircraft. A larger scale test would also allow the advantages of a movable inlet lip to be investigated.

The TeDP concept shows significant promise from both an aerodynamic and systems stand point. The current investigation has shown that the low overall aero/propulsive interaction effects coupled with the advantages of a distributed system make the concept very attractive and deserving of further research.

10. References

[1] Kerho, M., "Turboelectric Distributed Propulsion Test Bed Aircraft," NASA LEARN Phase I final report, contract # NNX13AB92A, November, 2013.

[2] Drela, M., AVL, Software Package, Ver. 3.32, Cambridge, MA, 2012.

[3] *Flight Manual, USAF Series TG-14A Aircraft*, Ximango, F05611-00-DM-003, June 2, 2004.

[4] Barlow, J., Rae, W., and Pope, A., *Low-Speed Wind Tunnel Testing, 3rd Edition*, John Wiley and Sons, New York, 1999.

[5] McCormick, B., *Aerodynamics, Aeronautics, and Flight Mechanics*, John Wiley and Sons, New York, 1979.

[6] Abbott, I. H., and Von Doenhoff, A., E., *Theory of Wing Sections*, Dover Publications, New York, 1959.

[7] Nichols, R., H., and Buning, P., G., "User's Manual for OVERFLOW 2.2," Version 2.2, Aug. 2010.

[8] Raymer, D., P., *Aircraft Design: A Conceptual Approach*, American Institute of Aeronautics and Astronautics, Inc., Washington, D. C., 1992.

[9] Owens, L., R., Allan, B., G., and Gorton, S., A., "Boundary-Layer Ingesting Inlet Flow Control," *AIAA Journal of Aircraft*, Vol. 45, No. 4, July-August, 2008, pp. 1440.

[10] Schetz, J., A., *Boundary Layer Analysis*, Prentice Hall, New Jersey, 1993.

[11] White, F., M., *Viscous Fluid Flow, 2nd. Edition*, McGraw-Hill, New York, 1991.

[12] Drela, M., and Giles, M., "Viscous-Inviscid Analysis of Transonic and Low Reynolds Number Airfoils," *AIAA Journal*, Vol. 25, No. 10, October 1987, pp. 1347-1355.

[13] Braslow, A., and Knox, E., "Simplified method for determination of critical height of distributed roughness for boundary-layer transition at Mach numbers from 0 to 5," NASA TN 4363, 1958.

[14] Barlow, J. B., W.H. Rae, J., and Pope, A., *Low-Speed Wind Tunnel Testing*, John Wiley & Sons, Inc., NY, 3rd ed., 1999.

[15] Diebold, J., and Bragg, M.,. "Wake-Survey Technique for Iced Swept-Wing Aerodynamics", AIAA Journal, Vol. 53, No. 6 (2015), pp. 1712-1715.

REPORT DOCUMENTATION PAGE

Form Approved
OMB No. 0704-0188

1. AGENCY USE ONLY (*Leave Blank*)	2. REPORT DATE	3. REPORT TYPE AND DATES COVERED
	Sept 15, 2015	Phase II LEARN Final Report Mar. 16, 2014 to Sept. 15, 2015

4. TITLE AND SUBTITLE

Phase II LEARN Final Report: Turboelectric Distributed Propulsion Test Bed Aircraft

5. FUNDING NUMBERS

NNX14AF44A

6. AUTHOR(S)

Michael F. Kerho, Brian R. Kramer

7. PERFORMING ORGANIZATION NAME(S) AND ADDRESS(ES)

Rolling Hills Research Corporation
420 N. Nash Street
El Segundo, CA 90245-2822

8. PERFORMING ORGANIZATION REPORT NUMBER

TR15-003

9. SPONSORING/MONITORING AGENCY NAME(S) AND ADDRESS(ES)

NASA Dryden flight Research Center
COTR: Stephen Cumming
PO Box 273
Edwards, CA 93523-0273

10. SPONSORING/MENTORING AGENCY REPORT NUMBER

11. SUPPLEMENTARY NOTES

12a. DISTRIBUTION/AVAILABILITY STATEMENT

FAR 52.227-20 Rights in Data -- SBIR Program

12b. DISTRIBUTION CODE

13. ABSTRACT ***(Maximum 200 words)***

This report documents research performed under the Phase II LEARN project for the development of a turboelectric distributed propulsion test bed aircraft.

14. SUBJECT TERMS

TeDP, distributed propulsion, CFD, wind tunnel, aero/propulsive coupling, BLI

15. NUMBER OF PAGES

147

16. PRICE CODE

17. SECURITY CLASSIFICATION OF REPORT	18. SECURITY CLASSIFICATION OF THIS PAGE	19. SECURITY CLASSIFICATION OF ABSTRACT	20. LIMITATION OF ABSTRACT
Unclassified	Unclassified	Unclassified	Unlimited